Title
Nucleation and Growth of Pb Islands on Germanium Via Collective Diffusion

Author
Kim, Andrew

Publication Date
2022

Peer reviewed|Thesis/dissertation

Nucleation and Growth of Pb Islands on Germanium Via Collective Diffusion

By

ANDREW RAKYOUNG KIM
DISSERTATION

Submitted in partial satisfaction of the requirements for the degree of

DOCTOR OF PHILOSOPHY

in

Physics

in the

OFFICE OF GRADUATE STUDIES

of the

UNIVERSITY OF CALIFORNIA

DAVIS

Approved:

_____
Shirley Chiang, Chair

_____
Ching-yao Fong

_____
Donald Land

Committee in Charge

2022

ACKNOWLEDGEMENTS

I would like to first acknowledge Professor Shirley Chiang for her guidance throughout the entire research process. She was able to provide a good balance of autonomy while also being able to provide firm guidance when needed, and I found her vast knowledge of resources and options to be very illuminating in times when I felt lost. Between her seemingly infinite guidance and our more personal conversations, I regard her as a great mentor and friend.

I would also like to thank the late Professor Charles Fadley for his Surface Physics course, which provided me with a good theoretical foundation for my research. His expertise in X-Ray Spectroscopy (XPS) also was of great assistance when I was in the process of repairing the laboratory's XPS system. I also thank Professors Ching-Yao Fong and Donald Land for their support as members of my qualifying exam and dissertation committees.

In regard to the previous graduate students from this lab, I wish to acknowledge Yu Sato and Jason Giacomo, who helped me figure out how to use the LEEM when there was no one else to teach me. Yu Sato especially deserves special mention for her assistance during the extremely important repairs to the LEEM, when I was ill, with very unfortunate timing.

From the Physics Department, I would like to thank Dave Hemer (along with the entire machine shop crew), Seth Hillbrand, and Peter Klavins for their patience and expertise in helping me with the various repairs and troubleshooting that were very frequent at the lab. They were very professional, and my interactions with them were pleasant. I would also like to acknowledge undergraduate assistant Eli Baum, who may as well have been a graduate student with the level

of laboratory expertise he displayed. He was by far the most reliable undergraduate assistant with whom I have ever worked, and I wish him the best in his own graduate school career.

Next, I would like to acknowledge my friends outside the department. Firstly, I will begin with Hugo (Dermuda) Janacek, a recently graduated Physicist from Oxford, whom I met by chance at an online art community. Aside from sharing in our hobby of art, Hugo, as a theorist, used his stronger theoretical background to guide me in some tricky homework problems from my first-year classes. I also felt comfortable talking with him about my life as a graduate student, including my worries and frustrations. Secondly, I will mention my two very close friends, Kyle Doyle and Simon Dixon. To say I am grateful for their infinite patience and support in my endeavors would be a gross understatement. While they could not help with technical matters due to a lack of a physics background, their emotional and social support were vital to keeping me going through graduate school.

Lastly, but not least, I would like to thank my parents, not only for their unconditional support for everything I did, but also for their encouragement of my interest in science since early childhood. I like to think that it would be extremely difficult to find parents more loving and supporting than they.

ABSTRACT

Epitaxial growth of metal structures on semiconductor or other metal surfaces has been studied quite extensively in surface physics and materials science due to its potential applications towards nanotechnology as well as for fundamental research purposes. In particular, the Pb/Ge(111) system, as well as the Pb/Si(111) system, has gained considerable attention due to its being a prototypical 2D metal-semiconductor interface with an abrupt boundary between the overlayer and substrate.

The work done in this dissertation was inspired by previous work done on Pb/Si(111) at low temperatures by Tringides *et al*. in which Pb, upon reaching a certain critical coverage, exhibited explosive nucleation of islands with a certain height selection as well as unusually fast diffusion rate during growth, a rare phenomenon called collective diffusion. Since silicon and germanium are both Group IV semiconductors with identical crystal structures, this study sought to perform Pb deposition on Ge(111) to see how the system would behave (diffusion rate, temperature dependence, etc.) under similar conditions.

Low Energy Electron Microscopy (LEEM) was the primary technique used to study the evolution of the Pb/Ge(111) system in real time, with some supporting data obtained from Scanning Tunneling Microscopy. In the first part of this dissertation, defects on the clean faces of germanium were studied under various cleaning parameters to determine a better set of parameters beyond the accepted ones to more consistently produce surfaces suitable for experiments. It was found that performing multiple sequences of sputter-anneal cycles using

different Ar^+ ion bombardment energies rather than a single energy resulted in eliminating more unwanted defects by targeting specific features at each bombardment energy.

Next, Pb was deposited on Ge(111) over multiple experiments, with each experiment performed at a fixed temperature between -30°C and room temperature. Below saturation coverages, Pb was found to form a single, amorphous wetting layer without any remarkable properties. Upon reaching a critical coverage, measured to be 1.33±0.07ML with respect to Ge(111), an explosive nucleation of Pb islands was observed. The average size of the islands and the island number density showed a relationship with the temperature, with lower temperatures corresponding with smaller average island size and larger island number density. Quantitative analysis of the islands during the very early stages of nucleation revealed that each island formed by the movement of hundreds of thousands of atoms over distances on the order of a hundred nanometers in just a few seconds. It was found that part of the island nucleation was fueled by relieving compression in the wetting layer, as the 1.33ML critical coverage amounted to about 2% compression of the Pb atoms beyond the bulk Pb(111) value. Further analysis of the island growth with additional deposition beyond the nucleation phase was performed with assistance from our collaborators at the University of Central Florida (V. Stroup, T. Panagiotakopoulos, A. Childs, D. Le, T.S. Rahman), and the island growth rate was found to be linear with coverage, which is the rate for collective diffusion as compared to the $t^{1/2}$ dependence of classical diffusion. Our collaborators also provided simulations of chemical potential and the binding sites of the Pb/Ge(111) system as theoretical explanations for the experimental observations.

To verify the heights of the Pb islands, quantum size contrast in the LEEM intensity of the islands was measured with respect to the start voltage of the electron beam used to illuminate

the surface (IV curve). A Kronig-Penney model was used to simulate islands of various thicknesses, from which the reflectivity coefficient was calculated for each electron energy to produce simulated IV curves. The simulated curves were then matched with experimental IV curves until a proper fit was found. Using this technique, an island grown at -24°C was found to have a height of 7 Pb layers, while an island grown at +3°C was found to be a hybrid of 10 and 11 layers due to its growing over a step edge.

Lastly, Pb was deposited on the other germanium faces (100 and 110) in an effort to see how the different surface symmetry would affect island growth under similar conditions. Pb/Ge(100) exhibited very similar behavior, with explosive nucleation of Pb islands upon reaching a critical coverage, which was unsurprising given the highly-symmetric surface structure of Ge(100), similar to the three-fold symmetry of the Ge(111) surface. The critical coverage appeared to be dependent on the density of surface defects on the substrate, with the critical coverage measured up to 2.53±0.03ML with respect to Ge(100) for one experiment, which is an exceptionally high value compared to Pb/Ge(111).

Pb/Ge(110) was found to produce thin, 1-dimensional islands that grew along the $[1\bar{1}0]$ axis and did not exhibit the same height selection as the other germanium faces. This is similar Ag/Ge(110), which was found to exhibit 1-dimensional growth due to the substrate's rectangular symmetry. For Pb, the critical coverage was measured to be 1.06±0.06ML with respect to Ge(110), and the islands grew linearly with time, exhibiting collective diffusion.

For both Pb/Ge(100) and Pb/Ge(110), classical, 3-dimensional islands were observed coexisting with the nonclassical islands in a narrow range of temperatures between 0°C and room temperature. 0°C was found to be the boundary between the classical regimes in which thermal

diffusion is the dominating force, and nonclassical regimes, with only the nonclassical islands nucleating below this temperature, both types of islands nucleating in the coexistence region, and only the classical islands nucleating above room temperature. The classical Pb/Ge(110) islands formed in triangular and trapezoidal shapes that showed preference in how they oriented themselves with respect to the Ge(110) surface, and this behavior was explained by the different stability of the island sides, due to different arrangements of atoms forming the sides, compared to the atoms on the substrate.

TABLE OF CONTENTS

Acknowledgements ii
Abstract iv
Table of Contents viii
List of Figures xi
List of Tables xiv
1 Introduction 1
2 Instrumentation 7
2.1 Overview 7
2.2 Sample Holder 8
2.3 Low Energy Electron Microscopy 11
2.3.1 Introduction 11
2.3.2 Illumination column 13
2.3.3 Beam Separator and Objective 16
2.3.4 Imaging Column 20
2.3.5 Discussion of Different Imaging Modes 24
2.4 Scanning Tunneling Microscopy 28
2.4.1 Introduction 28
2.4.2 Operating Principles 29
2.4.3 Oxford Instruments Tops-3 Variable Temperature STM 33
2.5 X-Ray Photoelectron Spectroscopy 38
2.5.1 Introduction 38
2.5.2 X-Ray Source 40
2.5.3 Electron Energy Analyzer 44
3 Ion Bombardment and Sample Cleaning 49
3.1 Introduction 49
3.2 Low-Index Germanium Faces 50
3.3 General Sample Cleaning Procedure 52
3.4 Pyramid Formation from Ge(110) Cleaning 53
3.5 Tuning Cleaning Parameters 55
3.6 Conclusion 62
4 Pb Island Nucleation and Growth on Ge(111) 64

4.1 Introduction 64
4.2 Experimental Details 71
4.3 Calibrations 76
4.3.1 Thermocouple 76
4.3.2 Evaporator 79
4.4 Results and Discussion 83
4.4.1 Island Nucleation 87
4.4.2 Continued Island Growth Towards High Coverage 96
4.5 Discussion of Theoretical Results 100
4.6 Conclusion 104
5 Island Height Verification 109
5.1 Introduction 109
5.2 Discussion of Quantum Size Contrast 111
5.3 Experimental Procedures 117
5.4 Results and Discussion 120
5.5 Conclusion 129
6 Pb on Other Germanium Faces 133
6.1 Introduction 133
6.2 Coverage Calibration 135
6.3 Results and Discussion 139
6.3.1 Pb/Ge(110) 139
6.3.2 Pb/Ge(100) 147
6.4 Conclusion 153
7 Conclusions and Future Work 156
7.1 Optimizing Cleaning Parameters 156
7.2 Pb/Ge(111) Islands at Low to Room Temperature 157
7.3 Pb/Ge(110) and Pb/Ge(100) 160
Appendix A: XPS Cooling System Interlock 162
A.1 Circuit Diagram for Interlock Controller 162
A.2 Arduino Code for Interlock Controller 164
Appendix B: Real vs Thermocouple Temperature Relationship 168
B.1 Discussion of Method and Results 168
B.2 MATLAB Code for Extrapolation 172

Appendix C: MATLAB Codes for IV Curve Analysis 174
C.1 Image Processing 174
C.2. Parameter Generation 176
C.3 IV Curve Simulation 177
C.4 Curve Fitting 180
Appendix D: Areas of Unit Cells and Coverage Conversions 182
Permissions to Reproduce Figures 184

LIST OF FIGURES

Figure 2.1 Layout of instruments in laboratory vacuum system 7
Figure 2.2 Diagram of sample holder 9
Figure 2.3 Photo of sample tilt calibration platform 10
Figure 2.4 Diagram of LEEM electron source 12
Figure 2.5 Photos of LEEM electron beam at two different Wehnelt voltages 13
Figure 2.6 Diagram of a single gap magnetic lens 14
Figure 2.7 Diagram of simple beam separator using uniform magnetic field.....17
Figure 2.8 Diagram of LEEM beam separator using triangular pole pieces 18
Figure 2.9 Electron optics diagrams for LEED and LEEM mode 21
Figure 2.10 Photo and diagram of electron microchannel plate 22
Figure 2.11 Defects on LEEM images 23
Figure 2.12 Simple STM diagram of sample and tip 29
Figure 2.13 Diagrams of constant height and constant current scanning modes 30
Figure 2.14 Diagrams showing density of states of the tip and sample and resulting tunneling current for different bias voltages.....32
Figure 2.15 Photos of Oxford STM with parts identified 34
Figure 2.16 Photo of STM scanner with parts identified 35
Figure 2.17 Photos of STM coarse movement mechanism and diagram of Z-wedge 36
Figure 2.18 Full XPS spectrum of Au/Ge(111) with some peaks identified 39
Figure 2.19 XPS spectra using Al and Mg K_α X-rays showing how Auger peaks move depending on the X-ray energy 41
Figure 2.20 Photo of X-ray source and hemispherical energy analyzer 42
Figure 2.21 Photos of XPS cooling system interlock controller 43
Figure 2.22 Photo of energy analyzer aperture, X-ray source, manipulator, and wobblestick inside the XPS chamber 44
Figure 2.23 Diagram of a simple hemispherical electron energy analyzer 46
Figure 3.1 Simple ball-and-stick models of the surface arrangement of unreconstructed low-index germanium faces 51
Figure 3.2 LEED patterns of clean, low-index germanium faces 52
Figure 3.3 STM topographical images of bare Ge(110) after various cleaning cycles 54
Figure 3.4 LEEM images of defects on the low-index germanium faces after cleaning using new procedures 55
Figure 3.5 LEEM images of defect evolution on Ge(111) and Ge(100) with Pb deposition 56
Figure 3.6 LEEM images showing “mountain range” defects on Ge(100) 57
Figure 3.7 LEEM images of defects on the low-index germanium faces after cleaning using old procedures, performed by previous student 61
Figure 4.1 STM image of Pb/Si(111) islands along with histogram of island heights 66
Figure 4.2 Low temperature phase diagram of Pb/Ge(111) island heights with respect to temperature and coverage 68
Figure 4.3 High temperature phase diagram of Pb/Ge(111) 71

Figure 4.4 Sequence of LEEM images showing the Pb/Ge(111) α $\left(\sqrt{3}\times\sqrt{3}\right)R30°$ to (1x1) phase transition 72
Figure 4.5 LEEM images of Pb/Ge(111) showing region damaged by electron beam 74
Figure 4.6 Plot of extrapolated real temperature of sample vs thermocouple reading 77
Figure 4.7 Photos of two Pb evaporator designs 80
Figure 4.8 Plot of Pb deposition rate as a function of time for basket type evaporator 81
Figure 4.9 Sequence of LEEM images showing Pb island nucleation and growth 85
Figure 4.10 LEEM images of growth sequences of Pb islands at multiple temperatures 86
Figure 4.11 Pb islands imaged 10s after nucleation for each temperature 88
Figure 4.12 Calculated Pb collection range for 3°C experiment displayed over LEEM image 89
Figure 4.13 Pb collection range for 3°C experiment plotted as function of percent wetting layer contribution 91
Figure 4.14 LEEM images of Pb/Ge(111) islands grown on a different Ge(111) sample at various temperatures 94
Figure 4.15 LEEM images of Pb/Ge(111) islands at two different temperatures and processed images using computer vision 97
Figure 4.16 Plots of normalized total island lateral size and normalized island number density as a function of Pb coverage 98
Figure 4.17 Plot of Pb chemical potential as a function of coverage 101
Figure 4.18 Ball-and-stick models of the three simulated binding sites of Pb/Ge(111) along with their binding energies 102
Figure 4.19 Simulated charge density maps of the three binding sites of Pb/Ge(111) 103
Figure 5.1 Diagram of modified Kronig-Penney model for a thin film of multiple layers 113
Figure 5.2 Simulated IV curves for Cu/W(110) from source material and reproduction of the same curves using independently-written MATLAB code 115
Figure 5.3 Experimental IV curves for Pb/Ge(111) islands and their wetting layers at two different temperatures 119
Figure 5.4 Experimental IV curves of the wetting layer with simulated IV curves superimposed 122
Figure 5.5 Topographical STM image of the Pb wetting layer after heating to room temperature, along with a profile graph 124
Figure 5.6 Simulated IV curves for three different layer numbers superimposed on the experimental IV curves for a -24°C island 125
Figure 5.7 Simulated IV curves for two different layer numbers and their hybrid superimposed on the experimental IV curves for a 3°C island 127
Figure 6.1 Sequences of LEEM images of the Pb/Ge(100) (2x1) to (5x1) phase transition 136
Figure 6.2 LEED patterns of the c(8x4) and (5x1) phases of Pb/Ge(100) 137
Figure 6.3 Sequence of LEEM images of Pb/Ge(110) island growth at 4°C 138
Figure 6.4 Plot of the length of a Pb/Ge(110) island as a function of additional coverage 139
Figure 6.5 LEEM image of 4°C Pb/Ge(110) islands imaged at different start voltage 140
Figure 6.6 Sequence of LEEM images of Pb/Ge(110) islands during annealing at fixed coverage 141
Figure 6.7 LEEM image of Pb/Ge(110) islands grown at -4°C, showing much smaller islands 142

Figure 6.8 LEEM image of Pb/Ge(110) showing imprints of 1D islands after islands had collapsed from annealing 143
Figure 6.9 LEEM image of Pb/Ge(110) islands after re-cooling and after additional deposition, showing faceted islands 145
Figure 6.10 Diagrams showing the possible arrangement of faces of the faceted Pb/Ge(110) islands 146
Figure 6.11 Sequence of LEEM images showing the growth of Pb/Ge(100) islands at various coverages 148
Figure 6.12 LEEM images showing 3D Pb/Ge(100) islands at low and high temperatures 149
Figure 6.13 LEEM image of height-selected Pb/Ge(100) islands on a different Ge(100) sample, showing reduced coexistence with 3D islands 150
Figure 6.14 LEEM image of bare Ge(100) surface showing a high defect density 152
Figure A.1 Circuit diagram of the XPS cooling interlock controller 162
Figure B.1 Plot of real temperature of Ge(111) sample as a function of thermocouple reading, showing a linear relationship 169
Figure B.2 Plot of first extrapolation of real temperature vs thermocouple temperature 170
Figure B.3 Plot of extrapolation of real temperature vs thermocouple temperature, including low temperature extrapolations 172
Figure D.1 Ball-and-stick models of the three low-index germanium faces along with the areas of the primitive unit cells 182

LIST OF TABLES

Table 3.1 Properties of germanium ……50
Tab.e 4.1 Calculated values related to nucleation and growth of Pb/Ge(111) ……87
Table 5.1 KP simulation parameters used for best fit to experimental curves ……128
Table D.1 Unit cell values for various surfaces used in the dissertation ……183

1 INTRODUCTION

Surface science continues to grow as a field with the advancement of nanotechnology and computing to tackle a fundamental issue that arises from the continued miniaturization of components – as objects become smaller, their surfaces become the dominating features over the bulk, resulting in the need for understanding processes and interactions at these surfaces. Efforts are made to understand the properties of the materials and interfaces at these nano and mesoscales including electronic properties [1, 2] and optical properties [2-4]. Further efforts are made studying the fabrication process of nanostructures and semiconductor devices themselves [5-9], either for novel nanodevices exhibiting new properties or for more efficient, cheaper production methods of nanodevices already in use.

At our laboratory, we are concerned with bottom-up techniques of fabrication, in which controlled evaporation of metals on semiconductor surfaces allows the deposited metal to grow small structures according to their natural metal-semiconductor interactions. Many fascinating structures can be grown this way, including precipitated nanowires [10, 11], low dimensional surface structures such as 1-dimensional islands/nanowires [12-15] and 2-dimensional islands [16], and thin films of one or more layers and their phases [17-20]. We primarily focus on germanium as the substrate due to its unique properties such as high mobility of electrons and holes [21] and often compare and contrast it with studies performed by other groups on silicon, the current dominant semiconductor in electronic applications. Indeed, germanium and silicon

can be seen as friendly rivals, with many germanium-based studies performed with the goal of replacing silicon or bolstering silicon's performance in electronics [22-25].

Many different metals have been deposited and studied on germanium at our laboratory, including Au, Ag, Ir, and Pb [16, 18-20]. In particular, gold, silver, and lead have shown some form of collective mass transport either through alloying between metal and substrate as seen for Au and Ag islands [14, 26] or through collective diffusion of a very mobile wetting layer exhibited by Pb [27, 28]. It is this collective diffusion of Pb that is one of the focal points of this dissertation, since collective diffusion is a phenomenon that is rarely seen in nature. This behavior was studied quite extensively on Si(111) [27, 29], and it was one of our objectives to compare and contrast this behavior on a germanium substrate. Furthermore, Pb is quite a special metal in that it very readily exhibits Quantum Size Effects (QSE), where electrons become confined within crystal structures due to some dimensions of the crystal becoming comparable to the electron wavelength [30]. QSE has profound effects on the metal, such as selection in island heights or thin film thicknesses [31-33], as well as other properties such as surface energy or work function [34]. Therefore, the major topic of this dissertation is to study QSE and collective diffusion of Pb on germanium and see how they behave compared to silicon.

Using a Low Energy Electron Microscope (LEEM) as the primary instrument, with the Scanning Tunneling Microscope (STM) and X-Ray Photoelectron Spectrometer (XPS) as supporting instruments, we have studied Pb island formation on Ge(111) at low to room temperatures (-50°C to 20°C), which is near the boundary between classical regimes, defined as the range of temperatures where thermal diffusion is the driving force behind structure formation, and the nonclassical regimes. The three instruments, which are interconnected in a

single, ultrahigh vacuum (UHV) environment, are discussed in detail in Chapter 2, along with other components relevant to the experiments.

In Chapter 3, we discuss some developments made in the sputter-anneal sample cleaning procedure, inspired by a study done by a previous graduate student, Marshall van Zjill, where he observed the formation of pyramids on a Ge(110) surface due to Ag contamination [35, 36]. Since defects and other unwanted features on a substrate will have large effects on the experiments, the ability to minimize or even control the presence of these defects is an important topic. By extrapolating the behavior of the Ge(110) pyramids to defects on other germanium faces, we were able to tune the cleaning parameters to more consistently produce useful surfaces.

In Chapter 4, we discuss the explosive nucleation and collective diffusion of Pb on Ge(111) inspired by studies performed on Pb/Si(111) M.C. Tringides, one of our collaborators at Iowa State University. Thanks to the LEEM's ability to record island formation in real-time, we were able to track the islands' growths at all points during their lifetimes. By analyzing the growth rates of the islands and looking at their dependence on temperature, we could then quantify certain aspects of their collective diffusion, such as the rate of movement of atoms and the diffusion barrier of Pb during nucleation, which were found to be explosive due to the compression present in the wetting layer. We also made attempts to provide a theoretical explanation for this behavior of Pb, with help from our collaborators at the University of Central Florida (V. Stroup, T. Panagiotakopoulos, A. Childs, D. Le, Talat S. Rahman), since this phenomenon is still poorly understood.

In Chapter 5, we used a rather unconventional method to determine the heights of the islands studied in Chapter 4. By recognizing that electrons passing through various layers of the

islands would exhibit phase shifts that would then allow them to experience interference, we modeled the Pb islands using a Kronig-Penney model to simulate these interference patterns for various island heights as a function of electron energy. By matching these interference curves with experimental interference curves, we were able to deduce the heights of the islands and were even able to see an island of exhibiting two different heights, due to growth over a step edge.

Finally, in Chapter 6, we deposited Pb on the other two low-index faces of germanium (110 and 100) to see how their surface symmetries would affect island growth compared to the 111 face. Pb/Ge(100) turned out to be very similar to Pb/Ge(111), exhibiting a similar explosive nucleation, as well as collective diffusion in their height-selected islands. Pb/Ge(110), on the other hand, showed vastly different behavior due to its rectangular symmetry, with thin, 1-dimensional islands, with completely different heights from the other two faces, growing along a single axis.

With this dissertation, we show that the Pb on germanium system is an exciting, dynamic system, with many potential applications for controlled growth of mesoscale structures, as well as potential avenues for further research.

References

[1] W. Monch, Electronic Properties of Semiconductor Interfaces, (2017).
[2] Y. Pan, S. Chen, P. Wang, Y.Q. Li, Q.H. Zheng, Ge-vacancy improved the optical and electronic properties of GeAs2 semiconductor, Ceramics International, 45, (2019) 19534-19537.
[3] T.G. Dargam, B. Koiller, Interface roughness and the optical properties of quantum wells, Solid State Communications, 105, (1998) 211-214.
[4] A.V. Khomchenko, E.V. Glasunov, Interface effects on the nonlinear optical properties of thin films, Optical and Quantum Electronics, 34, (2002) 359-368.
[5] H.Y. Fan, Z.J. Wu, T. Sun, M. Yang, J.Y. Guo, K.H. Yang, Y. Li, Efficient plasma-assisted approach in nanostructure fabrication of tungsten, Materials & Design, 89, (2016) 78-84.
[6] J.K. Grepstad, H. Husby, A. Borg, B.O. Fimland, R.W. Bernstein, R. Nyholm, As Capping of MBE-Grown Compound Semiconductors - Novel Opportunities to Interface Science and Device Fabrication, Physica Scripta, 54, (1994) 216-225.
[7] R.G. Hobbs, N. Petkov, J.D. Holmes, Semiconductor Nanowire Fabrication by Bottom-Up and Top-Down Paradigms, Chemistry of Materials, 24, (2012) 1975-1991.
[8] S.W. Kim, M. Seol, Y. Cho, K.W. Shin, D. Lee, S.J. Jeong, H. Lee, J.G. Chung, H.M. Kim, K.B. Kim, S. Park, H.J. Shin, Graphene-Based Etch Resist for Semiconductor Device Fabrication, Acs Applied Nano Materials, 3, (2020) 4635-4641.
[9] C.S. Sunandana, D. Rajesh, Three strategies for fabrication of I-VII semiconductor nano(particles)structures, Indian Journal of Pure & Applied Physics, 51, (2013) 149-155.
[10] S. Misra, L.W. Yu, W.H. Chen, M. Foldyna, P.R.I. Cabarrocas, A review on plasma-assisted VLS synthesis of silicon nanowires and radial junction solar cells, Journal of Physics D-Applied Physics, 47, (2014) 393001.
[11] L.W. Yu, P.R.I. Cabarrocas, Growth mechanism and dynamics of in-plane solid-liquid-solid silicon nanowires, Physical Review B, 81, (2010) 085323.
[12] M. Jalochowski, E. Bauer, Growth of metallic nanowires on anisotropic Si substrates : Pb on vicinal Si(001), Si(755), Si(533), and Si(110), Surface Science, 480, (2001) 109-117.
[13] T.F. Mocking, P. Bampoulis, N. Oncel, B. Poelsema, H.J.W. Zandvliet, Electronically stabilized nanowire growth, Nature Communications, 4, (2013) 2387.
[14] C.H. Mullet, Growth of Ir on Ge(111) and Ge(110) and Growth of Ag on Ge(111), Ge(110), and Ge(001) Studied by Low Energy Electron Microscopy and Scanning Tunneling Microscopy, PhD dissertation in Physics, University of California Davis, Davis (2012).
[15] T. Watanabe, Y. Yamada, M. Sasaki, S. Sakai, Y. Yamauchi, Pt- and Au-induced monodirectional nanowires on Ge(110), Surface Science, 653, (2016) 71-75.
[16] B.H. Stenger, A.L. Dorsett, J.H. Miller, E.M. Russell, C.A. Gabris, S. Chiang, Growth and motion of liquid alloy droplets of Au on Ge(110), Ultramicroscopy, 183, (2017) 72-76.
[17] M.S. Altman, W.F. Chung, C.H. Liu, LEEM phase contrast, Surface Review and Letters, 5, (1998) 1129-1141.
[18] C.H. Mullet, S. Chiang, High temperature growth of Ag phases on Ge(111), Journal of Vacuum Science & Technology A, 31, (2013) 020602.
[19] C.H. Mullet, B.H. Stenger, A.M. Durand, J.A. Morad, Y. Sato, E.C. Poppenheimer, S. Chiang, Growth and phase transformations of Ir on Ge(111), Surface Science, 666, (2017) 96-103.

[20] Y. Sato, S. Chiang, Growth and morphology of Pb phases on Ge(111), Journal of Vacuum Science & Technology A, 35, (2017) 061405.
[21] M.V. Fischetti, S.E. Laux, Band structure, deformation potentals, and carrier mobility in strained Si, Ge, and SiGe alloys, Journal of Applied Physics, 80, (1996) 2234-2252.
[22] H. Gamble, B.M. Armstrong, P.T. Baine, Y.H. Low, P.V. Rainey, S.J.N. Mitchell, D.W. McNeill, Germanium Processing, in: A. Nazarov, J.P. Colinge, F. Balestra, J.P. Raskin, F. Gamiz, V.S. Lysenko (Eds.) Semiconductor-on-Insulator Materials for Nanoelectronics Applications, (2011), pp. 3-29.
[23] X. Gong, Y. Yang, P.F. Guo, W. Wang, R. Cheng, L.X. Wang, E.S. Tok, Y.C. Yeo, Germanium-Tin P-Channel Field-Effect Transistor with Low-Temperature Si2H6 Passivation, in: 6th SiGe, Ge, and Related Compounds - Materials, Processing and Devices Symposium held at the 2014 Joint International 226th Electrochemical-Society, Cancun, MEXICO, 2014, pp. 851-868.
[24] R. Ichikawa, S. Takita, Y. Ishikawa, K. Wada, Germanium as a Material to Enable Silicon Photonics, in: D.J. Lockwood, L. Pavesi (Eds.) Silicon Photonics Ii: Components and Integration, (2011), pp. 131-141.
[25] V.A. Tiwari, Y.W. Teh, D. Jaeger, R. Divakaruni, D.R. Nair, Effect of Germanium Preamorphization Implant on Performance and Gate-Induced Drain Leakage in SiGe Channel pFET, Ieee Electron Device Letters, 36, (2015) 531-533.
[26] S. Curiotto, F. Leroy, F. Cheynis, P. Muller, Self-propelled motion of Au-Si droplets on Si(111) mediated by monoatomic step dissolution, Surface Science, 632, (2015) 1-8.
[27] K.L. Man, M.C. Tringides, M.M.T. Loy, M.S. Altman, Superdiffusive Motion of the Pb Wetting Layer on the Si(111) Surface, Physical Review Letters, 110, (2013) 036104.
[28] Y. Sato, S. Chiang, N.C. Bartelt, Spontaneous domain switching during phase separation of Pb on Ge(111), Physical Review Letters, 99, (2007) 096103.
[29] M. Hupalo, M.C. Tringides, Ultrafast kinetics in Pb/Si(111) from the collective spreading of the wetting layer, Physical Review B, 75, (2007) 235443.
[30] M.C. Tringides, M. Jalochowski, E.T. Bauer, Quantum size effects in metallic nanostructures, Physics Today, 60, (2007) 50-54.
[31] T.R.J. Bollmann, R. van Gastel, H.J.W. Zandvliet, B. Poelsema, Quantum Size Effect Driven Structure Modifications of Bi Films on Ni(111), Physical Review Letters, 107, (2011) 176102.
[32] T.R.J. Bollmann, R. van Gastel, H.J.W. Zandvliet, B. Poelsema, Quantum size effects on surfaces without a projected bandgap: Pb/Ni(111), New Journal of Physics, 13, (2011) 103025.
[33] M. Hupalo, S. Kremmer, V. Yeh, L. Berbil-Bautista, E. Abram, M.C. Tringides, Uniform island height selection in the low temperature growth of Pb/Si(111)-(7 x 7), Surface Science, 493, (2001) 526-538.
[34] C.M. Wei, M.Y. Chou, Theory of quantum size effects in thin Pb(111) films, Physical Review B, 66, (2002) 233408.
[35] M. van Zijll, Scanning Tunneling Microscopy Studies of Ir on Ge(111), Ag on Ge(110), and the Effects of Sputtering Energy on Pyramids formed on Ge(110), PhD dissertation in Physics, University of California Davis, Davis (2014).
[36] M. van Zijll, S.S. Spangler, A.R. Kim, H.R. Betz, S.R. Chiang, Layer-by-Layer Pyramid Formation from Low-Energy Ar+ Bombardment and Annealing of Ge (110), Nanomaterials, 11, (2021) 2521.

2 INSTRUMENTATION

2.1 Overview

The laboratory is equipped with three major instruments – Scanning Tunneling Microscope (STM), X-ray Photoelectron Spectrometer (XPS), and Low Energy Electron Microscope (LEEM). The three instruments are connected together in a single vacuum system as shown in Fig. 2.1, with each individually kept at an ultrahigh vacuum (UHV) base pressure of 10^{-10} torr. The chambers can be separated from each other via gate valves. A series of transfer arms,

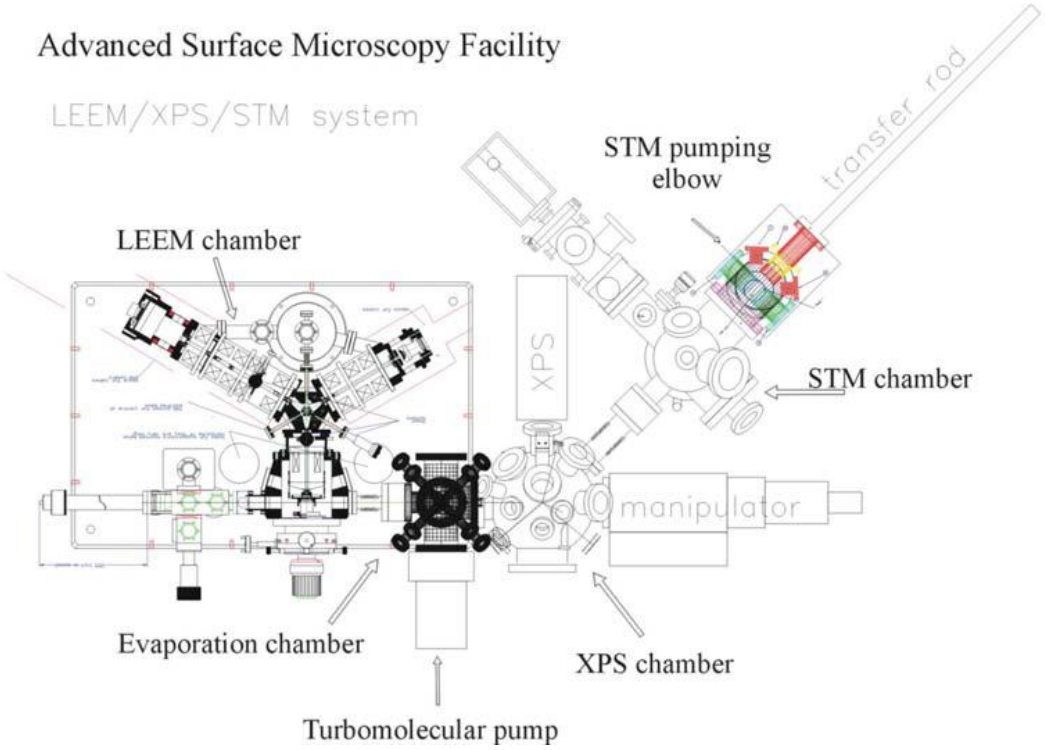

Figure 2.1. Layout of instruments in laboratory vacuum system. Reprinted from Materials Science and Engineering B-Solid State Materials for Advanced Technology, 96, C.L.H. Devlin, D.N. Futaba, A. Loui, J.D. Shine, S. Chiang, A unique facility for surface microscopy, 215-220, (2002) [4], with permission from Elsevier.

wobblesticks, and manipulators allow samples to be moved between the chambers, allowing for multiple techniques to be used on a single sample, which is a significant advantage of this connected system.

Each chamber can be outfitted with an evaporator for deposition of metals, either an electron-beam evaporator or a resistive evaporator, with the LEEM capable of having more than 1 evaporator installed at a time. The chambers can accept mass spectrometers (two in use of the brands SRS RGA and Transpector) to assist with monitoring the vacuum of the chambers and leak testing with helium. Lastly, the sample can be heated and cooled in each chamber, with cooling done through continuous-flow cryostats that use of liquid nitrogen. Although the STM cryostat was designed to use liquid helium, it can also use liquid nitrogen. Since the cooling systems lack robust temperature isolation systems, the lower temperature limits were measured to be about 200K in the LEEM and 190K in the STM. (XPS was not measured since its cooling system was very rarely used). Sample heating is done via an electron beam heating system within the sample holders themselves, as discussed further below.

2.2 Sample Holder

Samples are mounted into sample holders designed by Elmitec Gmbh for the LEEM that have been modified to be compatible with the rest of the system. The original sample holder parts provided by the manufacturer are made from molybdenum intended for use in high temperatures, but many of the sample holders used in our experiments were replaced by

stainless steel or titanium alternatives that are more easily fabricated. A diagram of the modified sample holder is provided in Figure 2.2.

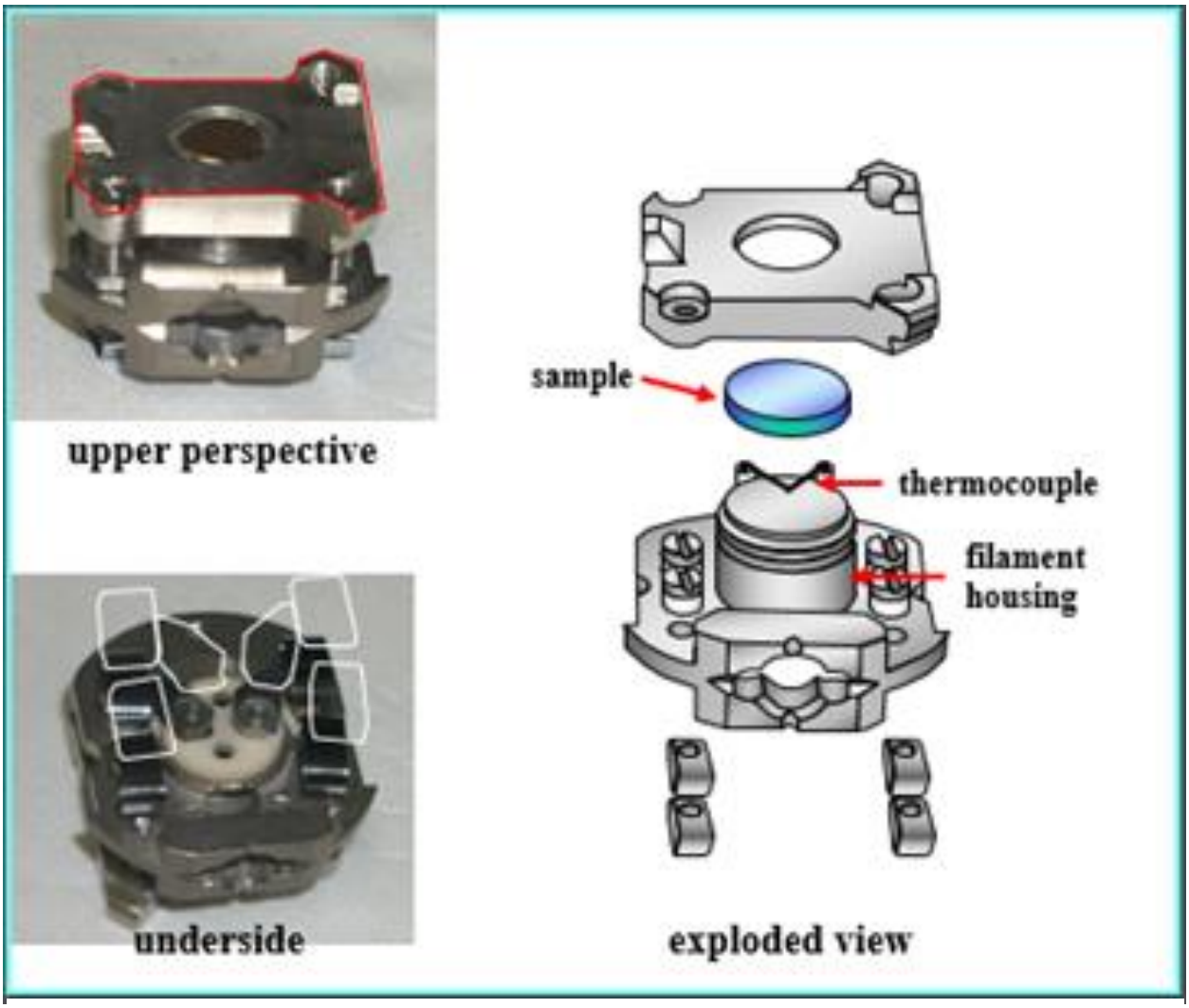

Figure 2.2. Various views of the sample holder used in experiments, reproduced with permission from [1].

Sample holders had a tungsten filament placed under the samples, and the samples themselves could be biased for electron-beam heating. Thermocouples spot-welded to a support ring underneath the sample could be used to measure the sample temperature. As mentioned previously, all three instruments in the vacuum system have electrical contacts to make use of

the heating and thermocouple elements of the sample holders. The thermocouples used were Type K (primarily used in the STM and XPS) and Type C (LEEM).

Because of variances in how the samples were mounted, along with the top plate holding them down, the samples were often slightly tilted if aligned by eye. Because sample tilt had a lot of importance in LEEM experiments, with the LEEM being able to correct only a few degrees of tilt, a sample tilt calibration mechanism was designed and constructed to correct any tilt before placing a sample into vacuum.

As shown in Figure 2.3, a laser diode was used to shoot light through a long pinhole, which would block the laser if it deviated too much from a straight path. The sample holder would be placed in the mount on the other side of the platform, and the laser light would reflect from the surface, back towards the pinhole, illuminating a spot near the pinhole depending on the tilt of the sample, with the laser going back through the pinhole in the case of near-perfect alignment. Because a near-perfect alignment did not necessarily correspond to acceptable alignment of a sample in the LEEM, a Ni(111) sample was first used in a series of trial-and-error tests until it was verified to have a tilt that was able to be corrected in the LEEM's manipulator. Then it was placed onto the platform as the calibration point. The position of the reflected laser was marked, and a

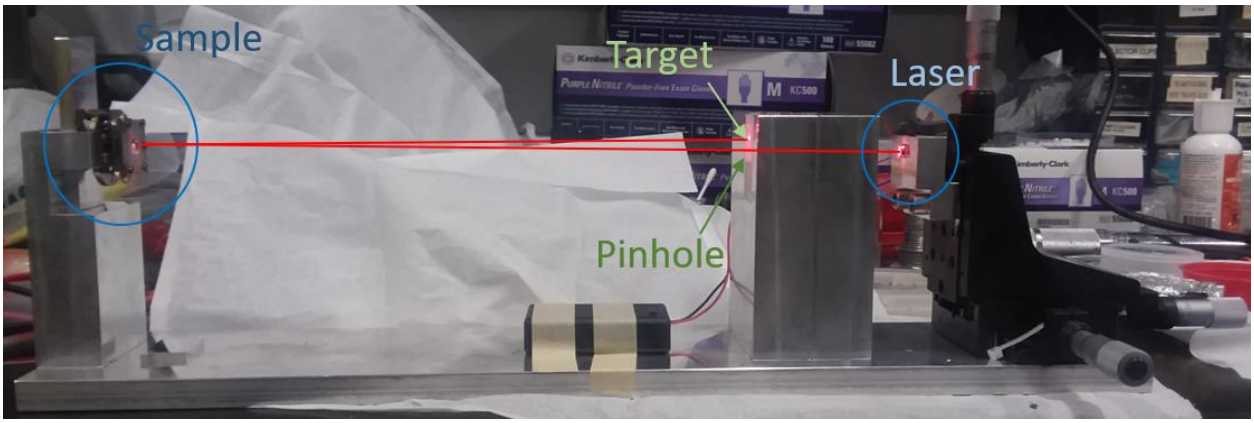

Figure 2.3. Sample tilt calibration platform.

circle corresponding to a 1˚ of tilt error was drawn around the point. Other samples to be used in LEEM experiments were adjusted on the platform so that the reflected laser would be within the circle, usually by a combination of placing a thin tantalum foil beneath the sample and adjusting the screws on the top plate. Since the LEEM manipulator had a significant systematic tilt of about 3˚, the tilt correction was significant enough to create a slight temperature gradient on the sample during heating.

2.3 Low Energy Electron Microscopy

2.3.1 Introduction

LEEM was first developed by Ernst Bauer in 1962 and refined over the following years into a powerful surface analysis tool, culminating in the first LEEM images of the Si(111) phase transition between (7x7) and (1x1) [5]. With its ability to directly view surface processes at video rate and with mesoscale (~10nm) resolution, LEEM was shown to be a powerful and versatile analysis tool for surface science. The technique has been refined and improved since then, especially in terms of aberration reduction, and the instrument model used by this laboratory is the LEEM III, designed and manufactured by Elmitec Gmbh.

The LEEM's surface sensitivity comes from the inelastic free path of electrons at low energies (1-100eV). Theoretical [6] and experimental [7] results show that at around 10 to 100eV, the mean free path is around 10Å and below, with the mean free path rising back up to 100Å below 10eV. This means low energy electrons do not penetrate the samples very far (only a few

atomic layers), and thus only interact with the surface. The resulting backscattered electrons can then be used to glean information about the structures on the surface, from surface periodicity to island growth to various structural domains.

One example of the kinds of study that can be done with the LEEM is work done by Yu Sato *et al*. regarding phases of Pb on Ge(111). In one particular study, it was found that Pb would spontaneously switch between small domains of the (1x1) phase and the β phase in the coexistence region of the phase diagram [8]. Another example is the study of Ag crystal growth on Si(001) done by B.Q. Li *et al*. in which Ag crystals showed a preferred direction of growth on the surface, along with a strange growth mechanism [9]. It was found that the Ag crystals grew in various segments, which could be seen by various contrast in the LEEM images. This was a rather unusual growth morphology, compared to conventional nucleation and growth.

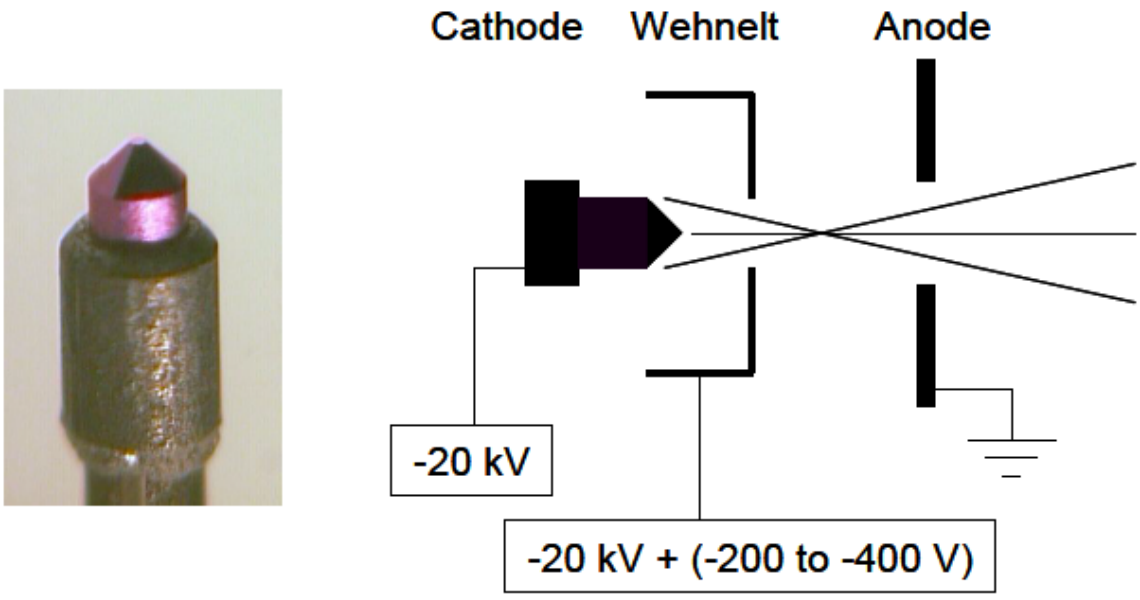

Figure 2.4. Diagram of electron source. Left image shows the LaB_6 crystal (purple). Diagram on right shows how emitted electrons are gated by the Wehnelt and accelerated by high voltage. Reproduced with permission from [3].

2.3.2 Illumination column

The illumination column begins with the electron source, responsible for producing a tight, high-intensity electron beam to illuminate the sample. The LEEM III uses a LaB_6 cathode produced by Kimball Physics, Inc. as the electron emission source, as shown in Figure 2.4. It is a hot emitter, using high temperatures to thermally excite electrons above the vacuum level, and generally has higher beam intensity than cold emitters, although at the cost of resolution as cold emitters have a smaller energy spread [10].

The emitted electrons are accelerated towards the anode by a potential difference of -20kV, also shown in Figure 2.4, but they first must pass through the Wehnelt grid, which sits at a slightly lower (more negative) voltage to block lower-energy electrons. By adjusting the Wehnelt voltage, whose magnitude typically varies between 200 and 400 volts, the intensity of the electron beam can be adjusted, but the actual adjustment depends on the temperature of the

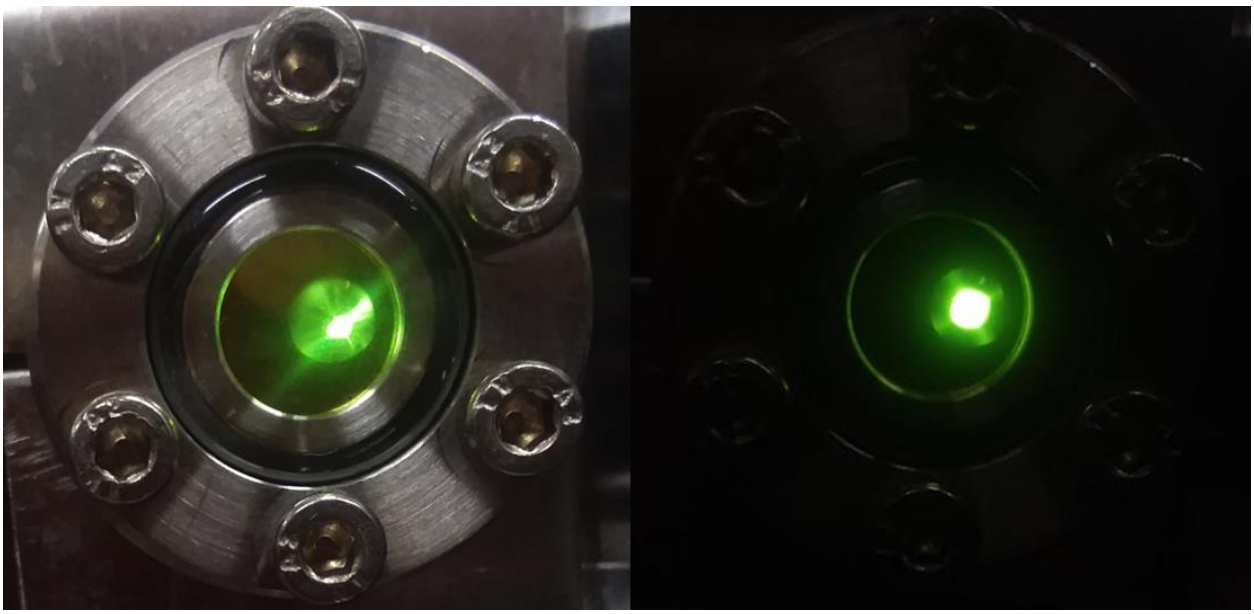

Figure 2.5. Electron beam imaged on a phosophor screen at low (left) and high (right) magnitude of Wehnelt voltage.

LaB_6 crystal – a hotter crystal means a higher average electron energy, which can pass through a higher magnitude of the Wehnelt voltage and thus only require a small reduction in the Wehnelt voltage magnitude to achieve emission through the grid. It is also more desirable to get electrons only from the very tip of the LaB_6 crystal – electrons emitted from the sides of the crystal do not have uniform beam intensity, as seen in the left side of Figure 2.5. Since electrons emitted from the sides have more of their energy in the transverse direction, they can only pass through sufficiently low Wehnelt voltage. Therefore, having a high crystal temperature and high Wehnelt voltage is better for allowing only electrons from the tip of the crystal to pass through. Due to the nature of the electric fields at the Wehnelt grid, the grid has a slight focusing effect, with a

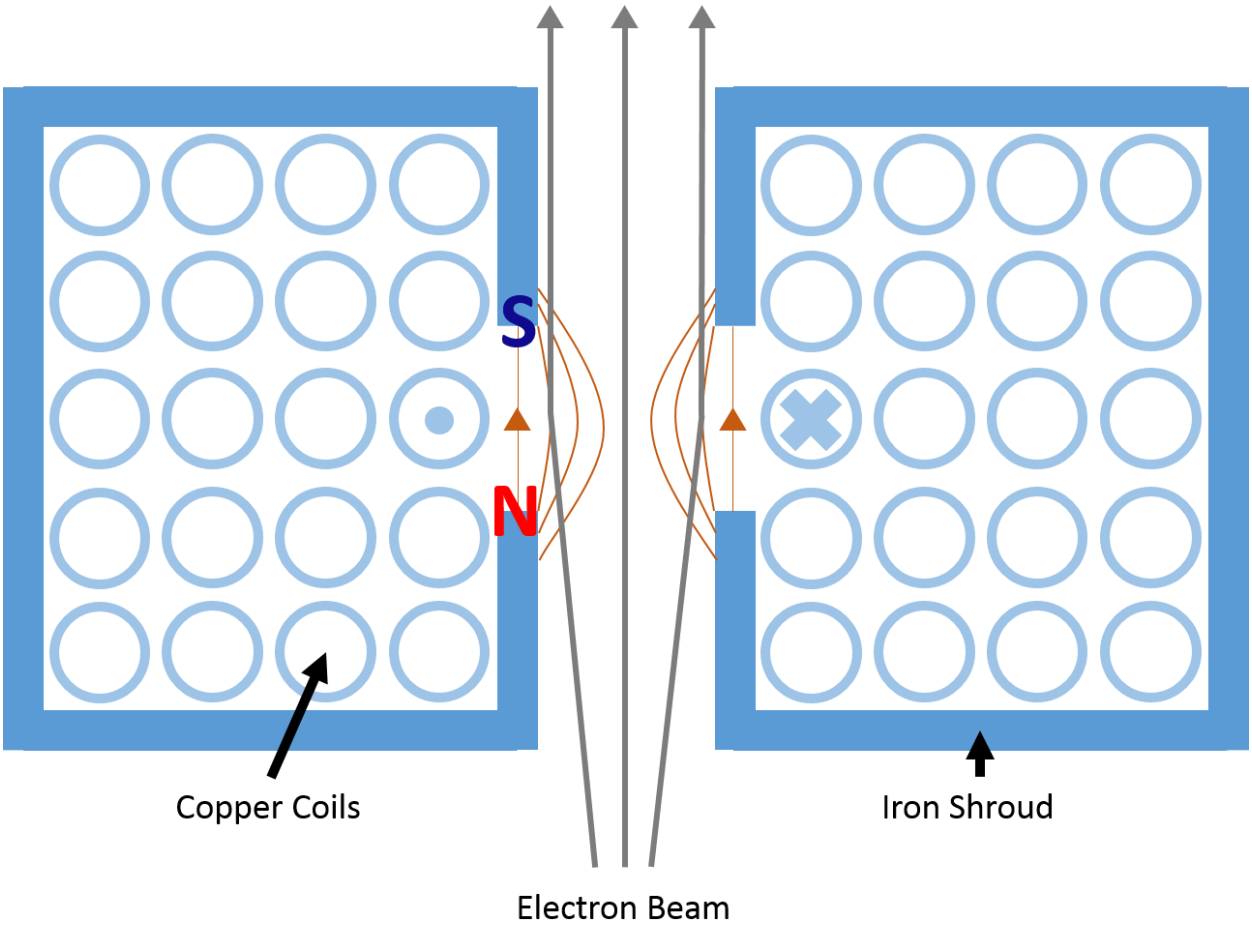

Figure 2.6. Cross section of the single gap magnetic lens, showing the magnetic field lines with the electron path going through.

crossover point between the grid and the anode, such that the beam is divergent before entering the rest of the illumination column.

The electron beam from the electron source must be collimated to the back focal plane of the objective lens so that the objective can focus the beam on the sample. This is done by a series of three condenser lenses on the illumination column.

The condenser lenses are single gap magnetic lenses formed by electric coils inside an iron shroud, as in Figure 2.6. All the lenses in the LEEM III are single gap lenses, with the exceptions being the second projective lens and the objective (which will both be discussed in later sections of this chapter). A cylindrical case around the beam path is formed by electric coils, while the iron shroud encasing the coils concentrates the magnetic field into the gap, with the two sides of the gap forming the magnetic poles. While the magnetic field lines at the exact middle region between the entry and exit points align with the optical axis, the field lines closer to the entry and exit points have transverse components. The strength of the field also becomes greater at larger distances from the optical axis. The magnetic field has two effects on the electron beam – firstly, due to the increasing strength away from the optical axis, electrons farther from the optical axis are given a greater impulse towards the center, resulting in the desired focusing effect; secondly, the transverse components of the fields cause the electron beam to rotate about the optical axis. Aside from the rotation, the magnetic lenses behave much like spherical lenses in optics, and much like with optical lenses, imperfections in lens construction cause some asymmetry in the magnetic fields and thus cause astigmatism. These are corrected by quadrupole stigmators, located at the end of the illumination column, before the objective lens, and at the start of the imaging column.

Accompanying the lenses are deflector coils used for centering the electron beam through each lens. The deflector coils come in pairs, one for each transverse direction to the optical axis and provide simple impulse in those directions as necessary. Correction of beam trajectory is done by slightly oscillating the lens's magnetic field, thereby oscillating the beam's focusing as well as rotation, in a process called "breathing." If the beam is off the optical axis, then the beam will rotate and change in size with respect to a point that is not the center of the beam. The deflector coils are used to deflect the beam until the beam oscillation happens about the center of the beam.

2.3.3 Beam Separator and Objective

The beam separator is responsible for deflecting the electron beam from the illumination column through the objective and onto the sample, and then to separate the reflected beam and guide it into the imaging column. Due to the nature of the Lorentz Force, electrons traveling through a uniform magnetic field will experience opposite directions of deflection when traveling to and from the sample. Therefore, the very basic design for the beam separator would use a uniform field suspended between two magnetic poles, as shown in Figure 2.7.

However, in order to minimize distortions and astigmatism produced by imperfections introduced during fabrication of the parts, the beam separator is designed to focus the beams in addition to separating them. In the Elmitec LEEM III, this is done using a magnetic prism array, whose arrangement can be seen in Figure 2.8. Focusing in the plane normal to the deflection field is done by virtue of path length difference. Because electrons in the beam feel the same

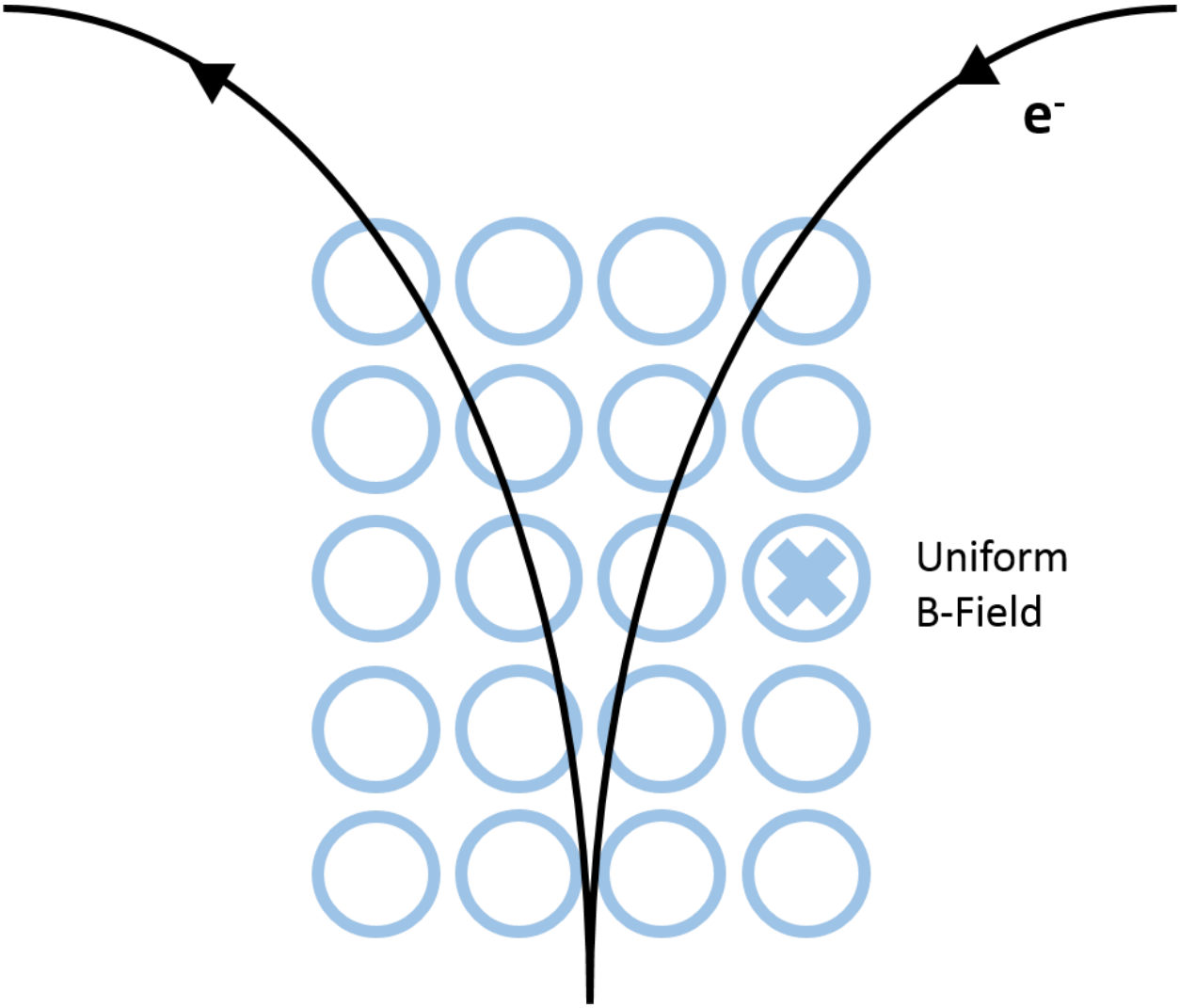

Figure 2.7. Simple beam separator consisting of a uniform magnetic field through which an electron beam travels.

magnitude of force, electrons that stay within the field longer will receive a greater impulse than those traveling a shorter path, thus receiving a greater deflection. Focusing in the other transverse direction is accomplished by the fringe fields that occur on the edges of the pole pieces, as the magnetic fields depart from their parallel arrangement and instead curl from one pole to the other. The nonparallel components of the magnetic fields interact with the component of electron velocity perpendicular to them (introduced by the deflection), and thus produce a force towards the center of the beam. The focusing effect in both directions are shown in Figure 2.8.

The inner prism elements and the ring-shaped, outer prism element are controlled by different magnetic coils, so their magnetic fields can be individually tuned to eliminate as much astigmatism and distortion as possible, as in tuning a series of lenses.

Also shown in Figure 2.8 is the illumination aperture. There are three aperture sizes that can be selected using a linear translator – 400, 100, and 50µm. These apertures limit the size of the electron beams to only allow electrons close to the optical axis. This not only cuts out

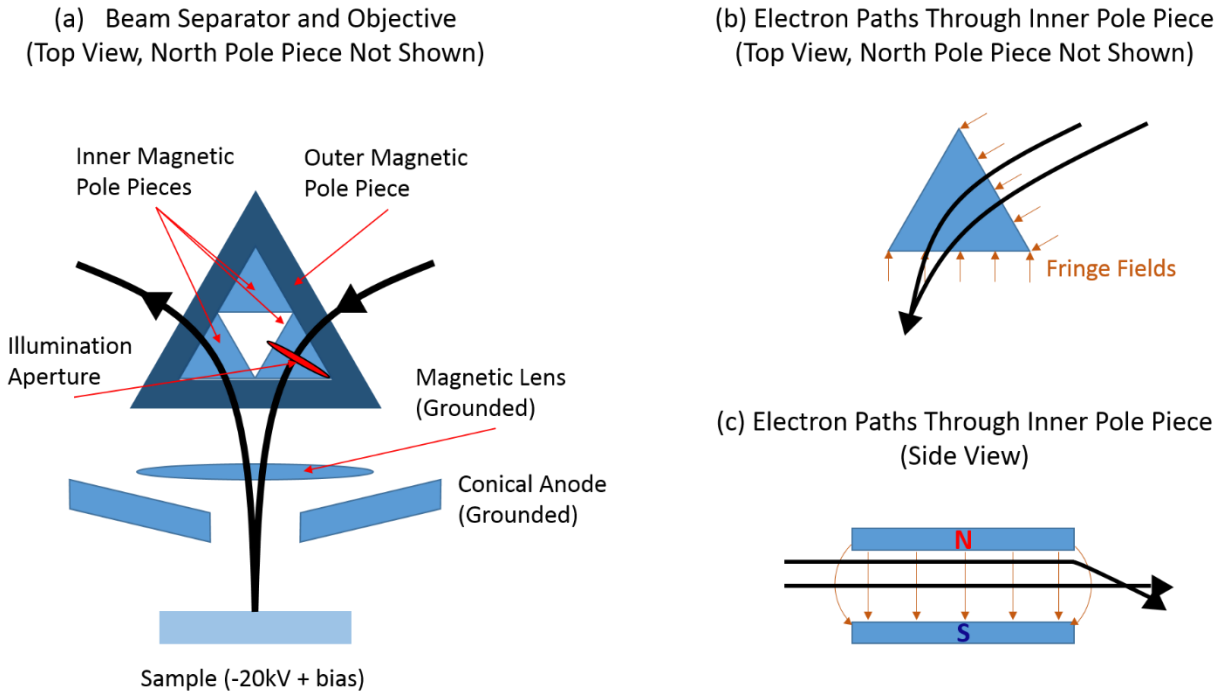

Figure 2.8. Various views of the beam separator with the electron paths (black arrows) shown. (a) Top view of the prism array consisting of three inner, triangular pole pieces and an outer, triangular-ring pole piece. Only the bottom (south pole) pieces are shown. The objective, consisting of a magnetic lens, conical anode, and sample (acting as cathode) are also shown. (b) Isolated inner triangular pole piece, with accompanying fringe fields at the edges. The electrons travel mostly parallel to the fringe fields upon entry and thus feel very little deflection into or out of the page. The beam on the left is deflected more than the beam on the right due to its longer path over the pole piece's deflection field, causing horizontal focusing. Once the beams exit, the electrons have a velocity component perpendicular to the fringe fields, causing vertical focusing. (c) Side view of the electron paths through the inner pole piece, showing how the fringe field has no horizontal component at the center, thus causing no vertical deflection for the central beam, while fringe fields away from the center cause deflection.

electrons with higher transverse energy, it also reduces the unwanted, imperfect focusing of the lenses farther away from the optical axis. This vastly increases the quality of low energy electron diffraction (LEED) patterns and the LEEM images, at the cost of electron intensity which can be handled by increasing the overall intensity of the electron beam from the source. Using smaller apertures will also limit the maximum field of view for LEEM images, since a smaller area of the sample will be illuminated. The illuminated area is smaller than the aperture size due to the focusing of the beam; for example, the 100µm aperture illuminates about 25µm of the sample, while the 50µm aperture's illumination is only suitable for high resolution LEED.

Once the electron beam is deflected by the beam separator, the beam enters the objective. The objective lens is a cathode lens that has a magnetic lens, and then a conical anode, and finally the sample that acts as the cathode and is considered a part of the lens (see Figure 2.8). The magnetic lens and the conical anode are both grounded, and the sample is held at -20kV plus some bias in order to decelerate the electrons and give them surface sensitivity. The bias to the sample can be adjusted to be between -5V and +100V to control the energy of the electrons striking the sample.

The objective is the biggest limiting factor to the resolution of the LEEM III, due to the spherical and chromatic aberrations caused by the decelerating electric field on a larger scale than that of other lenses [10]. The aberrations can be reduced by increasing the electric field strength [11], but the maximum electric field is limited by the vacuum breakdown voltage of 10kV/mm, which occurs at a sample-to-objective distance of 2mm. In practice, the typical sample-to-objective distance is forced to be greater than 2mm due to imperfections in the

sample holders, the sample itself, and the environment in general, which cause arcing before the breakdown voltage distance.

2.3.4 Imaging Column

Once the electrons scattered by the sample, they are once again accelerated by the objective and deflected into the imaging column. The first lens, the transfer lens, is responsible for transferring the diffraction pattern from the back focal plane of the objective to the second lens, which is called the field lens. From there, the third lens, called the intermediate lens, transfers the diffraction plane to the object plane of the projective lens to be projected for viewing. There are two projective lenses, but in LEED mode, as well as for smaller field-of-view (FOV), only the second projective lens is used. The second projective lens is a double gap magnetic lens, which has two gaps in the iron shroud instead of one, behaving like two adjacent lenses and thus preserving the focal length of the first lens while magnifying the image.

If one wishes to view an image in LEEM mode using the diffraction spots, then the values of the field lens and the intermediate lens must be adjusted to bring the image plane at the middle of the beam separator to the object plane of the projective. In order to control which electrons are used to form the image, a contrast aperture, located at the field lens, is used to select a diffraction spot to be used for imaging. If the (00) spot is selected, the image mode is called bright field LEEM, while selecting higher order spots is called dark field LEEM. These modes will be discussed later in this chapter. To minimize distortions in dark field LEEM, the higher order diffraction spot must be moved to the optical axis, which can be done by adjusting the steering coils on the illumination side such that the electron beam strikes the sample at oblique incidence

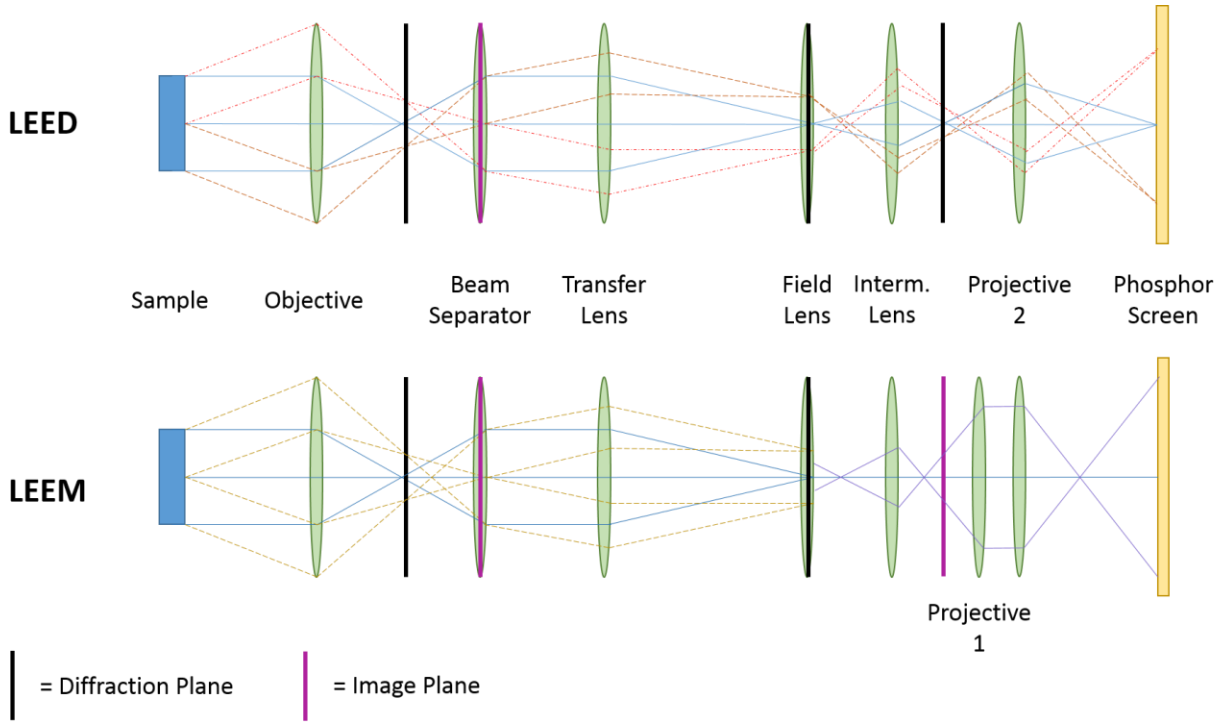

Figure 2.9. Lens arrangement and accompanying beam paths for LEEM and LEED modes. In the LEED mode diagram, the different-colored lines trace individual LEED spots. In the LEEM mode diagram, only the central spot is allowed through by the contrast aperture (located in the middle of the field lens). The purple lines after the field lens follow the finite-size LEED spot (actual size exaggerated for visual clarity) as it is magnified by the lenses to form the LEEM image.

instead of normal incidence. The different lens setups along with the electron beam's optical paths for both LEED and LEEM mode are outlined in Figure 2.9.

The last part of the imaging column is the system for visualizing the image. Once the electron beam is magnified by the projective lenses, the electrons enter a microchannel plate (MCP), which consists of a densely packed array of small tubes (on the order of 10µm diameter). When an electron hits the wall of a tube, secondary emissions of electrons are produced, which then strike the tube walls and cause further emissions. Thus, a cascading of emissions occurs, multiplying the first electron into a much larger signal. However, MCPs consisting of straight

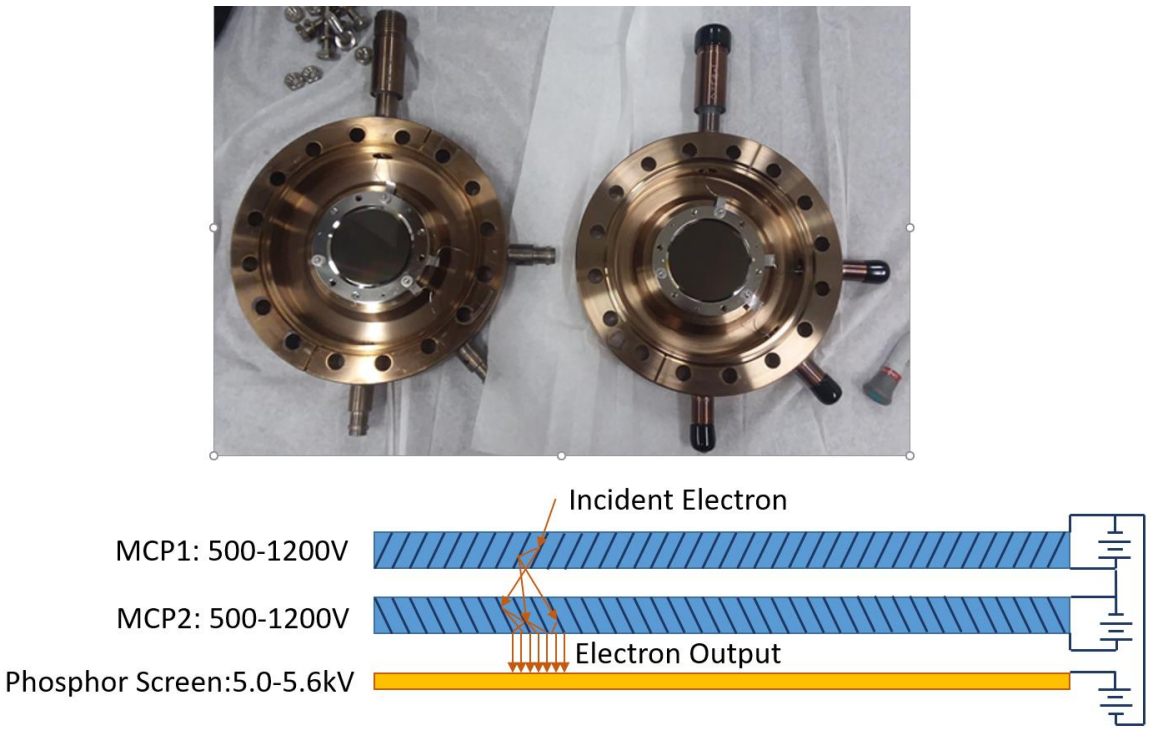

Figure 2.10. Chevron stack microchannel plates manufactured by Photonis (top). The left one is the original that came installed with the LEEM, and the right one is the new one installed in fall 2021. Diagram at bottom shows the chevron arrangement of the channelplates as well as the phosphor screen.

tubes with respect to incoming electrons have reduced efficiency because the electrons do not strike the walls very often. Therefore, the LEEM III uses two multiplier plates arranged in a chevron pattern, in which the tubes are at an angle with respect to the electron beam, with one plate being the reflection of the other, as shown in Figure 2.10. Not only does this design increase the probability of electrons striking the tube walls, it also helps prevent positive ions (which result from electron impact on ambient gases) from drifting through the tube and causing interference. The gain of the chevron pattern design is on the order of 10^7 [12]. The MCP assembly was recently changed out for a new one (same manufacturer and same model), as the original MCP was beginning to lose resolution as well as gain due to age. Both MCPs exhibit some defects and damage due to burnt-out tubes, which show up on the images, and both plates display some

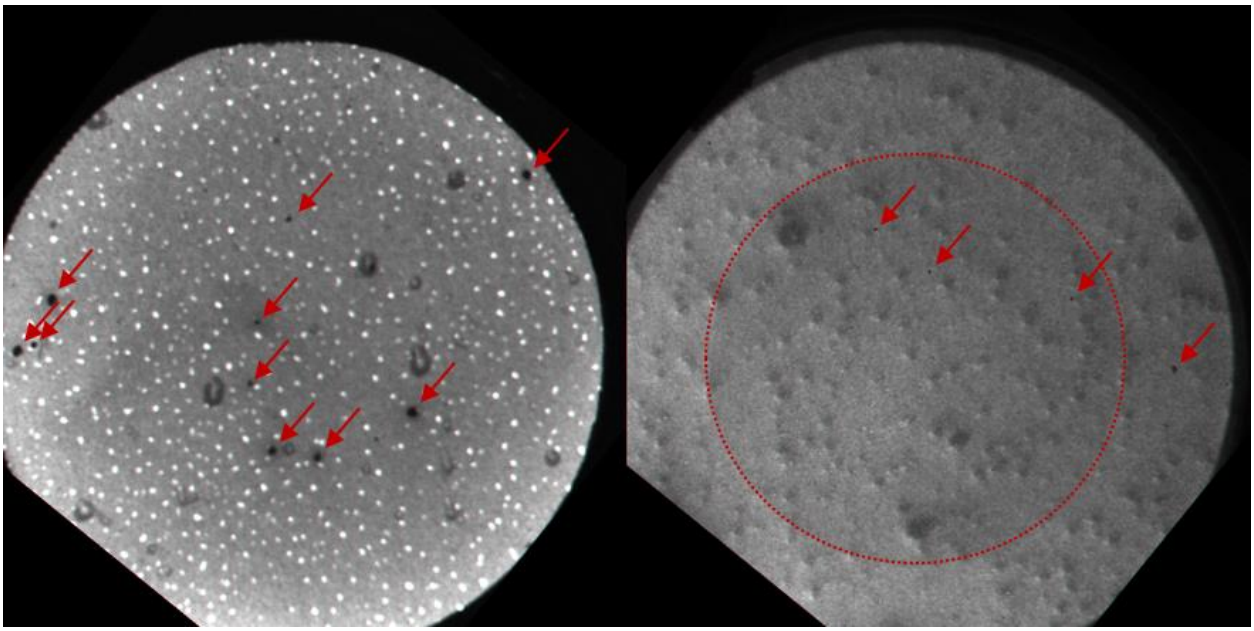

Figure 2.11. LEEM images showing MCP defects, marked by red arrows. Original MCP is on the left, while the new MCP is on the right. The circle on the new MCP image marks the boundary of a large, slightly-worn region that causes the image to be darker within by a uniform amount. Aside from these defects, the left MCP has an intensity gradient where the image is brightest at the edge and gradually becomes darker towards the center. The right MCP has an intensity gradient where the image is brightest on the bottom left and becomes darker towards the upper right.

intensity gradient due to nonuniform gain across the channels. These features are identified on Figure 2.11 and should be ignored when examining LEEM data.

After the electron signal is multiplied by the MCP, the electrons are accelerated onto a phosphor screen, usually with a potential difference of at least 4kV, which converts the electron signal into photons that can be imaged using a video camera. The video camera is located outside vacuum and sends its footage to a digital recording program on a computer, where the video can be recorded, saved, and analyzed. Analysis was done using the manufacturer's provided software (U-View®) as well as a custom software developed in 2010 by an undergraduate researcher from our group, Eric Poppenheimer [13].

2.3.5 Discussion of Different Imaging Modes

Here, we go over the uses and features of the different imaging modes offered by the LEEM III. I have already mentioned the two primary modes, the LEED and LEEM modes, but the instrument can also be used in two additional modes – mirror electron microscopy (MEM), and photoelectron emission microscopy (PEEM). LEED is the only diffraction method, while the LEEM, MEM, and PEEM are all imaging modes with different contrast mechanisms.

We will begin with the discussion of the LEED mode. When electrons with a wave vector $\boldsymbol{k_0}$ are incident on the surface and scattered with a wave vector $\boldsymbol{k}$, the scattered electrons constructively interfere (and thus form a diffraction spot) when the Laue condition is satisfied, given by

$$\boldsymbol{k} - \boldsymbol{k_0} = \boldsymbol{g_{hkl}},$$

where

$$\boldsymbol{g_{hkl}} = \boldsymbol{h}\boldsymbol{a}^* + \boldsymbol{k}\boldsymbol{b}^* + \boldsymbol{l}\boldsymbol{c}^*,$$

with (h, k, l) being integers and $\boldsymbol{a}^*$, $\boldsymbol{b}^*$, and $\boldsymbol{c}^*$ being the primitive reciprocal lattice vectors of the crystal. Since low energy electrons only sample the surface, this reduces to

$$\boldsymbol{k} - \boldsymbol{k_0} = \boldsymbol{g_{hk}}$$

and

$$\boldsymbol{g_{hk}} = \boldsymbol{h}\boldsymbol{a}^* + \boldsymbol{k}\boldsymbol{b}^*$$

with $\boldsymbol{a}^*$ and $\boldsymbol{b}^*$ being the primitive two-dimensional reciprocal lattice vectors of the crystal surface. Since LEED patterns are determined by the reciprocal lattice of the surface, which depends on the real space lattice of the surface, studying LEED patterns gives information about

the periodicity of surface structures. Because the surface periodicity can change as various parameters such as temperature and coverage are changed, by looking at the LEED patterns as they change during an experiment, one can study phase transitions of different structural arrangements [14]. Once these phases are known, they can then be used for calibration purposes, both for temperature and the deposition rate of metal evaporators [2]. The biggest drawback of LEED is that the periodicity of the surface does not give any information about the actual, atomic structure of the surface, as the periodic structures can consist of multiple atoms in a unit cell. This is why the STM, with its atomic resolution, is often used as a complementary technique to study atomic structures [15]. One can glean some information on the atomic structure by analyzing the intensity of the LEED spots as electron energy is changed, a technique called spot profile analysis (SPA). Since the LEEM III is not specialized for SPA, this is not a prominent technique in this laboratory.

Next we discuss the LEEM mode. Its biggest advantage is that one can study the sample surface along with processes that occur on it in real time, which means the LEEM is ideal for studying dynamic processes such as growth, diffusion, and phase transitions. While unable to study atomic structures due to its resolution on the order of nanometers, it is still able to study larger scale processes in high detail with time resolution on the order of several image frames per second.

With any imaging mode, it is useful to discuss the contrast, i.e., which features look brighter in the image and which features look darker. We will begin with bright field imaging, which uses the central diffraction spot to form the image. Since the central spot consists of electrons from every part of the surface, the differences in intensity come from the reflectivity

of the local structures on the sample. Different reconstructions or phases will have different reflectivity, and contamination can also affect how electrons are scattered from the surface. This is similar to how contrast in optical viewing is established, based on how different wavelengths of light are scattered from an object. In this sense, bright-field imaging is simply shining a "flashlight" of electrons on the sample to view it.

When a higher order diffraction spot is used to form the image, the mode is called dark-field imaging. Because higher order diffraction spots come from a structure of particular periodicity, only features with said periodicity will appear bright in the image, while the other regions remain dark. This allows for clear identification of the structures from which the chosen diffraction spot is formed and is especially useful for tracking the coverage of the structure due to the sharp contrast. When there are multiple domains that are rotationally equivalent, dark-field imaging can distinguish among them by selecting the diffraction spot for one rotation. Thus, dark-field LEEM can be used to determine the spatial distribution of various domains on the surface.

One final source of contrast in the LEEM comes from atomic step edges. Electrons reflected from a lower step will have a path length difference of $2z$ compared to the electrons reflected from the higher step, where z is the atomic step height. Then the electrons for a given energy will have a phase difference given by

$$\theta = \frac{2\pi}{\lambda}(2z),$$

with the electron wavelength $\boldsymbol{\lambda}$ related to its incident energy E by

$$\lambda = \frac{h}{\sqrt{2mE}}.$$

When this phase difference is an odd integer of π, destructive interference occurs. Solving for λ then gives

$$\lambda = \frac{4z}{(2\mathrm{m}+1)},$$

where m is an integer. Thus, electrons whose wavelengths are on the order of Ångstroms, will destructively interfere from path length differences of similar size, which are on the scale of step edges. By tuning the energy of the electrons that are incident on the sample, one can achieve destructive interference on the sample's step edges, thereby achieving sharp, dark contrast.

The third mode, MEM, is similar to LEEM in that one shines a beam of electrons on the sample and then images the resulting electron beam. The major difference comes from the fact that the electrons are at near-zero energy when they reach the surface (usually around -0.5eV) and thus do not scatter from the surface. Instead, they interact with the retarding electric field close to the surface, and the contrast comes from the changes in the retarding field across the different heights on the surface. While it is not as flexible as LEEM imaging in resolution or sensitivity to detail, MEM is useful as a basic testing tool for maintenance and alignment.

Like MEM, PEEM mode is another imaging mode mostly used for testing in our laboratory. It involves exciting secondary electrons from the sample using radiation, typically ultraviolet (UV) radiation. For the LEEM III, the radiation source is an Hg lamp that is focused through a UV viewport. Contrast primarily comes from the different work functions of various structures, with higher work functions giving lower intensity. For some samples with exceptionally high work functions or very little surface variation, this imaging mode is not very useful. Because PEEM does not rely on an electron source, it allows for the alignment of the imaging column without having to deal with the extra complication introduced by the illumination column. As such, PEEM is used

for the initial steps in alignment of the lenses for our LEEM instrument, with MEM being used to check and adjust the combined alignment of the illumination and imaging columns after the two columns are individually aligned.

2.4 Scanning Tunneling Microscopy

2.4.1 Introduction

The STM was developed by Gerd Binnig and Heinrich Rohrer in the early 1980s at the IBM Zurich Research Laboratory [16-18] and was quickly used to produce atomic-scale images never before seen [19, 20]. For this revolutionary achievement in the ability to measure surfaces on the atomic scale, Binnig and Rohrer were awarded half of the 1986 Nobel Prize in Physics. With a vertical resolution on the order of 10^{-12}m and a horizontal resolution on the order of 10^{-10}m, the STM quickly became a major instrument in surface and condensed matter physics. The STM used at our laboratory is the Tops-3 Variable Temperature STM, designed and manufactured by Oxford Instruments.

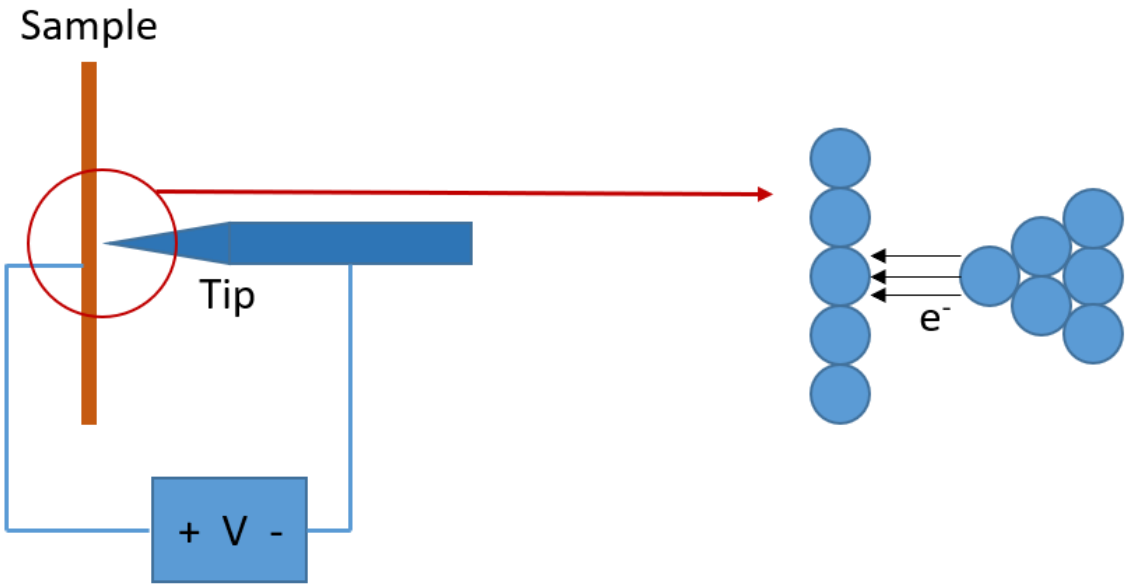

Figure 2.12. Diagram showing the basic arrangement of sample and tip in the STM.

2.4.2 Operating Principles

The STM makes use of the fact that wavefunctions can penetrate potential barriers, such that if the barrier were to be narrow enough, alongside other conditions, the electron can "tunnel" to the other side with reasonable probability. The ideal STM brings an atomically sharp scanning tip within a few Ångstroms of a sample with a bias voltage between them, as shown in Figure 2.12. Electrons can begin tunneling between the tip and the sample, with the direction on the sign of the bias voltage. The tunneling current is described by the relationship [21]

$$I \propto exp(-2Kd), \tag{2.1}$$

where d is the distance between the sample and tip, and

$$K = \sqrt{2m\phi}/\hbar$$

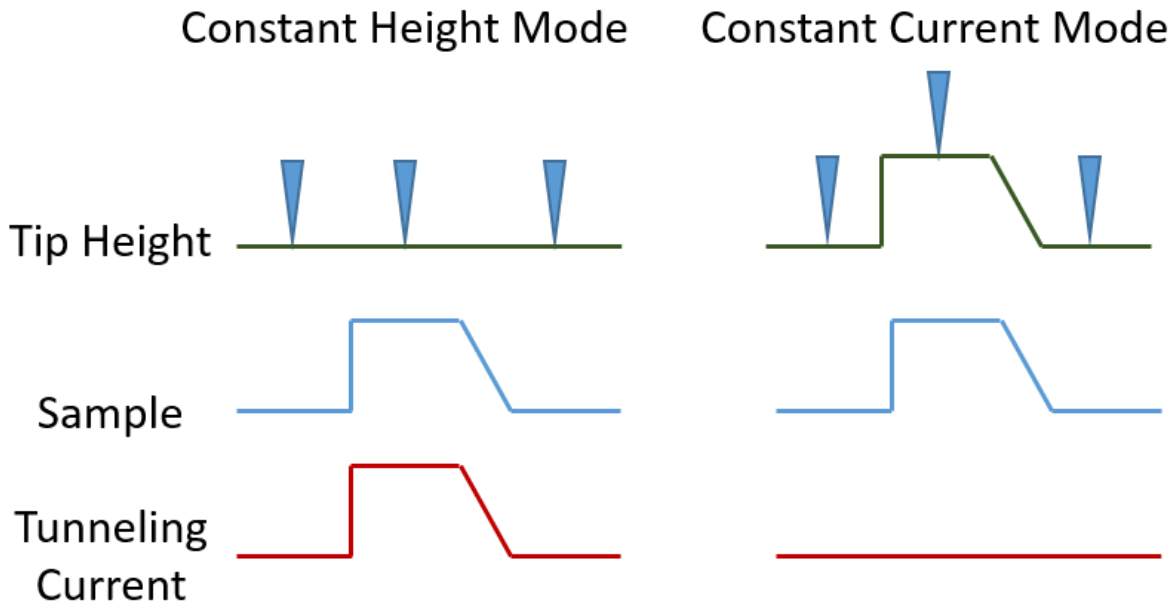

Figure 2.13. Diagram showing the two scanning modes for a hypothetical sample contour provided in the middle row.

is the characteristic exponential decay length for electron mass m and effective local work function ϕ. This relationship is extremely sensitive to changes in the distance d, with a change of 0.01Å causing the tunneling current to change by a few percent under normal operating conditions. The tunneling current is usually on the order of nanoamps, for which a few percent change is accurately measurable, resulting in the incredible vertical resolution mentioned above.

By measuring the tunneling current as the tip moves across the sample, it is then possible to obtain topological information about the sample. There are two modes for topological scanning – constant height mode, and constant current mode. As depicted in Figure 2.13, the constant height mode is the basic application of the current-distance relationship, where the tip's height is left unchanged, such that the distance between the tip and sample is determined by the contour of the sample, which then determines the tunneling current measured by the tip. Plotting this current forms a direct image of the sample's topology, making this mode very simple

to use. The drawback is that the sample must not have any feature that is tall enough to physically collide with the tip and thereby ruin its high-resolution property.

The constant current mode uses a proportional-integral-differential (PID) feedback circuit which attempts to move the scanning tip in order to keep the tunneling current constant. The movement of the tip is recorded and used to form the topological image, and unlike the constant height mode, the maximum height of sample features is only limited by the feedback circuit's ability to respond to the change in height and move the tip out of the way in time. The drawback, of course, is the increased complexity in the design, requiring both the feedback circuit, as well as a mechanism to move the tip at such a small scale. Modern designs use tips mounted on a piezoelectric tube divided into quadrants, with x-y movement controlled using voltages on individual quadrants while the z movement is controlled using voltages on all four quadrants at once [22].

One final thing to note is that the current-distance relationship given in Equation 2.1 does not capture the entirety of the interaction between the sample and tip. By modeling the end of the tip as a spherical potential well and assuming small voltages and temperatures, one can derive a dependence of the tunneling current using first-order perturbation theory [23]:

$$I \propto \sum_v |\psi_v(\vec{\boldsymbol{r}}_{\mathbf{0}})|^2 \delta(E_v - E_F),$$

where $\vec{\boldsymbol{r}}_{\mathbf{0}}$ is the center of curvature of the tip, E_v is the energy of the sample state ψ_v, and E_F is the Fermi level. This suggests that the tunneling current is proportional to the local density of states (LDoS) of the sample at the tip's location. Depending on the polarity of the applied bias voltage, the tunneling current will represent filled states or the empty states, as depicted by the simplified diagram in Figure 2.14.

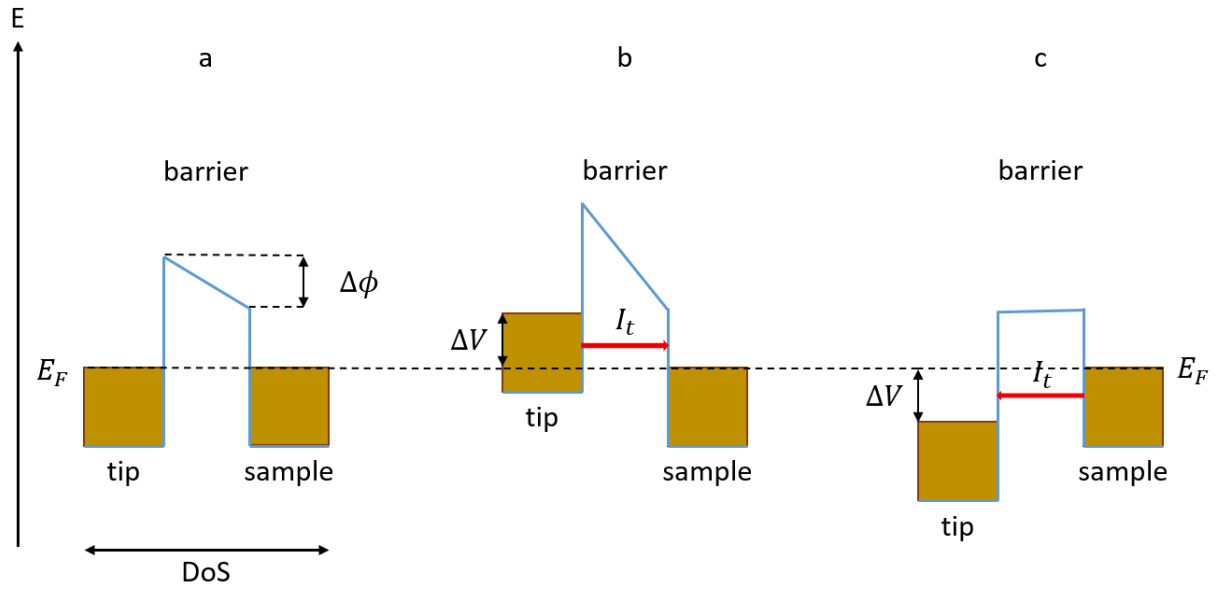

Figure 2.14. Diagrams showing the density of states (DoS) of the tip and sample for different bias voltage scenarios. (a) The tip and sample are in electrical equilibrium after they have been brought close at zero bias. (b) The sample is positively biased, and the electrons tunnel into the sample's empty states. (c) The sample is negatively biased, and the electrons tunnel out of the sample's filled states.

One consequence of this relationship is that the apparent "height" of the electron will depend on the availability of the states, with the greatest intensity corresponding to peaks in the LDoS that are accessible at the given bias voltage. Even the apparent shape of the atom will be affected, since different orbitals have different shapes – for example, d-orbitals are much more localized than s-orbitals, making their tunneling amplitudes smaller on average. The behavior of the tunneling current is further complicated by bonds between atoms, which will deform the orbitals and thus shift the LDoS peaks to locations that sometimes will not even correspond to the position of any individual atom. A clear example of LDoS imaging can be seen in work done on Ge(111)-c(2x8) by Hirschorn *et al.*, in which the c(2x8) surface was imaged with the STM, but the bias voltage was changed about halfway through the scan, resulting in very different depictions of the same surface [24]. Comparing the image to an atomic model of the surface also

shows that the intensity maxima of the image do not correspond at all to the atoms in the atomic model.

Because of this interaction with the LDoS, interpreting atomic-resolution STM images is much more complicated than one might expect, especially when one's goal is to determine the atomic arrangement of the surface. However, this interaction also provides very valuable information on the electronic structure of the sample that cannot be obtained by simple height measurements. For larger structures such as islands or defects, the LDoS does not matter, as the current-height relationship becomes more relevant for direct, topological imaging.

2.4.3 Oxford Instruments Tops-3 Variable Temperature STM

Figure 2.15 shows a photo of the Oxford Instruments STM, with many of its parts identified by arrows. It was designed with a liquid helium cryostat meant to allow cooling towards 100K, but it could also be cooled with liquid nitrogen, with some modifications to a liquid nitrogen dewar so that it could accept a liquid helium transfer arm. Due to some design flaws in the cooling system, the lowest temperature that could be achieved with liquid nitrogen was measured to be a little under 200K after a few hours. The heating system used the internal heating system of the sample holder described in section 2.2 and could be controlled either manually or automatically with a Eurotherm 818 PID temperature feedback controller. This could maintain the sample's temperature at values either above or below room temperature.

Vibration isolation of the instrument was achieved in two stages. The STM and XPS chambers rest on three Newport 2000 Series High Performance Laminar Flow Isolators, which are inflated with nitrogen gas for the first, basic stage of vibration isolation. The second stage of

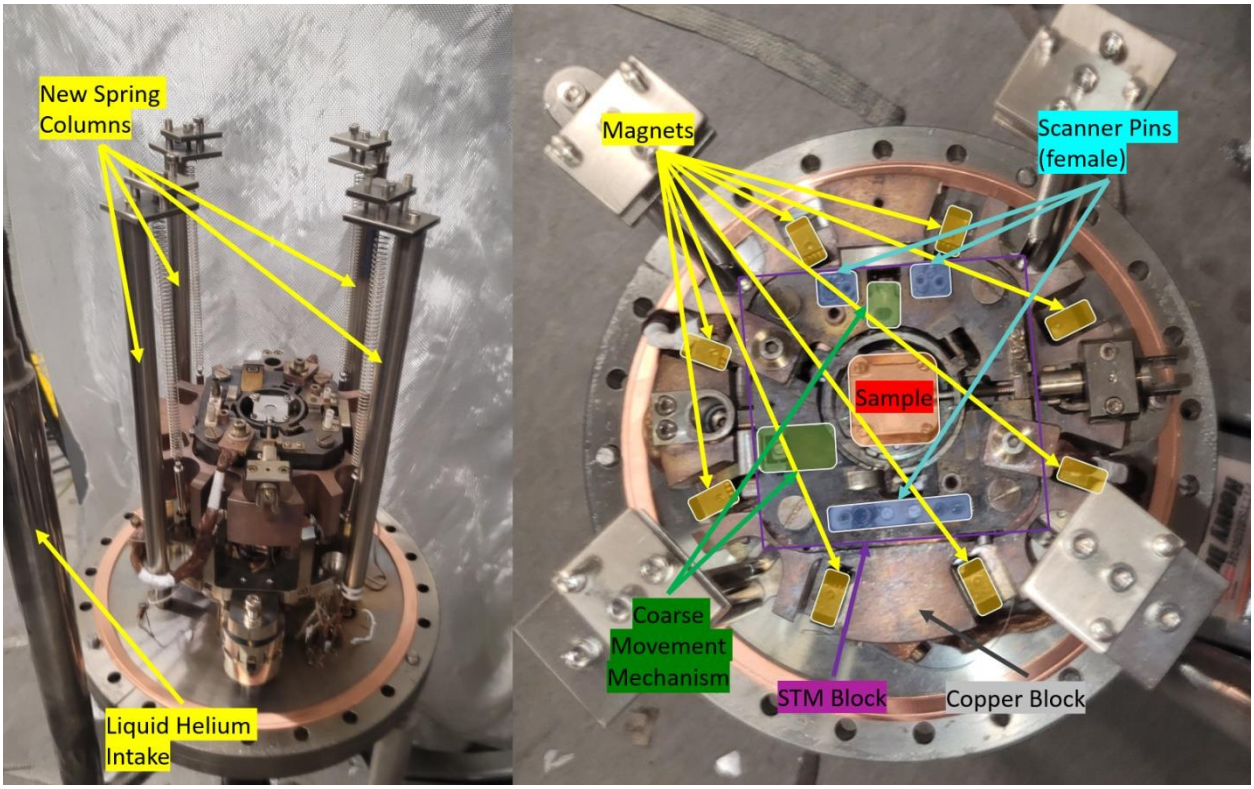

Figure 2.15. Left: Side view of the Oxford STM. Right: Top view of the Oxford STM. Various parts of the STM are marked by arrows.

vibration isolation consists of a spring suspension with eddy-current damping between an array of magnets and slots in a supporting copper block. The copper block, which supported the STM block, was suspended on four springs fixed to four columns attached to the STM frame. The spring suspension system and the magnets have been changed from the original design; the spring system was redesigned to increase the ease of adjustment for leveling, while the old magnets required replacement due to having lost too much strength, possibly from exposure to too many UHV bakeouts. Proper spring suspension of the copper block could be verified by checking the electrical contact between the copper block (which is electrically isolated save for a diagnostic lead), and the magnets, which are grounded via the STM frame.

The STM block has a central slot in which the sample holder is placed, with female pins on the sides for accepting male pins on the scanner. The STM scanner is shown in Figure 2.16,

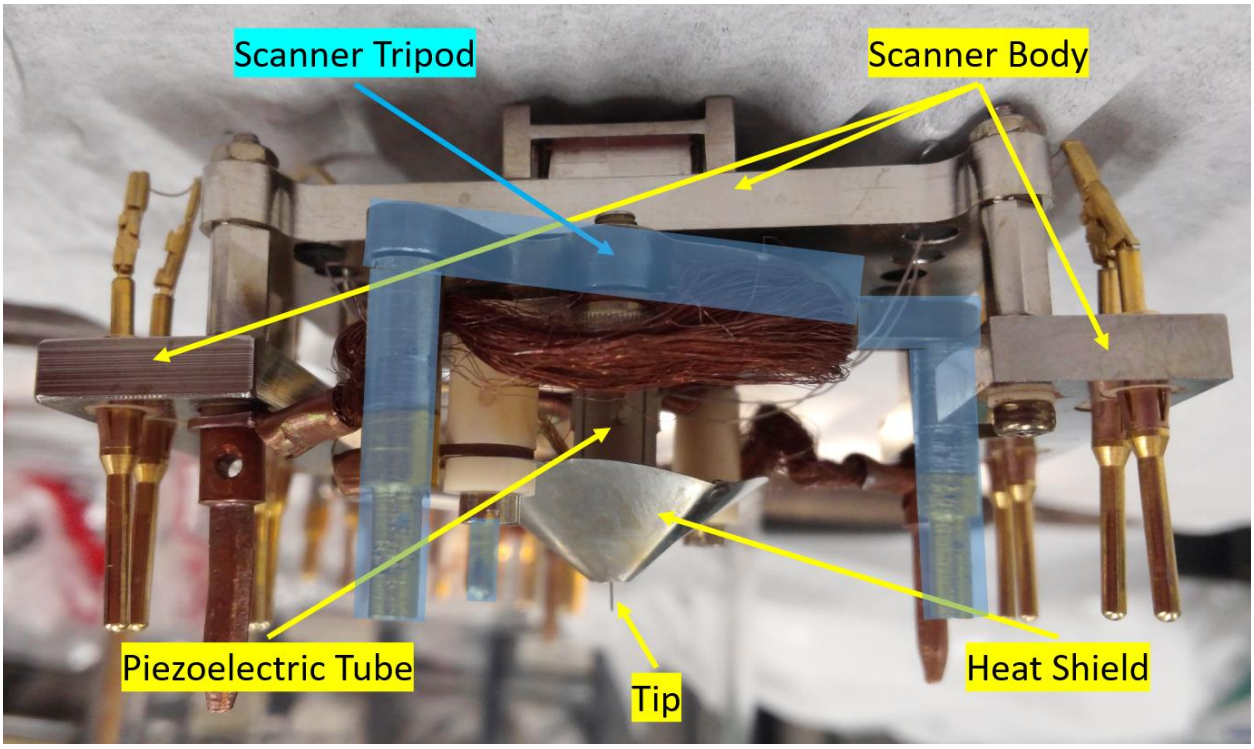

Figure 2.16. Photograph of the STM Scanner, with its parts identified by arrows.

and it consists of two parts - the main scanner body that houses the male pins, and the scanner tripod on which the piezoelectric tube and the scanning tip are mounted. The piezoelectric tube can be biased up to 140V in either direction for a vertical movement range of ±350nm, while the quadrants can receive up to an additional 60V in either direction for a horizontal range of about ±750nm depending on the length of the tip. The tips are produced from 0.08mm tungsten wires via electrochemical etching in KOH etching solution, as described in [25]. The tip is mounted in a syringe tube that is mounted on an insulating disk at the end of the piezoelectric tube and is adjusted for height outside the STM, using a scanner storage stand with a micrometer attached. The tripod is responsible for the coarse movement of the tip. While some STM designs move the sample itself for coarse tip positioning and move only the tip by the piezoelectric tube for fine motion control, the Oxford STM design performs both coarse and fine movements on the tip assembly.

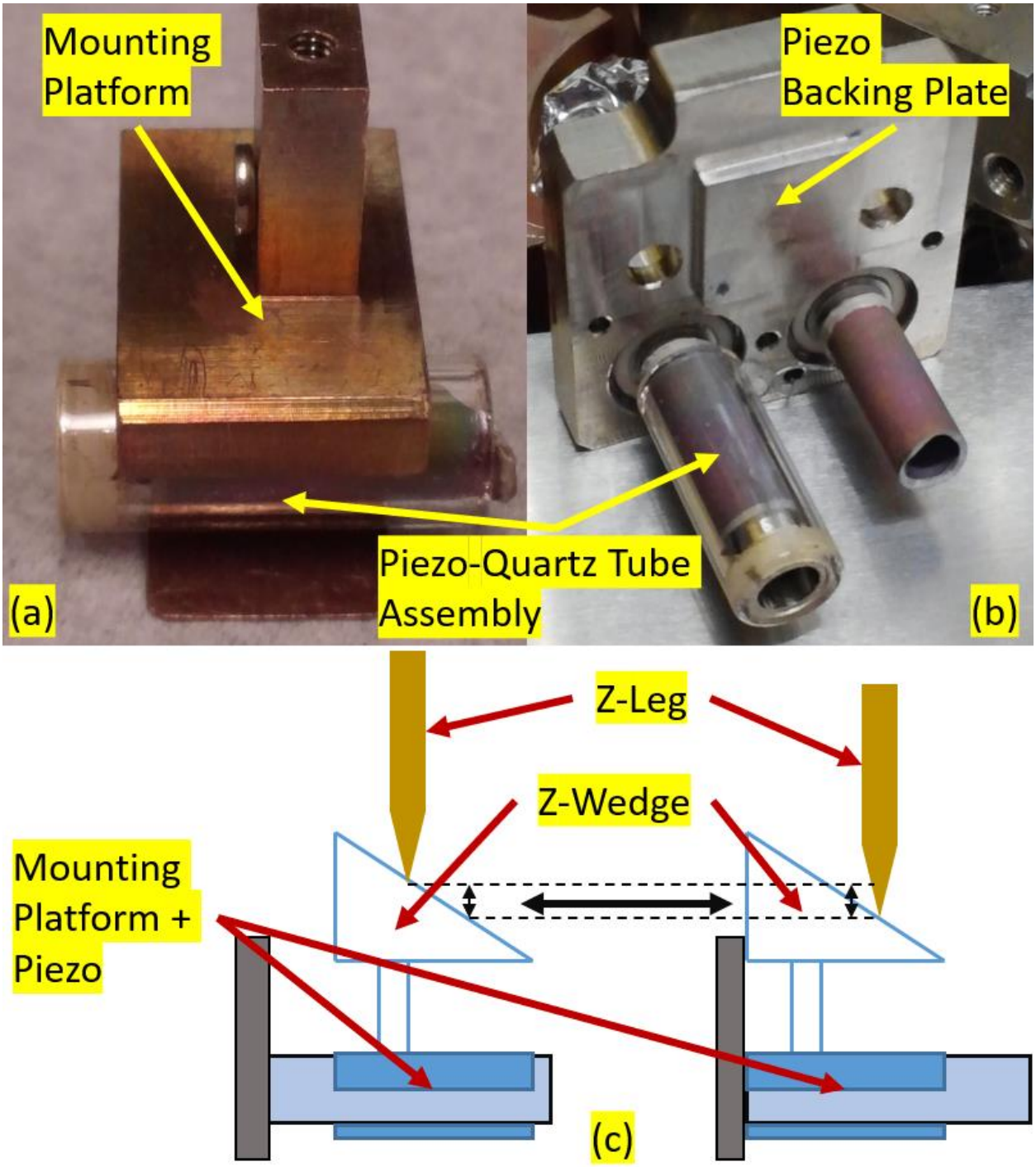

Figure 2.17. (a) Photo of a part of the coarse movement mechanism, showing the mounting platform fitted on the piezo-quartz tube assembly. (b) Photo showing the piezo-quartz tube assembly (one without the quartz tube) mounted on a backing plate to be attached to the STM frame. (c) Diagram showing how the z-wedge moves the z-leg up and down as the mounting platform is moved horizontally.

The tripod has a range of movement of a few millimeters in the x- (horizontal) and z- (vertical) directions, and no movement in the y-direction. The z-leg rests on top of a triangular wedge, while the x-leg rests in a copper ring, both of which are marked as “Coarse Movement Mechanism” in Figure 2.15. These two components each sit on top of a mounting platform, which then sit on pairs of piezoelectric tubes inside quartz cylinders, as shown in Figure 2.17. The piezo-quartz tube assembly moves the mounting platform using the stick-slip method in which the piezo is extended slowly and then retracted quickly (and vice versa for reversed movement), with each extension-retraction cycle moving the platform on the order of 1µm. These cycles are performed at high enough frequencies for visible movement. For movement in the x-direction, the platform will simply move the copper ring horizontally, dragging the x-leg with it. For movement in the z-direction, the triangular wedge is moved horizontally while the z-leg is allowed to slip on the slope such that it moves up and down depending on the position of the wedge, as depicted in Figure 2.17. The third leg of the tripod rests in a guiding slot which prevents motion in the y-direction.

The coarse movement is used in conjunction with a video camera providing a live, zoomed-in view of the tip and sample, until the tip is close to the sample as seen on the video monitor. The automatic approach can then be activated, and it uses a combination of coarse and fine control by using a single stick-slip step followed by the extension of the fine-movement piezoelectric tube. If the tip does not detect a tunneling current, the fine-movement piezoelectric tube is fully retracted, and the coarse movement is taken forward by one more step; this cycle is repeated until a tunneling current is detected, at which point the constant-current feedback circuit takes over.

The STM used to be operated with original electronics (STM controller) provided by Oxford Instruments, along with their TOPS3 software for image acquisition. Due to degradation of electronic components over time, the Oxford STM controller began exhibiting resolution problems and was replaced with a controller built by RHK Technology, along with their own acquisition software. The migration of electronics as well as the subsequent testing and calibration was performed by undergraduate student Eli Baum. Data processing and analysis was performed using Nanotec Electronica's WSxM Software [26].

2.5 X-Ray Photoelectron Spectroscopy

2.5.1 Introduction

The XPS takes advantage of the well-known photoelectric effect in which a photon is absorbed by an electron in one of the core levels of an atom, causing the electron to be ejected from the atom if this energy exceeds the sum of the binding energy E_b and work function ϕ. The electron's kinetic energy KE can be measured by an electron energy analyzer and can be written as

$$KE = h\upsilon - E_b - \phi,$$

where $h\upsilon$ is the photon energy. Because the binding energy of each core level of each atom is unique, knowing the kinetic energy, photon energy, and work function means one can accurately determine where the electron came from, providing information about the composition of the surface.

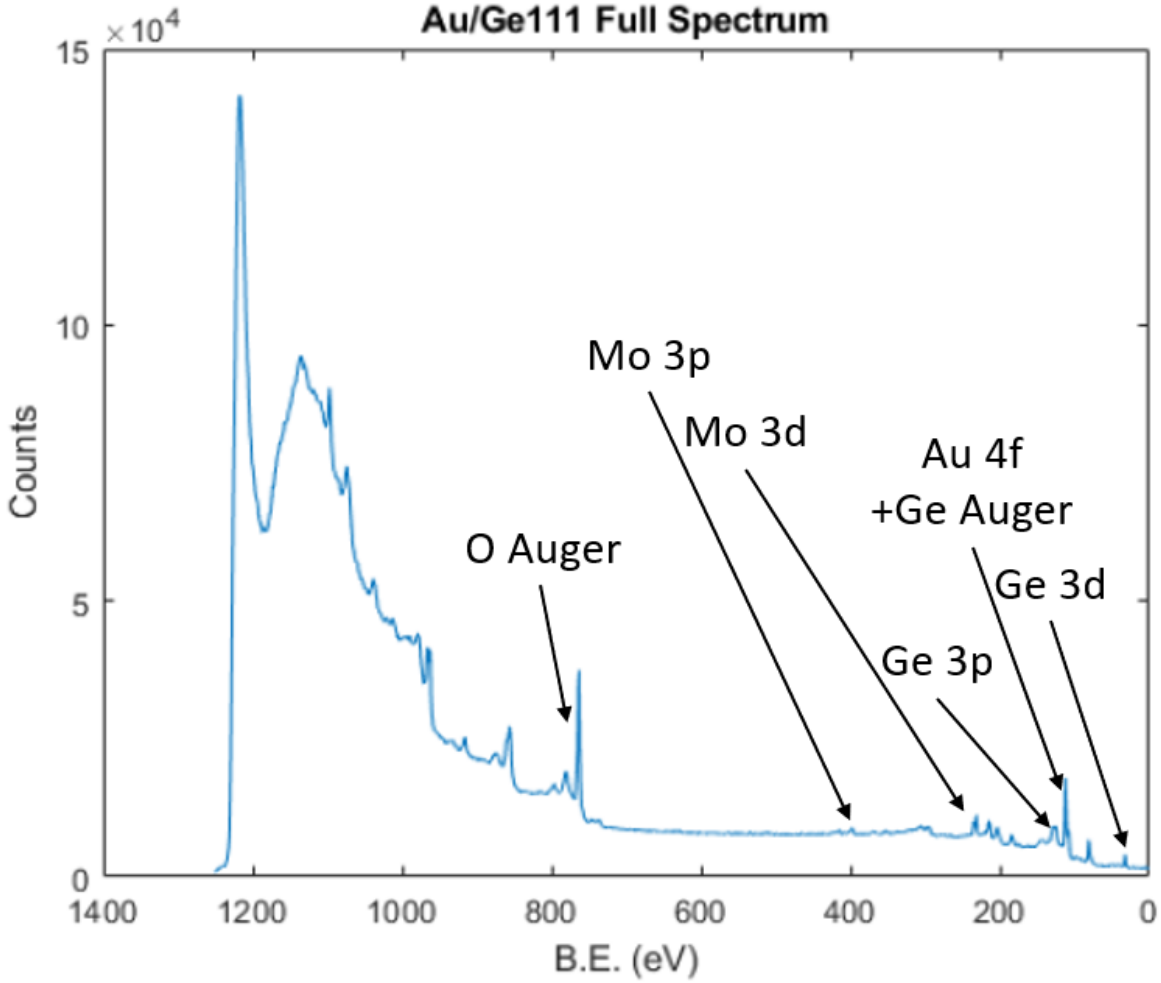

Figure 2.18. A full-spectrum scan of Au/Ge(111) using Mg K_α X-rays, with some peaks identified. The Ge Auger peak is very close to the Au 4f peak, making them difficult to distinguish. Some small Mo peaks can also be identified due to the sample holder's top plate.

The most basic function of the XPS, therefore, is to perform a scan across a wide range of binding energies to obtain a spectrum of peaks that reveals what elements are present on the surface [27]. This is the primary use of the XPS at our laboratory as well, where XPS is typically used for checking the samples for contamination. The locations of common peaks for most elements are very well-documented [28], which is why the XPS is such an easy, convenient method for checking the basic composition of the sample. An example spectrum for an Au/Ge(111) sample taken using our XPS is provided in Figure 2.18. The secondary use of the XPS

at our laboratory is for evaporator calibration by looking at the ratio of areas under the peaks for the substrate and the overlayer [29]. By comparing the experimental ratio with the ratio simulated by the software, Simulation of Electron Spectra for Surface Analysis (SESSA) [30], it is possible to determine the coverage of the overlayer and thus calculate the average deposition rate of the evaporator.

Of course, the simplistic equation given above does not capture the full complexity of the photon capture process. Additional spectroscopic effects are discussed in more detail in [31] and are widely studied in other laboratories. Other than multiplet splittings and chemical shifts, more sophisticated XPS techniques are beyond the scope of analyses performed at this laboratory.

2.5.2 X-Ray Source

The X-rays used in XPS can come from two types of sources. One is using radiation from a synchrotron light source, where charged particles, usually electrons, are injected by a particle accelerator into a storage ring where they radiate light because of their acceleration in circular orbits. The particles can be also rapidly oscillated using an array of magnets called wigglers or undulators, causing them to emit photons according to the oscillation frequency [32, 33]. The main advantage of this source is that it is highly tunable in terms of photon energy, which can usually be selected using a monochromator, as well as much higher photon flux than conventional laboratory X-ray tubes.

The other type of X-ray source, which is used at our laboratory, involves bombarding a chosen anode material with high energy electrons, creating holes in the core electron shells [21]. The core holes are then filled by electrons from higher shells, releasing photons in the decay

process. Only a few materials have desirable characteristics for an experimental X-ray source, such as a low bremsstrahlung background and narrow line emission. The most common anode materials for X-ray production for XPS experiments are aluminum and magnesium, using K_α emissions that have peaks at 1486.6eV and 1253.6eV respectively, and the emission spectra have been well-documented for a quite a long time [34, 35].

Many X-ray sources use both Al and Mg emissions, with the ability to switch between them as needed. A major reason for switching is to avoid certain, non-XPS peaks that can overlap

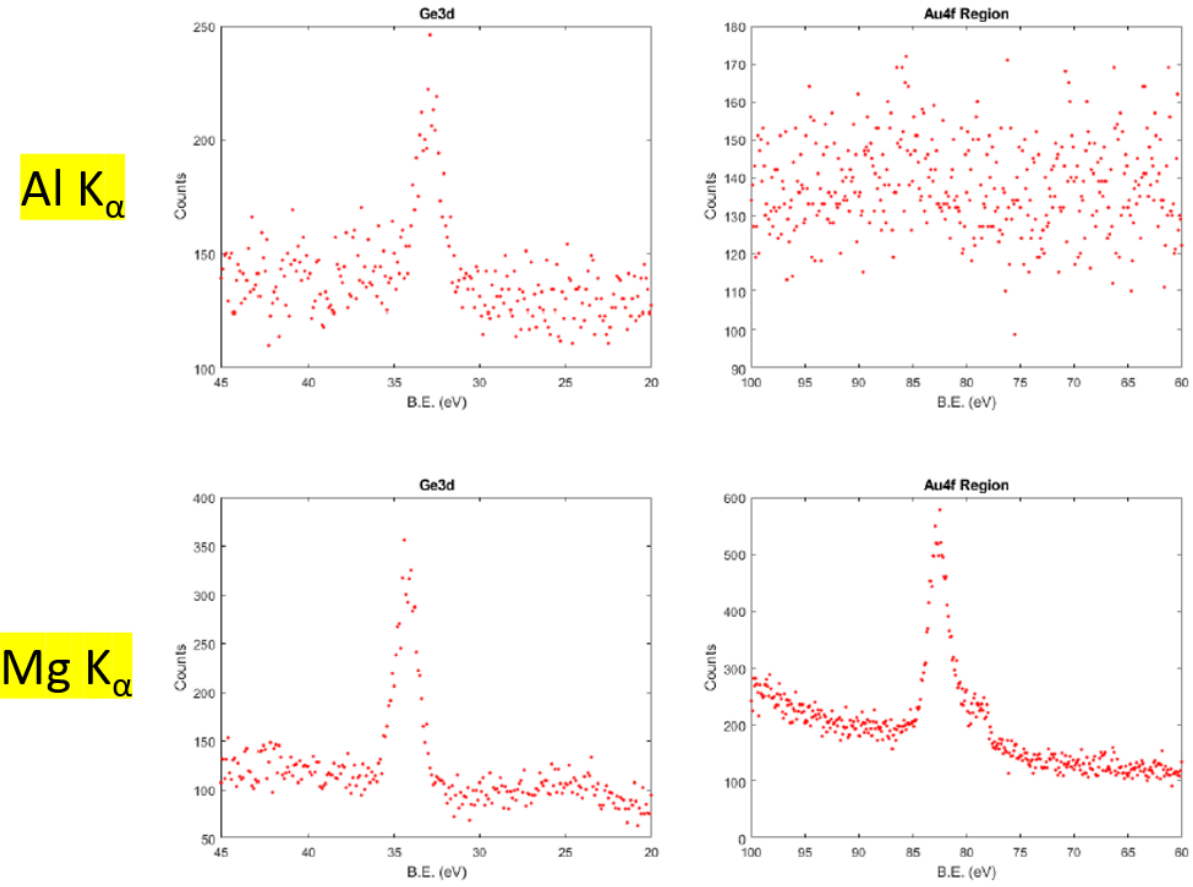

Figure 2.19. XPS spectra obtained using Al and Mg emissions on a clean Ge(111) sample. The spectra on the left clearly show the Ge 3d peak. The spectra on the right were taken over an energy region in which Au 4f peaks would be observed if some were to be deposited on the substrate. The Au 4f spectrum produced by Al emission shows only background as expected, while the spectrum produced by Mg emission shows a Ge Auger peak.

with some XPS lines depending on the X-ray energy. Auger peaks have the same kinetic energy independent of the X-ray energy, but when plotted on the usual XPS spectrum as a function of binding energy, the line positions will appear in different binding energy locations for Al and Mg emissions. Figure 2.19 shows how Ge Auger peaks under Mg emissions will appear directly over the region in which Au 4f peaks are expected, meaning they will interfere with any XPS

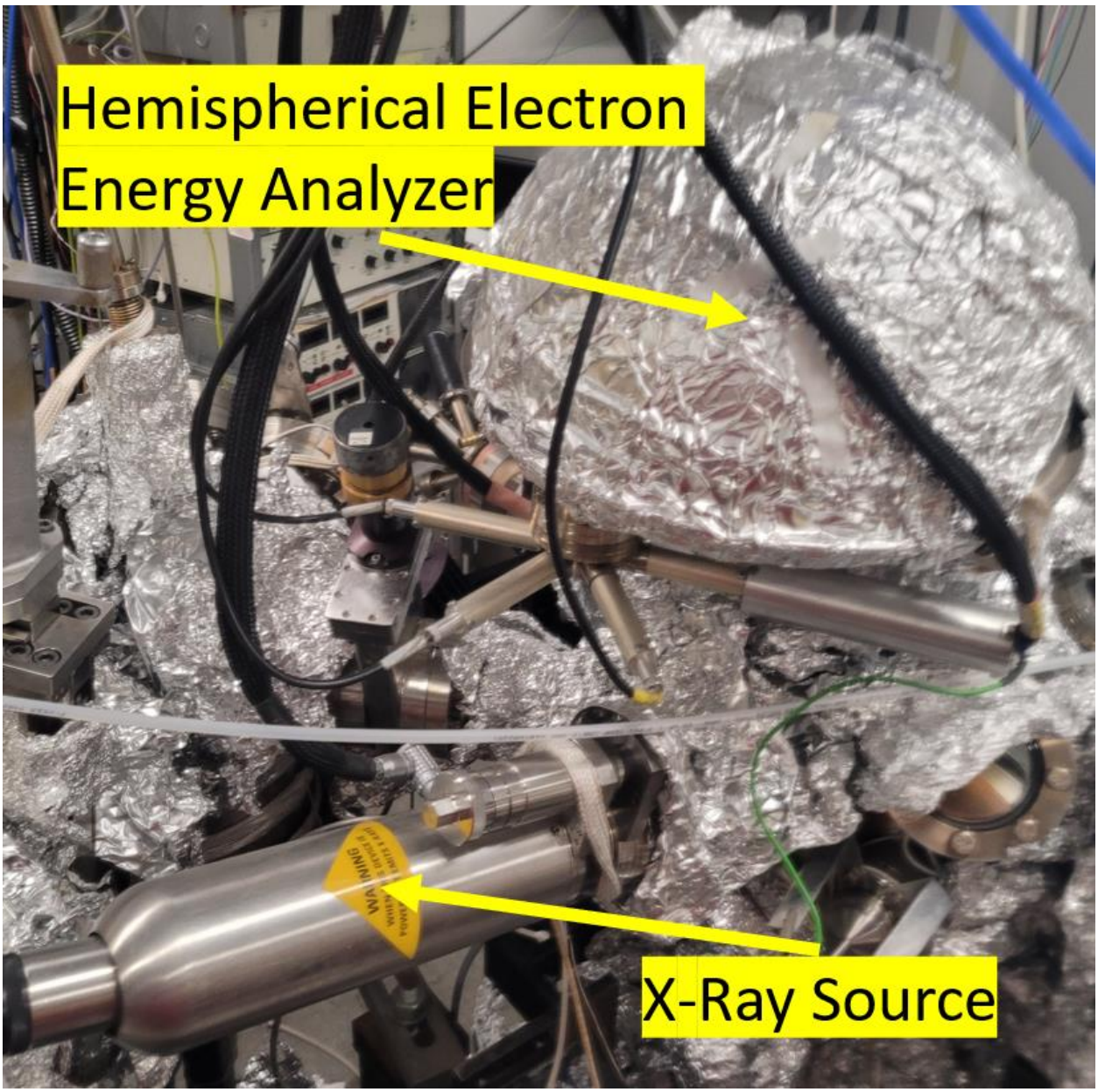

Figure 2.20. Photo showing the X-ray source and the hemispherical electron energy analyzer on the XPS chamber.

experiment involving both Ge and Au. This means it is preferable to use Al emissions for such experiments, and similar considerations must be made for other materials and their Auger spectra with relation to their XPS spectra.

The X-ray source used at our laboratory is the Dual Anode X-ray Sources System built by FISONS Instruments, shown in Figure 2.20. The source operates at up to 5mA of filament current, with a bombardment voltage of 15kV. It includes some safety interlocks that check for the proper grounding cover over the exposed anode connection point, as well as sufficient water flow for the cooling system. The cooling system is a closed-circuit system consisting of a reservoir and a 1/2 horsepower booster pump with a flow rate of about 1 gallon per minute. A filter keeps the cooling water free of particulates, and a heat exchanger with an external water circuit helps maintain the temperature of the closed circuit. Due to an accident involving a large water leak that led to the failure of the booster pump as well as damage to the X-ray source, a new cooling system interlock was designed using an Arduino to monitor the flow rate and to cut the power to critical components if a fault were detected. Photos of the new interlock controller are provided in Figure 2.21, and the circuit diagram and the Arduino code are provided in Appendix A.

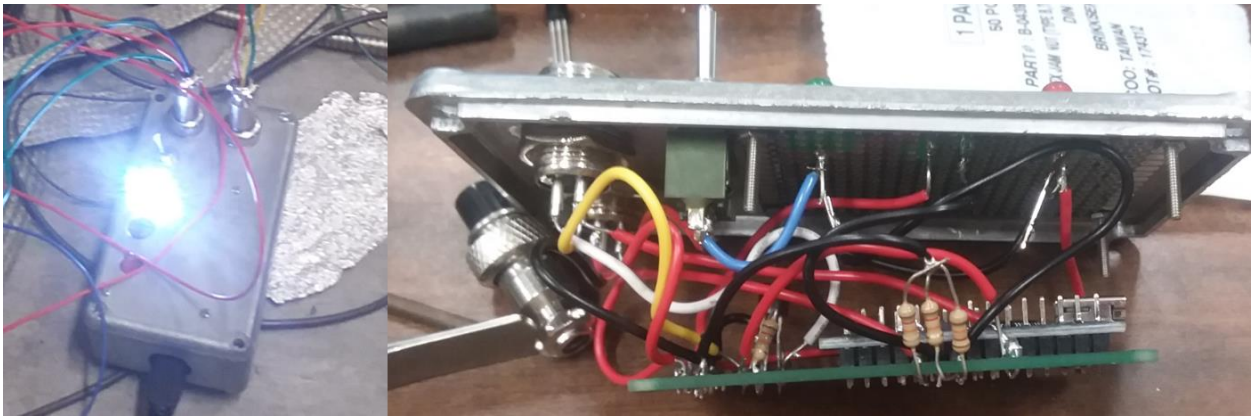

Figure 2.21. Photos of the new XPS cooling system interlock controller, showing both the exterior (left) and the interior (right).

2.5.3 Electron Energy Analyzer

Figure 2.20 also shows the VG100AX hemispherical electron energy analyzer, also built by FISONS Instruments, along with the related electronic controller units. It used to be operated using the manufacturer-provided software called VGX900, until the computer interface board failed. A third-party interface board (SPCI721F) was used as the replacement, along with the SPECTRA Version 8 software written by R. Unwin. The entrance to the energy analyzer was fitted with a circular array of apertures of different sizes (Figure 2.22), designed by Yu Sato [2]. Since the X-ray source irradiates the sample holder's top plate as well as the sample, electrons from the core levels of the top plate material (molybdenum, titanium, or stainless steel) will appear on measured XPS spectra and can interfere with other peaks of interest. Thus, a selected aperture

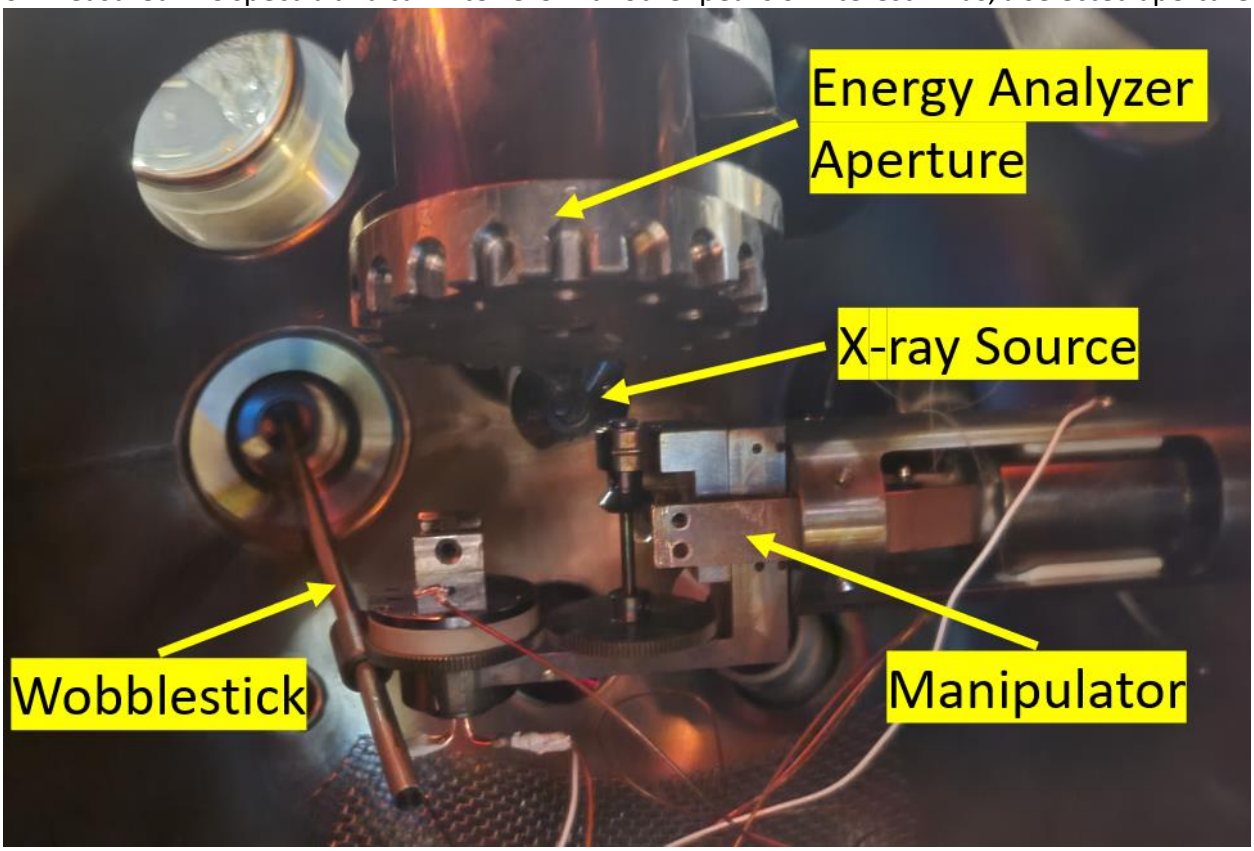

Figure 2.22. Photo of the interior of the XPS chamber, showing the manipulator, X-ray source, the custom energy analyzer aperture [2], and the wobblestick used to turn the aperture wheel.

is used to limit the sampling area of the XPS. The aperture size can be chosen by turning the aperture wheel using a wobblestick, until peaks from the top plate material no longer appear on the XPS scans.

The hemispherical analyzer consists of two hemispherical shells with inner and outer radii of R_1 and R_2 respectively and inner and outer voltages of V_1 and V_2 respectively. In the middle of the two hemispherical shells, which would be at the radius $R_0 = \frac{1}{2}(R_1 + R_2)$, the electrical potential is then $V_0 = \frac{1}{R_0}(V_1 R_1 + V_2 R_2)$. With this, we can set up a simple expression for the potential inside the hemisphere:

$$V(r) = \frac{V_0 R_0}{r},$$

and we can take the derivative and use the expression for centripetal acceleration v^2/r to get

$$\frac{mv^2}{r} = -\frac{eV_0 R_0}{r^2}.$$

Finally, after substituting $r = R_0$ and solving for electron pass energy in eV, $E_p = \frac{mv^2}{2e}$, we get the simple relationship

$$E_p = -\frac{V_0}{2}.$$

Since the radii of the hemispherical shells are fixed, one can tune the voltages on the shells to change V_0 and thereby choose the energy of electrons that can pass through the energy analyzer. A diagram showing the arrangement of the energy analyzer is provided in Figure 2.23. The XPS spectrum is therefore measured by varying the voltage difference between the two shells and recording the number of electrons that pass through the exit slit and into the channeltron detector at each voltage step. Of course, as with any experimental apparatus, there

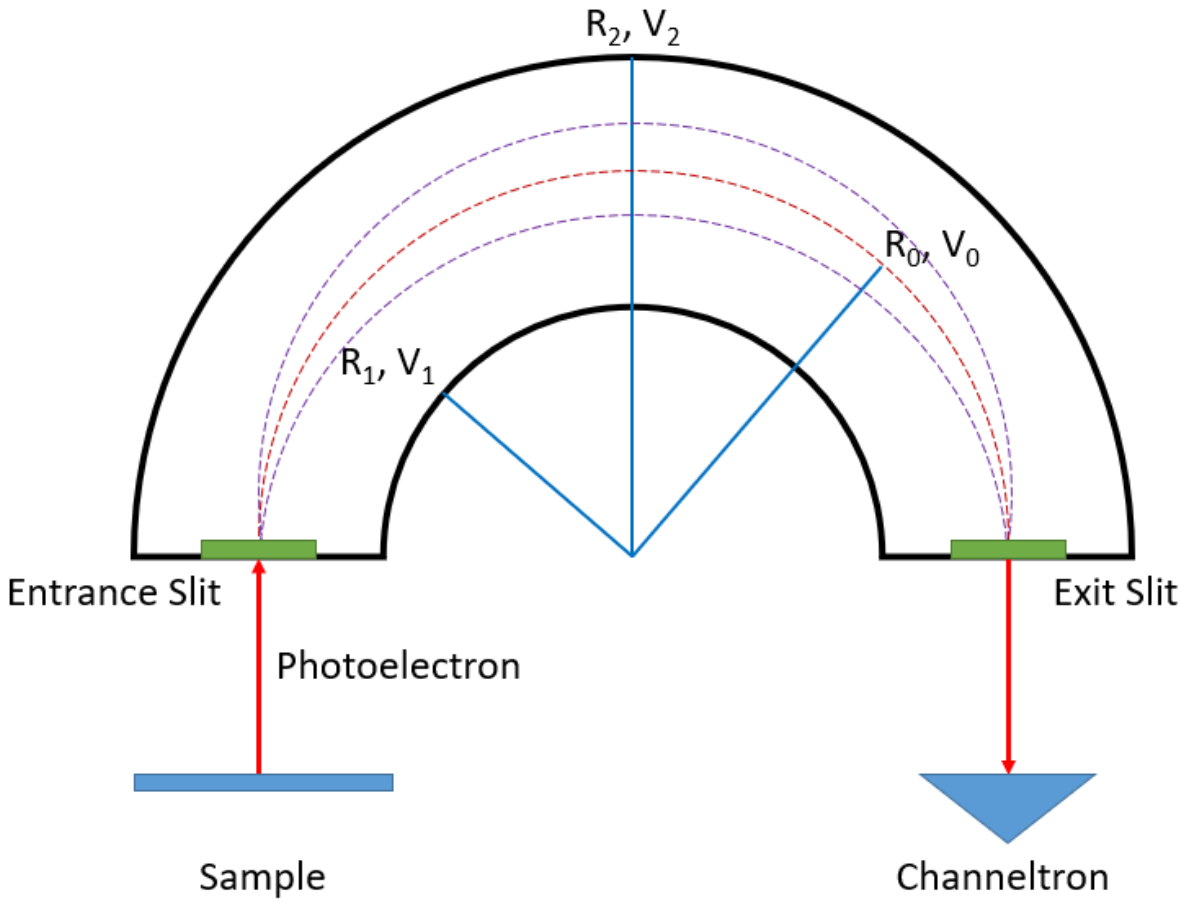

Figure 2.23. Diagram showing the operating principles of a hemispherical electron energy analyzer. Photoelectrons from the sample are sent through a semicircular tunnel whose inner and outer walls are biased at different voltages. Based on the voltage difference, only electrons of a certain energy can form the necessary arc to reach the exit slit on the other side. The dashed, red arc is the ideal path for electrons entering exactly normal to the entrance slit, while the dashed, purple arcs are nonideal paths taken by electrons entering at an angle.

will be nonideal factors, such as electrons entering at different angles and a spread of electron energies due to the finite sizes of the entrance and exit slits; these will affect the resolution of the energy analyzer and are discussed in more detail in literature such as [36]. Modern controller units have various settings designed to limit these extra effects, albeit at the cost of signal intensity, requiring longer scans to achieve an acceptable signal-to-noise ratio.

References

[1] A. Loui, An Experimental and Theoretical Study of Furan Decomposition on Pd(111) Using Scanning Tunneling Microscopy and Density Functional Theory, PhD dissertation in Physics, University of California Davis, Davis (2005).
[2] Y. Sato, Thin Film Microscopy of Pb on Ge(111) Phase Transitions and FexNi(1-x) on Cu(111) Magnetic Surface Alloy, PhD dissertation in Physics, University of California Davis, Davis (2005).
[3] J. Giacomo, A Low Energy Electron Microscopy Study of the Growth and Surface Dynamics of Ag/Ge(111) and Au/Ge(111), PhD dissertation in Physics, University of California Davis Davis (2009).
[4] C.L.H. Devlin, D.N. Futaba, A. Loui, J.D. Shine, S. Chiang, A unique facility for surface microscopy, Materials Science and Engineering B-Solid State Materials for Advanced Technology, 96, (2002) 215-220.
[5] W. Telieps, E. Bauer, The (7x7) - (1x1) Phase Transition on Si(111), Surface Science, 162, (1985) 163-168.
[6] D.R. Penn, Electron Mean Free Paths for Free-Electron-Like Materials, Physical Review B, 13, (1976) 5248-5254.
[7] T.N. Rhodin, J.W. Gadzuk, The Nature of the Surface Chemical Bond, North-Holland, Amsterdam, (1979).
[8] Y. Sato, S. Chiang, N.C. Bartelt, Spontaneous domain switching during phase separation of Pb on Ge(111), Physical Review Letters, 99, (2007) 096103.
[9] B.Q. Li, W. Swiech, J.A. Venables, J.M. Zuo, A LEEM study of bamboo-like growth of Ag crystals on Si(001) surfaces, Surface Science, 569, (2004) 142-148.
[10] R.M. Tromp, Low-energy electron microscopy, IBM Journal of Research and Development, 44, (2000) 503-516.
[11] E. Bauer, The Resolution of the Low-Energy Electron Reflection Microscope, Ultramicroscopy, 17, (1985) 51-56.
[12] J.L. Wiza, Microchannel Plate Detectors, Nuclear Instruments & Methods, 162, (1979) 587-601.
[13] E. Poppenheimer, *LEEM Data Analyzer*, (2010).
[14] C.H. Mullet, S. Chiang, High temperature growth of Ag phases on Ge(111), Journal of Vacuum Science & Technology A, 31, (2013) 020602.
[15] C.H. Mullet, S. Chiang, Reconstructions and phase transition of clean Ge(110), Surface Science, 621, (2014) 184-190.
[16] G. Binnig, H. Rohrer, Scanning Tunneling Microscopy, Helvetica Physica Acta, 55, (1982) 726-735.
[17] G. Binnig, H. Rohrer, Vacuum Tunnel Microscope, Helvetica Physica Acta, 55, (1982) 128-128.
[18] G. Binnig, H. Rohrer, C. Gerber, E. Weibel, Tunneling Through a Controllable Vacuum Gap, Applied Physics Letters, 40, (1982) 178-180.
[19] G. Binning, H. Rohrer, C. Gerber, E. Weibel, Surface Studies by Scanning Tunneling Microscopy, Physical Review Letters, 49, (1982) 57-61.
[20] H.J. Scheel, G. Binnig, H. Rohrer, Atomically Flat LPE-Grown Facets Seen by Scanning Tunneling Microscopy, Journal of Crystal Growth, 60, (1982) 199-202.

[21] D.P. Woodruff, T.A. Delchar, Modern Techniques of Surface Science, Cambridge University Press, Cambridge, (1994).
[22] G. Binnig, D.P.E. Smith, Single-Tube 3-Dimensional Scanner for Scanning Tunneling Microscopy, Review of Scientific Instruments, 57, (1986) 1688-1689.
[23] J. Tersoff, D.R. Hamann, Theory and Application for the Scanning Tunneling Microscope, Physical Review Letters, 50, (1983) 1998-2001.
[24] E.S. Hirschorn, D.S. Lin, F.M. Leibsle, A. Samsavar, T.C. Chiang, Charge-Transfer and Asymmetry on Ge(111)-c(2x8) Studied by Scanning Tunneling Microscopy, Physical Review B, 44, (1991) 1403-1406.
[25] J.P. Ibe, P.P. Bey, S.L. Brandow, R.A. Brizzolara, N.A. Burnham, D.P. Dilella, K.P. Lee, C.R.K. Marrian, R.J. Colton, On the Electrochemical Etching of Tips for Scanning Tunneling Microscopy, Journal of Vacuum Science & Technology a-Vacuum Surfaces and Films, 8, (1990) 3570-3575.
[26] I. Horcas, R. Fernandez, J.M. Gomez-Rodriguez, J. Colchero, J. Gomez-Herrero, A.M. Baro, WSXM: A software for scanning probe microscopy and a tool for nanotechnology, Review of Scientific Instruments, 78, (2007) 013705.
[27] J. Mahoney, C. Monroe, A.M. Swartley, M.G. Ucak-Astarlioglu, C.A. Zoto, Surface analysis using X-ray photoelectron spectroscopy, Spectroscopy Letters, 53, (2020) 726-736.
[28] A.C. Thompson, D.T. Attwood, E.M. Gullikson, M.R. Howells, J.B. Kortright, A.L. Robinson, J.H. Underwood, K. Kim, J. Kirz, I. Lindau, P. Pianetta, H. Winick, G.P. Williams, J.H. Scofield, X-ray Data Booklet, 2 ed., Lawrence Berkeley National Laboratory, University of California, (2001).
[29] C.H. Mullet, B.H. Stenger, A.M. Durand, J.A. Morad, Y. Sato, E.C. Poppenheimer, S. Chiang, Growth and phase transformations of Ir on Ge(111), Surface Science, 666, (2017) 96-103.
[30] W. Smekal, W.S.M. Werner, C.J. Powell, Simulation of electron spectra for surface analysis (SESSA): a novel software tool for quantitative Auger-electron spectroscopy and X-ray photoelectron spectroscopy, Surface and Interface Analysis, 37, (2005) 1059-1067.
[31] C.S. Fadley, X-ray photoelectron spectroscopy: Progress and perspectives, Journal of Electron Spectroscopy and Related Phenomena, 178, (2010) 2-32.
[32] P.M. Koch, Atomic Physics Experiments Combining Synchrotron Radiation and Lasers - Present Capabilities and Future Possibilities, Aip Conference Proceedings, (1982) 645-660.
[33] H. Winick, J.E. Spencer, Wiggler Magnets at SSRL - Present Experience and Future Plans, Nuclear Instruments & Methods, 172, (1980) 45-53.
[34] M.O. Krause, J.G. Ferreira, K X-Ray Emission Spectra of Mg and Al, Journal of Physics B-Atomic Molecular and Optical Physics, 8, (1975) 2007-2014.
[35] V. Kunzl, About the K Series of Al, Mg and Na, Zeitschrift Fur Physik, 99, (1936) 481-491.
[36] C. Tusche, Y.J. Chen, C.M. Schneider, J. Kirschner, Imaging properties of hemispherical electrostatic energy analyzers for high resolution momentum microscopy, Ultramicroscopy, 206, (2019) 112815.

3 ION BOMBARDMENT AND SAMPLE CLEANING

3.1 Introduction

Sample cleaning via bombardment of ions of noble gases is a common and well-known procedure for many surface experiments. In particular, bombardment using argon ions is the preferred method and the one used in this laboratory, as briefly mentioned in Chapter 2. Because it is such a common method, many studies have been done investigating exactly how it affects the sample surface, ranging from assessment of surface damage [3, 4] to analysis of surface defects and formations [5, 6]. Understanding and controlling defect formation is extremely important, since many phase transitions and island formations tend to nucleate at step edges and defects [7, 8], since these features represent a break from an otherwise repeating surface pattern.

In this chapter, we discuss some of the defects and features present on the various faces of germanium as well as challenges faced in controlling the presence of such defects and features. We also discuss the details of the cleaning procedure developed in order to consistently produce germanium samples suitable for experiments presented in this study.

Table 3.1. Properties of germanium[1].

Property	Value
Atomic Configuration	[Ar] $3d^{10}4s^24p^2$
Atomic Mass	72.59 amu
Crystal Structure	Diamond
Density	5.32 gm cm^{-3}
Melting Point	1211 K
Lattice Constant	5.658 Å
Electron Configuration	[Ar] $3d^{10}4s^24p^2$

3.2 Low-Index Germanium Faces

Germanium has a diamond structure with a lattice constant of 5.658 Å and a melting point of about 1211K, among other properties as shown in Table 3.1. Its three, primary, low-index faces in their unrelaxed form have a hexagonal symmetry (111), square symmetry (100), and rectangular symmetry (110), as shown by the simple models in Figure 3.1. These faces will display reconstructions depending on their temperature, which are well-documented from various forms of study including theoretical, STM, and diffraction techniques. The Ge(111) surface reconstructs to a c(2x8) structure that transitions to either (1x1) or (2x1) structure at around 300°C depending on conditions [9, 10]; the Ge(100) surface reconstructs to c(4x2) at lower

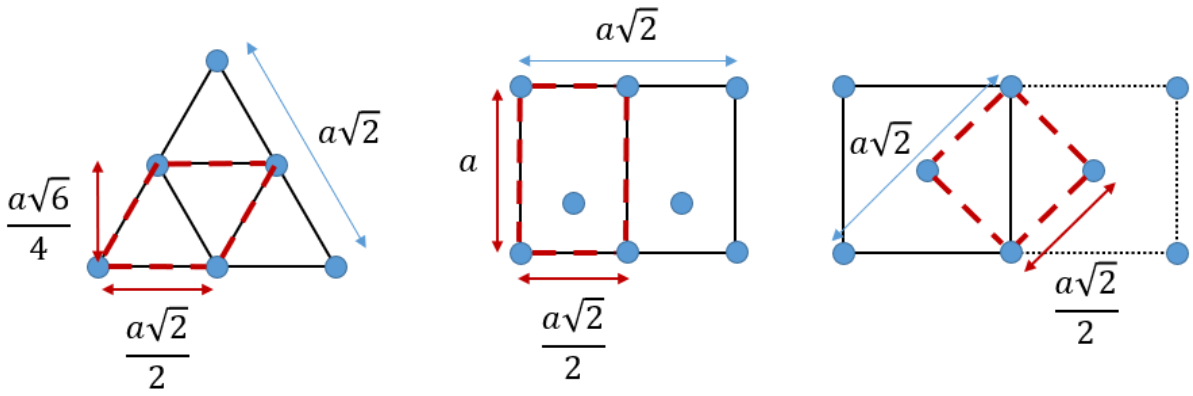

Figure 3.1. Simple ball-and-stick models of the surface arrangements of unreconstructed Ge(111) (left), Ge(110) (middle), and Ge(100) (right). The primitive unit cells are outlined with dashed, red lines, and some of the distances are provided. Atom sizes and distances are not to scale.

temperatures but can also display p(2x1) and p(2x2) structures at room temperature and higher, with p(2x1) typically dominating upon annealing and subsequent cooling despite c(4x2) being the lowest energy configuration [11, 12]; and finally the Ge(110) surface reconstructs to a c(8x10) structure for most temperatures but has a (16x2) reconstruction in a narrow range of temperatures around 400°C, typically displaying a mixture of both upon annealing and cooling [13, 14]. At a high enough temperature, typically close to the melting point of germanium, the reconstructions disappear and are replaced by a disordered phase.

When cleaning germanium samples, one of the most reliable indicators of the samples' quality is the sharpness of the LEED patterns related to their surface reconstructions. It is the preferred indicator, rather than an XPS spectrum, which can only be used to check for contaminants, since a contaminant-free surface can still have poor reconstruction due to an improperly repaired surface after argon sputtering. Example LEED patterns of the surface reconstructions of the 3 low-index faces are shown in Figure 3.2, displaying some of the reconstructions mentioned previously. These LEED patterns are representative of the kind of surfaces expected after proper cleaning, with the higher-order spots appearing sharp with

Figure 3.2. LEED Patterns of clean Germanium surfaces, showing Ge(111) c(2x8) at 10.4eV (left); Ge(100) p(2x1) and c(4x2) at 12.0eV (middle); and Ge(110) c(8x10) and (16x2) at 8.3eV (right).

minimal streaking or blending. The samples should also properly go through the aforementioned phase transitions to different reconstructions upon annealing through the transition temperatures, before recovering the room-temperature reconstructions upon cooling back down.

3.3 General Sample Cleaning Procedure

Here we describe the general procedure used at the laboratory to clean most semiconductor samples. Using a diamond scribe, the samples are cut from polished, 2- or 3-inch diameter, 0.5mm thick wafers that are n-doped (germanium samples are doped with Sb), into pieces that are small enough to fit in the sample slot of the sample holder. The samples are purchased from MTI Corporation and have a reported miscut of <0.5° and have resistivities under 1.0ohm-cm (exact resistivity varies depending on availability at the time of purchase). The sample is then sonicated in a methanol bath for 1-3 minutes in order to eliminate any oils as well as dust and other small particles, after which the sample is soaked in 50% H_2O_2 solution for about a minute to form a uniform oxide layer. The sample is rinsed in methanol one more time and then

dried using lens tissue paper before being mounted on the sample holder. This is the *ex situ* preparation, after which the sample can be placed into vacuum and baked in the airlock.

The *in situ* cleaning is performed in the XPS chamber's manipulator mentioned in Chapter 2. The sample's annealing temperature is first calibrated by heating the sample with the sample holder's e-beam heating system while the sample is facing the XPS chamber's main window. An infrared pyrometer is used to measure the temperature of the sample, with its emissivity set to 0.42 for germanium, a value that was empirically obtained by previous students by comparing to the melting point of the crystal [2, 15]. Typically, the annealing temperature is chosen to be above the transition temperature for disordered phases of surface reconstruction and below the melting point of the material. For germanium, an annealing temperature of around 800°C is used. Once the annealing temperature is chosen and calibrated, the sample is turned to face the ion sputter gun and cleaned using cycles alternating between Ar^+ sputtering and annealing. These cycles are repeated many times, on the order of a few tens of cycles, after which the sample quality can be checked either via XPS, which is done occasionally to make sure the procedure is properly eliminating contamination, or via imaging in LEEM/LEED mode, which more directly confirms the sample's viability for experiments.

3.4 Pyramid Formation from Ge(110) Cleaning

Before discussing how the specific values of some of the cleaning procedures were chosen, we must first briefly discuss work done by a former student, Marshall van Zijll, in his study of Ag-induced pyramid formation on Ge(110) as a result of sputter-annealing cleaning cycles [6, 16],

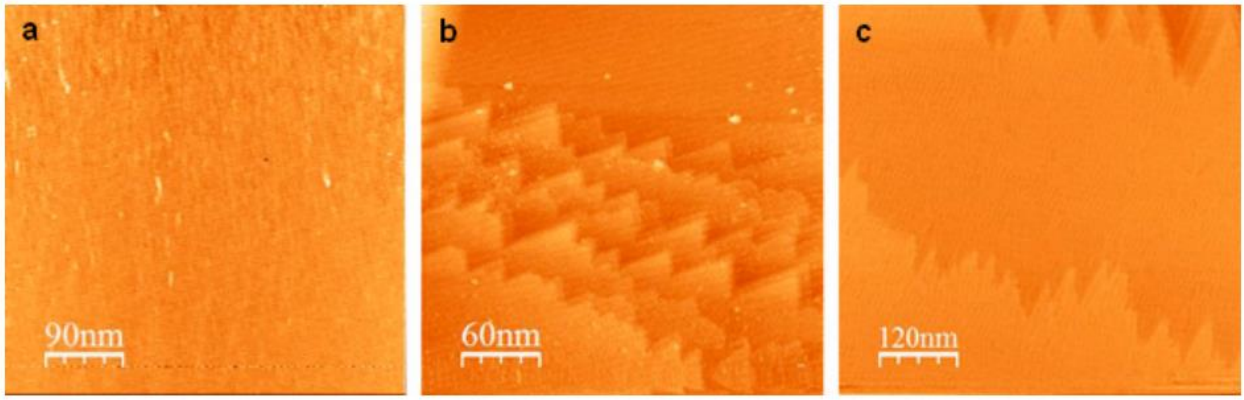

Figure 3.3. STM topographical images of bare Ge(110) after (a) 6 cleaning cycles, (b) 14 cleaning cycles, and (c) 21 cleaning cycles on a completely new sample holder sputtered with 400 eV Ar^+ ions. Imaging parameters are (a) 1nA, 1V tip bias; (b) 4nA, 1.5V tip bias; (c) 3nA, 2V tip bias.

and my own work assisting with the project. In this study, residual Ag on sample holders from previous experiments contaminated new Ge(110) samples during the cleaning process, creating a form of protective cap against the ion sputtering that would otherwise cause exposed step edges to retreat, leaving pyramid structures once the unprotected germanium layers were sputtered away. In order to verify that Ag contamination was responsible for the pyramids, STM imaging was done on clean Ge(110) mounted on a new sample holder built from completely new components that did not have any residual Ag. The results are shown in Figure 3.3 for various numbers of cycles for a given sputter energy of 400eV; these STM images lacked the pyramids seen in [6] and confirmed the Ag contamination hypothesis.

From this, one can conclude that contamination can act as nucleation points for bigger defects by inhibiting the movement of step edges as they are sputtered away, and such defects will only get larger as more layers continue to be lifted through subsequent sputtering cycles. Contamination could come from residual material left on sample holders like the Ag contamination in this study, but it could also come from very small particles left on the surface after *ex situ* treatment, or simply from defects already on the surface. It is also clear that these

nucleation points are highly resistant to being sputtered away, and their impact was found to only diminish at higher bombardment energies, as noted by a lack of pyramid growth in [6], with the tradeoff being a large amount of surface damage that cannot be sufficiently repaired via annealing. Because the energy of bombardment has such different impact on surface features, one could consider what bombardment energy to use for cleaning a particular sample, in order to optimize the sample's quality.

3.5 Tuning Cleaning Parameters

There are multiple parameters one could vary for the sputter-anneal cleaning cycles: ion flux rate, sputtering duration, sputtering angle, sputtering energy, sample temperature during sputtering, annealing duration, annealing temperature, and the total number of cycles. The

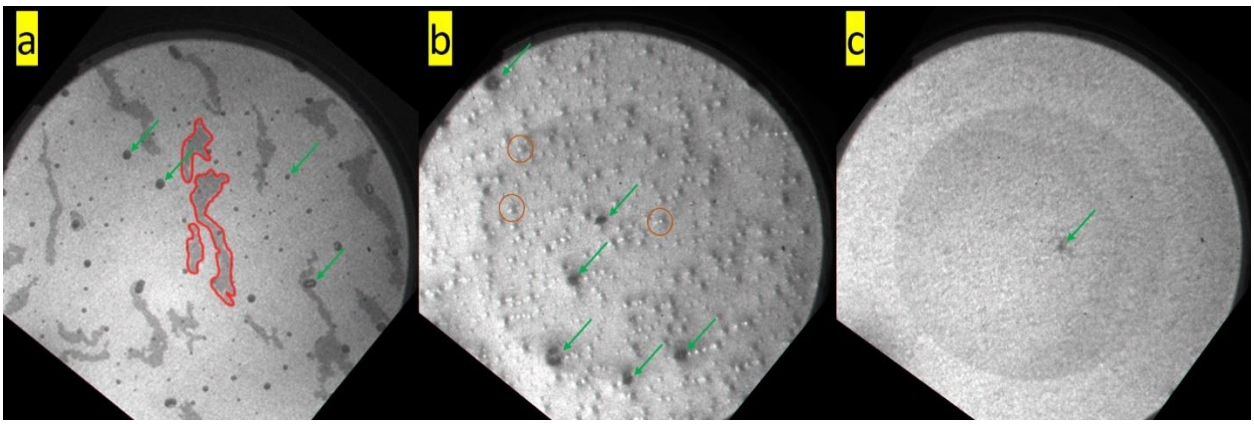

Figure 3.4. LEEM images of the three germanium faces, showing examples of defects after cleaning. (a) Ge(111) surface, 15µm FoV. Green arrows point to examples of defects consisting of high-density steps, while the red outline surrounds examples of defects consisting of medium-density steps. (b) Ge(100) surface, 15µm FoV. Green arrows point to examples of high-density step defects similar to the ones on Ge(111), while the orange circles show a few of many smaller, high-density step defects that have sharper peaks. (c) Ge(110) surface, 10µm FoV. This surface exhibits only one type of defect, which is the high-density step defect like on the other two faces.

parameters should affect how different defects are removed from the surface and can be optimized to target certain defects over the others.

Figure 3.4 shows the types of defects expected from germanium faces. It is easy to see that the most common defects are very dark, circular blobs consisting of high-density steps, marked by green arrows in each image. Ge(111) and Ge(100) faces also have defects that are specific to their faces and are marked accordingly. The high-density step defects are generally tall enough so that they persist through high amount of deposition on the substrate, while the other defects can become partially or completely covered, as seen in Figure 3.5. The high-density step

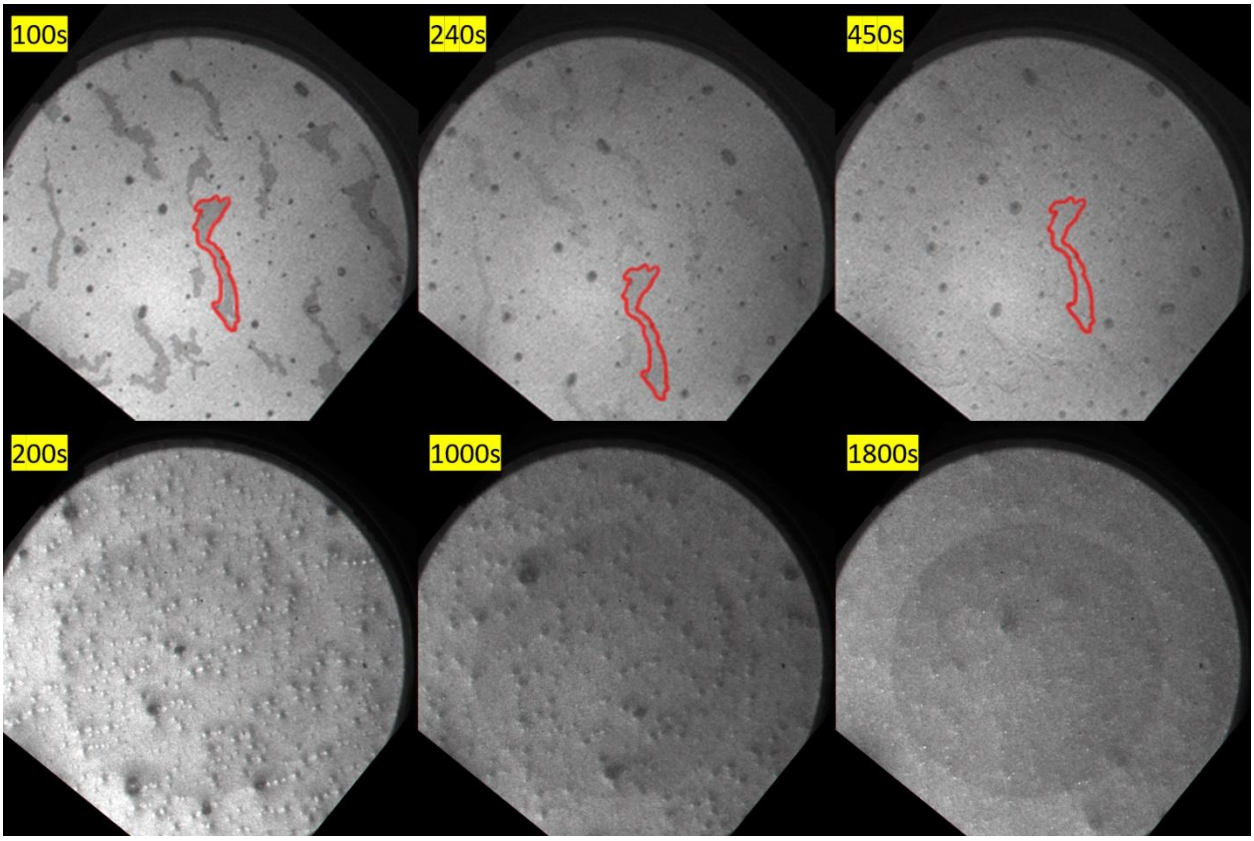

Figure 3.5. Evolution of surface defects on Ge(111) (top) and Ge(100) (bottom) with deposition of Pb. For Ge(111), one defect is highlighted in red to make it easier to track as it becomes fainter with increasing Pb coverage. For Ge(100), the lower parts of the defects gradually become covered such that only the peaks are distinguishable at high Pb coverages. FoV is 15µm for both sets of images.

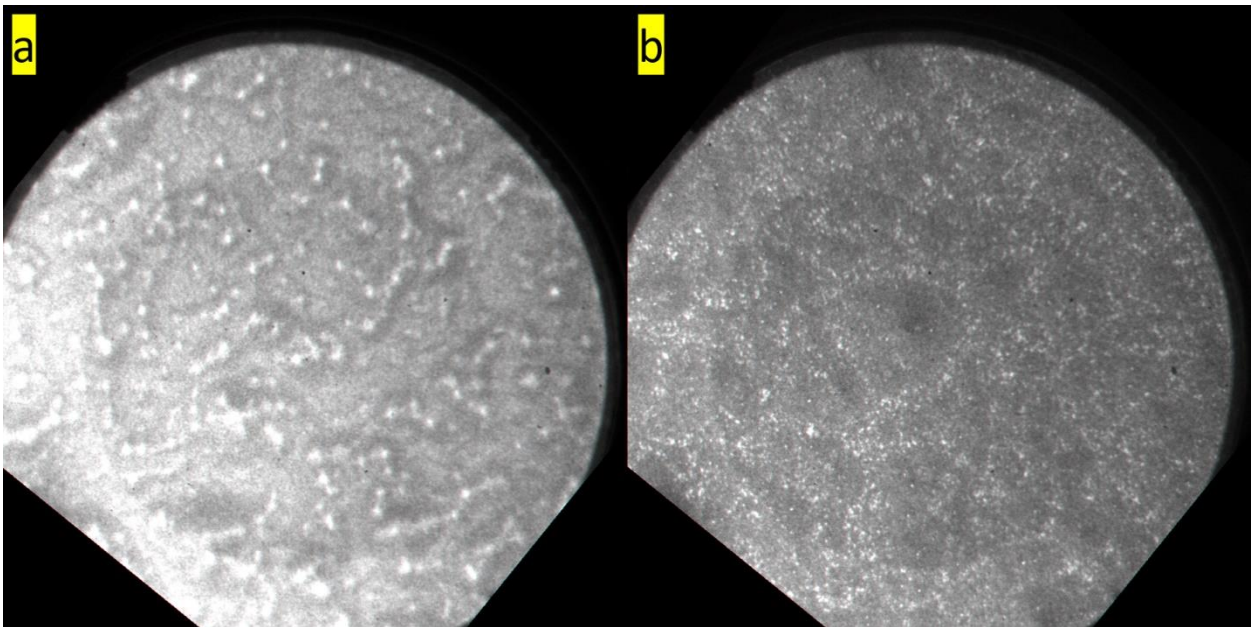

Figure 3.6. Ge(100) surfaces showing the obstruction caused by surface defects. (a) The surface was imaged slightly out of focus to make the “mountain ranges” of defects more visible. (b) Ge(100) surface with Pb deposition. The bright, white dots are regions of Pb underdoing a phase change. Note how they only form in the valleys between the “mountain ranges” of defects. FoV is 15µm.

defects generally are not an issue for experiments as long as they do not become too large in size or number, but the other defects tend to take up a larger portion of the surface area and can constrain phase transitions to the areas in between (shown in Figure 3.6), even if the defects are covered by the deposited material. We take these into consideration for deciding what cleaning parameters to use.

The first parameters to be discussed involve the annealing part of the cleaning cycles, namely the annealing temperature and the annealing duration. Annealing at high enough temperatures is certainly necessary to repair surface damage caused by ion bombardment and should be 30-60% of the melting point as a minimum [17]. The 800°C chosen for germanium samples exceeds the threshold by a considerable amount, but higher temperatures should only help surface atoms diffuse to repair the surface, at least up to the point the material

macroscopically begins changing shape as it gets close to melting. 800°C is a safe amount below the melting point for the sample such that it will not pose a danger to the sample, even if the annealing temperature drifts due to changes in the sample heating system, while maximizing the surface diffusion. Temperature drift mostly occurs during early cleaning cycles, either increasing or decreasing from the calibrated temperature by up to 20°C, and it is attributed to contamination or oxide layers on the tungsten filament being gradually burned away. The temperature eventually settles and no longer changes given the same settings, as long as the sample is not taken out of vacuum. Since there was no noticeable difference in sample quality among samples annealed between 700-800°C, the exact temperature is not important. For the annealing duration, there is some minimum time required for the surface to be repaired, but after a certain period, the surface achieves equilibrium and no longer benefits from annealing. One can easily see this in the LEEM, where even quickly flashing the sample for a few minutes will recover LEED patterns after a damaging event such as a high voltage arc, and continued heating of the sample does not improve the quality by any noticeable amount. 10 minutes, therefore, will give plenty of time for the sample to reach its target temperature and repair the damage received during sputtering.

Next, we discuss the sputtering parameters. There are some sputtering parameters that were not considered for the purposes of this study. Sputtering angle was not varied because there is only one position on the manipulator that will place the sample in line with the Ar^+ ions. The sputtering duration of 15 minutes was not varied since it was also not a factor that was varied in [6], which is the foundation for the tuning process. However, sputtering duration, total number of cycles, and flux rate contribute to the fluence of ions on the sample. Fluence has a measurable

effect on the sample roughness, with a direct correlation between roughness and fluence [18]. The ion current was typically kept at around 6μA for a flux on the order of 10^{13} s^{-1} cm^{-2}, but the exact value would vary depending on the sputtering energy. The main control factor for the flux rate was the partial pressure of argon leaked into the chamber through the sputter gun, which was always set at 5×10^{-5} torr. The major factor affecting the fluence is then the total number of cycles, which was the least consistent part of the cleaning process and could vary between 20 and 50 cycles. Typically, samples would begin displaying some form of surface reconstruction at around 20 cycles, but some would take up to 50 cycles before the LEED patterns were clear. Because of this, the procedure was standardized to do 40 cycles minimum, and to perform more cycles as needed if the sample still displayed poor LEED patterns. This would put the fluence on the order of 10^{17}-10^{18} cm^{-2}, which is relatively low compared to some ion bombardment studies such as [18].

Temperature during the sputtering cycle is also extremely important, and the choices were typically limited by engineering constraints. When performed manually, all parts of the cleaning procedure can be carefully tuned; unfortunately, due to the length of each cleaning cycle (25min minimum for sputter + anneal), and the total number of cycles required, manually cleaning the sample became a prohibitively inefficient task. To address this, the cleaning cycles were automated, which introduced the engineering constraints. An older version of the automated system used by a former student only involved turning the e-beam high voltage on and off using a timed relay. This left both the Ar^+ sputtering and the sample heating filament active during every part of the cleaning cycles, with the sample only cooling to an intermediate temperature determined by the heating filament (400-600°C depending on filament-sample

distance) whenever the high voltage was turned off. This posed a problem because ion bombardment tends to do more damage at higher temperatures, mainly due to point defects becoming free to migrate across the surface and merge into large defects [3]. Sputtering at the lowest possible temperature was found to be the most ideal, so a system was designed by undergraduate student Eli Baum to turn off all sample heating during the sputtering process, using a programmable surge protector to cut power to the high voltage power supply and a MOSFET to divert current away from the heating filament (gently, in order to avoid thermal shock on the fragile filament), all controlled by an Arduino. Based on temperature readings in the LEEM when flashing the sample, the sample generally quickly cools to below 300°C in under a minute after heating elements are turned off and more gradually approaches room temperature afterwards. It is estimated that the samples reach about 100-150°C by the end of the sputtering cycle. The automated cleaning system can also activate/deactivate the sputter gun, but it cannot turn the argon gas off due to mechanical limitations in design. This means the sample is exposed to argon gas during annealing, but a noble gas like argon should have minimal interaction with the sample.

Finally, the main parameter in consideration is the sputtering energy, one of the two major factors involved in [6], alongside total number of cycles. As noted in section 3.4, higher sputtering energies tended to cause more damage to the surface but also inhibited pyramid growth. The pyramids were grown layer-by-layer as the substrate's steps were pinned to the Ag defects. Since the most common defects found on germanium are high-density steps, one can infer that these defects form in a similar fashion, as the germanium steps become pinned around point defects on the surface. Then it is reasonable to also infer that they can be affected in a

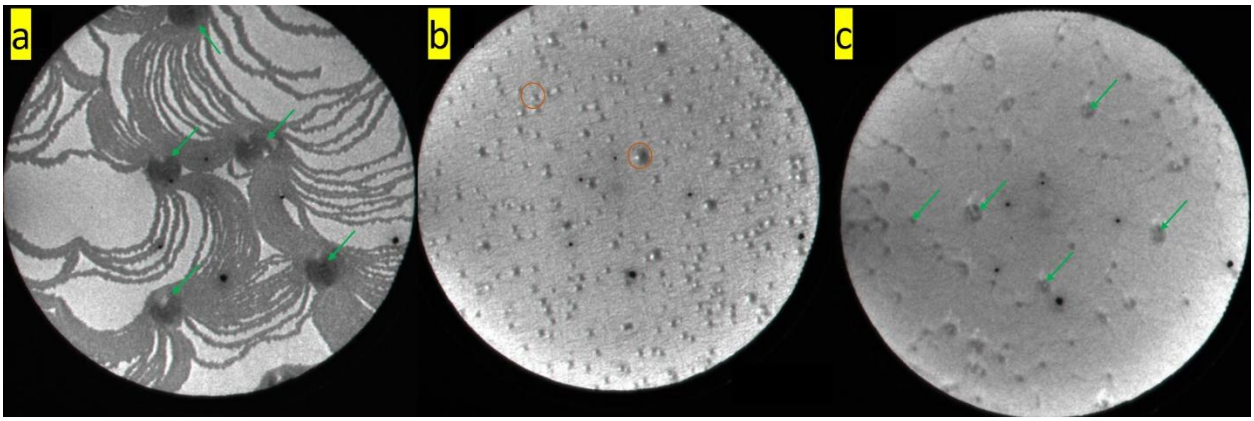

Figure 3.7. Examples of defects reproduced with permission from [2], to compare with defects in Figure 3.4. (a) Ag/Ge(111) with some large, high-density step defects. (b) Clean Ge(100) showing mountain-like, high-density step defects. (c) Clean Ge(110) showing numerous high-density step defects. All images are 10µm FoV.

similar way as the Ag pyramids, namely with higher energy bombardment. Previous students only cleaned samples using one sputtering energy, typically 200-300eV, which is good for promoting quality surface reconstruction but does not properly inhibit defect growth. One could simply clean at higher sputtering energy, but this means the samples will become too damaged for annealing to repair. To benefit from each sputtering energy, the procedure was revised to use both: the sample would initially be cleaned at 500eV ions for 10 cycles to reduce defect formation and growth, and then finished off with cleaning at 200-250eV for the remaining 30 cycles. One could change the ratio of the number of cycles for high and low-energy cleaning cycles to be more even, such as 20:20, but since low-energy cleaning cycles are generally more important due to their role in producing surface reconstruction, the ratio was chosen to favor those cycles.

3.6 Conclusion

We have carefully considered each of the parameters involved in the cleaning process and chose them to consistently produce useful samples. Figure 3.4, used to show examples of the possible defects, is also the result of the revised cleaning procedure. It can be compared with Figure 3.7, which shows the results of the original cleaning procedure that used a single sputtering energy [2]. For Ge(111), there is a definite reduction in the average size of the high-density step defects, but the revised method also produces the large splotches of medium-density steps. This is not as much of an issue because the splotches are easily covered with Pb and do not severely hinder phase transitions, and they were also found to gradually disappear over multiple experiments. The splotch defects also have a use as a reference point for focusing the objective on the sample, and their relevance will be discussed in a later chapter. As for the Ge(100) defects, it seems that the results are about the same between the old and new methods, suggesting that the defects on this surface are extremely resistant to even high-energy ion bombardment. This is likely due to the nature of bonds on the Ge(100) surface, which may be too strong to break easily; It may perhaps be beneficial to try an even higher energy up to 1kV. Finally, for the Ge(110) surface, there is a very noticeable reduction in the number of high-density step defects overall, which suggests that the Ge(110) face is highly sensitive to this method. Overall, the revised sample cleaning procedure consistently produces acceptable samples for experiments and was used for most of the samples presented in this dissertation.

References

[1] N.W. Ashcroft, N.D. Mermin, Solid State Physics, Holt, Rinehart and Winston, New York, (1976).
[2] C.H. Mullet, Growth of Ir on Ge(111) and Ge(110) and Growth of Ag on Ge(111), Ge(110), and Ge(001) Studied by Low Energy Electron Microscopy and Scanning Tunneling Microscopy, PhD dissertation in Physics, University of California Davis, Davis (2012).
[3] J.C. Bean, G.E. Becker, P.M. Petroff, T.E. Seidel, Dependence of residual damage on temperature during Ar+sputter cleaning of silicon, Journal of Applied Physics, 48, (1977) 907-913.
[4] K. Sumitomo, K. Tanaka, I. Katayama, F. Shoji, K. Oura, TOF-ICISS Study of Surface Damage Formed by Ar Ion-Bombardment on Si(100), Surface Science, 242, (1991) 90-94.
[5] Z. Szczudlo, S. Zuber, A. Ciszewski, Cleaning of W(001) by Ar-ion bombardment for STM investigation, Vacuum, 72, (2003) 47-52.
[6] M. van Zijll, S.S. Spangler, A.R. Kim, H.R. Betz, S.R. Chiang, Layer-by-Layer Pyramid Formation from Low-Energy Ar+ Bombardment and Annealing of Ge (110), Nanomaterials, 11, (2021) 2521.
[7] C.H. Mullet, S. Chiang, High temperature growth of Ag phases on Ge(111), Journal of Vacuum Science & Technology A, 31, (2013) 020602.
[8] L. Seehofer, R.L. Johnson, STM Study of Gold on Ge(111), Surface Science, 318, (1994) 21-28.
[9] R.J. Phaneuf, M.B. Webb, A LEED Study of Ge(111) - a High-Temperature Incommensurate Structure, Surface Science, 164, (1985) 167-195.
[10] A. Selloni, N. Takeuchi, E. Tosatti, Reconstructions and Phase-Transitions at Semiconductor Surfaces - Ge(111), Surface Science, 331, (1995) 995-1001.
[11] K. Noatschk, E.V.S. Hofmann, J. Dabrowski, N.J. Curson, T. Schroeder, W.M. Klesse, G. Seibold, Ge(001) surface reconstruction with Sn impurities, Surface Science, 713, (2021) 121912.
[12] L. Spiess, A.J. Freeman, P. Soukiassian, Ge(100) 2x1 and c(4x2) Surface Reconstructions Studied by Ab Initio Total-Energy Molecular-Force Calculations, Physical Review B, 50, (1994) 2249-2258.
[13] T. Ichikawa, T. Sueyosi, T. Sato, M. Iwatsuki, F. Udagawa, I. Sumita, Ge(110) Surface Reconstruction Observed with Scanning-Tunneling-Microscopy, Solid State Communications, 93, (1995) 541-545.
[14] B.Z. Olshanetsky, S.M. Repinsky, A.A. Shklyaev, LEED Investigation of Germanium Surfaces Cleaned by Sublimation of Sulfide Films - Structural Transitions on Clean Ge(110) Surface, Surface Science, 64, (1977) 224-236.
[15] J. Giacomo, A Low Energy Electron Microscopy Study of the Growth and Surface Dynamics of Ag/Ge(111) and Au/Ge(111), PhD dissertation in Physics, University of California Davis, Davis (2009).
[16] M. van Zijll, Scanning Tunneling Microscopy Studies of Ir on Ge(111), Ag on Ge(110), and the Effects of Sputtering Energy on Pyramids formed on Ge(110), PhD dissertation in Physics, University of California Davis, Davis (2014).
[17] E. Taglauer, Surface Cleaning Using Sputtering, Applied Physics a-Materials Science & Processing, 51, (1990) 238-251.
[18] D. Chowdhury, D. Ghose, Fabrication of nanoscale topographies on Ge(100) surface by low energy Ar+ ion sputtering, Nuclear Instruments & Methods in Physics Research Section B-Beam Interactions with Materials and Atoms, 409, (2017) 197-201.

4 PB ISLAND NUCLEATION AND GROWTH ON GE(111)

4.1 Introduction

Pb on Ge or Si surfaces has been studied quite thoroughly for quite a few decades, owing to Pb's insolubility with Ge and Si, allowing for an atomically abrupt interface that eliminates a lot of complications that could arise from intermixing of the materials [3]. In particular, Pb on Ge(111) has received a large amount of attention due to its potential technological applications as well as for purposes of fundamental understanding [3-12]. There has been extensive work done on high temperature phases of Pb/Ge(111) [3, 5, 11], with multiple phases identified such as α $\left(\sqrt{3}\times\sqrt{3}\right)R30°$, a denser β $\left(\sqrt{3}\times\sqrt{3}\right)R30°$ phase, and a (1×1) phase towards saturation coverages. Work has been done on low temperature behavior of the system as well [6-8], revealing a (3×3) phase along with unusual layer-by-layer growth of Pb films that are in stark contrast to the traditional Stranski–Krastanov growth mode observed at room temperature and above.

It is also worth noting the numerous studies done on the Pb/Si(111) system that show a wide range of phases and related surface morphology [13-20]. Low temperature work on this system shows similar phases including the transition from a $\left(\sqrt{3}\times\sqrt{3}\right)R30°$ phase to a (3×3) phase [14, 15] as well as unusually fast motion of Pb atoms making up the wetting layer on the Si(111) surface in stark contrast to classical diffusion [21-25]. Silicon and germanium, due to both being semiconductors with the same crystal structure, do share very similar properties and

behavior under the same conditions. However, because of their differing lattice constants as well as their differing surface reconstructions, one can expect even similar behavior to have some nuanced differences that can be picked up in experiments. Indeed, there have been compare-contrast studies done on systems involving germanium and silicon, especially between Ge(111) and Si(111) for Pb deposition [13, 26-30] as well as for other deposited metals [26, 31].

The inspiration for this study came from work done on the Pb/Si(111)-(7x7) system at low to room temperatures (100K to RT), performed by Tringides *et al.*, in which Pb was found to grow islands displaying certain height selection [2, 32-37] while drawing Pb atoms from the wetting layer with an unusually fast transport mechanism [22-25, 37-39]. Pb at first forms an amorphous wetting layer on the Si(111) surface, which mostly obscures the (7x7) reconstruction underneath. When the Pb coverage exceeds the natural surface density of crystalline Pb(111) surface, one would normally expect the wetting layer to become saturated, so that Pb would begin growing a second layer or forming clusters, similar to how it forms islands on top of a saturated β $(\sqrt{3} \times \sqrt{3})R30°$ on Ge(111) [40]. However, Pb does neither, instead remaining within a single wetting layer and compressing the Pb atoms beyond their natural state. The compression in the wetting layer grows until a critical coverage of 1.22ML, corresponding to 22% compression, at which point Pb islands grow "explosively" from the wetting layer at rates that defy classical nucleation theory. These islands were found to be remarkably flat with steep sides, and most importantly, these islands displayed some preference in height, as shown in Figure 4.1, reproduced from [2].

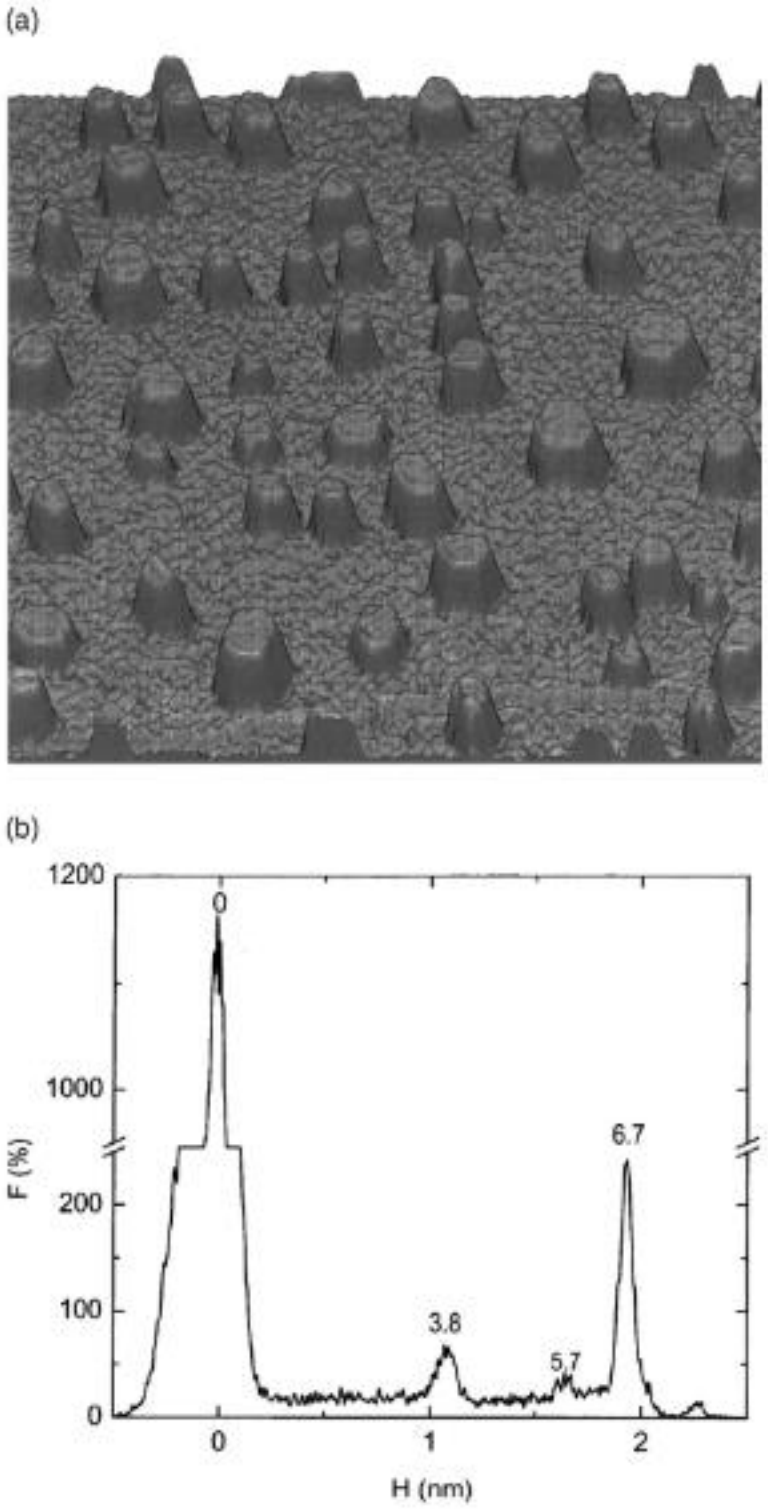

Figure 4.1. (a) STM image of Pb/Si(111) showing flat-topped Pb islands on top of an amorphous wetting layer. (b) Histogram of heights of islands in the STM image, showing island height selection. Reprinted from Surface Science, 493, M. Hupalo, S. Kremmer, V. Yeh, L. Berbil-Bautista, E. Abram, M.C. Tringides, Uniform island height selection in the low temperature growth of Pb/Si(111)-(7 x 7), 526-538, (2001) [2], with permission from Elsevir.

Going into further details on their study, we see that Pb, for both thin films and islands, seems to prefer growing in two-layer increments, with stable island heights at 5, 7, 9, and 11 layers, among others. 7-layer islands were found to be particularly stable, but the typical island height distribution depended on temperature as well as coverage. This bilayer-by-bilayer growth is attributed to Quantum Size Effect (QSE), in which certain structures on the sample become comparable to the electron wavelength such that electrons will be able to interact with the boundaries of the structures and thus exhibit behavior different from what would be expected from electrons interacting in a crystal's periodic potential. Pb happens to have a rather unique property in that its Fermi wavelength, $\lambda_F = \frac{2\pi}{k_F}$ where $k_F = (3\pi^2\rho)^{1/3}$ for electron density ρ in a nearly free-electron model, has a special relationship $2d \cong \frac{3\lambda_F}{2}$ where $d = 0.286nm$ is the thickness of one Pb layer [33, 41, 42]. This means that every two layers of Pb will add 3 nodes to the electron wavefunction spanning the total thickness of the thin film or island, such that the wavefunction almost neatly fits inside as a sort of standing wave in a finite potential well. Because the relationship is not exact, however, each stable layer thickness does not have the same level of stability, with the most exact fitting occurring for 7 layers, making this the most stable configuration. This also means at some point the slight incommensurability causes the height selection to eventually start favoring even number of layers rather than odd, and then switch back again to favoring odd number of layers, and so on [27]. Through their experiments, Tringides

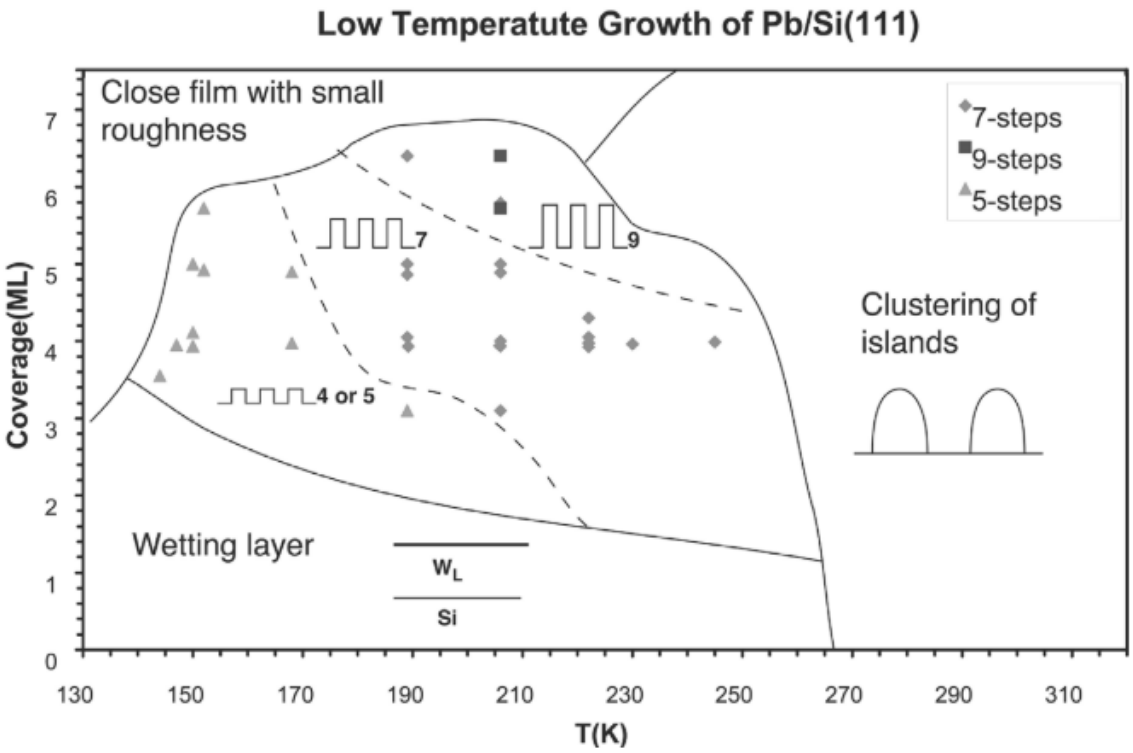

Figure 4.2. Phase diagram of Pb island height selection as a function of temperature and coverage. Reprinted from Surface Science, 493, M. Hupalo, S. Kremmer, V. Yeh, L. Berbil-Bautista, E. Abram, M.C. Tringides, Uniform island height selection in the low temperature growth of Pb/Si(111)-(7 x 7), 526-538, (2001) [2], with permission from Elsevir.

et al. were able to create a phase diagram showing the island height distribution as a function of coverage and temperature, reproduced from [2] in Figure 4.2.

The mechanism of growth of these islands is called collective diffusion, a phenomenon that is rarely seen in nature but is of much interest due to the speed at which it can form structures compared to classical diffusion. Classical diffusion, based on random walk motion of adatoms across the surface, is known to have a $t^{1/2}$ dependence on the root mean square displacement of each particle, whereas Pb was found to display superdiffusion, with a linear time dependence [21, 22, 36]. From STM studies that closely examined the formation of additional layers on top of these islands [22, 23], it was found that the entire wetting layer would move in a seemingly coordinated motion, first forming rings on the tops of the islands and then gradually

moving inwards to fill the area. This sort of superdiffusive and collective behavior of the Pb wetting layer is still poorly understood, with very few theoretical models to explain it.

Given this extensive study of Pb islands on Si(111) at low temperatures, one could quite reasonably wonder if a similar behavior could be seen on the Ge(111) surface under similar conditions. Despite this, there are relatively few studies done on the Pb/Ge(111) system at low temperatures, and the studies that have been done seem to mostly focus on thin film growth on the Ge(111) surface rather than islands [6, 27]. These studies clearly show that Pb still displays similar preference in growing by two layers at a time, with the same preferred thicknesses. This is unsurprising and quite expected since the QSE dictating layer stability is something intrinsic to Pb and should not be affected by the substrate. The preferred number of layers at a given coverage or temperature, however, likely would not be the same, since that should be affected by how the wetting layer contributes to the growth of the islands, and surface diffusion should be dependent on the substrate.

Indeed, we can expect the behavior of the wetting layer to be slightly different on Ge(111) compared to Si(111). Insight into their differences is provided by a comparison work on commensurate and incommensurate phases of Pb done by Seehofer *et al*., in which the authors observed that Pb would form either commensurate or incommensurate phases on both Ge(111) and Si(111) depending on coverage, with some phases being composed of domains of both commensurate and incommensurate phases [29, 30]. What is interesting to note from their study is the commensurability of the closely-packed phases of Pb, which are the β $\left(\sqrt{3}\times\sqrt{3}\right)R30°$ phase on Ge(111) and the $\sqrt{3}i$ or α $\left(\sqrt{3}\times\sqrt{3}\right)R30°$ on Si(111) (not to be confused with a Pb/Ge(111) phase of the same notation). On Ge(111), the closely-packed phase is commensurate,

while it is incommensurate on Si(111). The reason for this is due to the degree of lattice mismatch between Pb and the substrate. The Pb overlayer can become commensurate with the Ge(111) lattice with a very slight compression of about 1% beyond the bulk Pb value, while the Si(111) lattice requires a much larger compression, which the Pb overlayer cannot support and thus it remains incommensurate. With respect to the wetting layer at low temperatures, one can deduce that this lattice mismatch will affect the compression of the wetting layer before the explosive nucleation of the islands, so that the critical coverage is expected to be different. The superdiffusive behavior of the wetting layer should also be different, if it is superdiffusive at all depending on the diffusion barrier on the Ge(111) surface.

The purpose of the experiments discussed in this chapter, therefore, is to examine Pb island formation on Ge(111) under similar conditions as the studies performed by Tringides *et al.* in order to look for similarities and differences. While the Pb/Si(111) experiments were primarily performed using STM, which had the resolution required to explore the finer details of island structures and morphology, the Pb/Ge(111) experiments were performed on the LEEM, which had the added benefit of being able to examine island growth in real time, particularly the nucleation event which takes place on a timescale that is too fast for STM image acquisition rates. With the LEEM, we were able to observe island nucleation events and track the island growths over time with additional deposition, and thus we could measure the movement of Pb atoms as they formed the islands.

4.2 Experimental Details

The Ge(111) samples were prepared and cleaned according to the procedures discussed in Chapter 3. Some Ge(111) samples received a simpler *ex situ* treatment in that they were only dipped in methanol and dried before mounting, which affected the presence of some surface defects but otherwise did not critically interfere with the experiments. A sample would then be moved into the LEEM chamber, where the LEED pattern and direct imaging of the clean surface were examined to check the sample's quality. The sample was also flashed at its annealing temperature one more time to remove any contamination that may have formed during the transfer process as well as to repair damage done from high voltage arcing that is common when high voltage is applied to a freshly cleaned sample.

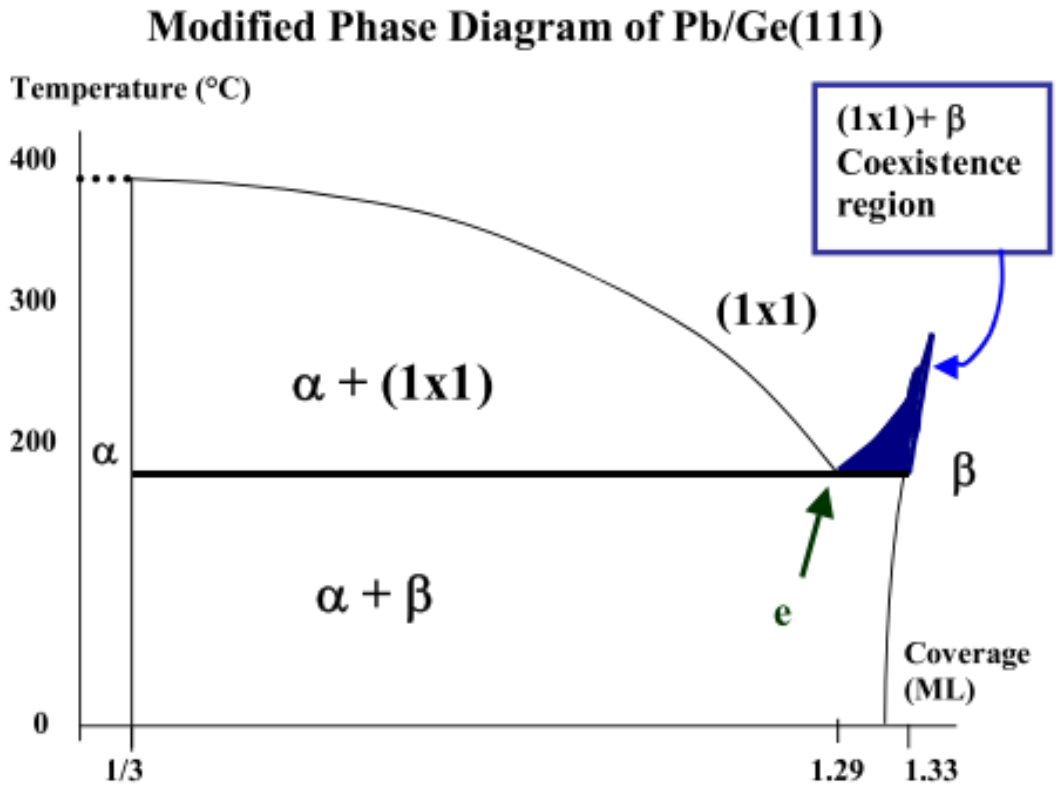

Figure 4.3. High temperature phase diagram of Pb/Ge(111). Reproduced with permission from [1].

The Pb evaporator was then calibrated by measuring the time it took to begin the α $(\sqrt{3} \times \sqrt{3})R30°$ to (1x1) phase transition, according to the phase diagram shown in Figure 4.3, reproduced from [1]. At very low coverages, Pb forms the well-known α $(\sqrt{3} \times \sqrt{3})R30°$ phase, and this occurs at a very wide range of temperatures, up to the temperature at which Pb is well beyond its melting point and desorbs from the surface. When Pb reaches a coverage of 1/3 ML, depending on its temperature, the α phase begins transitioning to one of its closely-packed phases where each unit cell has the density of bulk Pb. From the phase diagram, these phases are the β $(\sqrt{3} \times \sqrt{3})R30°$ phase below about 180°C and the (1x1) phase otherwise. For purposes of calibrating deposition rate, the phase transition to the (1x1) phase was chosen, since the (1x1) domains had a very distinguishable contrast that would make it easy to identify the start of the phase transition. As shown in Figure 4.4, at a start voltage of 11.5V, the α phase has a mostly gray contrast that is just slightly darker than the clean Ge(111) surface, while the (1x1) phase has a very bright contrast that stands out from the rest of the surface. The moment these bright (1x1)

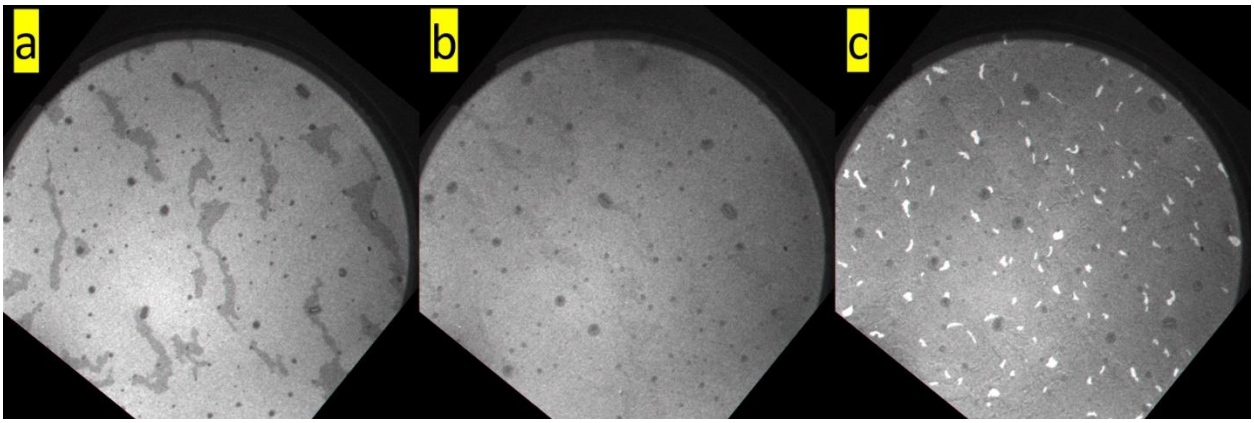

Figure 4.4. Pb/Ge(111) deposition showing the α $(\sqrt{3} \times \sqrt{3})R30°$ to (1x1) phase transition. (a) Clean Ge(111) surface. (b) Surface with a mostly complete α $(\sqrt{3} \times \sqrt{3})R30°$ phase, with the surface looking slightly darker and with the medium-density step defects covered up. (c) Surface showing many domains of (1x1) phase, with bright white contrast, signaling that the coverage has passed 1/3 ML. All images are 15µm FoV, with 11.5V start voltage. Temperature was around 240°C at the start but cooled to about 220°C at the end.

domains begin appearing is when 1/3 ML has been reached, and the elapsed time could be recorded and used to calculate the deposition rate during the calibration trial. Since this transition occurs at a wide range of temperatures, precise temperature control was unnecessary aside from keeping the sample's temperature from drifting too much, which added to the ease of calibration. However, the full extent of calibrating coverage for Pb experiments was found to be more complicated beyond measuring the phase transition, and these issues will be discussed in the next section.

After the first evaporator calibration, the sample was heated at its annealing temperature for about 5 minutes to remove the deposited Pb. As an aside, this was found to be quite a convenient feature of Pb. Due to its low melting point, the same Ge(111) sample could be reused over many experiments simply by heating the Pb off each time a new trial were to be performed. This would keep many features of the sample constant across the series of experiments, including the presence of defects, step density, and even the exact imaging location if the sample was never moved. The sample did lose quality over time, that could be detected through degradation of the LEED pattern, and since this could not be repaired through simple annealing, the sample would be replaced with a new one when the higher-order LEED spots had sufficiently faded. Returning to the topic at hand, once the Pb from calibration had been heated off, the sample was cooled towards the experiment's target temperature via liquid nitrogen. The cooling process took a very long time – 1.5 hours for 0°C and up to 3 hours for -50°C – during which the evaporator was kept on (but shutter closed to prevent deposition), and the LEEM's electron beam was kept off.

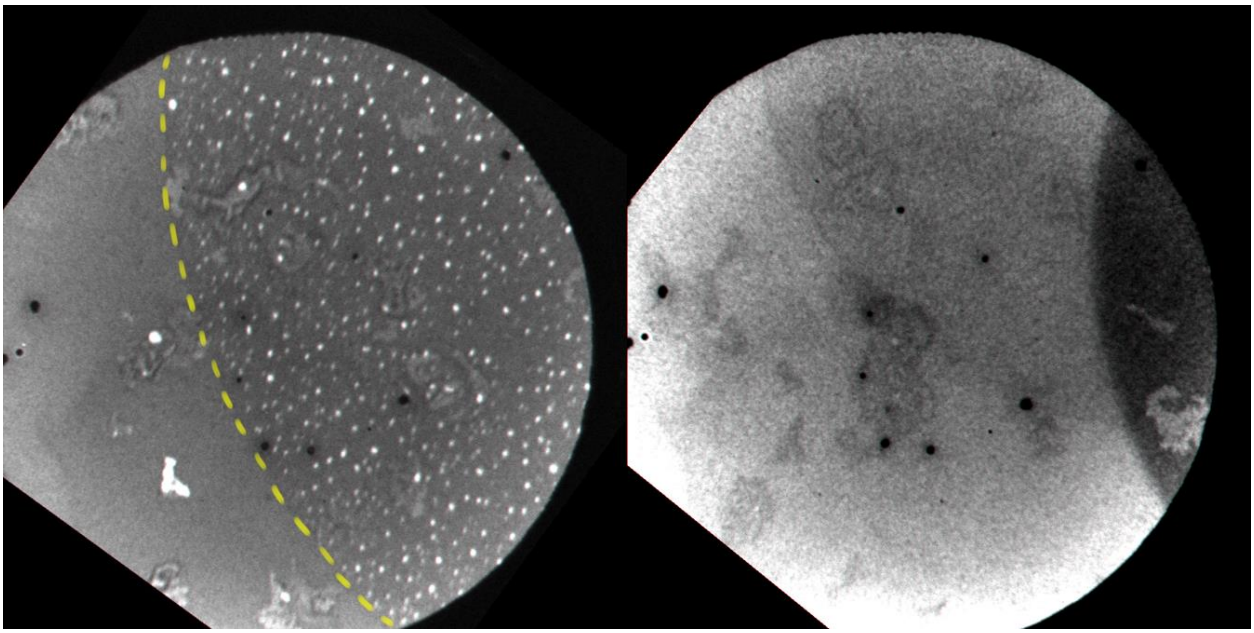

Figure 4.5. (Left) Pb/Ge(111) system showing the region damaged by the LEEM's electron beam (right of dashed line). Pb islands are bright-white, and it is clear they behave differently in the damaged region compared to the undamaged region. FoV is 10µm, and start voltage is 9.1V. (Right) Pb/Ge(111) system showing overlapping regions of electron beam damage due to the sample being moved relative to the electron beam, denoted by differences in contrast. FoV is 15µm, and start voltage is 9.2V.

Keeping the electron beam off as much as possible during the experiment was important because the electron beam caused damage to the sample's surface over time. As shown in Figure 4.5, a damaged zone, whose dimensions match the shape and size of the electron beam used to illuminate the sample, can appear due to extended exposure to the electron beam. Generally, the damaged zone has a darker contrast compared to the rest of the surface and displays a subdued LEED pattern, which would imply either a disruption of structural arrangements in that region, or depletion of material deposited in that region. Pb would behave differently in the damaged region compared to the rest of the sample, and the severity of the damage tended to correlate with the intensity of the electron beam as well as the total duration that the electron beam was incident on the surface. Moving the sample slightly would lead to overlapping regions of damage that would appear similar to Venn diagrams but could reduce damage overall if the

sample was moved often. It is still a mystery exactly what the electron beam does to the surface and why, but careful measures were taken to minimize the damage during the experiment by only activating the electron beam during recording and keeping the electron beam's intensity as low as possible by relying more on the gain of the MCP and camera.

Once the sample reached the target temperature, the flow of liquid nitrogen was reduced, and the heating filament on the sample holder was used to maintain the target temperature for the duration of the experiment. The LEEM software only supported automatic temperature controls for high temperatures, so temperature controls had to be done manually; this led to some variation in temperature during the experiments, typically within ±3°C of the target temperature. Pb deposition was performed, with evaporator settings left unchanged since its initial activation. During the early stages of deposition (<1ML), the imaging electron beam was kept off to minimize electron beam damage as previously discussed, as well as to reduce the size of the recording, since nothing of interest was found to occur before island nucleation. This ran the risk of sometimes waiting too long and missing the nucleation event, so estimates were performed carefully and conservatively to have a reasonable chance of success. Once the island nucleation was recorded, Pb deposition continued to much higher coverages as needed for the goals of the experiment, after which the evaporator shutter was closed and the sample annealed to remove the Pb. One final evaporator calibration was performed using the same procedure discussed earlier, and the resulting layer of Pb was allowed to remain on the sample to protect the germanium surface until the next experiment.

4.3 Calibrations

4.3.1 Thermocouple

As mentioned in Chapter 2, the sample holders have thermocouples mounted on a metal ring support underneath the samples in order to measure the temperature. Since thermocouples measure the temperature at their contact point, they do not necessarily measure the temperature of the sample, which is some distance away from the thermocouple's contact point and is more directly heated by the sample holder's heating filament. This would naturally create some sort of temperature gradient across the sample holder, which can be easily noticed by the fact that when the sample is glowing red, the portions of the sample holder around it are not glowing, even parts that are in immediate contact. The sample itself is not uniform in its temperature, with an approximately radially-symmetric gradient from the center of the sample due to the heating filament, and a linear gradient due to the tilt of the sample.

At annealing temperatures, it is a simple task to determine the sample's temperature using the infrared pyrometer, which is the primary temperature calibration method for sample cleaning as discussed in Chapter 3. Temperature calibration becomes a more difficult problem at temperatures below the point at which the sample emits enough infrared light for the pyrometer to measure (<550°C). Here we are forced to use the thermocouples, which we have discussed and concluded were inaccurate. Therefore, it is necessary to calibrate the thermocouples so that their readings can be extrapolated to determine the real temperature of the sample.

Thermocouple calibration is done using two known temperatures. The first temperature is the annealing temperature, whose filament current and bombardment voltage can be used in

the LEEM to reproduce the same temperature originally recorded in the XPS chamber. The thermocouple reading for the annealing temperature is then recorded. The second known temperature is the ambient temperature of the lab (varies near 21-23°C depending on the status of the building's heating/cooling system), which the thermocouple reads correctly within a few degrees. This was confirmed by leaving the sample holder in the LEEM overnight to reach thermal equilibrium with the vacuum chamber, and it makes sense that the thermocouple would read the correct temperature in this case since there would be no temperature gradient under these conditions. Then, by assuming the temperature difference between the sample and

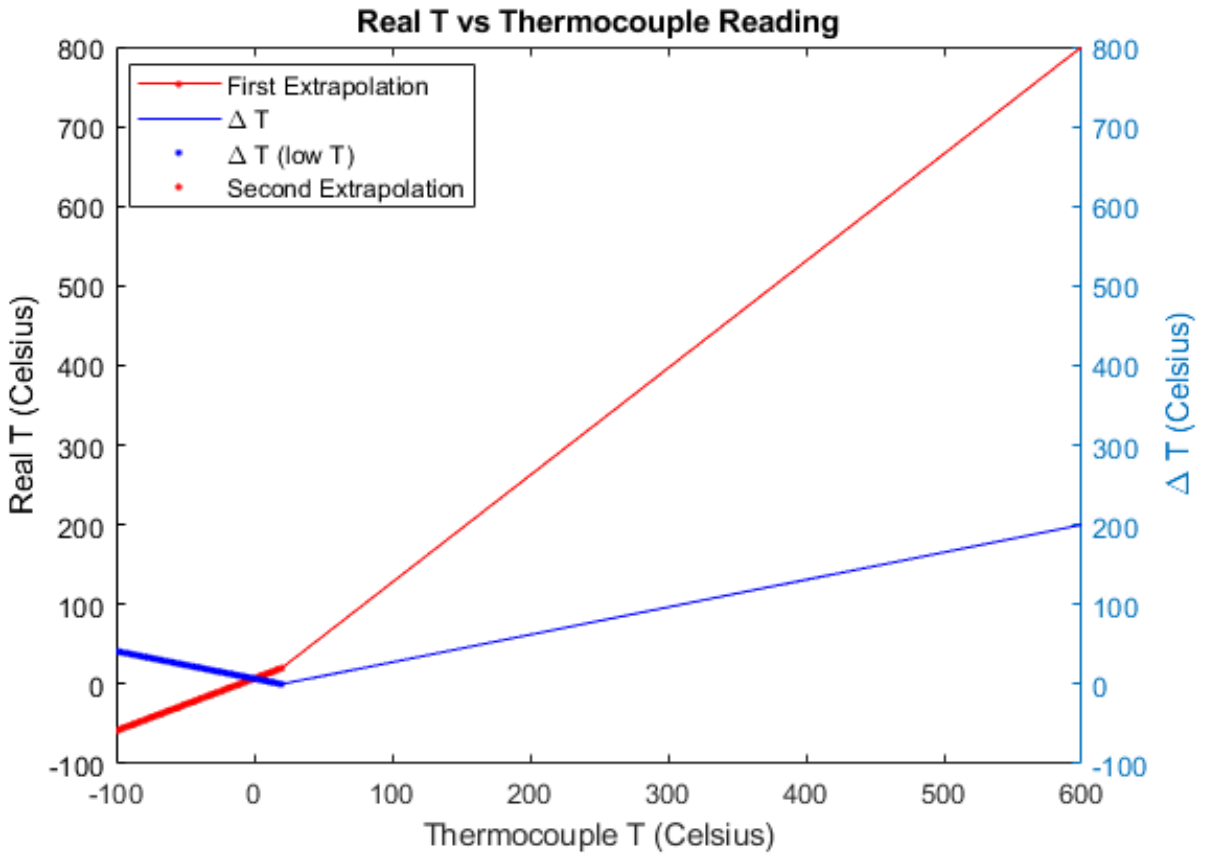

Figure 4.6. Red line: Plot of real temperature versus the thermocouple reading of the sample as extrapolated from the annealing temperature and room temperature for a case where the thermocouple reads 600°C when the real temperature is 800°C. Blue line: Plot of the difference between the real temperature and the thermocouple temperature, $\Delta \boldsymbol{T} = \boldsymbol{T}_{\boldsymbol{real}} - \boldsymbol{T}_{\boldsymbol{thermocouple}}$. The thicker lines are the second set of extrapolations for low temperatures.

thermocouple grows linearly (proof of linear relationship is given in Appendix B), one can extrapolate all temperatures between room temperature and annealing temperature, as shown by the thin, red line in Figure 4.6. From this the effect of the temperature gradient is clear – the thermocouple will always read a lower temperature than the real temperature, meaning the difference between the real and thermocouple temperatures is always above zero, as denoted by the thin, blue line in the figure. It is important to note that the annealing temperature is measured at the hottest part of the sample, namely the center, whereas the edges tend to be 50-100° C lower. However, the center temperature is most important since almost all LEEM imaging is done at the center of the sample.

At temperatures below room temperature, one needs to make a similar consideration for calibrating the thermocouple. In this case, the sample is actually the farthest away from the cooling elements in terms of physical contact, since the cooling elements are installed onto the manipulator that holds the sample holder. Thus, we expect the sample to have a higher temperature than the rest of the sample holder, including the thermocouple. In practice, this effect is quite negligible during the cooling phase of the experiments, as it was found that different sample holders with different samples and thus different gradients during heating would take similar time to reach the same temperature thresholds – this is due to the very long cooling period, which allows the entire sample holder to stay at thermal equilibrium. The effect, however, should become more significant when the heating filament is activated to maintain the sample at the target temperature, since then the effect operates with essentially the same principle as in the high temperature case, in that the thermocouple should always read a lower temperature than the real temperature and that the difference should always be positive. This is

shown by the thick, blue line in Figure 4.6, a mirror image of the thin, blue line for the high temperature case maintaining the same gradient effect. By using this temperature difference as a constraint, we can construct the low-temperature extrapolation, as shown by the thick, red line in Figure 4.6. The mathematics and other details behind the extrapolation process is provided in Appendix B.

The temperature gradient is an unavoidable problem due to the design of the sample holders, but because they have predictable behavior, this extrapolation method should give reasonably accurate temperatures based on the thermocouple readings. Temperatures provided in this chapter as well as the rest of the dissertation will use this method unless stated otherwise. One final thing to note is that the LEEM's type-C thermocouples were intended for high temperature work and have some level of uncertainty at low temperatures, according to the manufacturer. Such uncertainties were not quantified, but most of the issues should be with temperature resolution at tenths and hundredths of degrees due to type-C thermocouples displaying a large range of temperatures for relatively small changes in voltage, which is the reason why they are used for high temperature work. As such, the temperatures provided in this dissertation will be rounded to the nearest degree, even though the LEEM software can display tenths and hundredths of degrees.

4.3.2 Evaporator

The Pb evaporators provided challenges of their own due to Pb's relatively low melting point. Metals with sufficiently high melting points tend to wet the surface of filaments upon being melted, forming films across the filament loops similar to how water would form films if the

Figure 4.7. Left: Pb evaporator using a tungsten basket design. Right: Pb evaporator using a crucible design.

filaments were to be dipped in them. These materials adhere to the filaments and are not likely to drip off, allowing for the simple, easily built designs consisting of a coil of tungsten wire with the material melted inside. Pb, on the other hand, does not form films or adhere to the tungsten filaments at all, instead forming a spherical droplet under its own surface tension. This causes the molten Pb droplet to easily fall through gaps in the evaporator, even holes that are just a few millimeters wide if hot enough.

The LEEM had a Pb evaporator installed on it at time of purchase, consisting of a crucible wrapped in tungsten wire, as seen in Figure 4.7. This design was determined unsuitable for the experiments performed in this dissertation, mostly due to the lack of a shutter. Evaporators require some time to reach equilibrium upon activation, with bulkier evaporators requiring more time. This poses a problem when deposition may have to be paused in the middle of experiments, which would require deactivating and reactivating the evaporator, with differing behavior towards equilibrium each time depending on how much the evaporator cools between reactivations. This problem is resolved by the shutter, which can pause the deposition while the evaporator continues to run. The crucible evaporator design is one that can only be facing

upwards, otherwise the Pb would drip out upon becoming molten, but the LEEM was initially found not to have space for shutters for upward-facing evaporators (to be elaborated upon later). Shutters could only be installed on downward-facing evaporators, so a new, downward-facing Pb evaporator had to be custom designed and calibrated.

Figure 4.7 also shows the evaporator that was designed for use in most of these experiments. It consists of a cone-shaped "basket" made from a coil of tungsten, connected to electrical feedthroughs and filled with Pb that was melted in an external chamber before being installed in the LEEM. The bottom of the basket is open, so a very thin tungsten wire was woven

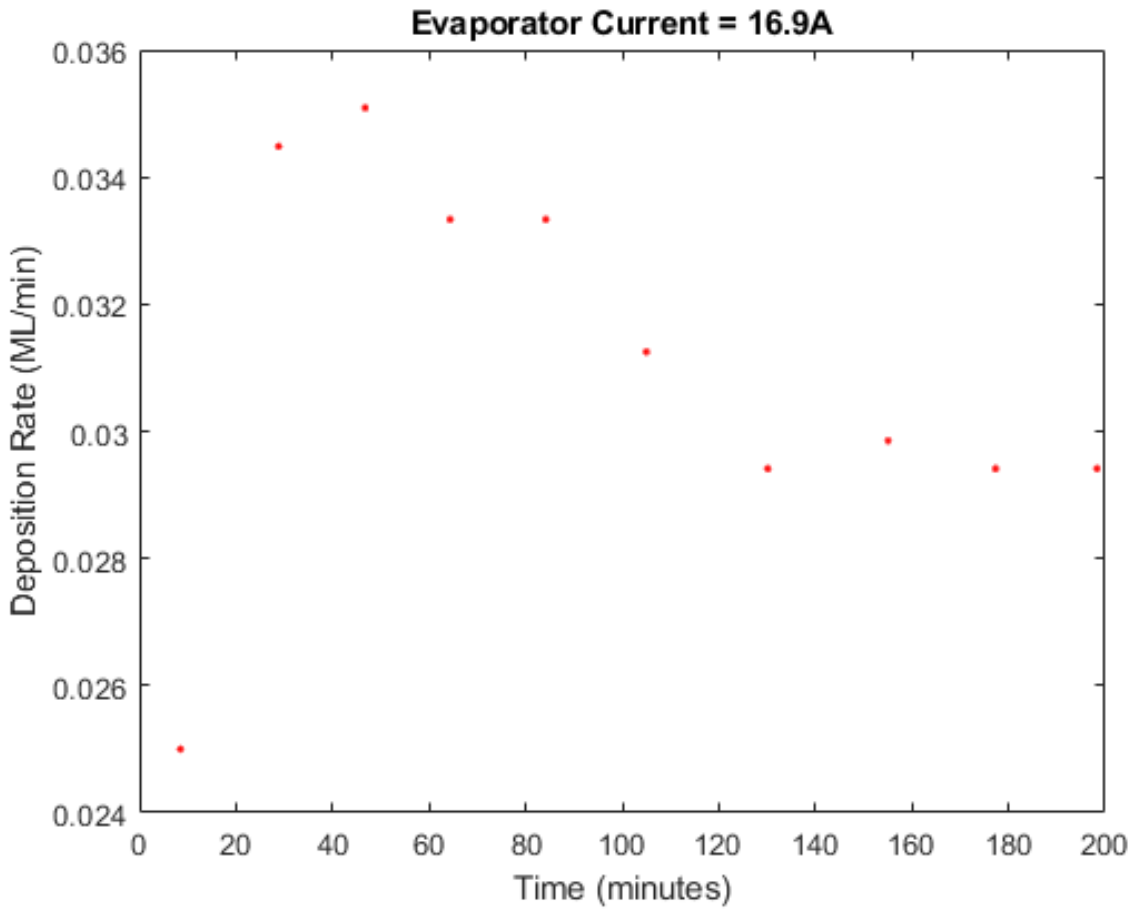

Figure 4.8. Deposition rate of the basket type evaporator versus time after activation, for an evaporator current of 16.9A. Note the initial rise during the startup period followed by a gradual fall towards an asymptote.

across the opening to form a sort of net or grid that would maintain the size of the opening while keeping the individual holes small enough such that Pb would not drip through. It is a rather bulky design, requiring up to 20A of current to properly heat the entire basket to get enough deposition, and it also had a calibration issue.

The evaporator's deposition rate varied with time, though in a somewhat predictable way. The deposition rate is plotted in Figure 4.8, and it shows that the evaporator takes about 45 minutes to ramp up to a maximum, after which changes in electrical contact between the molten Pb and the tungsten basket causes the heating profile to change, resulting in a gradual reduction in deposition rate towards an asymptote. The timing of the initial rise and peak is generally consistent, but the time to reach the asymptote tends to vary between activations, even at the same current. Unfortunately, there is no way to find the deposition rate immediately before the experiment, since the experiment requires that the sample be cooled for about an hour, while the calibration must be done at high temperatures. However, we can note that due to the cooling period, the evaporator, which is kept on during the entire time, is certain to be past the deposition peak and should be on the approximately linear, downward portion of the curve. Thus, it should be possible to extrapolate the deposition rate throughout the experiment by getting two points on the downward slope.

One of the two points is relatively easy to obtain, and it is taken after the end of the experiment when it is no longer necessary to keep the sample cooled, using the phase transition depicted in Figure 4.4 and discussed in section 4.2. The other point is much more difficult to obtain, and there was a lot of uncertainty until it was discovered very late into the experimental phase that a shutter could be barely fit onto the original, crucible evaporator. The crucible

evaporator was found to be greatly more consistent than the basket evaporator, with a much narrower range of fluctuations as well as a fast startup period. With this evaporator, the trigger coverage θ_C for the Pb island nucleation was measured to a reasonable certainty, which could be used as a calibration point for older data that used the basket evaporator. If the basket evaporator took a time $t = \tau$ from the start of deposition to the first nucleation event, we would know that the average deposition rate during that period was θ_C/τ. With these two points, an equation for the line can be obtained and then integrated through various moments in time of the experiment to calculate the coverage at those moments. The vast majority of the data was taken using the basket evaporators, so unless otherwise noted, it should be assumed the coverages were calculated using this extrapolation method.

4.4 Results and Discussion

During the early phases of deposition, nothing remarkable happens – the surface looks mostly the same with a slight shift in brightness due to the reflectivity of the developing Pb wetting layer. The LEED pattern shows a very weak $\left(\sqrt{3} \times \sqrt{3}\right)$ pattern, meaning the wetting layer is mostly disorganized and amorphous, which is an expected result based on the Pb/Si(111) experiments mentioned before.

Upon reaching a certain critical coverage, various Pb islands nucleate on top of the wetting layer, after which the islands continue growing in lateral size with additional deposition. An example sequence of island nucleation and growth is shown in Figure 4.9, with the islands

initially growing in all directions but eventually preferring to grow along step edges and defects once the island edges reach such features. The critical coverage θ_C was measured using the crucible evaporator and was found to be about 4/3ML with respect to Ge(111) with an uncertainty of ±0.07ML due to evaporator fluctuations and drift. This critical coverage did not appear to change with the temperature of the sample within the range of temperatures used in these experiments (-45 to 10°C), or if it did change, it was within the level of uncertainty and could not be detected. It was reported for Pb/Si(111) that the critical coverage increases with decreasing temperature [2] but over a range of temperatures much larger than was performed for Pb/Ge(111), which may explain why changes in critical coverage could not be detected for this system.

The critical coverage is the first point of difference between Ge(111) and Si(111). Recall from the introductory discussion that the critical coverage for Pb islands on Si(111)-(7x7) was 1.22ML with respect to Pb(111), meaning the Pb wetting layer was compressed by 22% beyond its bulk value [36, 37]. In the case of Ge(111), however, the critical coverage of 4/3ML with respect to Ge(111) is almost exactly 1ML with respect to Pb(111), only about 2% higher. Even accounting for the uncertainty in measurement, it is clear that the Pb wetting layer does not compress as much on the Ge surface as it does on Si. Such behavior can be explained by the different lattice constants of the two substrates, especially in light of the saturation coverage study performed in [30] that was also discussed in the introduction – the densely packed (~4/3ML) Pb phase is commensurate with Ge(111) but not with Si(111) due to a lattice mismatch with the Si surface. Although the Pb wetting layer differs from the densely packed phase in that the wetting layer shows no ordered structure, so that commensurability should not apply, one can

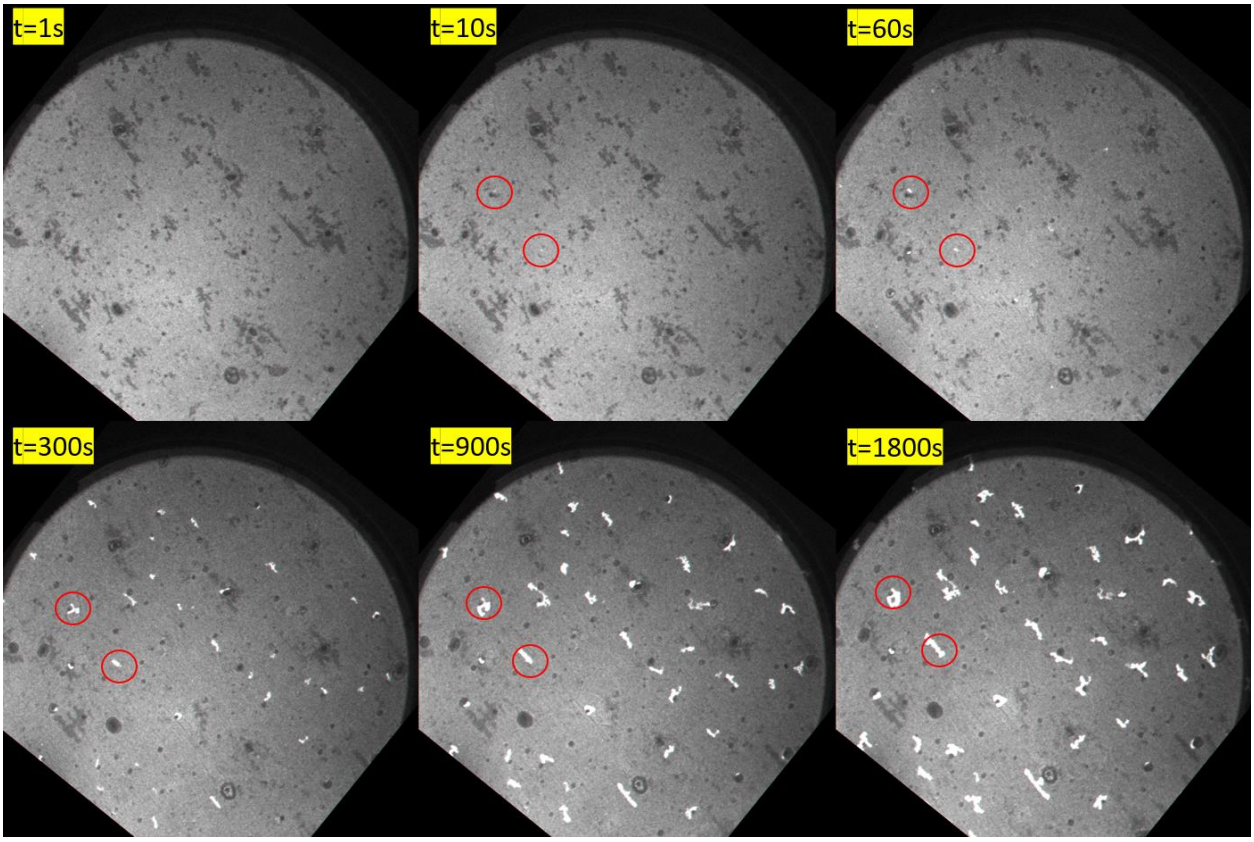

Figure 4.9. Sequence of images showing Pb island nucleation and growth at T=3°C over 30 minutes of deposition. Two of the islands are circled for easier identification and tracking. FoV=15µm, SV=8.2V.

still reasonably infer that there is a relationship between the surface density of Pb(111) and the surface density of Ge(111) which makes the 4/3ML wetting layer very energetically favorable. In the case of Si(111), the wetting layer already has a large degree of mismatch at the same coverage. Therefore, the degree of mismatch should have less of an effect on how additional deposition energetically favors the compression of the wetting layer compared to forming islands.

Since these experiments were repeated for different temperatures, the sequences of growths could be laid out for each temperature. The sequences are shown in Figure 4.10 for four temperatures for four different times after initial nucleation. From these, one can easily see the effect of temperature on the island growth morphology. At higher temperatures, the individual islands are bigger on average, but they are fewer in number. The island count remains relatively

constant throughout the course of deposition (not counting mergers that inevitably occur at very high coverages), with very few new islands appearing over time, and no sign of large island coarsening at the expense of smaller islands. The approximate island number density for each temperature is listed in Table 4.1.

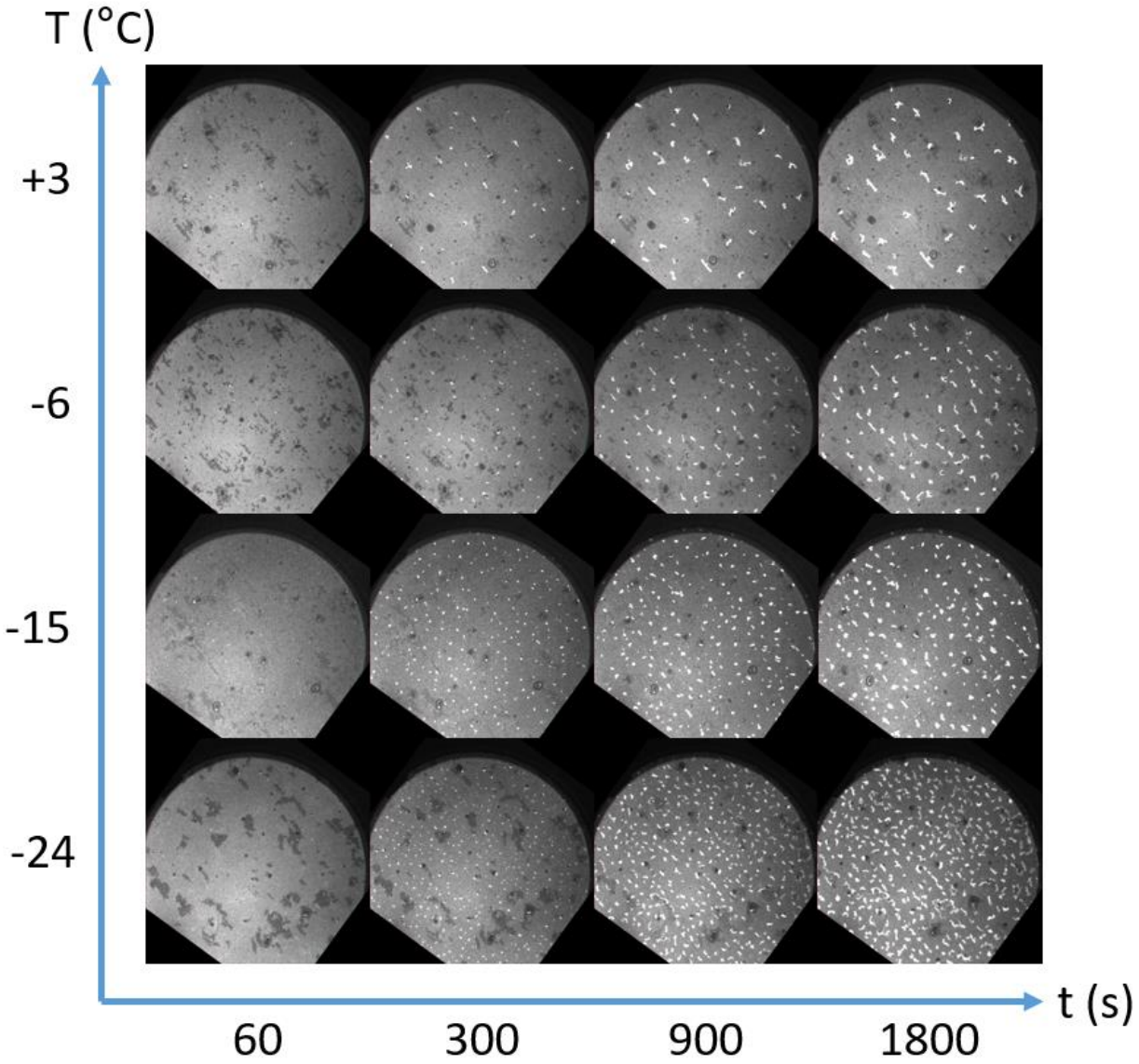

Figure 4.10. Growth sequences of Pb islands on Ge(111) at four different temperatures. The time is given with respect to the first nucleation of the islands, i.e., when the critical coverage of 4/3ML is reached. FoV is 15µm for the top half and 10µm for the bottom half.

4.4.1 Island Nucleation

We can begin analyzing these sequences with the first important event – nucleation. Classical nucleation as described by random walk diffusion typically begins with adatoms that diffuse across the surface until a pair meets and forms a stable cluster [43, 44], with the kinetics of diffusion usually characterized by a diffusion constant in an Arrhenius form $D = D_0 e^{-E_m/kT}$ where E_m is the diffusion barrier [45]. Further island growth occurs via capture of additional adatoms that form a terrace, either from external deposition or from smaller islands that tend to have greater fluctuations in adatom concentrations at the edge, which is the classical coarsening mechanism called Ostwald ripening [46]. In the case of the Pb/Ge(111), the islands show evidence of nonclassical nucleation, since stable islands seem to require much more than simple pairs of adatoms – the nucleation is explosive, with many Pb atoms coalescing over a relatively large

Table 4.1. Calculated values related to nucleation and growth of Pb/Ge(111).

T (°C)	Island # Density (μm^{-2})	# of Atoms in 10s (thousands)	Collection Range, Deposition Only (nm)	Collection Range, WL Contribution (nm)
+3	0.20	541	2327	134
-6	0.79	376	1818	111
-15	4.08	167	995	74
-24	13.15	107	868	59

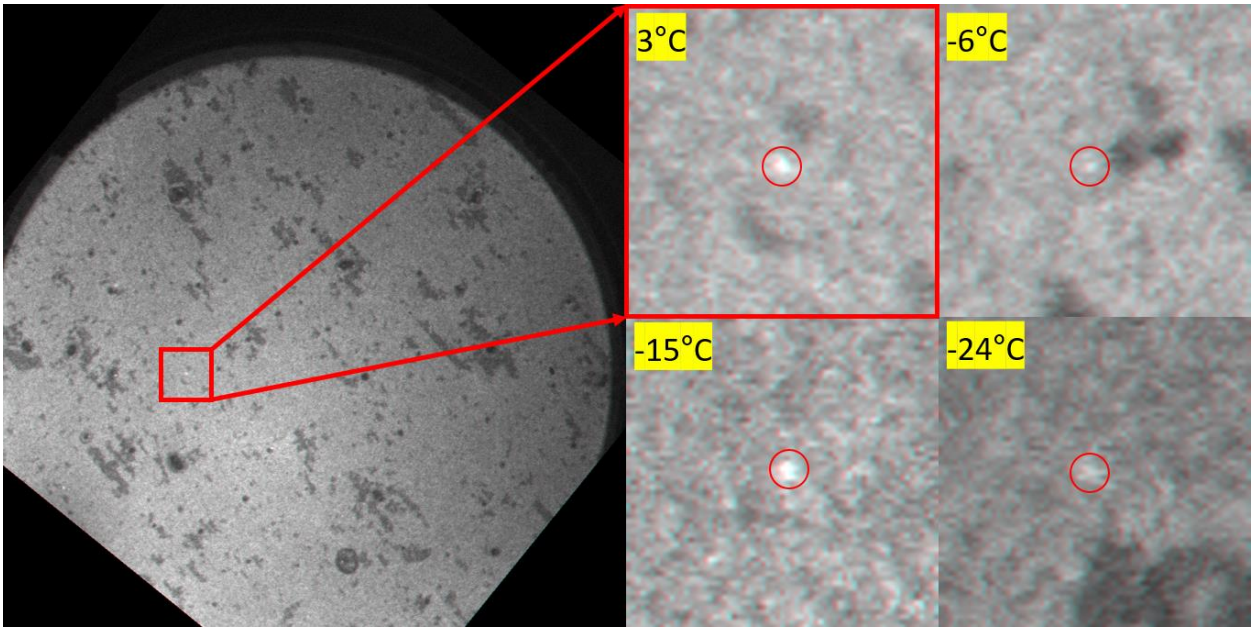

Figure 4.11. Islands imaged 10s after nucleation (11s for -24°C) for each temperature, zoomed in for extra clarity.

distance. In order to calculate the movement of atoms during first nucleation, we simply measure the sizes of these islands shortly after they appear.

Figure 4.11 shows the first of the islands 10 seconds after first detection. Because LEEM data is recorded at 1 frame per second, there is an uncertainty of 1 second in exactly when the island nucleates. There is also a resolution limitation of 1 pixel, whose real size depends on the field of view of the image. Since each image is 1024 by 1024 pixels, it is sufficient to divide the field of view by 1000 to get the approximate size of each pixel. For ease of analysis, we consider the islands 10 seconds into their growth rather than the first frame, while still looking early enough in the process to properly display the explosive nature of their nucleation. The number of pixels that the islands cover in the images will give their lateral area and multiplying them by the island height will give their volume. Even without knowing their exact heights (to be discussed later), we can take a very conservative estimate based on the Pb/Si(111) studies and assume the super-stable height of 7 crystalline Pb(111) layers as a starting point [2]. With these values, we

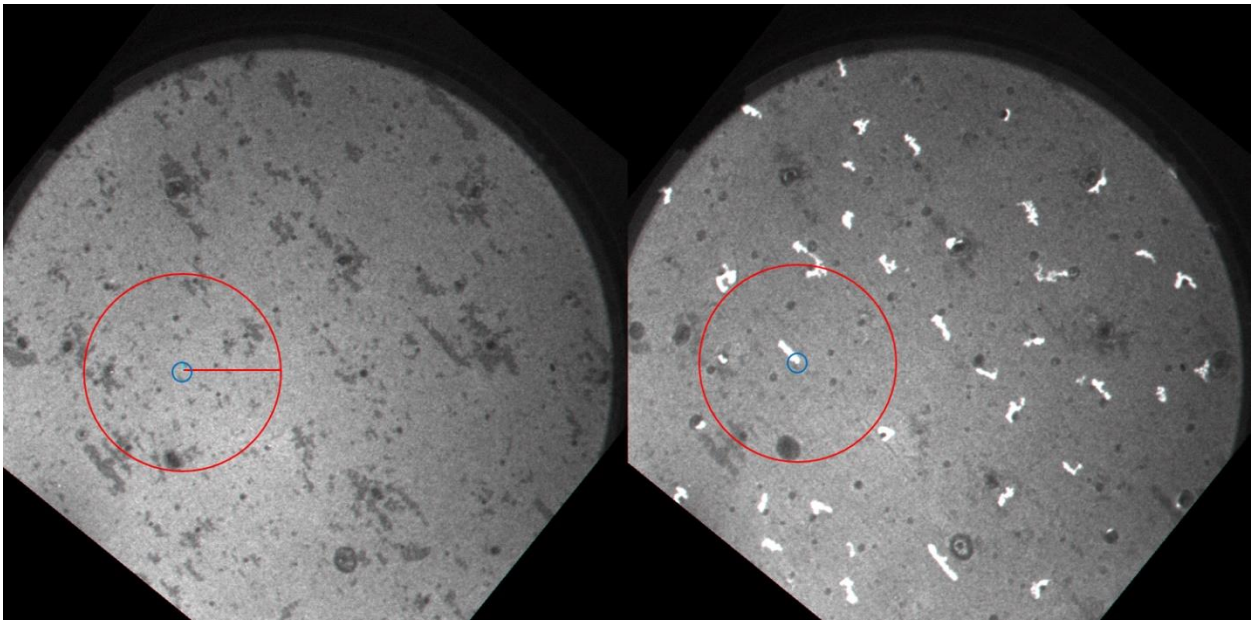

Figure 4.12. Collection range and area of the +3°C island used for the calculations in Table 4.1. The two images are of the same sample, but the left image is of the island at 10s after nucleation as used for the calculations, while the right image is at 15min, to better show how the collection range looks with respect to the position of other islands. The red circle is the collection area accounting only for evaporator deposition, while the blue circle is the collection area with maximum wetting layer contribution.

can calculate the total number of Pb atoms that must have coalesced to form the islands within the first ten seconds of their nucleation, and Table 4.1 lists these numbers.

It is remarkable from these numbers that within only 10 seconds, hundreds of thousands of atoms have organized to form these islands. These atoms can come from two sources – the wetting layer and continued deposition from the Pb evaporator. With regards to deposition, the flux rate for these experiments was kept relatively similar, ranging between 0.025 and 0.045ML/min. Within the space of 10 seconds, these deposition rates would have contributed between 0.03 and 0.05 atoms directly on top of these islands, meaning deposition directly on the islands contributes essentially nothing to the initial nucleation. If we assume that the islands are then pulling the atoms that are deposited on top of the wetting layer around them but not pulling directly from the wetting layer itself, we can calculate the radius of the area from which the

islands must draw the atoms within the 10 seconds. This area for +3°C is shown in Figure 4.12 as an example, for better visual representation with relation to the field of view and other islands.

From the images, it is clear that the collection range only for deposition is quite large and overlaps with potential collection ranges for the other islands, meaning there must be some contribution from the wetting layer in addition to the deposition. This is supported by work done on Pb/Si(111), where partial order developed in the wetting layer as atoms were transferred from the wetting layer to the islands [22]. Since it is impossible to know exactly how much of the wetting layer is transferred, we once again assume an extreme case in which all 4/3ML of the wetting layer is transferred. The new collection ranges combining both deposition and full contribution from the wetting layer are listed in Table 4.1, and the area for the +3°C case is shown as a blue circle in Figure 4.12. With the wetting layer, the collection range is reduced by an entire order of magnitude, but it is still many tens of nanometers at the minimum. Just looking at the spacing between the islands, one can speculate that the actual collection range is perhaps 1/4-1/2 of the maximum (deposition only) range, which would put the collection range on the order of hundreds of nanometers. To see how much contribution from the wetting layer is required to bring the collection range within those values, we can plot the collection range as a function of wetting layer contribution, as shown in Figure 4.13. According to the plot, this corresponds to 1-5% contribution from the wetting layer, which is a curious result because the critical coverage of 4/3ML results in about 2% compression of Pb beyond its Pb(111) density, and the uncertainty (in

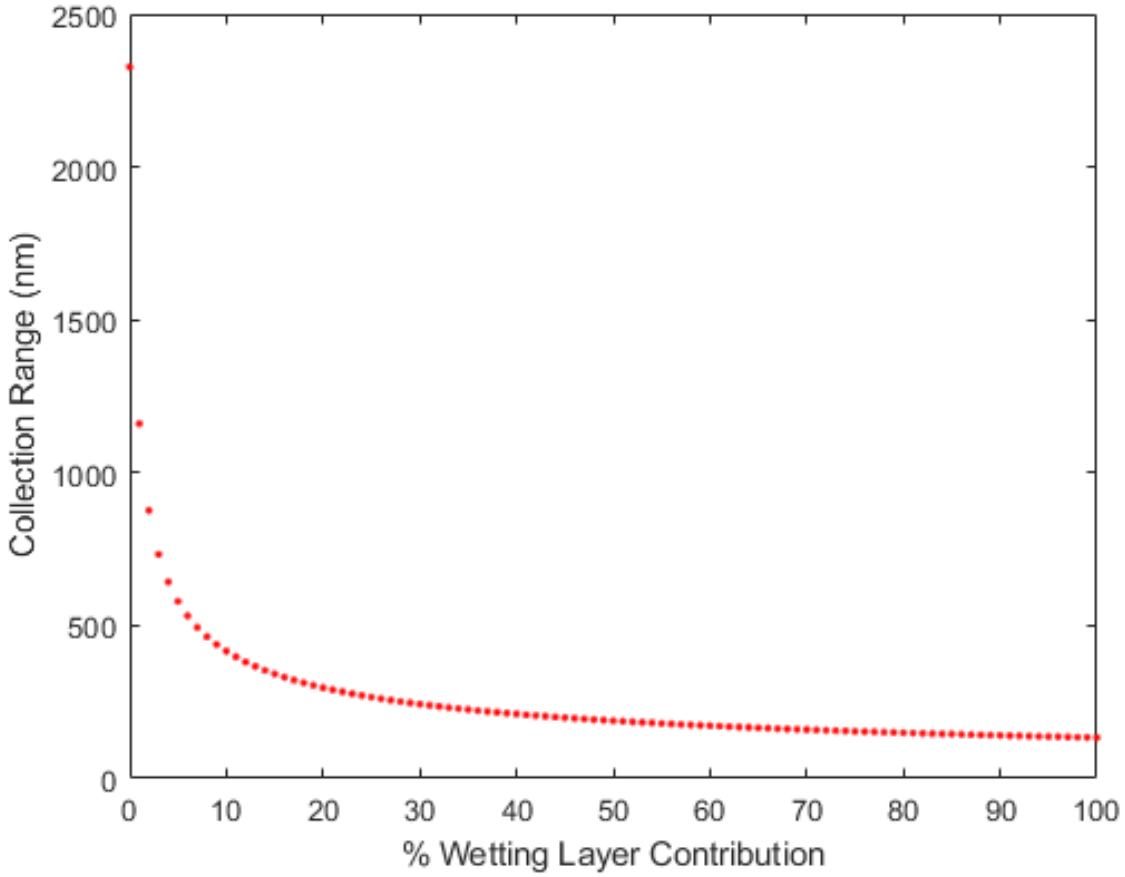

Figure 4.13. Pb collection range for the +3°C island as a function of percent contribution from the wetting layer. The first and final values are represented in Figure 4.12 as the radius of the red and blue circles respectively.

the upper range) goes a little above 7% compression. This suggests that the islands initially nucleate by relaxing the compression built into the wetting layer and also explains why the nucleation seems so quick and explosive. In any case, this extraordinary collection range even at its minimum is far greater than what is expected for random walk diffusion at these temperatures. As an example, we can look at the empirically derived diffusion coefficients of Re/W(211) [47] and use them to calculate the average displacement of rhenium atoms within a 10-second window of time. The average square of total displacement Δr is given by the relation $\langle|\Delta r|^2\rangle = 4Dt$, which gives the $t^{1/2}$ dependence for classical diffusion [45]. At 273K, rhenium has

a diffusion coefficient of about $10^{-18}\,cm^2/s$ which leads to an average total displacement of about 0.063nm, which is not even one interatomic distance. The collection range involved in Pb/Ge(111) is many orders of magnitude greater, showing the incredible speed at which collective diffusion operates. As a final note regarding the diffusion speed, the reader should be reminded that the true diffusion rate and collection range are very likely to be even *higher*, given that the island height assumption of 7 layers is an intentional underestimation based on height selection in the Pb/Si(111) system, which should be an intrinsic property of Pb due to QSE and should hold for Pb/Ge(111) as well.

Another calculation that can be performed is the diffusion barrier between the wetting layer and the islands. Classical nucleation theory gives a dependence of the island number density n on the deposition flux rate F and the diffusion coefficient D [17, 22, 44]:

$$n \propto \left(\frac{F}{D}\right)^{\chi} \tag{4.1}$$

where $\chi = \frac{i}{(i+1)}$ with i representing the number of atoms required for the island to be stable. While this is meant to apply for classical nucleation events in which adatom pairs nucleate the first islands on a mostly bare substrate at very low coverages, it can still be argued that it can apply for Pb islands first nucleating on top of a completed Pb wetting layer, where the Pb wetting layer can be taken as the bare substrate. The diffusion coefficient D is also part of classical diffusion, which should not apply to the superdiffusive Pb/Ge(111) system, but this is presently the best analytical tool since superdiffusion is still poorly understood at a theoretical level. For the Pb islands, the critical cluster size i is much greater than 1, as shown by the number of atoms calculated earlier, which means $\chi = 1$ for explosive nucleation.

Now, for a particular experiment j, the island density of n_j is observed, for flux rate F_j and diffusion coefficient $D_j = D_0 e^{-E_m/kT_j}$ where E_m is the diffusion barrier that we wish to find. Since we do not know the value of the diffusion constant D_0, we cannot directly solve for the diffusion barrier with one experiment; instead, to eliminate it altogether, we must divide n_j by the island density from another experiment n_k to get

$$\frac{n_j}{n_k} = \frac{F_j}{F_k} exp\left[\frac{E_m}{k}\left(\frac{1}{T_j} - \frac{1}{T_k}\right)\right]. \tag{4.2}$$

Solving for E_m then gives us

$$E_m = \frac{k}{\left(\frac{1}{T_j} - \frac{1}{T_k}\right)} \ln \frac{n_j F_k}{n_k F_j} \tag{4.3}$$

which should ideally give the same value for any pair of experiments. Using the island number densities provided in Table 4.1, E_m was found to be 0.87eV between +3 and -6°C; and 0.82eV between -6 and -15°C and between -15 and -24°C, which is surprisingly very similar to the diffusion barriers for some classical diffusion systems such as Re/W(211) previously used as an example. This suggests that the nucleation events for Pb/Ge(111) on their own are fairly classical in nature but are nonclassical in their mechanisms of growth.

One final aspect of nucleation to discuss is the effect of defects and surface features on island nucleation and, by extension, the diffusion coefficient. Figure 4.14 depicts an older set of data for which Pb islands were grown on a sample that did not have the medium-density step defects and had comparable numbers of high-density step defects (see chapter 3 for a reminder on the types of defects). While this set of data lacked the more rigorous evaporator calibration used for the main data analyzed in this chapter, the deposition rates recorded for this set of data

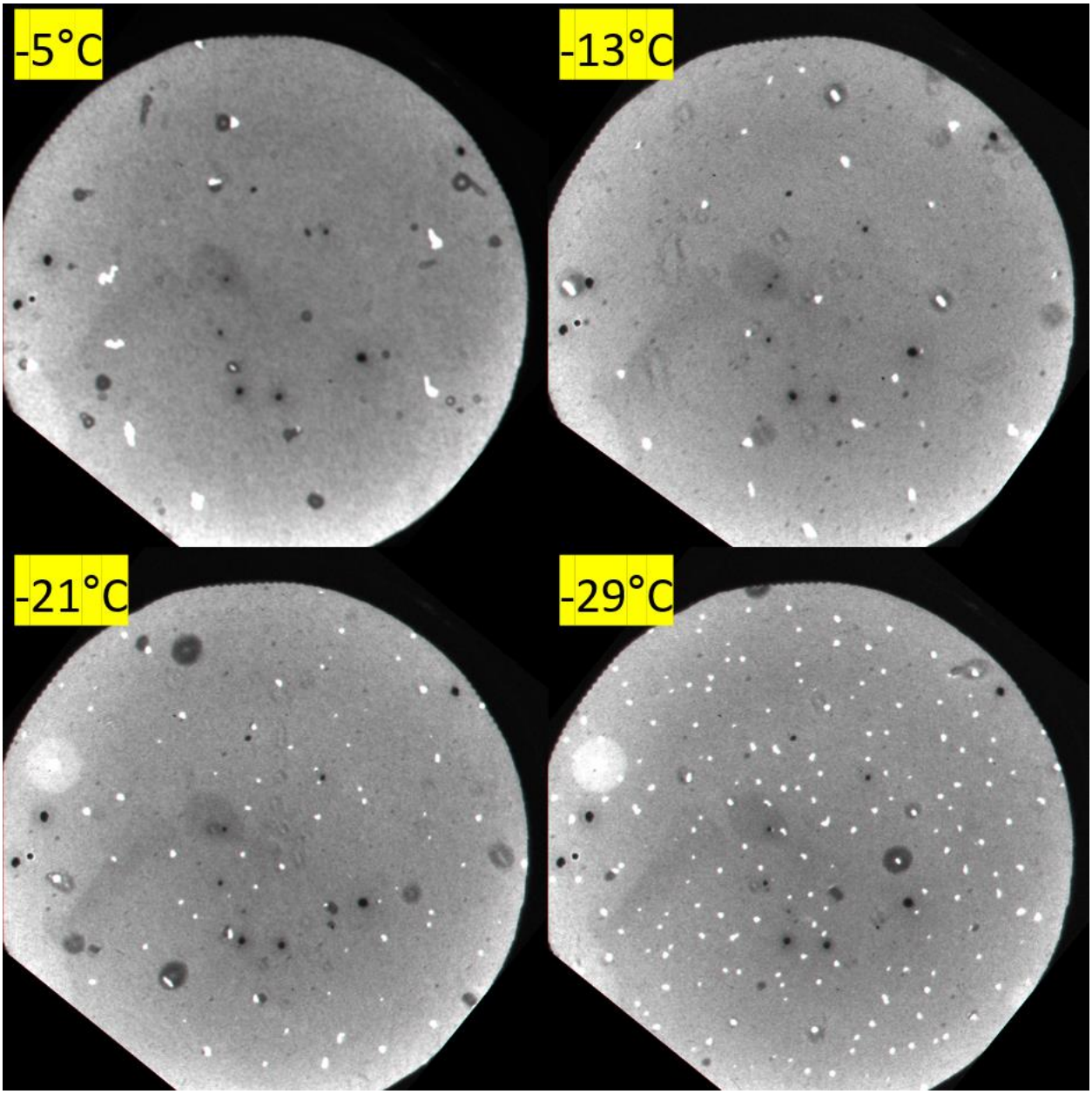

Figure 4.14. Pb islands grown on a different sample without medium-density step defects, showing a much lower island number density overall compared to the first set of data. Images were taken 5 minutes after nucleation (0.1-0.2ML beyond critical coverage), enough time for island number density to saturate. FoV is 15µm, and start voltage is 8.5V.

were still comparable based on the evaporator calibrations performed after the experiments. By comparing the island number densities between the two sets of data, we can clearly see that the densities depicted in Figure 4.14 are far lower than those shown in Figure 4.10 for matching temperatures for 300s and above (when new islands stop nucleating). Lower island density

implies that each island has a larger collection range on average, which further implies that Pb is much more mobile. This suggests that the defects, at least the medium-density step defects, play a role in restricting the mobility of the wetting layer, by changing either the diffusion barrier E_m or the diffusion constant D_0 in the expression for the diffusion coefficient.

We once again take equation 4.2 and try to examine where the two sets of data differ. The logical starting point is to compare the island number densities for the same temperature, so we will take the -6°C density from the main data set and the -5°C density from the old data set and take their temperature to be approximate equal for simplicity. Since we no longer assume the diffusion constant or the diffusion barrier is the same for the two sets of data, the diffusion coefficient expression becomes $D_j = D_{0,j} e^{-E_{m,j}/kT_j}$, and equation 4.2 becomes

$$\frac{n_j}{n_k} = \frac{F_j D_{0,k}}{F_k D_{0,j}} exp\left[\frac{1}{kT}\left(E_{m,j} - E_{m,k}\right)\right]. \quad (4.4)$$

If the diffusion barrier is the same for both sets, then the exponential term no longer matters, and the ratio of island density is simply $\frac{n_j}{n_k} = \frac{F_j D_{0,k}}{F_k D_{0,j}}$. The -5°C island density is $0.057\ islands/\mu m^2$, giving a number density ratio of 13.9 between the main data and the old data, over an order of magnitude larger. We further assume the flux rates are the same, since we do not have accurate information on the flux rates of the old data set but know that they were comparable and certainly cannot account for even a small part of the 13.9 ratio. Thus, if the diffusion barrier were the same, the island number density ratio between the two sets of data is only dependent on the inverse of the ratio between the two diffusion constants, or $13.9 = \frac{D_{0,k}}{D_{0,j}}$.

Likewise, if we assume that the diffusion constants are the same, equation 4.2 becomes, after making the same assumption about the flux rate,

$$\frac{n_j}{n_k} = exp\left[\frac{1}{kT}\left(E_{m,j} - E_{m,k}\right)\right]. \tag{4.5}$$

Solving for $\Delta E_m = E_{m,j} - E_{m,k}$ then gives us

$$\Delta E_m = kT \ln \frac{n_j}{n_k}, \tag{4.6}$$

or $\Delta E_m = 0.06eV$. It does not seem likely that the diffusion constant would be affected by the presence of Ge surface defects, since it is more like an intrinsic property of Pb itself. The diffusion barrier is the more reasonable candidate for change since it represents the interaction between the diffusing material and the surface, as exemplified by the different diffusion barriers for rhodium atoms diffusing across different single crystal surfaces of rhodium [48]. Therefore, we conclude that the presence of additional defects has the tendency to increase the diffusion barrier and hinder the overall diffusion rate of the Pb wetting layer, a perfectly reasonable result.

4.4.2 Continued Island Growth Towards High Coverage

The islands' growth rates can be tracked beyond the initial nucleation. It can be expected that the majority of the contribution of Pb atoms should now come from external deposition, since the wetting layer will have already contributed a significant amount during the nucleation phase and will no longer have sufficient material to supply the continued growth. Thus, it is reasonable to conclude that the growth rate should slow down to be limited by the deposition rate, i.e., island growth rate should be proportional to the deposition rate. It is also useful to compare the growth rates between different temperatures, since the classical behavior is for

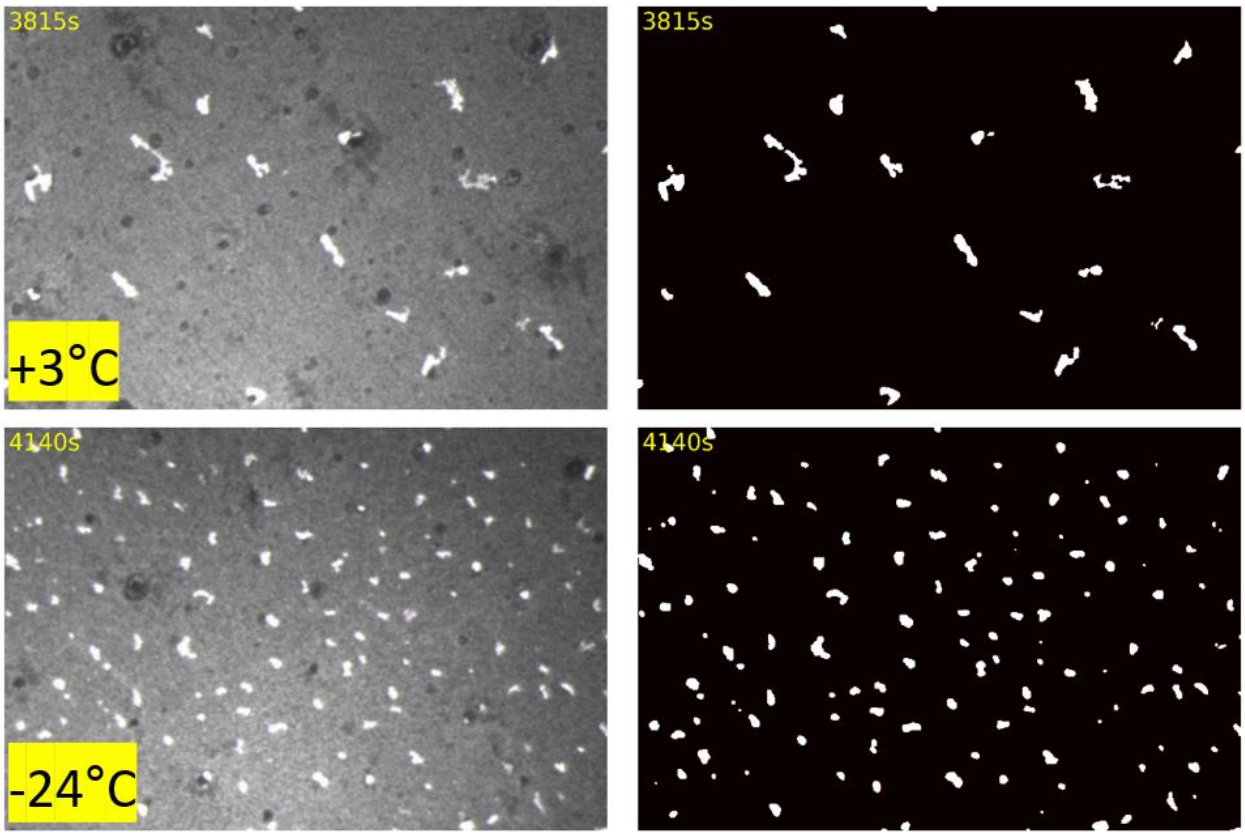

Figure 4.15. Examples of regions measured by computer vision, for two different temperatures. Left is the original image from the raw data, and right is the processed image showing only the islands.

growth rate to be higher for higher temperatures due to the increased thermal diffusion. Since this relationship may not hold for a superdiffusive system like Pb/Ge(111), looking at thermal dependence is important. Since the experiments do not have the same deposition rate, the island growths should be considered with respect to total coverage rather than time.

To assist with processing the data, which involves thousands of frames of island growth in realtime, our collaborators at University of Central Florida (V. Stroup, D. Le, and T.S. Rahman) developed a procedure using computer vision to track and measure the island sizes. They would take a representative area of the sample as shown in Figure 4.15 and isolate the islands, whose pixels could be summed and then converted to total area (15x15nm or 10x10nm per pixel depending on FoV). The program could also count the number of individual islands, which could

be used to track additional nucleation over time as well as the average size of the islands. Since the processed areas differed in size for each experiment because areas had to be chosen to avoid the darker region on the microchannel plate, the results had to be normalized per unit area of the surface for proper comparison.

The computer vision results are shown in Figure 4.16. There is a clear temperature dependence of the growth rate on the temperature, with the growth rate tending to be higher for lower temperatures. This paradoxical, inverse relationship with temperature is further evidence of superdiffusion occurring for the Pb/Ge(111) system, as compared to thermal diffusion which sees a positive relationship between growth rate and temperature. There is one potential problem in that these graphs only measure the lateral size of the islands rather than volume, and one could argue that this inverse relationship only arises because the islands are taller at higher temperatures, which would make them appear smaller from the LEEM's top-down

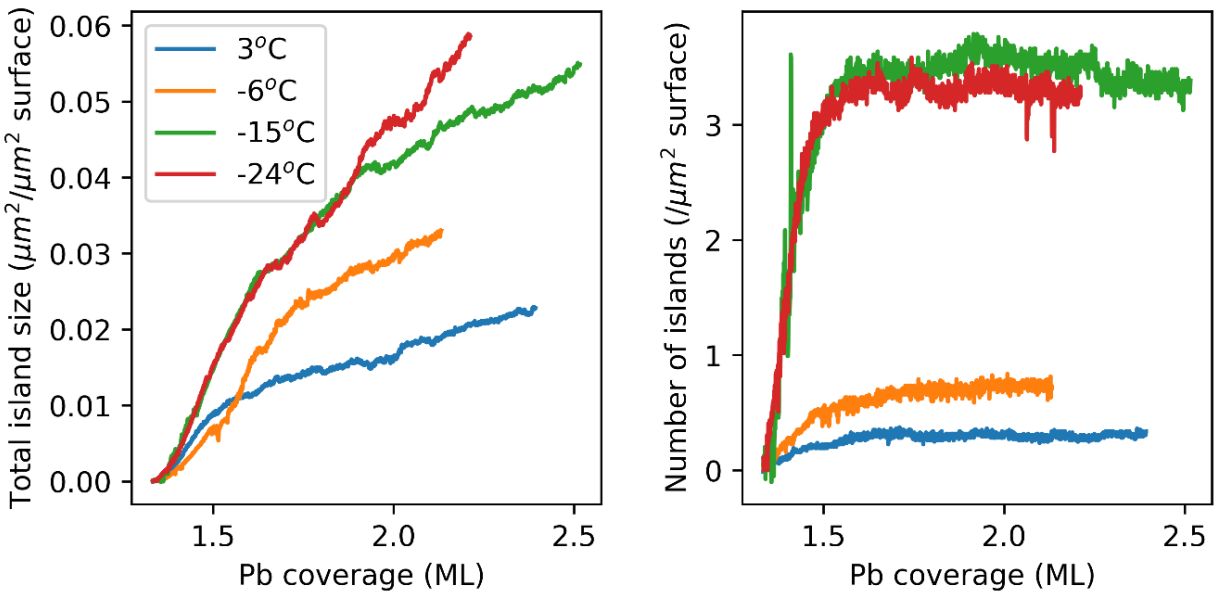

Figure 4.16. Left: Normalized total island lateral size as a function of Pb coverage. Right: Normalized island number density as a function of Pb coverage. All the curves begin at the critical coverage.

view. However, if we consider the possible island heights and apply them to the curves in Figure 4.16, it turns out that the island heights are not enough to nullify this inverse relationship. For example, if the average island height starts at 7 layers for -24°C and increases by 2 layers for each temperature (9 for -15°C, 11 for -6°C, 13 for +3°C), which almost certainly overestimates the height increase given the narrow temperature range according to the Pb/Si(111) phase diagram in [2], only the -15°C curve overtakes the curve above it, and the rest are unable to catch up. For a more realistic estimate, the average island heights for -24°C and -15°C should be very similar, so their relative growth curves should not be affected by height considerations.

Another feature of the island growth curves is the change in slope with additional deposition. At first, it seems that the growth curves may follow the $t^{1/2}$ dependence expected for classical diffusion, with the growth rate slowing down over time. To more accurately analyze the change in slope, we look at the island number density curve on the right side of Figure 4.16. The number of islands takes some time to reach saturation, showing a quick rise followed by a plateau at around 1.6ML, or about 0.27ML after the critical coverage. Looking back at the total island size curve, the point where the growth rate changes is located around 1.6ML, suggesting the existence of two stages in the growth sequence. The first stage is when the islands are still nucleating, and the additional islands in addition to the growth of the already existing islands lead to a high total growth rate. Upon reaching saturation, the total island area is no longer bolstered by new island nucleation, so the growth rate decreases. At both stages, the growth curves are linear, with a nonlinear intermediate transitional phase around the island saturation point connecting the two linear stages. It should be noted that the island number density curves for the -15°C and -24°C experiments are inaccurate, especially the -24°C case. These two

temperatures were low enough such that some of the nucleated islands were extremely small and were quickly absorbed by larger islands that were undergoing coarsening. These small islands were generally dim and were not easily recognized by computer vision before they were absorbed. This effect is expected to become more pronounced at lower temperatures, which is why the -15°C experiment only suffered very minor inaccuracies while the -24°C experiment showed an island number density far lower than it actually was. The number densities given in Table 4.1 were obtained through manual counting and should be more accurate as far as the initial nucleation is concerned, while the values shown in Figure 4.16 give better equilibrium values after island coarsening is mostly complete.

4.5 Discussion of Theoretical Results

As mentioned before, many of the mechanisms behind the explosive nucleation and collective diffusion exhibited by Pb/Ge(111) as well as Pb/Si(111) are poorly understood. The only explained part of this phenomenon is the island height selection, which occurs due to QSE and is easy to understand. On this front, our collaborators at the University of Central Florida have attempted to provide theoretical explanations using Density Functional Theory (DFT) calculations.

Their first goal was to explain the slight compression of the wetting layer and the sudden, explosive nucleation of the islands at the critical coverage, as well as why the compression (and thus the critical coverage) differs from Pb/Si(111). Our collaborators (T. Panagiotakopoulos, D.

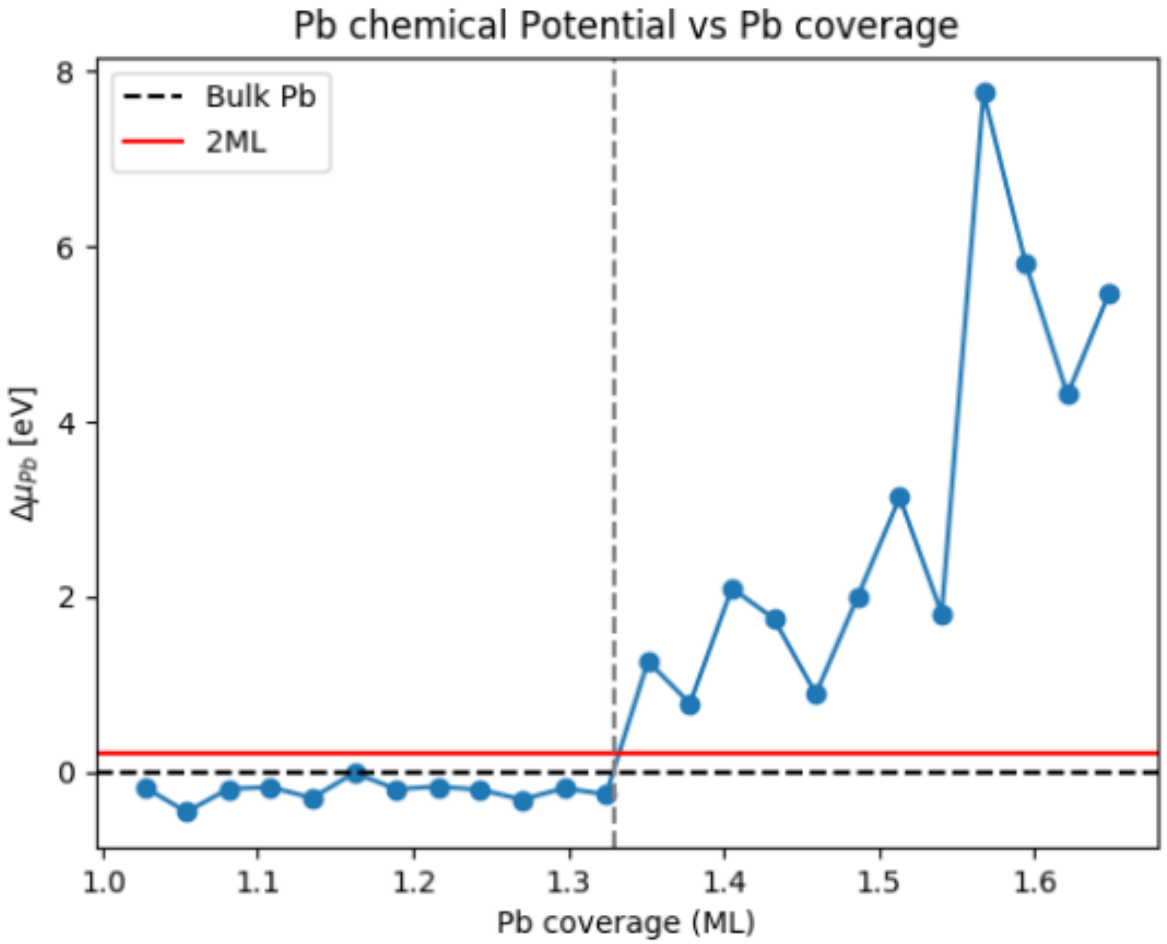

Figure 4.17. Plot of Pb chemical potential as a function of coverage, under the condition that all Pb atoms must stay in a single layer. The chemical potentials of bulk and bilayer of Pb are also shown for comparison.

Le, T.S. Rahman) performed DFT relaxation of a model Pb/Ge(111) system at various coverages above 1ML, with the condition that all Pb atoms must stay within a single layer. Once the configuration of atoms for a particular coverage had converged, the average chemical potential was calculated from the system. From this, they were able to plot the chemical potential of the system as a function of coverage, as shown in Figure 4.17.

The results agree remarkably well with the experimental observations. Below 4/3ML, the chemical potential consistently stays below the chemical potential of bulk Pb (set as 0 for the reference point), meaning that the Pb atoms prefer to stay in the wetting layer as the most energetically favorable configuration. Upon reaching 4/3ML, however, the chemical potential shows a very rapid increase, and the wetting layer no longer becomes energetically favorable compared to the bulk or the bilayer, as expected from the compression that would occur beyond that point. Since the bilayer's chemical potential is greater than that of bulk Pb, the Pb atoms

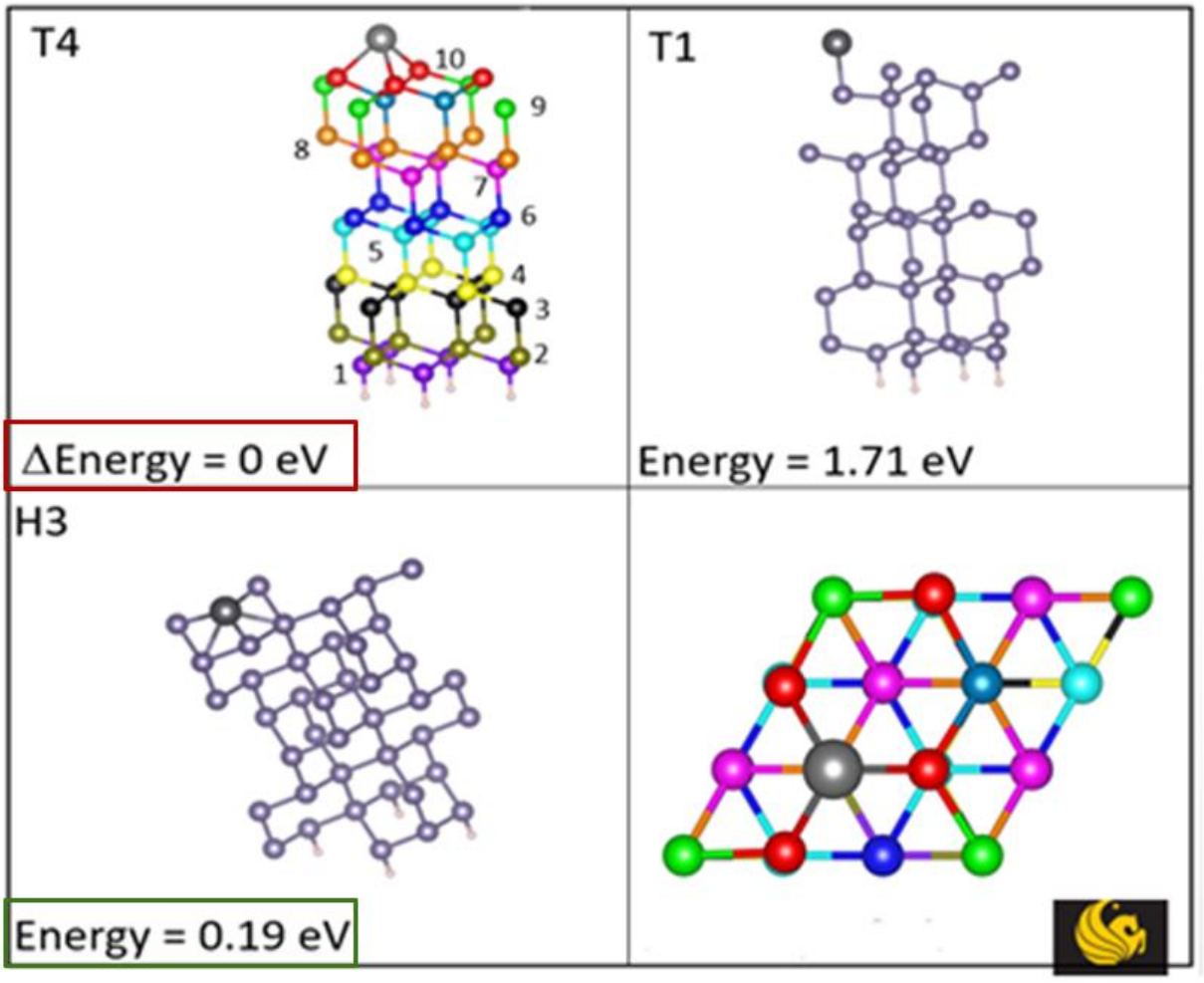

Figure 4.18. Ball-and-stick models of the three binding sites of Pb on Ge(111), as calculated using DFT. The bottom-right configuration is a top-down view of the T4 site, which is the most energetically favorable.

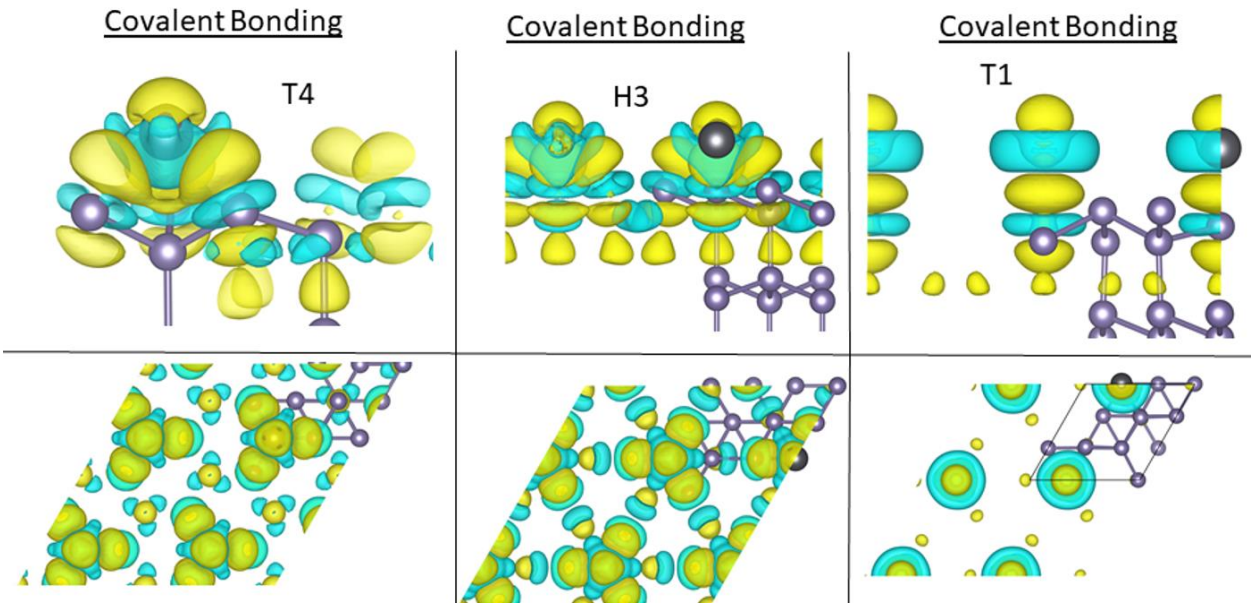

Figure 4.19. Charge density maps of the three binding sites depicted in Figure 4.18. The bottom row shows a top-down view of the bonding in the top row.

would then begin favoring crystalline Pb structures or islands rather than forming a second layer, which is exactly what was observed in the experiments. These results also suggest that the true critical coverage should be quite close to 4/3ML.

Their second goal was the explanation of the origins of the collective diffusion exhibited by the Pb wetting layer. Our collaborators (A. Childs, D. Le, T.S. Rahman) used density function theory (DFT) in a Quantum Espresso simulation to calculate the energies of various binding sites of Pb on the Ge(111) surface. The results are provided in Figure 4.18, which shows ball-and-stick models of three binding sites as well as their energies, and Figure 4.19, which shows the charge density maps of the three binding sites.

From both figures, it is easy to see that the T1 binding site is the odd one out, with a single, covalent bond that has a much higher energy than the T4 site, which is the most energetically favorable binding site used as the reference point in binding energy. The H3 site, on the other hand, is extremely similar to the T4 site due to both having a triple covalent bond, such that the

H3 site's binding energy is only 0.19eV higher. This means Pb atoms can easily hop from one binding site to the other, allowing for great mobility of the atoms across the surface.

There are a few problems with the binding site simulations to be noted, however. The first issue is that the simulation only calculates bonding for a single Pb atom, whereas the Pb/Ge(111) system involves a densely-packed wetting layer at the time of island formation. The atoms in the wetting layer should occupy many binding sites at once as well as bind with each other, and the Pb atoms must move together in a coordinated fashion to sustain the high diffusion rate observed during island formation. The second issue is that the simulation does not explain the diffusion of Pb on top of the wetting layer, as is the case during island growth after the explosive nucleation phase. While nucleation is fueled in part by the compression of the wetting layer, the rest of the island growth is fueled by external deposition or absorption of Pb from other islands through coarsening. Both sources of Pb involves Pb atoms diffusing on top of the wetting layer, involving Pb-Pb bonds rather than Pb-Ge bonds. As such, the simulations explain only a small part of the collective diffusion phenomenon, and more comprehensive simulations may be very difficult, if not impossible, due to the large number of atoms involved.

4.6 Conclusion

We have seen that Pb/Ge(111) at low temperatures is a very unusual and fascinating system with many nonclassical behaviors rarely seen in nature. Similar to Pb/Si(111) at low temperatures, Pb was found to form a single, amorphous wetting layer during initial deposition,

until a certain critical coverage was reached. This coverage was determined to be 4/3ML with an uncertainty of ±0.07ML, amounting to a small (2-7%) amount of compression of Pb beyond its bulk value. At the critical coverage, sudden, explosive nucleation of crystalline Pb islands was observed, pulling hundreds of thousands of atoms per island over hundreds of nanometers in mere seconds by relieving the slight compression that had built up in the wetting layer. The number density and the average size of these islands showed a relationship with the temperature, with the number density seemingly following classical nucleation theory, even though the speed at which the islands formed was nonclassical. Once the number of islands had stabilized, the remainder of island growth was linear with additional deposition, which is the characteristic dependence of collective diffusion and is faster than random-walk diffusion's $t^{1/2}$ dependence.

Considering these results, our collaborators at the University of Central Florida have offered theoretical explanations for the observed phenomena. They used chemical potential calculations to explain the critical coverage and explosive nucleation, and they simulated Pb-Ge bonding to obtain binding energies of the various binding sites to explain the unusually fast diffusion rate of Pb in its collective diffusion behavior.

References

[1] Y. Sato, Thin Film Microscopy of Pb on Ge(111) Phase Transitions and FexNi(1-x) on Cu(111) Magnetic Surface Alloy, PhD dissertation in Physics, University of California Davis, Davis (2005).
[2] M. Hupalo, S. Kremmer, V. Yeh, L. Berbil-Bautista, E. Abram, M.C. Tringides, Uniform island height selection in the low temperature growth of Pb/Si(111)-(7 x 7), Surf. Sci., 493, (2001) 526-538.
[3] J.A. Carlisle, T. Miller, T.C. Chiang, Photoemission Study of Pb on Ge(111), Phys. Rev. B, 47, (1993) 3790-3796.
[4] J. Avila, A. Mascaraque, E.G. Michel, M.C. Asensio, Fermi surface of a triangular lattice overlayer: Pb/Ge(111) alpha-phase, J. Electron Spectrosc. Relat. Phenom., 101, (1999) 361-365.
[5] S.A. de Vries, P. Goedtkindt, P. Steadman, E. Vlieg, Phase transition of a Pb monolayer on Ge(111), Phys. Rev. B, 59, (1999) 13301-13308.
[6] L. Grill, D. Cvetko, L. Petaccia, F. Ratto, S. Modesti, Layer-by-layer growth of lead on Ge(111) at low temperatures, Surf. Sci., 562, (2004) 7-14.
[7] A. Mascaraque, J. Avila, M.C. Asensio, E.G. Michel, Band structure and gap opening in Pb/Ge(111), Surf. Sci., 402, (1998) 742-745.
[8] A. Mascaraque, J. Avila, M.C. Asensio, E.G. Michel, Electronic band structure of Ge(111)(3 x 3)-Pb, Surf. Sci., 433, (1999) 337-341.
[9] A. Ohiso, Y. Sugimoto, M. Abe, S. Moritai, Tip-induced local reconstruction on the Pb/Ge(111) surface using frequency modulation atomic force microscopy, Jpn. J. Appl. Phys. Part 1 - Regul. Pap. Brief Commun. Rev. Pap., 46, (2007) 5582-5585.
[10] M.F. Reedijk, J. Arsic, D. Kaminski, P. Poodt, H. Knops, P. Serrano, G.R. Castro, E. Vlieg, Melting behavior of the beta-Pb/Ge(111) structure, Phys. Rev. B, 67, (2003) 165423 5.
[11] Y. Sato, S. Chiang, Growth and morphology of Pb phases on Ge(111), J. Vac. Sci. Technol. A, 35, (2017) 061405.
[12] R.G. Zhao, Y. Zhang, W.S. Yang, Intermixing at Pb/Ge(111) and Pb/Ge(001) Interfaces Studied with Electron-Energy-Loss Spectroscopy, Phys. Rev. B, 48, (1993) 8462-8465.
[13] G. Benedek, I.Y. Sklyadneva, E.V. Chulkov, P.M. Echenique, R. Heid, K.P. Bohnen, D. Schmicker, S. Schmidt, J.P. Toennies, Phonons and electron-phonon anomalies in ultra-thin Pb films on Si(111) and Ge(111), Surf. Sci., 678, (2018) 38-45.
[14] P. Cudazzo, G. Profeta, A. Continenza, Low temperature phases of Pb/Si(111) and related surfaces, Surf. Sci., 602, (2008) 747-754.
[15] O. Custance, J.M. Gomez-Rodriguez, A.M. Baro, L. Jure, P. Mallet, J.Y. Veuillen, Low temperature phases of Pb/Si(111), Surf. Sci., 482, (2001) 1399-1405.
[16] M. Jalochowski, Si(111)-(6 x 6)Au surface morphology and nucleation of Pb at low temperature, Progress in Surface Science, 74, (2003) 97-107.
[17] C.A. Jeffrey, R. Feng, E.H. Conrad, P.F. Miceli, C. Kim, M. Hupalo, M.C. Tringides, P.J. Ryan, The growth of Pb nanocrystals on Si(111)7 x 7: Quantum size effects, Superlattices and Microstructures, 41, (2007) 168-177.
[18] W.J. Li, Y.J. Sun, X.G. Zhu, G. Wang, Y.F. Zhang, J.F. Jia, X.C. Ma, X. Chen, Q.K. Xue, Growth and Stability of Ultra-Thin Pb Films on Pb/Si(111)-alpha (root 3 x root 3), Surface Review and Letters, 18, (2011) 77-82.

[19] F. Palmino, P. Dumas, P. Mathiez, C. Mouttet, F. Salvan, U. Kohler, Scanning Tunneling Microscopy Investigations of Pb/Si(111), Ultramicroscopy, 42, (1992) 928-932.
[20] J. Slezak, P. Mutombo, V. Chab, STM study of a Pb/Si(111) interface at room and low temperatures, Phys. Rev. B, 60, (1999) 13328-13330.
[21] L. Huang, C.Z. Wang, M.Z. Li, K.M. Ho, Coverage-Dependent Collective Diffusion of a Dense Pb Wetting Layer on Si(111), Physical Review Letters, 108, (2012) 026101.
[22] M. Hupalo, M.C. Tringides, Ultrafast kinetics in Pb/Si(111) from the collective spreading of the wetting layer, Phys. Rev. B, 75, (2007) 235443.
[23] Z. Kuntova, M. Hupalo, Z. Chvoj, M.C. Tringides, Non-classical kinetics processes and morphologies in QSE driven growth in Pb/Si(111), Surf. Sci., 600, (2006) 4765-4770.
[24] K.L. Man, M.C. Tringides, M.M.T. Loy, M.S. Altman, Anomalous Mass Transport in the Pb Wetting Layer on the Si(111) Surface, Physical Review Letters, 101, (2008) 226102.
[25] K.L. Man, M.C. Tringides, M.M.T. Loy, M.S. Altman, Superdiffusive Motion of the Pb Wetting Layer on the Si(111) Surface, Physical Review Letters, 110, (2013) 036104.
[26] T. Nakamura, A. Takayama, R. Hobara, D.V. Gruznev, A.V. Zotov, A.A. Saranin, S. Hasegawa, Superconducting single-atomic-layer Tl-Pb compounds on Ge(111) and Si (111) surfaces, Applied Surface Science, 479, (2019) 679-684.
[27] M.M. Ozer, Y. Jia, B. Wu, Z.Y. Zhang, H.H. Weitering, Quantum stability and reentrant bilayer-by-bilayer growth of atomically smooth Pb films on semiconductor substrates, Phys. Rev. B, 72, (2005) 113409.
[28] X.Y. Ren, H.J. Kim, S. Yi, Y. Jia, J.H. Cho, Spin-orbit coupling effects on the stability of two competing structures in Pb/Si(111) and Pb/Ge(111), Phys. Rev. B, 94, (2016) 075436.
[29] L. Seehofer, D. Daboul, G. Falkenberg, R.L. Johnson, STM Study of the Incommensurate Structures of Pb on Ge(111) and Si(111) Surfaces, Surf. Sci., 307, (1994) 698-703.
[30] L. Seehofer, G. Falkenberg, D. Daboul, R.L. Johnson, Structural Study of the Close-Packed 2-Dimensional Phases of Pb on Ge(111) and Si(111), Phys. Rev. B, 51, (1995) 13503-13515.
[31] G. Ballabio, G. Profeta, S. de Gironcoli, S. Scandolo, G.E. Santoro, E. Tosatti, Disproportionation phenomena on free and strained Sn/Ge(111) and Sn/Si(111) surfaces, Physical Review Letters, 89, (2002) 126803.
[32] S.M. Binz, M. Hupalo, M.C. Tringides, Height-dependent nucleation and ideal layer by layer growth in Pb/Pb(111)/Si(111), Phys. Rev. B, 78, (2008) 193407.
[33] S.M. Binz, M. Hupalo, M.C. Tringides, Quantum size effect dependent critical size cluster and finite size effects, Journal of Applied Physics, 105, (2009) 094307.
[34] K. Budde, E. Abram, V. Yeh, M.C. Tringides, Uniform, self-organized, seven-step height Pb/Si(111)-(7X7) islands at low temperatures, Phys. Rev. B, 61, (2000) 10602-10605.
[35] T.L. Chan, C. Wang, M. Hupalo, M. Tringides, K. Ho, Quantum size effect on the diffusion barriers and growth morphology of Pb/Si(111), Physical Review Letters, 96, (2006) 226102.
[36] H. Hattab, M. Hupalo, M.T. Hershberger, M.H. von Hoegen, M.C. Tringides, A combined STM and SPA-LEED study of the "explosive" nucleation and collective diffusion in Pb/Si(111), Surf. Sci., 646, (2016) 50-55.
[37] M.T. Hershberger, M. Hupalo, P.A. Thiel, C.Z. Wang, K.M. Ho, M.C. Tringides, Nonclassical "Explosive" Nucleation in Pb/Si(111) at Low Temperatures, Physical Review Letters, 113, (2014) 236101.

[38] A. Menzel, M. Kammler, E.H. Conrad, V. Yeh, M. Hupalo, M.C. Tringides, Kinetics measurements of Pb island growth on Si(111), Phys. Rev. B, 67, (2003) 165314.
[39] M. Yakes, M. Hupalo, M.A. Zaluska-Kotur, Z.W. Gortel, M.C. Tringides, Low-temperature ultrafast mobility in systems with long-range repulsive interactions: Pb/Si(111), Physical Review Letters, 98, (2007) 135504.
[40] M.F. Reedijk, J. Arsic, D. Kaminski, P. Poodt, J.W.M. van Kessel, W.J. Szweryn, H. Knops, E. Vlieg, New (root 3 x root 3)R30 degrees phase of Pb on Ge(111) and its consequence for the melting transition, Physical Review Letters, 90, (2003) 056104.
[41] C.A. Jeffrey, E.H. Conrad, R. Feng, M. Hupalo, C. Kim, P.J. Ryan, P.F. Miceli, M.C. Tringides, Influence of quantum size effects on island coarsening, Physical Review Letters, 96, (2006) 106105.
[42] M.C. Tringides, M. Jalochowski, E.T. Bauer, Quantum size effects in metallic nanostructures, Physics Today, 60, (2007) 50-54.
[43] J.A. Venables, G.D.T. Spiller, M. Hanbucken, Nucleation and Growth of Thin Films, Reports on Progress in Physics, 47, (1984) 399-459.
[44] J. Villain, A. Pimpinelli, L. Tang, D. Wolf, Terrace Sizes in Molecular Beam Epitaxy, Journal De Physique I, 2, (1992) 2107-2121.
[45] A. Zangwill, Physics at Surfaces, Cambridge University Press, Cambridge, (1988).
[46] M. Zinkeallmang, L.C. Feldman, M.H. Grabow, Clustering on Surfaces, Surface Science Reports, 16, (1992) 377-463.
[47] K. Stolt, W.R. Graham, G. Ehrlich, Surface Diffusion of Individual Atoms and Dimers: Re on W(211), Journal of Chemical Physics, 65, (1976) 3206-3222.
[48] G. Ayrault, G. Ehrlich, Surface Self-Diffusion on a FCC Crystal: Atomic View, Journal of Chemical Physics, 60, (1974) 281-294.

5 ISLAND HEIGHT VERIFICATION

5.1 Introduction

In the calculations presented in chapter 4, the number used for island heights was a conservative estimate based on Pb/Si(111) experiments [1-4]. The obvious method of obtaining precise island heights would be imaging using the STM, but there were several issues that prevented its use for such purposes.

Firstly, the STM was not fully operational and had very poor resolution, making it unsuitable for taking high quality data. Secondly, it was impossible to properly transfer samples with Pb islands between the LEEM and the STM. Since the transfer bars do not have a cooling system, the samples would heat towards room temperature during the transfer process. While this is not too much of an issue on its own, as islands should exhibit some height selection at room temperature, the bigger issue is that the islands will coarsen to sizes that are too large for the STM's image size limit of 1500x1500nm. Since this process is irreversible even upon cooling back down to the original temperature, the Pb islands must be grown inside the STM itself. Our STM originally was not designed to have an evaporator in the chamber, especially with its bulky scanner that had to be removed before any deposition could happen. An evaporator was designed for the STM, but calibrating it is a lengthy task, especially because the STM cannot take images at video rate, which was the advantage the LEEM had that allowed using the $\left(\sqrt{3}\times\sqrt{3}\right)$ to (1x1) phase transition for calibration. The only other method available for calibrating an STM

evaporator would be doing an XPS scan of a layer of Pb and comparing the ratio of the areas under the Pb and Ge peaks [6, 7]. This is a relatively difficult process requiring careful background subtraction and curve fitting and would add to the difficulty of using the evaporator in the STM.

Since the STM was deemed to be mostly unsuitable for this purpose, it was necessary to use the LEEM instead. At first glance, the LEEM does not seem capable of measuring heights aside from telling step edges apart, since all it is doing is giving a top-down view of the sample, but the same mechanism that gives the LEEM remarkable resolution in viewing step edges can also be used for height measurements.

Since LEEM images are formed using electrons that interact with the sample surface, one can expect these interactions to affect how many electrons are reflected to create the image. These interactions depend on various factors such as the wavelength (energy) of the electron, the angle of incidence, and the penetration depth – essentially the same factors that are considered for imaging using photons. Some of these interactions also affect LEED patterns, changing the intensity and shape of certain spots that can be analyzed with a high-resolution LEED instrument [3, 8, 9], which is not available at our laboratory. One important parameter regularly controlled during LEEM operations is one of the factors that were just mentioned, and that is the electron wavelength, controlled by the start voltage. By varying the start voltage and observing the changes in the contrast of a feature of interest, it is possible to extract information about the feature, as discussed by Altman *et al*. for contrast in step edges [10] and for contrast due to QSE [5]. This effect of QSE on contrast occurs due to interference of electrons as they are reflected by multiple layers in a thin film (or islands), with characteristic peaks under certain resonant conditions determined by the number of layers. This makes it possible to determine the

heights of our Pb islands, by observing the interference of the electrons as their wavelength is changed, i.e., by measuring an intensity vs. voltage (IV) curve of the islands.

5.2 Discussion of Quantum Size Contrast

The following discussion revolves around work done on the topic by Altman *et al*. previously mentioned [5] and is the basis for the experiments performed in this chapter. We begin with a very basic model of how an electron beam interacts with a surface.

In a vacuum, an electron's wavelength λ is related to its wave vector k and thus its energy E by the simple relation

$$k = \frac{2\pi}{\lambda} = \frac{\sqrt{2mE}}{\hbar} \tag{5.1}$$

where m is the electron's mass. An electron that is reflected by the surface will have the same wave vector (same magnitude, but direction reversed), assuming normal incidence, as should be the case for the LEEM. However, not all electrons are reflected, and they have a penetration depth according to their energy. Once inside the surface, electrons are shifted in energy according to the inner potential of the material V_0, resulting in a new wave vector

$$k' = \frac{\sqrt{2m(E+V_0)}}{\hbar}. \tag{5.2}$$

If the thin film that the electron penetrates has a thickness d, then upon being reflected at the other boundary and traveling back to the surface, the electron will have a phase shift of

$$\Delta\phi = k' \times 2d = \frac{2d}{\hbar}\sqrt{2m(E+V_0)}. \tag{5.3}$$

This gives an easy way to calculate the conditions in which the reflected electrons will constructively or destructively interfere with each other. Conversely, one can measure the interference patterns of a surface layer and match the positions of the peaks with predicted curves generated by equation 5.3 to obtain the thickness of the layer.

Unfortunately, this model has some limitations, which makes it a somewhat usable but poor model to apply to features of sufficiently large thicknesses. This is because the model assumes that the thin film is a continuous, uniform region with a constant inner potential with defined boundaries at the start and end of the film. This may apply for thin films of a single layer, with the atoms making up the surface providing a potential well that can be approximated by an inner potential. When a second layer is involved, then an additional boundary is introduced at the interface between the two layers, from which the electrons can be reflected. These electrons will pick up a phase shift corresponding to $2d$ as usual, while the electrons that traverse through both layers will pick up a phase shift corresponding to $4d$. These will interfere with each other as well as the electrons reflected from the surface itself, and it is clear that such calculations will become increasingly more complex as more layers are introduced. More critically, this model does not provide a way to calculate the reflectivity and transmittivity at each boundary due to its assumptions of a continuous, uniform region. This prevents the model from predicting the total intensity of the reflected electrons and therefore the contrast of the surface, instead giving only the positions of maxima and minima in the contrast. Given the square root dependence of the electron phase shift on the electron energy, the model predicts that each subsequent peak will become farther and farther away with increasing energy. However, according to empirically derived IV curves for many-layer Cu films on W(110) in [5], the peaks' positions are about the

same distance apart, clearly showing that this model is insufficient. The model should still be accurate enough to determine the thicknesses of thin films consisting of one or two layers, but a better model is required for analyzing the contrast of the Pb islands studied in this paper.

We can construct an improved model by using a familiar quantum mechanical problem of particles tunneling through a 1D finite potential well. For an island of n layers, each atomic layer is modeled by two potential wells of different depths and widths representing the potential of the atomic nucleus and the potential of the gap between layers, as shown in Figure 5.1. This is a slightly modified version of the Kronig-Penney model, which is normally used to represent a periodic lattice, with the periodicity of the layers truncated on either end by the vacuum level and the substrate level, which we assume to extend infinitely in space in their respective directions with an inner potential V_0. In addition to the first boundary between the vacuum and the first layer, each layer adds 2 more boundaries, for a total of $2n + 1$ boundaries for a thin film

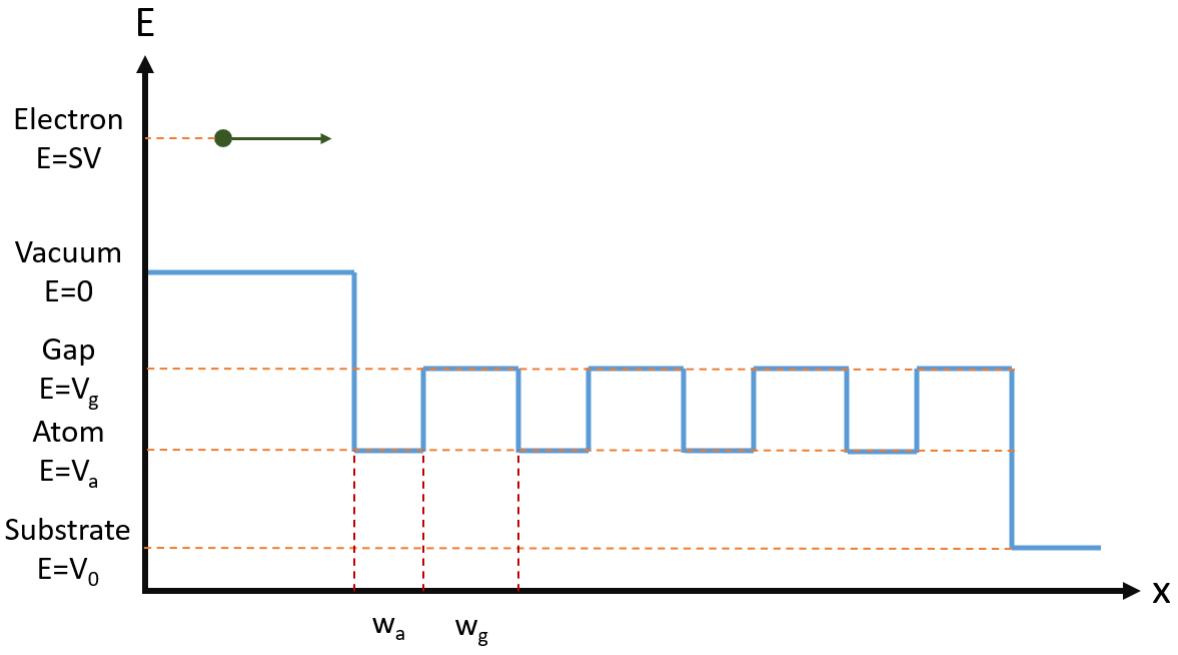

Figure 5.1. The modified Kronig-Penney model for a thin film consisting of n=4 layers of material on top of a substrate.

consisting of n layers. In each region between boundaries, the electron wavefunctions have the form

$$\psi(x) = Ae^{ikx} + A'e^{-ikx} \tag{5.4}$$

where $k = \frac{\sqrt{2m(E-U)}}{\hbar}$ for electron energy E and potential of the region U; these wavefunctions and their derivatives must be continuous at each boundary, giving a total of $4n + 2$ boundary conditions that must be satisfied. For the first boundary, equation 5.4 can be written in the form

$$\psi_{vacuum} = e^{ik_0 x} + re^{-ik_0 x} \tag{5.5}$$

where $k_0 = \frac{\sqrt{2mE}}{\hbar}$ as the energy of the electron in the vacuum, while the first coefficient is taken as 1 since it represents the full electron beam incident on the sample, and the second coefficient r is the reflectivity coefficient, which is related to the intensity of the electrons that will form the LEEM image by $I \propto |r^2|$. This is the critical coefficient that we must calculate using the model; all the other coefficients are irrelevant beyond their use in calculating the reflectivity coefficient.

To solve these systems of equations, which would otherwise be extremely tedious, if not impossible, by hand, a MATLAB script was written to construct the series of equations in matrix form according to the model using the set of parameters $(n, w_a, w_g, V_a, V_g, V_0)$ as input and then numerically solve for the intensity. The full MATLAB codes used for this purpose are provided in Appendix C. These codes were verified to perform the calculations properly by reproducing IV curves simulated by Altman *et al*. in [5] to fit empirically measured IV curves for Cu/W(110), using their simulation parameters. Their simulated curves are displayed alongside curves produced using the MATLAB code in Figure 5.2, showing a perfect match for each layer thickness.

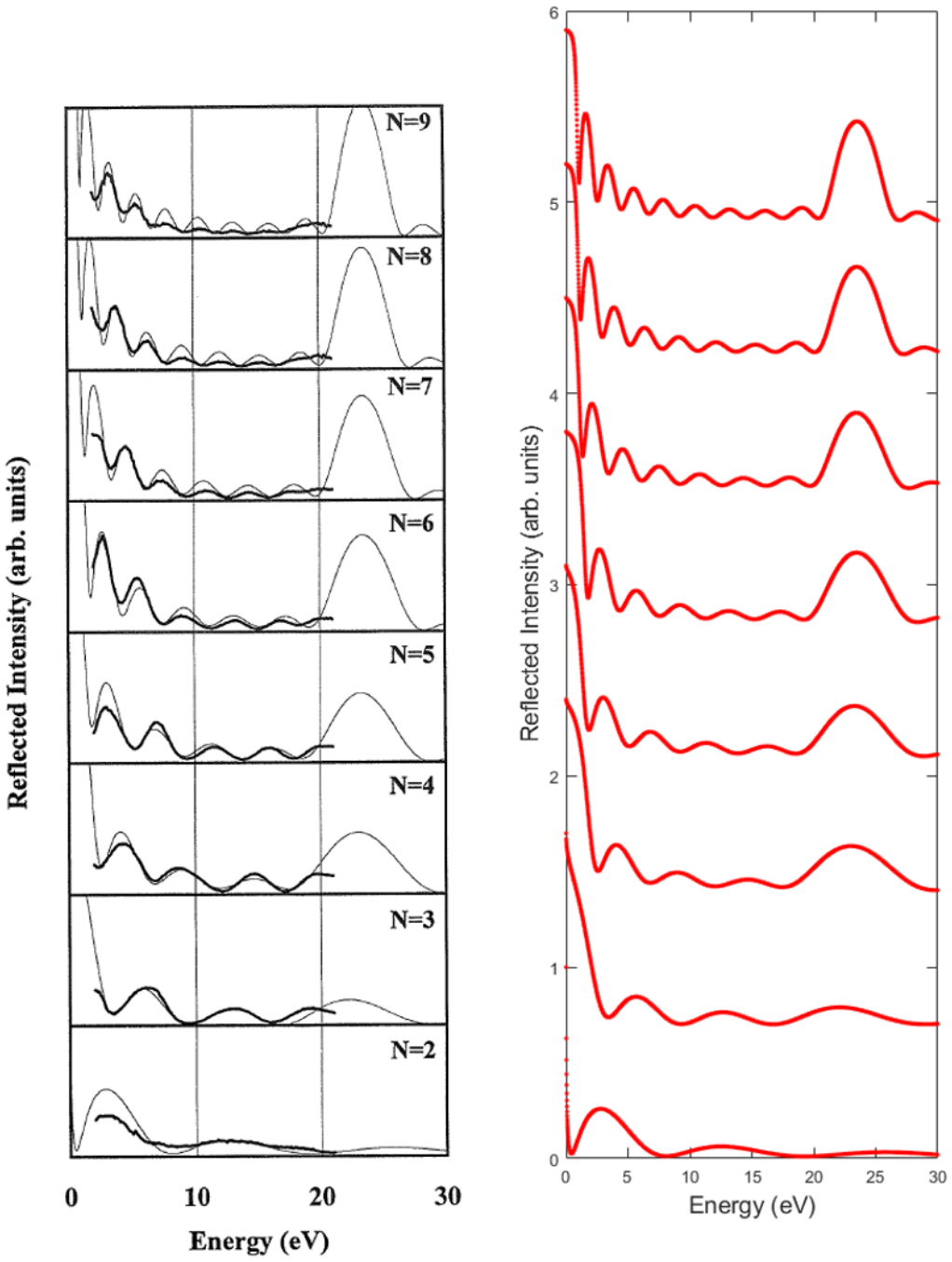

Figure 5.2. Left: IV curves for Cu/W(110) (thick lines) with curves produced using the Kronig-Penney model (thin lines) for various number of layers, republished with permission of World Scientific Publishing Co. PTE. LTD., from LEEM phase contrast, M.S. Altman, W.F. Chung, C.H. Liu, Surface Review and Letters, 5, (1998) [5]; permission conveyed through Copyright Clearance Center, Inc. Right: Independent reproduction of the simulated curves on the left, using parameters given in [5] as inputs for custom code written in MATLAB. The locations and number of peaks match exactly, proving that the code works properly.

Thus, with the Kronig-Penney model, it becomes possible to analyze IV curves obtained from the Pb islands and to fit the simulated curves to determine the island heights. One major hurdle, however, is obtaining the parameters themselves. It was noted in [5] that the parameters were chosen via educated guessing within certain limits set by some known theoretical/experimental values until the simulated IV curves gave the best fit. The first constraint is the layer thickness t, which must be the sum of w_a and w_g; for Pb layers, $w_a + w_g = 0.286nm$ [3]. The second constraint involves the potential of the atom and the gap, because the average of the two must equal the inner potential V_{avg} of the atom, or $V_{avg} = \frac{w_a V_a + w_g V_g}{w_a + w_g}$. The inner potentials for various materials exist in the literature for both empirically derived values as well as theoretical ones. For Pb, the inner potential seems to be around -13V [11, 12], and for Ge the inner potential was calculated to be somewhere between -13.8 and -14.9V depending on the details of the simulation [13]. There does not seem to be any literature for the size or energy depth of the Pb atom or gap in the context of the KP model, since these values are likely only useful for the model itself, and this technique is not widely used. It is expected that the true values for the potentials would be slightly different from the values just listed, since the values were derived under simpler conditions not involving a combined Pb/Ge system. Even with these known values to help constrain the KP parameters, fitting simulated curves to island IV curves would still require trying many combinations of parameters to get the best fit, which poses the greatest drawback to this method.

Before any serious curve-fitting attempt was made, many parameters were tested to see their effects on the simulated IV curves, so that the curve-fitting process could be streamlined. Generally, the simulations produced two peaks of interest, characterized by their high intensity

compared to the peaks between them, and they do not change positions regardless of the number of layers. The higher-energy characteristic peak is called the Bragg peak, which coincides with the edge of the Brillouin Zone and satisfies the Bragg condition [5], while the lower-energy peak is unnamed. For n layers, it was found that the simulations produce n-1 peaks between the two characteristic peaks. The ratio between w_a and w_g seems to change the ratio of the heights of the two characteristic peaks but seems to be indirectly coupled to the inner potential, since w_a and w_g need to be readjusted to maintain the same height ratio if the inner potential is changed. The inner potential of the Pb layers itself seems to mainly affect the location of the characteristic peaks and is likely the easiest value to tune since the peak locations do not seem to be coupled with any other parameter. Finally, the inner potential of the substrate seems to affect the overall intensity of the reflected electrons, changing the amplitude of the oscillations.

5.3 Experimental Procedures

The Pb islands were grown using the same procedures described in chapter 4. However, instead of continuing deposition to high coverages, deposition was stopped once the islands were large enough for easier processing for taking IV curve measurements. The electron beam intensity and the camera's gain were adjusted so that the highest intensity remained below the pixel intensity's saturation value of 255 for the entire range of start voltages to be sampled. A surface feature was identified that could be easily located and focused, since maintaining proper focus of the objective lens was critical for measuring the correct intensity of the islands. Usually, the chosen reference feature was a medium density step defect, as discussed in chapter 3,

because of its size and sharp boundary that made it an ideal candidate for a reference point. Because the start voltage affected the velocity of the electrons, different start voltages required different objective lens values to be focused. Therefore, the objective lens was adjusted for every 1-volt increment of the start voltage. Each image used for the data points on the IV curve was averaged over 16 or 32 frames depending on the level of noise, and care had to be taken to measure the images between periodic vibrations caused by the liquid nitrogen.

The image taking process was done twice – once for the islands, and a second time for the wetting layer. For the wetting layer IV curve, the overall image intensity was increased to the point that the islands' brightness was saturating, since the wetting layer was much dimmer than the islands and needed the intensity boost for improved signal-to-noise ratio. The relative intensity was the reason why both IV curves could not be taken on a single pass in some experiments. Due to the very long time required to take both sequences of images, some electron beam damage was unavoidable, but it mostly affected the wetting layer and not the islands themselves.

The entire data processing procedure to generate the IV curve had to be performed manually. Because the sample drifted in position over time, any automated script would have to track the island (or a chosen reference point) over time. The intensities of the islands and the wetting layer varied to the point that at some electron energies, the islands were mostly indistinguishable from the wetting layer aside from some subtle outlines that a simple script would be unable to recognize. The areas inside the islands had to be isolated and cut out of the images to be averaged over by the image processing script. Due to the tedious nature of manually processing and analyzing the data, IV curves were deemed unsuitable for generating histograms

of island height distribution, which would require processing IV curves for every island in the images; they were simply used to verify the height of a representative island at different temperatures.

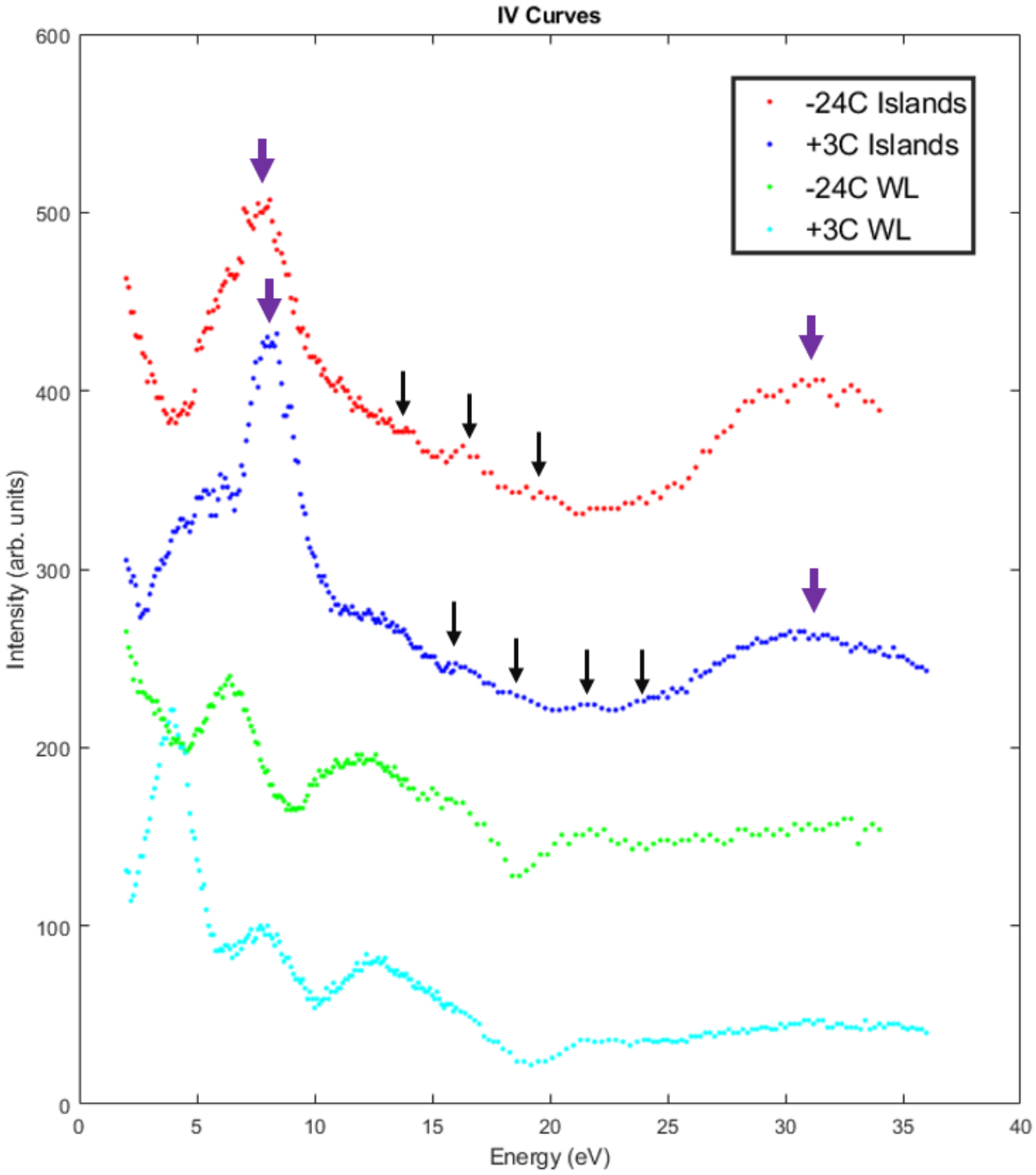

Figure 5.3. IV Curves for Pb/Ge(111) islands and their wetting layers at two different temperatures. The thick, purple arrows mark the characteristic (major) peaks, while the thinner, black arrows mark the minor peaks.

5.4 Results and Discussion

Figure 5.3 shows the IV curves taken for Pb islands and their wetting layers grown at -24°C and at 3°C, the two extremes of the temperature ranges explored in chapter 4. The two characteristic peaks (around 8eV and 32eV) are easily identified and thus make good candidates for the first iteration of basic curve fitting. These peaks are marked with the thick, purple arrows in Figure 5.3. As mentioned before, these two peaks do not change positions regardless of the number of layers and appear to arise from intrinsic properties of Pb(111) layers including the layer thickness and the inner potential.

The position of the Bragg peak at 32V makes a good check for some of the parameter values discussed in the previous section. Because of the periodicity introduced by the multiple Pb layers, a Brillouin Zone can be defined, with a 1-dimensional reciprocal lattice with a lattice spacing of $k = \frac{2\pi}{d}$, where $d = 0.286nm$ is the thickness of a single layer. Electrons entering with the same wave vector will satisfy the Bragg condition and constructively interfere, which should give rise to an interference peak. Using the relation $E = \frac{\hbar^2 k^2}{2m}$, we get that the energy corresponding to $d = 0.286nm$ is 18.39eV. At first glance, this does not seem to correspond to the 32eV location of the Bragg peak, but this is due to the inner potential of the Pb layer, which modifies the electron's energy inside the crystal, $E_{crystal} = E_{vacuum} + V_{inner} + \phi$, and therefore its wave vector. The inner potential of Pb as mentioned previously is around -13V, and the final term ϕ is the work function difference between the cathode and Pb layer. The LaB_6 cathode was reported to have a work function of 2.3-2.4eV [14], while Pb(111) was shown to have a work function that varies depending on the number of layers, with values mostly between

3.5 and 3.9eV as well as over 4.0eV for bulk Pb(111) [15, 16]. For simplicity we will take ϕ to be -1.6V. Entering all of these values and solving for E_{vacuum}, we get 32.99eV, which is very close to the peak of the experimental curve. The small discrepancy can be explained by the inner potential, which had to be shifted slightly from the values taken from [11, 12] for proper IV curve fitting (to be discussed later in this section). Regardless, the good agreement between the calculated and experimental location of the Bragg peak confirmed that the value for the inner potential as well as the layer thickness was correct (in case there may have been relaxation of interlayer distances between Pb layers as was observed in [17]).

The oscillations between the major peaks are much harder to identify, and some of them are marked by the thin, black arrows in Figure 5.3. It was expected that the minor peaks would have a poor intensity compared to the rest of the data, since this was also the case for IV curves of Pb/Ni(111) [17]. Indeed, it appears that much of the Pb IV curves are dominated by what are likely to be band structure effects, since other systems not involving Pb seem to have peaks that can be more easily distinguished [5, 18]. Fortunately, one does not require every peak to properly identify the number of layers – the distances and positions of the peaks are rarely shared for oscillations of different layers, so just a few peaks can uniquely identify a particular layer number.

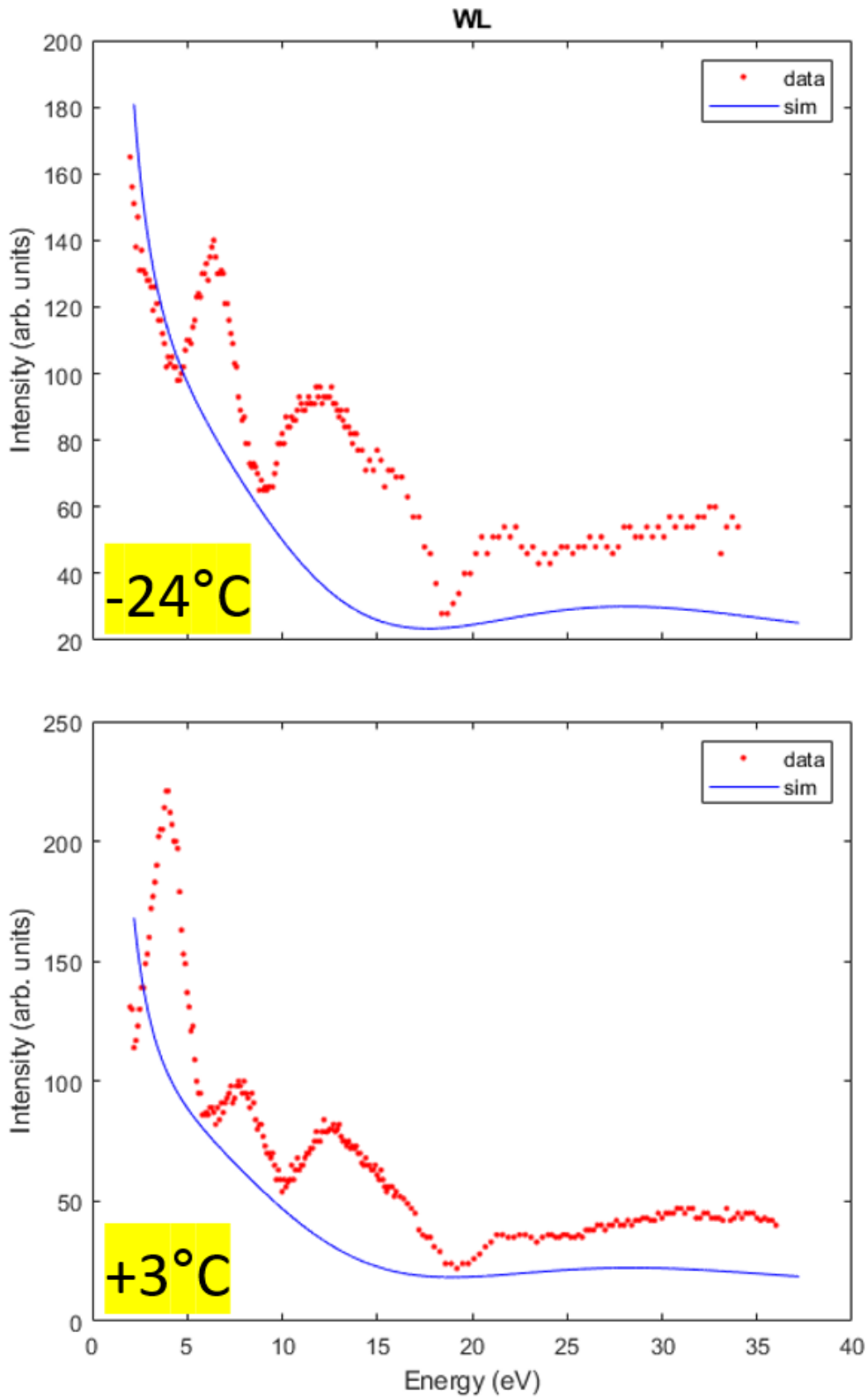

Figure 5.4. IV curves of the wetting layer with KP simulation curves superimposed, showing a match with the overall intensity trend, but no match at all with the peaks.

Moving on from the island IV curves, we next look at the wetting layer IV curves. The curves for the two temperatures look very different below 10eV, while they exhibit similar humps between 10 and 20eV, as well as a mostly flat plateau after the 20eV valley. What is interesting to note is that the 10-20eV hump also seems to be somewhat present on the island IV curves, meaning it most likely arises as a band structure effect and is responsible for obscuring the oscillations within that energy range. The peaks below 10eV also do not seem to correspond to any interference effect caused by the wetting layer itself, since a single layer should not give rise to that many peaks. The curves simulated by the KP model for the wetting layer are shown in Figure 5.4, and indeed one can see that the peaks are nowhere to be found on the simulated curve, which only manages to simulate the overall trend of the intensity variation, which drops rapidly at first before showing a slight rebound beyond 20eV.

Because the wetting layer does not conform to any KP simulation, the only conclusion that can be drawn is that the model is highly unsuited for the wetting layer. This makes sense because the wetting layer is known to be amorphous and almost liquid-like, unlike the islands which are crystalline Pb(111) with a definite, ordered structure. The wetting layer's local properties likely vary heavily based on the arrangement of the Pb atoms within that local region, so no single inner potential or relative atom-gap distance will be sufficient for modeling such a nonuniform system. An STM image of the wetting layer at room temperature, shown in Figure 5.5, also seems to imply that the wetting layer has many single-layer, pancake-like islands, meaning the proper KP simulation should be a hybrid of 1- and 2-layer curves, but hybrid curves were also found to be a poor fit with the experimental curves. It may also be the case that the pancake-like islands are simply features specific to a nonclassical, room temperature system and

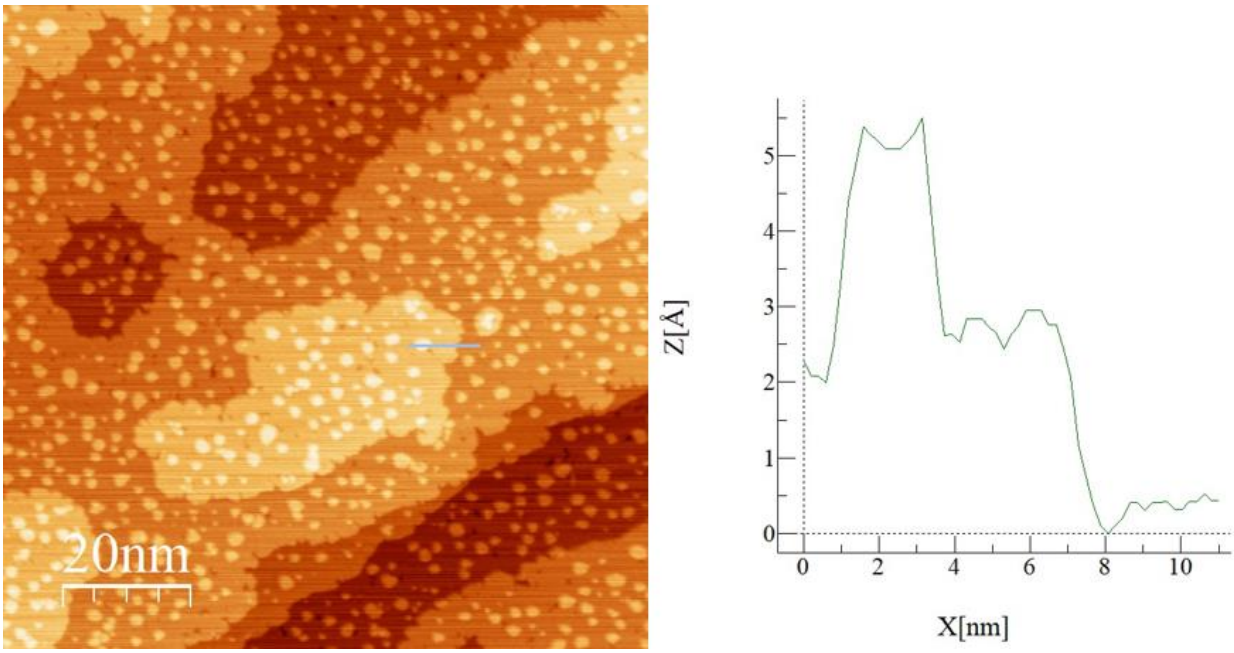

Figure 5.5. Topographical STM image of the Pb wetting layer at room temperature, along with a profile graph across the light-blue line. The heights of the islands and the steps all differ by single layers. Bias voltage is 1.1142V, and set point is 0.9nA.

may not apply to lower temperatures. Regardless, the conclusion is that the wetting layer must be treated as part of the substrate rather than an additional layer under the crystalline islands, offering some correction to the inner potential of Ge that must be determined through best fit, as well as an undetermined background effect that should arise from its amorphous nature.

Next, we apply the KP model to the island IV curves, and we obtain the following results. We first discuss the curve fitting done for the -24°C island, for which the best fit appears to be for a 7-layer island, as illustrated in Figure 5.6. The figure also shows fitting attempts for 5 layers as well as 9 layers, showing how they were not a good fit to the data. As mentioned previously, the two major peaks are not dependent on the number of layers, so the locations of the major peaks always matched. The positions of the minor peaks, on the other hand, clearly differ due to

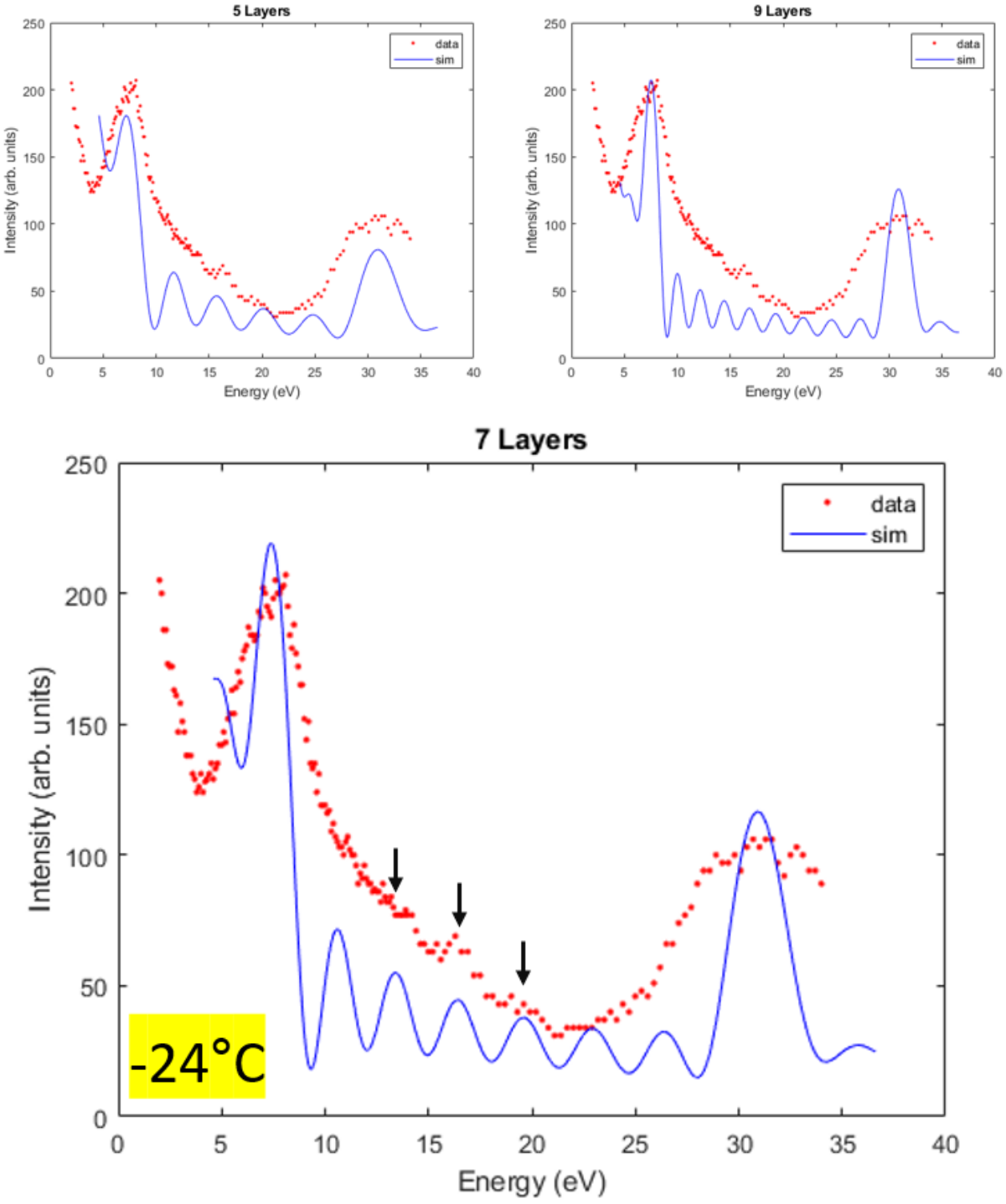

Figure 5.6. Simulated KP IV curves for 5, 7, and 9 layers placed with the data for the -24°C island, illustrating how the 7-layer curve has the best fit. The arrows mark the three minor peaks used for fitting.

the n-1 oscillations between the major peaks, and we can see from Figure 5.6 that the minor peaks simulated by the 5-layer model do not match the peaks on the data. The peaks for the 9-layer simulation are closer and seem to align with one of the identified peaks but not the other two, although one of them is close.

Beyond the positions of the peaks, the simulated curves, even the best fit at 7 layers, depart from the overall shape of the data. This is especially apparent from the widths of the two major peaks, which are much broader in the data compared to the simulations. There is yet no explanation for this difference aside from the possibility of instrumental broadening due to the spread of electron energies. Attempts were made to broaden the peaks in the simulations without success, meaning this was not a problem with parameter selection and indeed an issue on the experimental side. The simulation is also very inaccurate at low electron energies, but this was expected since other measurements using this method showed similar inaccuracies in this range [5, 17, 18]. These inaccuracies probably arise from electron interactions that cannot be modeled by the KP model or from the relative simplicity of the model itself.

For the 3°C island, the curve fitting process became more complicated because no single-layer simulation would fit to the data. As seen in Figure 5.7, the KP curves for 10 and 11 layers do not match with all the identified peaks, and this was the case for other numbers of layers that were simulated. The next logical step was to hypothesize that the island being imaged consisted of two different heights, either due to an incomplete top layer [1, 19], or due to the island growing over a step edge [20]. At this temperature, the islands were large enough to have a high likelihood of

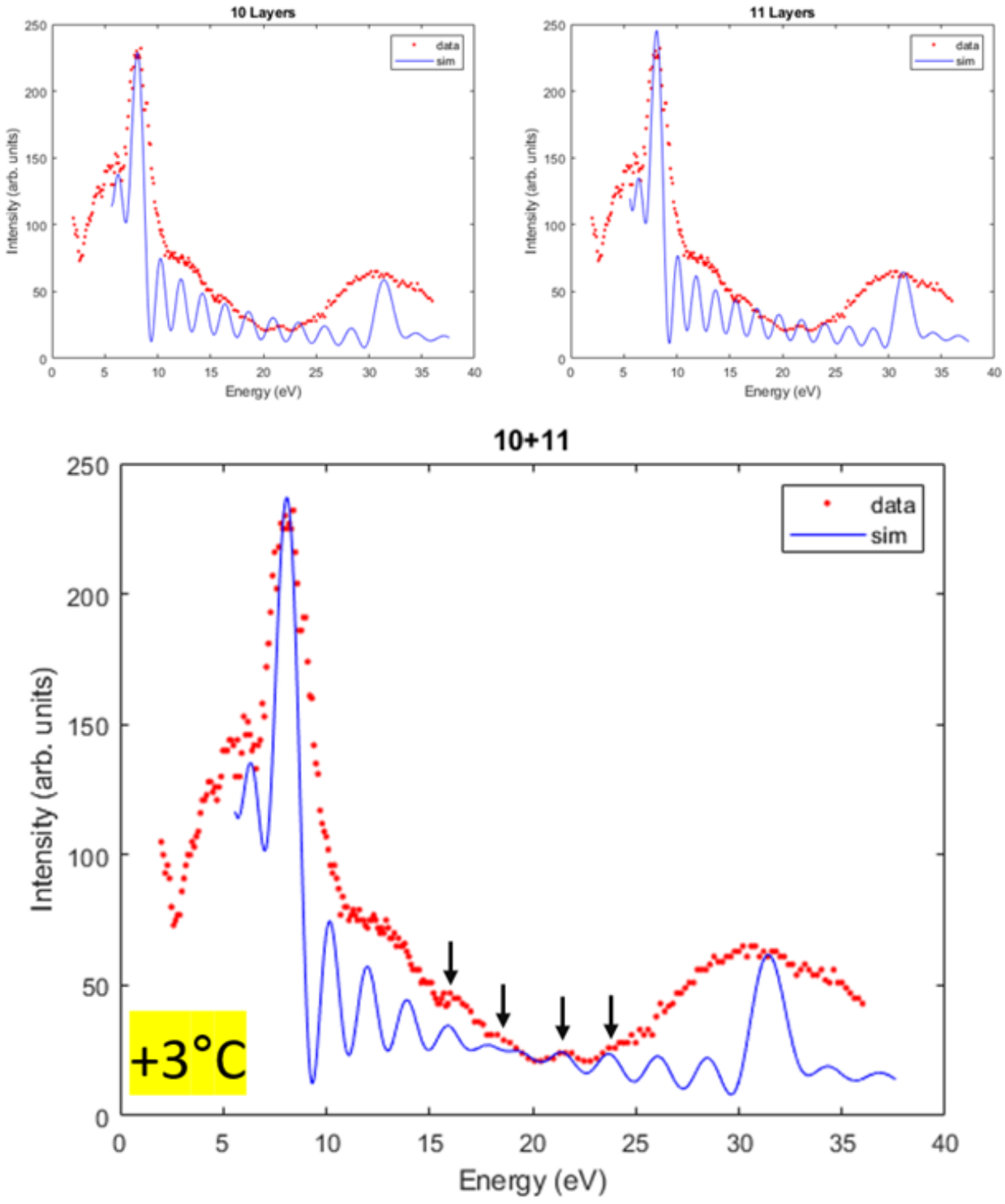

Figure 5.7. Simulated KP IV curves for 10, 11, and 10+11 hybrid layers placed with the data for the +3°C island, illustrating how the hybrid layer curve has the best fit. The arrows mark the four minor peaks used for fitting.

either possibility occurring. Since the experimental IV curve was obtained by averaging over a large portion of the island, it was reasonable to deduce that there was a hybridization of two different curves. There is a chance that islands growing over a step edge would split into two islands of stable heights instead of staying as merged islands with partial instability [17], but this likely requires certain conditions such as island dimensions (large islands with narrow step-edge bridge), or island mobility (islands can probably only move at higher temperatures when they are more liquid). Ultimately, a hybrid of 10-layer and 11-layer IV curves by direct addition gave the best fit to the experimental data as Figure 5.7 shows, with the assumption that the two heights had equal weight in the hybridization. It may be possible that the -24°C island was also a hybrid but with the secondary layer so small that the secondary layer's contribution does not appear in the data (and therefore very low weight in a hybrid simulation).

The parameters used for the two KP simulations are listed in Table 5.1. The ratio of w_a and w_g is very similar, with only slight shifts needed to obtain the correct ratio of the two major peaks' heights. The inner potential of Pb also was also very similar for the two temperatures, with -12.2V used for the -24°C case and -11.7V used for the +3°C case, but the atom-gap potential ratio differed significantly, which can be attributed to the hybridization of layers in the +3°C islands, where the 10-layer side is unstable and would exhibit different properties. The inner

Table 5.1. KP simulation parameters for best fit to experimental curves.

	w_a	w_g	V_a	V_g	V_0
-24°C	0.119nm	0.167nm	-14.50V	-10.56V	-16V
+3°C	0.115nm	0.171nm	-12.80V	-10.96V	-16V

potential differs from the -13V value derived from [11, 12], but this is likely because the KP model arbitrarily separates the atom and the gap potentials into two boxes, which is simple but ultimately unrealistic. As for the inner potential of the substrate, a large departure from the -13.8 to -14.9V range for germanium derived from [13] was expected because the wetting layer had to be combined with the germanium as a single substrate due to its nonconformity to the KP model, as discussed previously. The substrate inner potential at least did not affect the peak positions or spacing, so we fortunately did not need a better model for the substrate. Lastly, the simulated KP curves had to be shifted to the right by about 1.6V to account for the work function difference between the LaB_6 cathode and the Pb surface, as discussed for the Bragg peak location.

5.5 Conclusion

One of the reasons why the STM makes a great complementary instrument to the LEEM is that the STM can measure heights of the surface features, covering the LEEM's weakness in this matter. However, in this chapter we have seen that the LEEM is not completely helpless and can provide height measurements for certain features due to the marvels of quantum size effect. By modeling the Pb/Ge(111) islands using the Kronig-Penney model according to work done by Altman *et al*. [5], we were able to simulate oscillations in electron intensity with respect to electron energy and match them with the oscillations observed experimentally from the Pb islands to verify their heights.

The curve-fitting process turned out to be complicated, with many parameters to be considered in simulating the curves, and the experimental curves showing many unwanted

features due to effects not considered by the KP model. However, fitting was successfully performed, and we were able to measure a height of 7 layers for an island at -24°C and a hybrid height of 10 and 11 layers for an island at +3°C due to the island growing over a step edge. Overall, we saw that taking height measurements using LEEM phase contrast is a viable method when direct, topographical imaging is unavailable, but only for a few, select features of interest due to the difficulty of applying the technique. As a final note, all the MATLAB codes used in performing the IV curve analyses are provided in Appendix C.

References

[1] T.L. Chan, C. Wang, M. Hupalo, M. Tringides, K. Ho, Quantum size effect on the diffusion barriers and growth morphology of Pb/Si(111), Physical Review Letters, 96, (2006) 226102.
[2] Y. Han, M. Hupalo, M.C. Tringides, F. Liu, Quantum modulation of island nucleation on top of a metal nanomesa, Surface Science, 602, (2008) 62-66.
[3] M. Hupalo, S. Kremmer, V. Yeh, L. Berbil-Bautista, E. Abram, M.C. Tringides, Uniform island height selection in the low temperature growth of Pb/Si(111)-(7 x 7), Surface Science, 493, (2001) 526-538.
[4] M.M. Ozer, Y. Jia, B. Wu, Z.Y. Zhang, H.H. Weitering, Quantum stability and reentrant bilayer-by-bilayer growth of atomically smooth Pb films on semiconductor substrates, Physical Review B, 72, (2005) 113409.
[5] M.S. Altman, W.F. Chung, C.H. Liu, LEEM phase contrast, Surface Review and Letters, 5, (1998) 1129-1141.
[6] C.H. Mullet, B.H. Stenger, A.M. Durand, J.A. Morad, Y. Sato, E.C. Poppenheimer, S. Chiang, Growth and phase transformations of Ir on Ge(111), Surface Science, 666, (2017) 96-103.
[7] Y. Sato, Thin Film Microscopy of Pb on Ge(111) Phase Transitions and FexNi(1-x) on Cu(111) Magnetic Surface Alloy, PhD dissertation in Physics, University of California Davis, Davis (2005).
[8] I. Bartos, M.A. Van Hove, W.F. Chung, Z. He, M.S. Altman, Ag(111) electron band structure and channeling by VLEED, Surface Science, 402, (1998) 697-700.
[9] H. Hattab, M. Hupalo, M.T. Hershberger, M.H. von Hoegen, M.C. Tringides, A combined STM and SPA-LEED study of the "explosive" nucleation and collective diffusion in Pb/Si(111), Surface Science, 646, (2016) 50-55.
[10] W.F. Chung, M.S. Altman, Step contrast in low energy electron microscopy, Ultramicroscopy, 74, (1998) 237-246.
[11] A.Z. Camino, Electronic structure, dynamics and spectroscopy of metallic nanosized systems: Pb thin overlayers and Na nanocontacts, PhD dissertation in Physics, Universidad del Pais Vasco (2011).
[12] P. Czoschke, H. Hong, L. Basile, T.C. Chiang, Quantum size effects in the surface energy of Pb/Si(111) film nanostructures studied by surface x-ray diffraction and model calculations, Physical Review B, 72, (2005) 075402.
[13] R.S. Pennington, C.B. Boothroyd, R.E. Dunin-Borkowski, Surface effects on mean inner potentials studied using density functional theory, Ultramicroscopy, 159, (2015) 34-45.
[14] H. Yamauchi, K. Takagi, I. Yuito, U. Kawabe, Work Function of LaB6, Applied Physics Letters, 29, (1976) 638-640.
[15] Y. Qi, X. Ma, P. Jiang, S.H. Ji, Y.S. Fu, J.F. Jia, Q.K. Xue, S.B. Zhang, Atomic-layer-resolved local work functions of Pb thin films and their dependence on quantum well states, Applied Physics Letters, 90, (2007) 013109.
[16] C.M. Wei, M.Y. Chou, Theory of quantum size effects in thin Pb(111) films, Physical Review B, 66, (2002) 233408.
[17] T.R.J. Bollmann, R. van Gastel, H.J.W. Zandvliet, B. Poelsema, Quantum size effects on surfaces without a projected bandgap: Pb/Ni(111), New Journal of Physics, 13, (2011) 103025.
[18] T.R.J. Bollmann, R. van Gastel, H.J.W. Zandvliet, B. Poelsema, Quantum Size Effect Driven Structure Modifications of Bi Films on Ni(111), Physical Review Letters, 107, (2011) 176102.

[19] M. Hupalo, M.C. Tringides, Ultrafast kinetics in Pb/Si(111) from the collective spreading of the wetting layer, Physical Review B, 75, (2007) 235443.
[20] S.M. Binz, M. Hupalo, M.C. Tringides, Height-dependent nucleation and ideal layer by layer growth in Pb/Pb(111)/Si(111), Physical Review B, 78, (2008) 193407.

6 PB ON OTHER GERMANIUM FACES

6.1 Introduction

While this dissertation was mostly focused on Ge(111) as the substrate due to having used Pb/Si(111) as the starting point as well as a point of comparison, the next logical step was to see how Pb would behave on the other germanium faces under similar conditions. Little research has been done for Pb on other germanium faces, especially at low temperatures, with only two such studies found for Ge(100) after some literature search [1, 2]. Other work on Pb/Ge(100) involved phases at room temperature or higher [3, 4], or theoretical calculations on atomic structures of Pb on the surface [5]. For the Ge(110) surface, the only previous studies involved other metals on Ge(110), such as Au, Ag, and Pt [6-8]. This gave further motivation for studying these systems, since it is very apparent that they are not well-understood either experimentally or theoretically.

Even before the experiments were performed, we could make some hypotheses based on the few studies that exist and on the surface symmetries of the substrates. Ge(100) has a square symmetry, as opposed to Ge(110), which has a rectangular symmetry and is thus highly anisotropic. Structures grown on Ge(110) might therefore heavily favor one direction of growth over the other due to this reduced symmetry. This was the case for the other metals mentioned previously. Pt and Au grew as 1-dimensional (1D) nanowires on the atomic scale [8], while Ag and Au grew as similar, thicker nanowires (LEEM scale) with heavily monodirectional growth [6, 7], especially for Ag. The preferred direction of growth was always along the $[1\bar{1}0]$ direction and

occurred for growth induced by both direct deposition and through coarsening by annealing. This is the characteristic behavior for 1D growth, where the island only grows along a single axis in either direction, while the other two dimensions remain constant, as opposed to 2-dimensional (2D) or 3-dimensional (3D) growth, which involves growth in two or all axes, respectively. Even Si(110) exhibits this behavior, with 1D growth of Pb islands observed on Si(110) albeit after priming the surface with some prior deposition of Au [9]. The similarities in growth modes on Ge and Si surfaces are unsurprising, given their similar symmetries. Based on these prior studies, we also expected Pb/Ge(110) to show some directional preference in growth. We hypothesized that the usual explosive nucleation of height-selected islands would occur at a critical coverage similar to Pb/Ge(111), but further growth with continued deposition would cause the nucleated islands to grow along the $[1\bar{1}0]$ direction rather than primarily along step edges or defects.

As for Ge(100), it is tempting to think that Pb would behave much like it would on Ge(111), especially since Ge(100) has even greater symmetry than Ge(111), allowing for greater freedom of movement for island growth. However, the square symmetry could also result in directional growth as on Ge(110), except in two, orthogonal directions due to the square symmetry. This has been observed to be the case for Ag/Ge(100) [6], where 1-dimensional islands would grow in either $[1\bar{1}0]$ or $[\bar{1}\bar{1}0]$ direction depending on the orientation of the (2x1) domain at the location of growth. Both scenarios should be possible, since there was a study on Pb/Si(100) in which both 1D and 2D island growths were shown to occur on the surface including height-selected islands [10], as well as other studies showing 2D growth on Si(100) but no 1D growth [11, 12]. Therefore, Pb/Ge(100) was expected to show explosive nucleation of height-selected islands that would

either show 1D growth in two possible directions, no directional preference whatsoever, or some combination of both depending on the local surface structure.

6.2 Coverage Calibration

The Ge(110) and Ge(100) samples were prepared for experiments using the cleaning procedures discussed in Chapter 3. The evaporator used for these experiments was the crucible-type evaporator, which avoided the changing-rate issue of the basket-type evaporator that was discussed in Chapter 4.

The main experimental issue that needed consideration was the calibration of the deposition rate on the two surfaces. Similar to the calibration of Pb/Ge(111) by looking for the $\left(\sqrt{3} \times \sqrt{3}\right)$ to (1x1) phase transition with well-defined boundaries in both coverage and temperature, the goal was to look for a similar, abrupt phase transition for Pb on the other surfaces that had a bright, easily-identifiable contrast.

For Pb/Ge(110), there was no literature on such phases that could be identified. Performing various deposition trials at different temperatures and different start voltages did not reveal any phase transition that met the criteria above. Therefore, we were forced to use a separate Ge(111) sample to calibrate using the well-known $\left(\sqrt{3} \times \sqrt{3}\right)$ to (1x1) phase transition, and then we swapped out the samples to perform the experiment on the Ge(110) surface. While tedious, the upside of this calibration procedure is that it is very reliable.

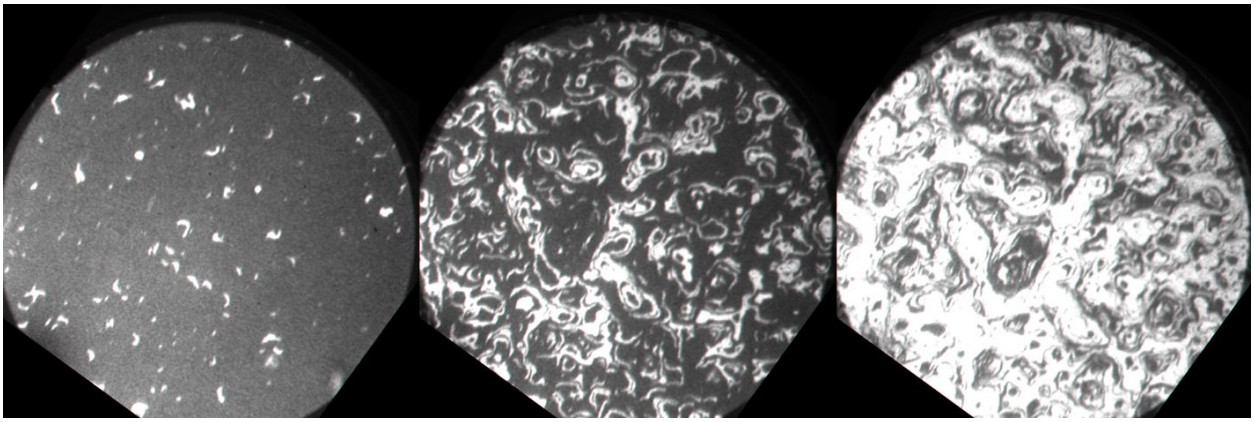

Figure 6.1. LEEM images showing the growth of the (5x1) phase (bright white) on the (2x1) phase (darker gray) at 246°C. FoV is 10µm, and start voltage is 10.0V.

For Pb/Ge(100), we found some literature on room to high temperature phases [1, 3-5, 13], but only two provided phase diagrams that could be used to perform the calibrations [4, 13]. Unfortunately, the two sources showed conflicting information in their phase diagrams, both in the existence of certain phases as well as the temperature and coverage boundaries of the phases that both agree exist. To resolve these inconsistencies, some deposition experiments were performed, and a useful phase transition was found.

Figure 6.1 shows a phase transition from (2x1) to (5x1) at 246°C, with bright domains of (5x1) gradually covering the entire surface. It looks very similar to the $\left(\sqrt{3} \times \sqrt{3}\right)$ to (1x1) phase transition on Ge(111), making it an ideal transition for coverage calibration. This phase transition was observed at various other temperatures as well, including 157°C, 165°C, and 288°C (not shown). This already conflicts with the phase diagrams from both sources, with [13] claiming the (5x1) phase should only exist above 300°C, while [4] claims said phase should only exist under 200°C. They also do not include a (2x1) phase at lower coverages, even though this phase was observed via LEED patterns, as shown in Figure 6.2 where a (2x1) pattern appears with the other patterns due to the phase transition being incomplete.

Upon cooling the sample below about 100°C, the (5x1) phase was found to reversibly transition to a c(8x4) phase. An exact transition temperature could not be identified due to both phases coexisting at a wide range of temperatures, but this does seem to imply that the phase diagram in [4] is more reliable in terms of the relative positions of the phases being considered in this chapter. The LEED patterns for both can be seen in Figure 6.2, and the c(8x4) image also includes some faint (5x1) spots since it was still in the middle of its transition towards c(8x4), alongside the (2x1) spots due to partial coverage.

The (2x1) to (5x1) phase transition was found to occur within similar times for depositions performed at the various temperatures mentioned before, meaning that the required coverage does not change with temperature, just like the $\left(\sqrt{3} \times \sqrt{3}\right)$ to (1x1) transition on Ge(111). Since this phase transition was indeed determined to have all the qualities for a primary calibration tool to be used on Ge(100), a final calibration check was performed using Pb/Ge(111) as a

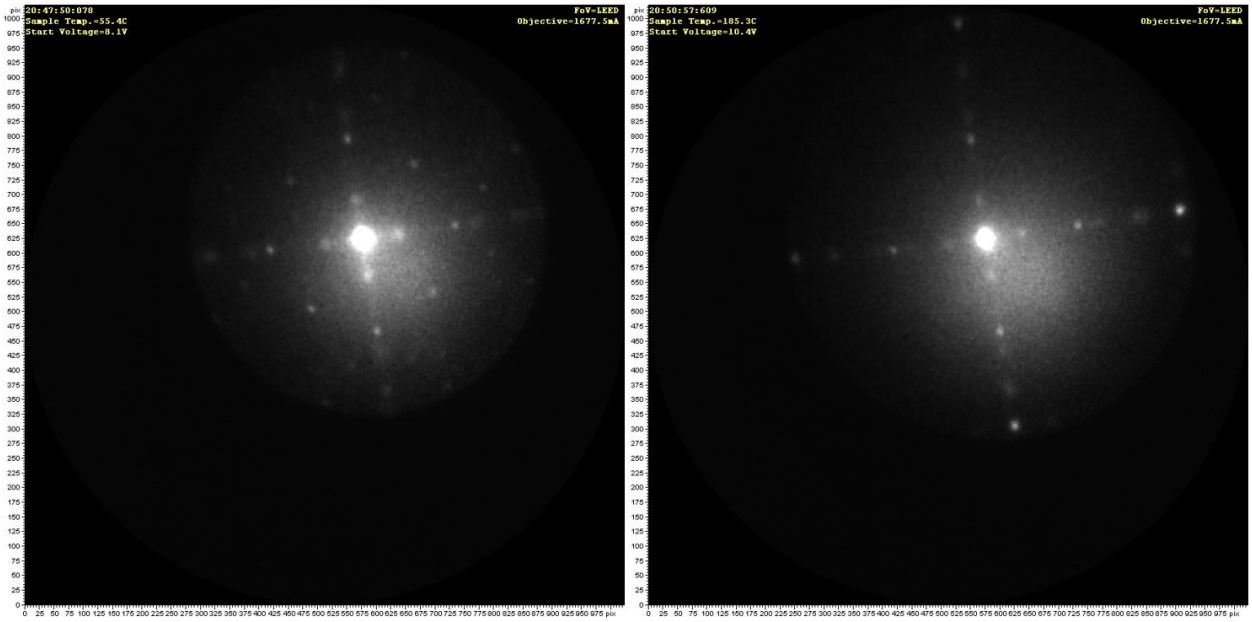

Figure 6.2. LEED patterns of the c(8x4) (left) and (5x1) (right) phases of Pb/Ge(100). Both phases show some (2x1) spots since the phase transition has not fully completed. The c(8x4) pattern was taken at 8.1V start voltage and 69°C, while the (5x1) pattern was taken at 10.4V start voltage and 253°C.

reference, in order to precisely verify the coverage at which the phase transition occurs. This transition coverage was measured to be 0.86±0.02ML with respect to Ge(111), or 0.99±0.02ML with respect to Ge(100), as opposed to 0.5ML reported by [4] and somewhat above 1ML reported by [13]. Thus, the low temperature Pb/Ge(100) coverage calculations were performed according to the phase transition coverage of about 1ML as determined here, without having to further rely on Pb/Ge(111) calibrations that would require swapping samples between experiments.

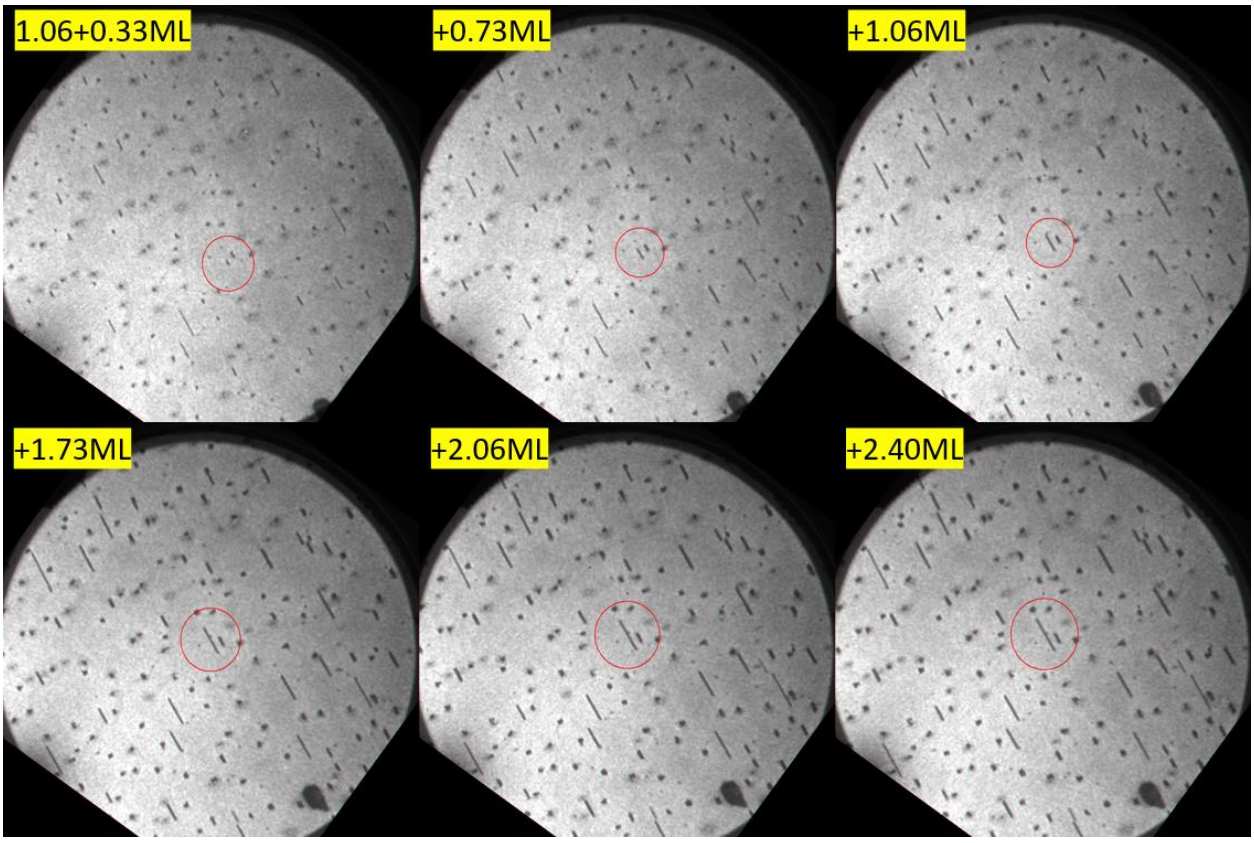

Figure 6.3. Sequence of LEEM images of Pb/Ge(110) at +4°C showing island growth for various coverages above the critical coverage. The islands are oriented in the $[1\bar{1}0]$ direction, and one island is circled so that it can be tracked across the images. FoV is 10µm, and start voltage is 11V. The large, black feature in the lower right corner is a surface defect and should be ignored.

6.3 Results and Discussion

6.3.1 Pb/Ge(110)

The first Pb islands were found to nucleate at a critical coverage of 1.06±0.06ML with respect to Ge(110), or 0.50±0.03ML with respect to Pb(111). However, the islands were not the height-selected type seen on Ge(111), instead growing 1D islands that had striking resemblance to the Ag/Ge(110) islands in [6] and the Pb/Si(110) in [9]. A sequence of LEEM images showing the growth of the islands at +4°C is shown in Figure 6.3. The islands were about 90-100nm wide

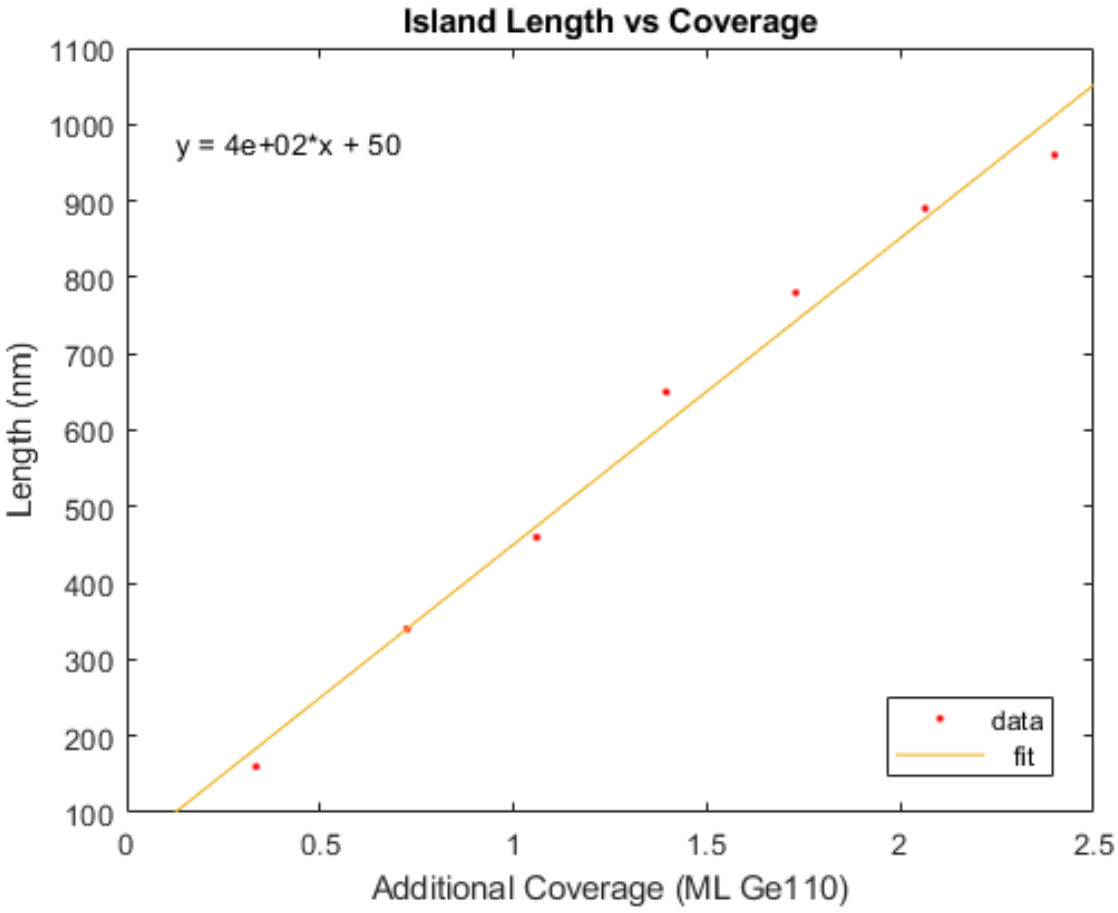

Figure 6.4. Plot of the length of the island marked by the red circle in Figure 6.3 with respect to additional coverage beyond the critical coverage. A best-fit line is also shown.

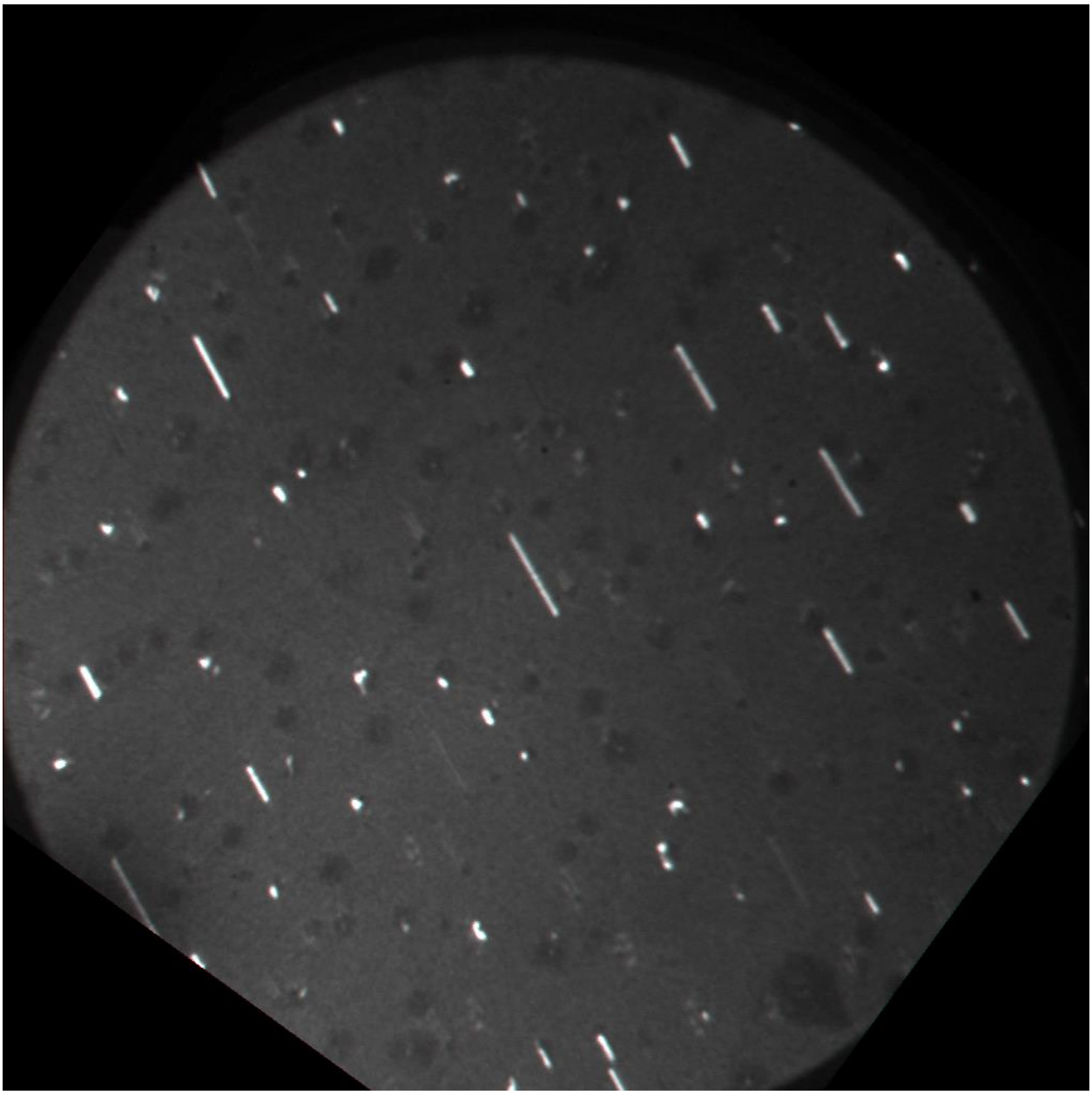

Figure 6.5. Pb/Ge(110) islands imaged at a start voltage of 19V, showing the only occurrence of bright contrast for the 1D islands.

and did not grow any wider during the entire growth phase, only increasing in length over time and grew in the $[1\bar{1}0]$ direction as expected. One such island, marked by the circle in Figure 6.3, was tracked over time with additional deposition, and its length is plotted in Figure 6.4. As shown by the linear fit, the island's growth rate appears to be linear in coverage/time, meaning collective diffusion was involved. There were some islands that stopped growing at various points

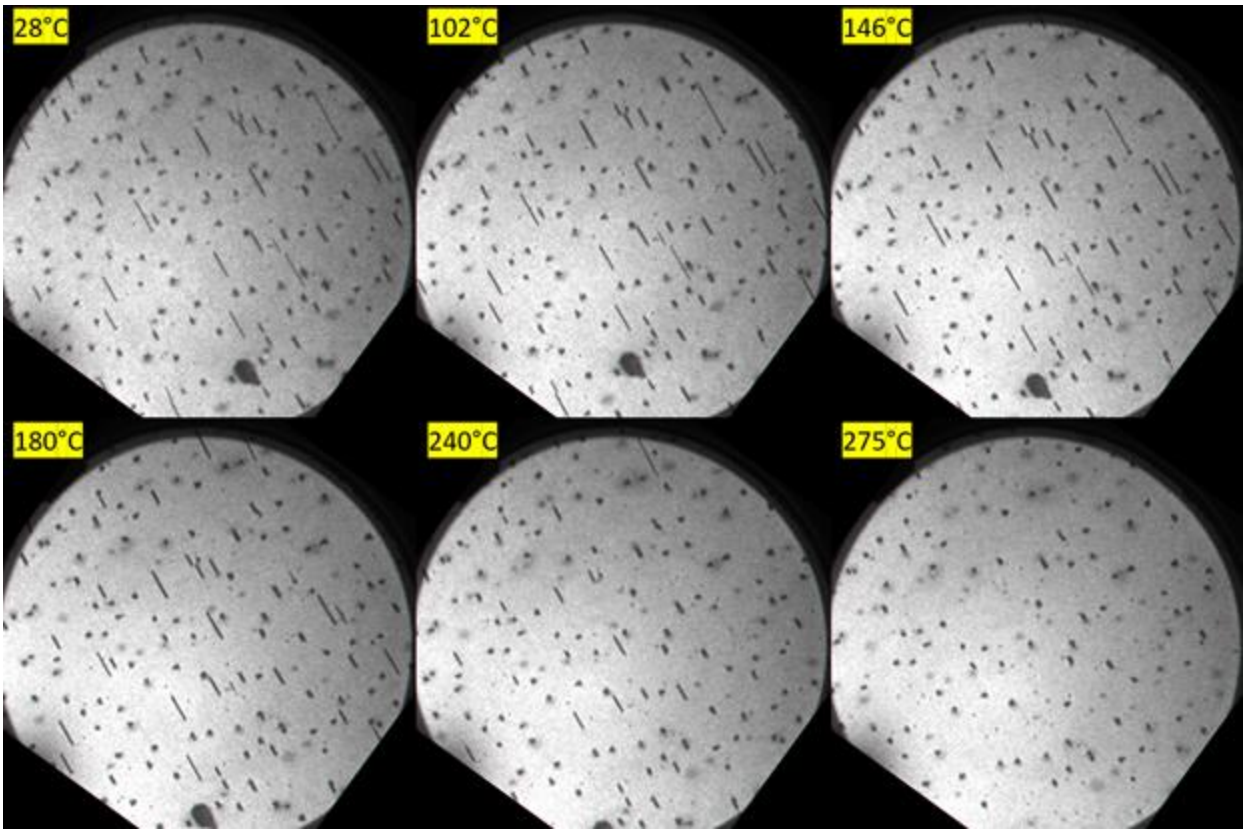

Figure 6.6. Sequence of LEEM images of Pb/Ge(110) being annealed at a fixed coverage of 3.29ML, showing the coarsening of 3D islands at the expense of 1D islands. FoV is 10μm, and start voltage is 11V. The 3D islands are identified by the black dots remaining after the 1D islands have disappeared.

during deposition, but the reason for their stopping is unclear. The islands also do not appear to be good candidates for the KP model for IV curve height analysis, with their contrast staying dark throughout most of the start voltages except for what appears to be a Bragg peak in intensity at around 19V, which offers the only bright contrast as shown in Figure 6.5. This means STM measurements are required to fully analyze the dimensions of these islands.

Furthermore, the 1D islands were not the only islands present on the surface. 3D islands were found to coexist with the 1D islands, nucleating at the same critical coverage. They can be identified as black dots of similar contrast as the 1D islands that also grow in size in Figure 6.3,

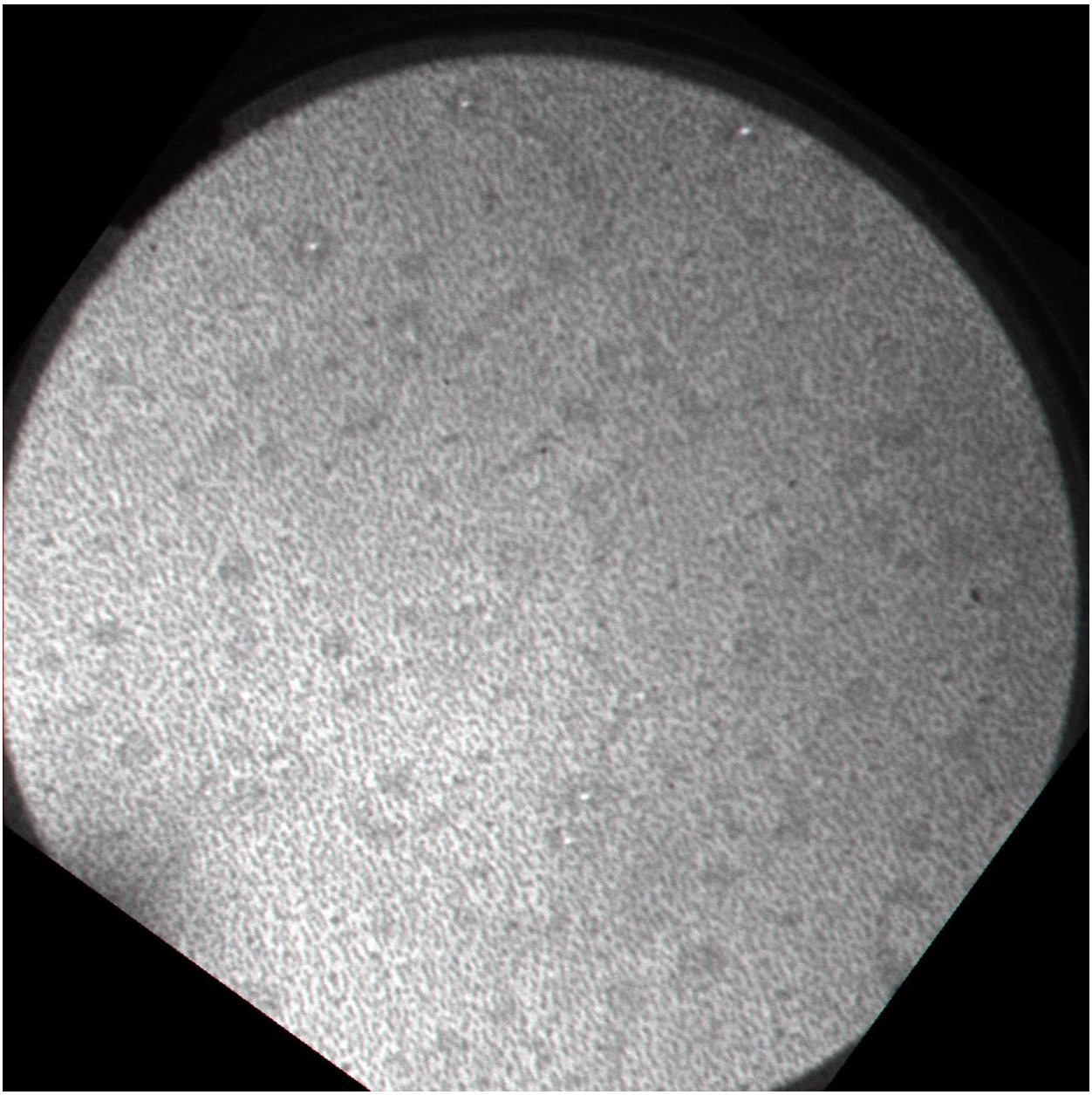

Figure 6.7. Numerous, small, 1D islands grown at -4°C in a separate experiment. FoV is 10µm, and start voltage is 11V.

and they can also be identified by looking at the black dots that remain after the 1D islands have collapsed during annealing in Figure 6.6. While these islands only appear to grow in 2 dimensions due to the LEEM's imaging limitations, it is possible that they can grow in height as well as lateral size. Since there is insufficient evidence to conclude if these islands only grow in 2 dimensions, we will conservatively call them 3D islands. Because the 1D islands are unstable at higher

temperatures while the 3D islands undergo coarsening, we can deduce that the 3D islands are high-temperature phenomena while the 1D islands occur for low temperatures. Indeed, the 1D islands could not be grown above room temperature, while no 3D island was observed under 0°C as shown in Figure 6.7. It appears that the temperature range between 0°C and room

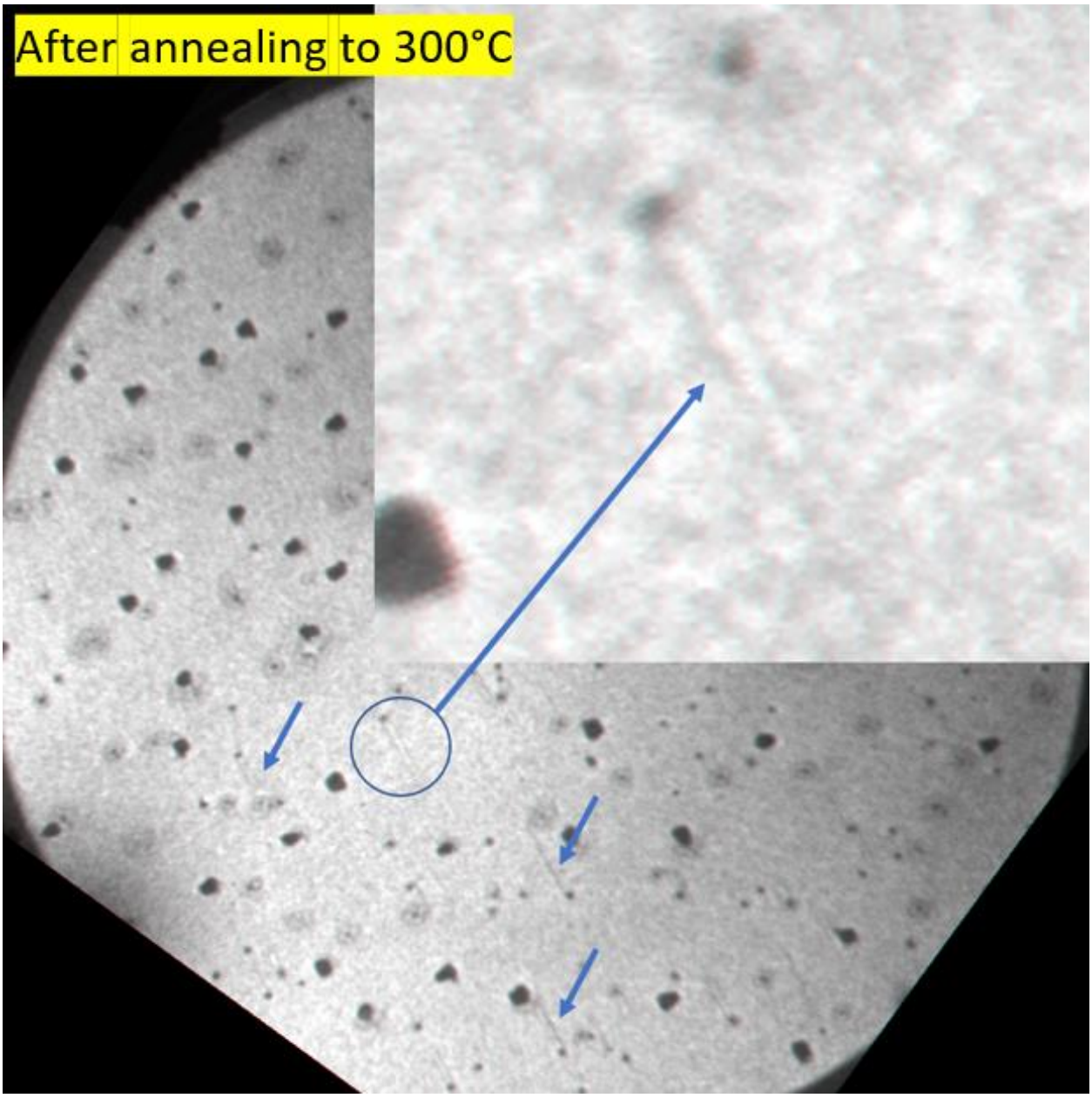

Figure 6.8. LEEM image showing imprints of 1D islands left behind on the wetting layer after the 1D islands have collapsed from annealing (continued from Figure 6.6). A few of the imprints are identified with the blue arrows, while one is shown zoomed-in for clarity.

temperature is the boundary between the low-temperature and high-temperature cases, with both types of islands nucleating and competing for the deposited Pb, which partially explains why some 1D islands stopped growing in Figure 6.3. Unfortunately, Figure 6.7 also shows how quickly the average island size decreases with temperature, meaning that the LEEM's resolution will quickly become insufficient for experiments further below 0°C, requiring the STM to properly image the islands. This problem can be slightly alleviated by using lower deposition rate, due to its relationship with island number density, as discussed in Chapter 4.

Even though low-temperature phenomena are the focus of this dissertation, some information about the high-temperature behavior of the islands is worth discussing here. First, it was observed that the 1D islands left behind imprints on the wetting layer after collapsing, and all of these imprints appear to terminate on a black dot, which may be either a defect or an island remnant, as shown in Figure 6.8. This was found to occur on Ag/Ge(110) as well [6], showing that the Pb/Ge(110) islands share many behaviors and attributes with Ag/Ge(110) islands, even though the two systems are at very different temperature regimes.

Secondly, the 3D islands, despite not exhibiting 1D growth, still displayed some directional preferences in the shapes they assumed. Figure 6.9 shows the Pb/Ge(110) system after the sample was cooled back down from annealing and after additional Pb was deposited to further grow the existing islands so that their shapes could be examined in more detail, since the 3D islands were quite small in previous figures. The islands in Figure 6.9 show triangular and trapezoidal shapes, pointing in either the $[001]$ or the $[00\bar{1}]$ direction. The trapezoids also had preferential orientations, with the straight edges facing the aforementioned directions, and it can be surmised that the trapezoids are triangular islands that have grown broader along the

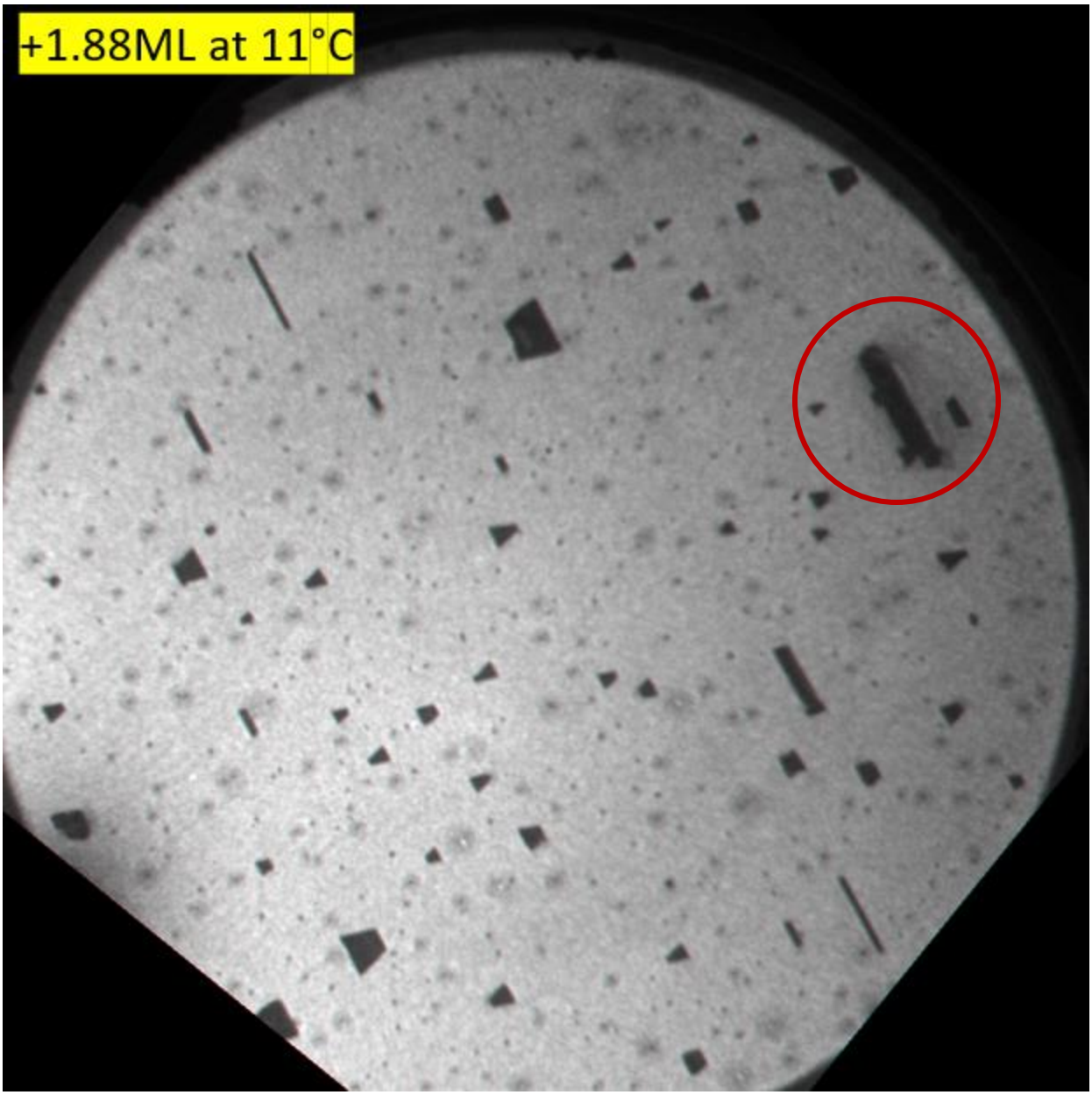

Figure 6.9. LEEM image of Pb/Ge(110) islands after the sample in Figure 6.8 was cooled to 11°C and then deposited with additional 1.88ML of Pb. Some 1D islands have grown again, while the 3D islands have increased in size, causing their shapes to appear more clearly. The thick, black bar circled in red is a defect and not a real island.

$[1\bar{1}0]$ axis. There is also the possibility that all these islands are actually hexagons but with some of the sides having very small lengths, which was described in [14] as occurring due to the arrangement of the atoms making up each side with respect to the arrangement of the atoms of the layer underneath. If the Pb islands are (111) islands, then the sides will have six basic

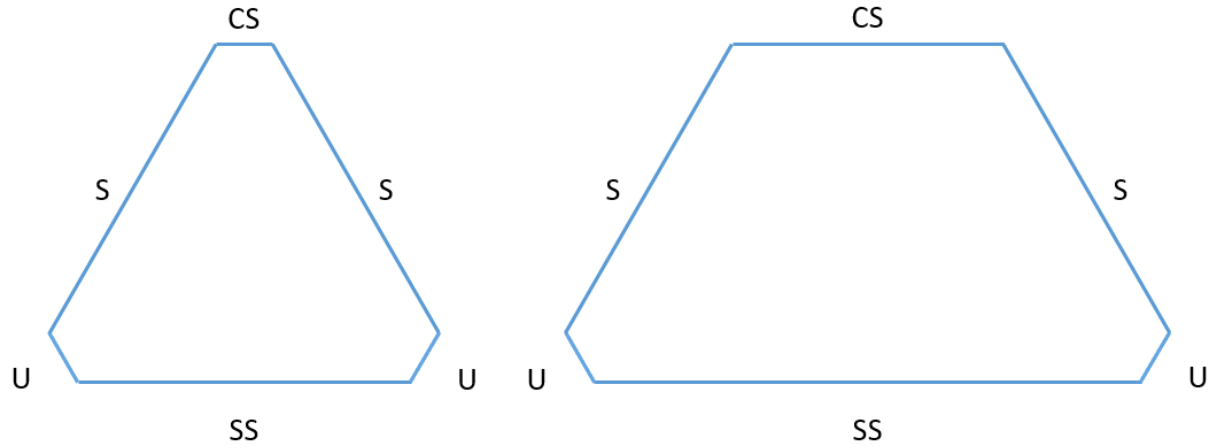

Figure 6.10. Diagrams showing the possible, true shapes of the triangular/trapezoidal Pb islands on Ge(110) surface, along with the stability of each side. SS stands for superstable, S stands for stable, U stands for unstable, and CS stands for conditionally stable.

orientations, $[1\bar{1}0]$ and its 60° rotated equivalents. It may be that one of these orientations is extremely stable and forms the base of the triangles/trapezoids that lines up along the $[1\bar{1}0]$ direction, and this is likely true for the 1-dimensional islands as well, only on a more extreme scale. Figure 6.10 depicts proposed models of possible island shapes constructed based on the principles discussed in [14], with each side marked according to its stability. While [14] only identifies two types of sides due to the highly symmetric substrate in their calculations, we propose four possible types with different levels of stability. The edge labeled SS is the superstable edge that always aligns with the $[1\bar{1}0]$ axis on the substrate, while the sides marked with U are unstable and thus do not grow large enough to be seen by the LEEM. The sides labeled S are stable edges, and they do not appear to be a 60° rotation of the superstable edge, since the triangular islands in Figure 6.9 do not form equilateral triangles but are instead isosceles triangles, suggesting that the stable edges are a different orientation type. The 1D stable edges may still be the same SS orientation type, however, which may explain their strictly 1D growth. Lastly, the edge labeled CS is a conditionally stable edge that is normally unstable but is forced to grow due

to the stable edges wanting to retain their orientation as the SS edge grows longer. The CS edge could also be a normally superstable edge that is suppressed due to its bordering the stable edges, unlike the other SS edge that easily grows due to the unstable sides at its borders. It should be possible to use theoretical calculations to predict the stability of each side, and STM experiments can verify the different orientations of the sides as well as the arrangement of the atoms of the layer underneath, providing avenues for future research.

6.3.2 Pb/Ge(100)

Upon depositing at +1°C, Pb/Ge(100) was found to nucleate the familiar, height-selected islands that we have seen on Ge(111), but at a critical coverage of 2.53±0.03ML with respect to Ge(100), or 1.68±0.02ML with respect to Pb(111), which implied that Pb was able to compress to an astonishingly high 68% beyond its natural value. We will discuss this critical coverage after we have discussed the results in more detail. A brief examination of the island intensities across various start voltages appeared to show similar IV curve characteristic peaks as the Pb/Ge(111) islands, verifying that the islands were indeed the same type, but a detailed IV curve has not been measured. The initial nucleation and growth times were the same, meaning explosive nucleation had occurred. Thus, aside from the critical coverage, the mechanism of island formation appeared to be the same for Ge(100) and Ge(111).

An attempt was made to track the growth of the islands with respect to additional deposition beyond the critical coverage, as was done in Chapter 4. The sequence of LEEM images showing the island growth is provided in Figure 6.11, with the height-selected islands appearing

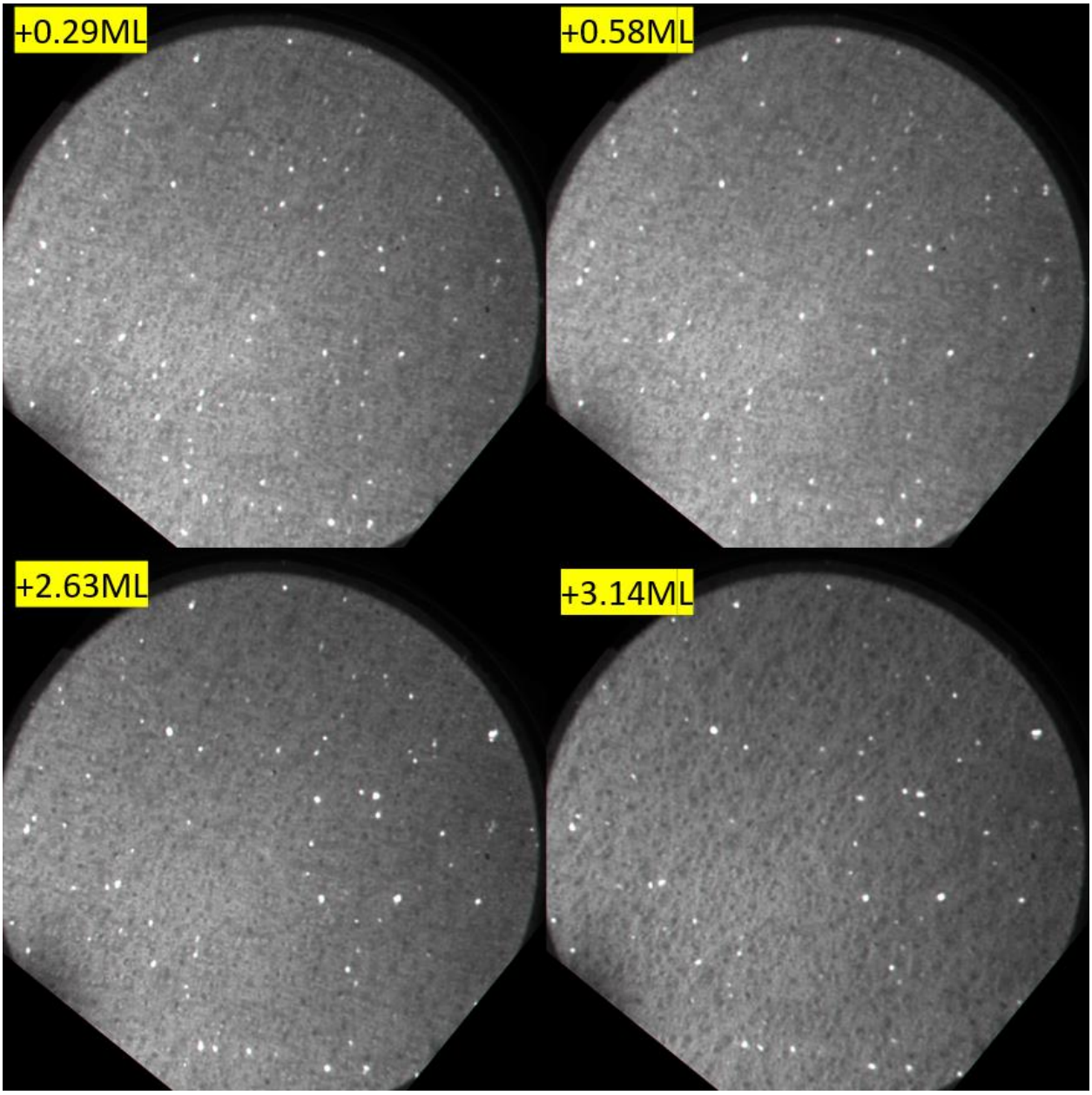

Figure 6.11. Sequence of LEEM images of the growth of Pb/Ge(100) islands at +1°C at different coverages beyond the critical coverage. The islands (bright white contrast) show very little growth despite the additional deposition. Numerous 3D islands (not height-selected) can be seen in these images (dark dots), but they are difficult to distinguish from the wetting layer. FoV is 15µm, and start voltage is 8.0V.

with bright, white contrast at the selected start voltage of 8.0V, just as it was selected for the Pb/Ge(111) islands. The images show very little change in the total area of the islands, with some new islands forming while very few islands show noticeable increase in size. Since the Pb must have been going somewhere on the sample, and since Pb/Ge(110) had already shown two types of islands competing for the deposited Pb, it was quickly hypothesized that Pb/Ge(100) must also have a second type of island that was drawing Pb away from the height-selected islands. Unlike Pb/Ge(110), however, the second type of island was not very apparent at the same start voltage where the height-selected islands were most visible.

The second type of island was revealed to be 3D, high-temperature islands similar to the ones found on Ge(110). They had very dark contrast, which was why they were difficult to notice against the gray contrast of the wetting layer at the start voltage of 8.0V used to image the height-

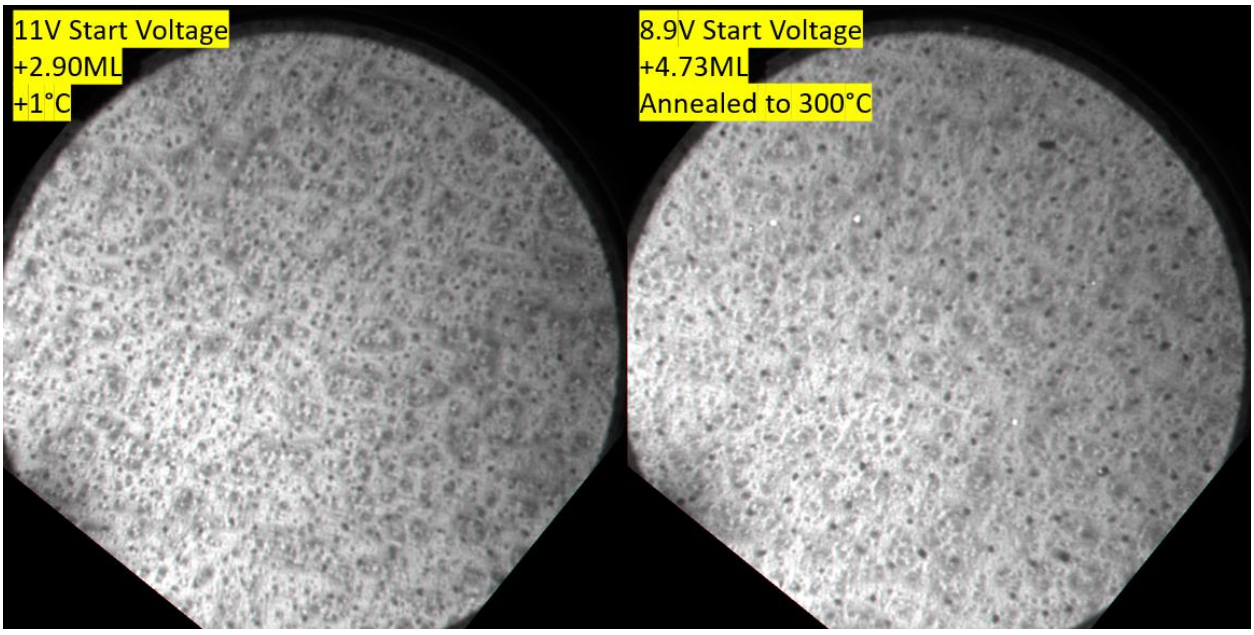

Figure 6.12. Images of the 3D Pb/Ge(100) islands. The left image was taken between the 3rd and 4th images in Figure 6.11 but at a different start voltage of 11V, where the height-selected islands can no longer be seen but the 3D islands appear as black spots on the bright wetting layer. The right image was taken after the sample was annealed to get rid of most of the height-selected islands while coarsening the 3D islands to make them even more visible. Note that the contrast of the wetting layer at this temperature allowed both types of islands to be easily identified.

selected islands. Upon changing the start voltage to 11V, which was the start voltage used for Pb/Ge(110), the wetting layer became brighter as expected, hiding the height-selected islands but making the dark, 3D islands stand out. In order to make sure these dark features were islands and not defects, the sample was annealed to 300°C to cause the islands to undergo coarsening,

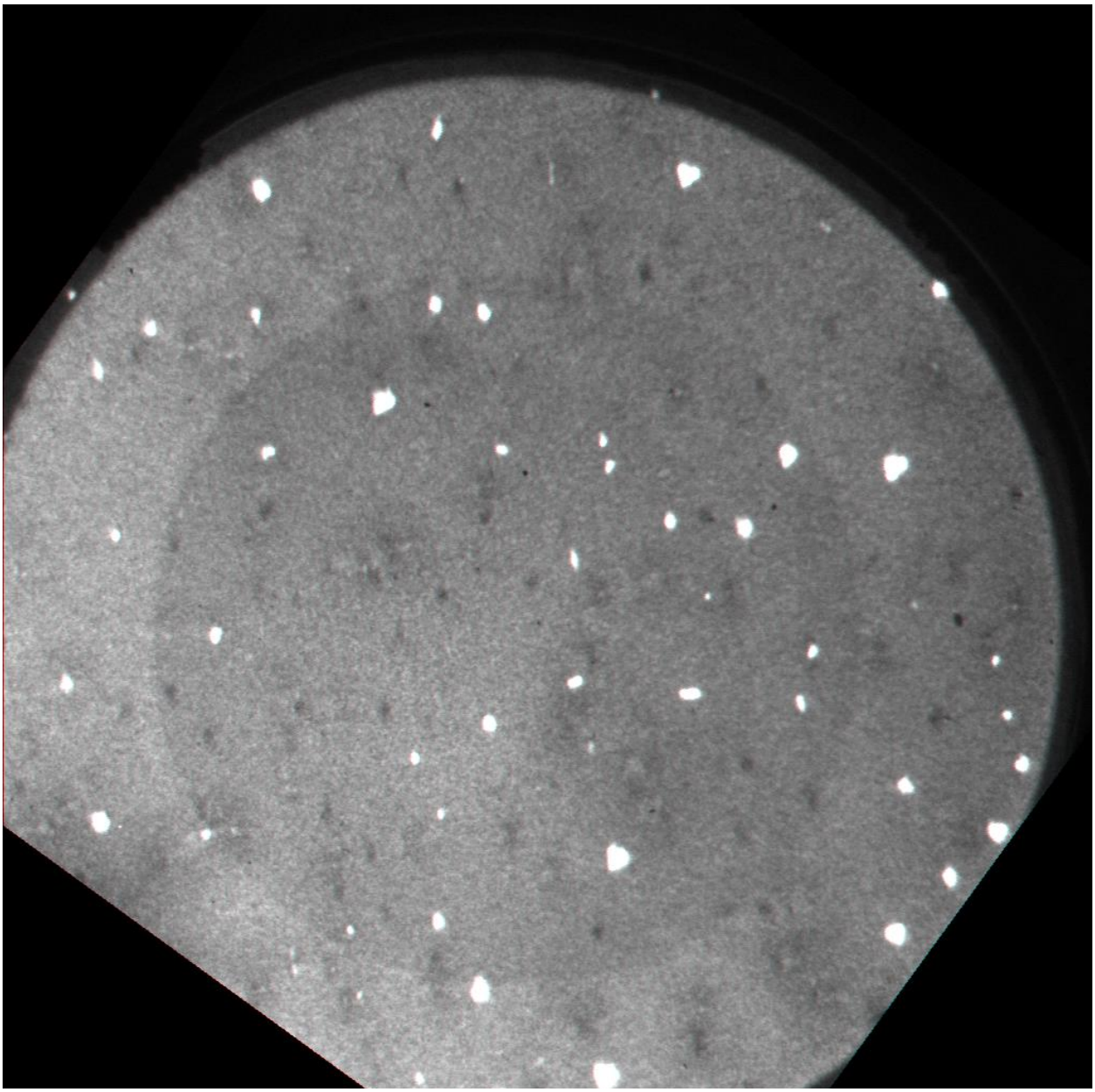

Figure 6.13. Pb/Ge(100) islands at -2°C from a different experiment, showing mostly height-selected islands with no noticeable 3D islands. Coverage is 3.13ML, FoV is 10µm, and start voltage is 8.2V. The dark circle is due to slight damage to the microchannel plate and is not a surface feature.

which was the same procedure used to verify the islands' presence on Ge(110). The height-selected islands collapsed for high temperatures, as expected, while the 3D islands increased in size through coarsening. The 3D islands as described are shown in Figure 6.12, and unlike the Pb/Ge(110) 3D islands, these islands do not appear to have a preferred shape, or they are too small to clearly tell.

Once again, there appears to be a temperature boundary between classical islands and nonclassical islands, and a transitional temperature range in which both types of islands can coexist. A previous Pb/Ge(100) experiment performed at -2°C with the basket-type evaporator showed very few 3D islands, if any, in Figure 6.13, suggesting that the boundary is around 0°C, which is unsurprising given the boundary determined for the Pb/Ge(110) case. This earlier, previous experiment also gave a critical coverage of 2.03±0.28ML with respect to Ge(100) or 1.35±0.19ML with respect to Pb(111), with the margin of error being large due to the unreliability of the basket-type evaporator. This is much lower than the critical coverage determined from the +1°C experiment, which seems to support the hypothesis that the 3D islands were hindering the formation of the height-selected islands, but this critical coverage still corresponds to much higher compression than was observed for Pb/Ge(111).

We attempt to explain this unusually high critical coverage partly by observing that the Ge(100) surface has a very high defect density compared to Ge(111). As noted in Chapter 3, Ge(100) appears to have "mountain ranges" of defects that greatly reduce the total area of surface that actually has the clean Ge(100) (2x1) reconstruction. The Ge(100) surface used for this experiment can be seen in Figure 6.14, and the roughness of the surface is immediately obvious. It is still unclear why the Ge(100) surface is so difficult to clean, aside from the

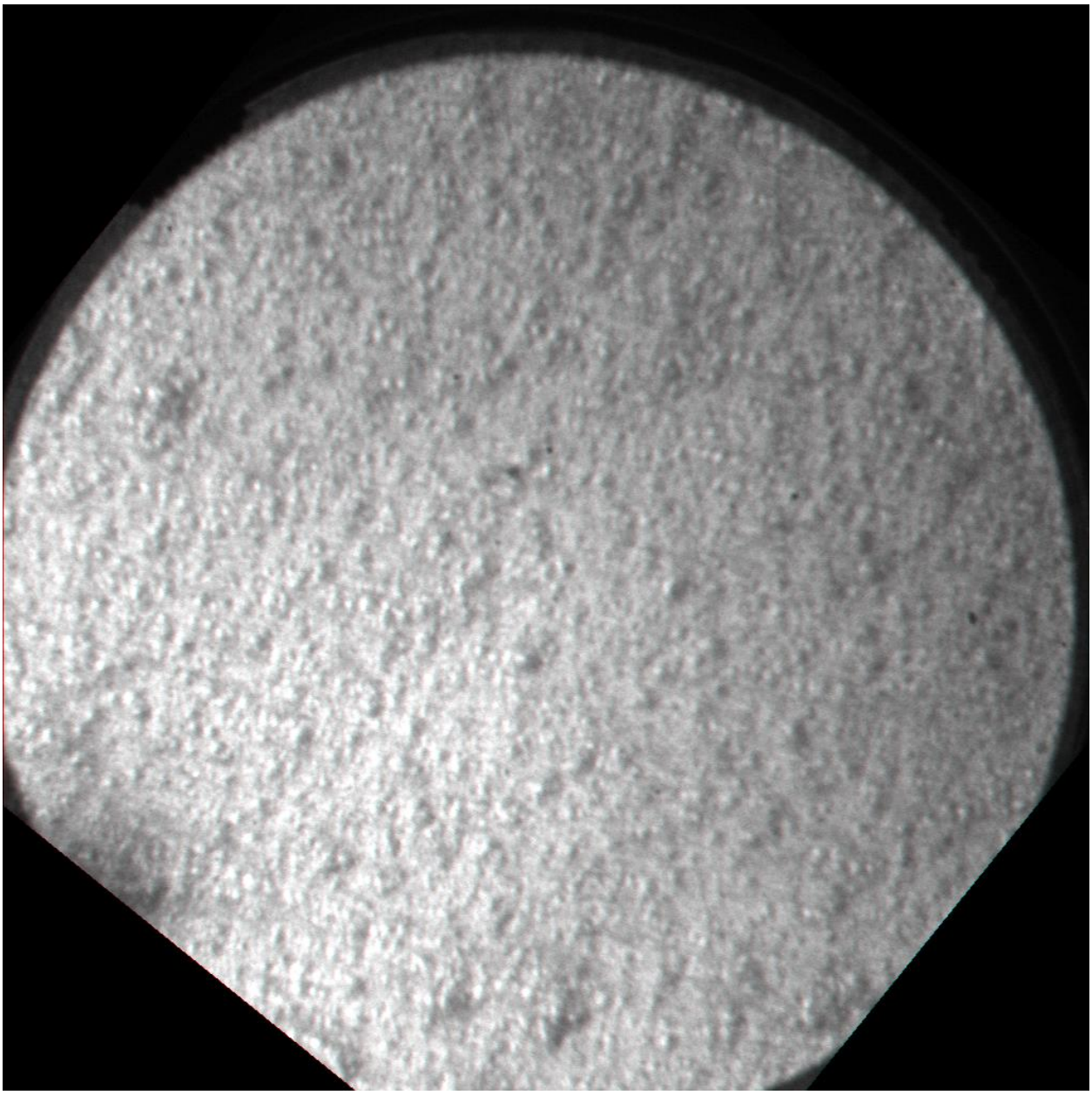

Figure 6.14. LEEM image of the bare Ge(100) surface used for the +1°C experiment, imaged at a start voltage of 10.7V. FoV is 15µm. The surface is extremely rough due to the numerous surface defects.

hypothesis that the defects have extremely strong bonding with the rest of the substrate, but it appears to be unavoidable even with the optimized cleaning procedures discussed in Chapter 3. These defects are likely constraining the movement of the deposited Pb such that the islands have a more difficult time nucleating, perhaps because the “mountains” allow the wetting layer

to grow additional layers instead of compressing in a single layer, delaying it from reaching the required critical compression despite having more overall Pb coverage. While the exact interaction between the defects and island nucleation is mostly conjecture, the evidence does seem to support the defects' role in the increased critical coverage, since Figure 6.13 shows a much cleaner surface, and the experiment used for Figure 6.13 measured a lower critical coverage.

6.4 Conclusion

We revisit the hypotheses made in the introduction. (1) Pb/Ge(110) would form height-selected islands that exhibit 1-dimensional growth. (2) Pb/Ge(100) would form height-selected islands that would either have 1-dimensional growth in two possible directions or not show directional preference at all.

We saw that the Pb/Ge(110) hypothesis was only partially correct; the islands indeed showed 1-dimensional growth in the $[1\bar{1}0]$ direction, but they were not height-selected and appeared more like 1D islands observed in previous studies for the Ag/Ge(110) and Pb/Si(110) systems. These islands grew linearly with deposition, meaning collective diffusion was their mechanism of growth. There was also an unexpected result in that a boundary between classical and nonclassical island formation was discovered, with two different types of islands coexisting in the temperature range between 0°C and room temperature. The classical, 3D islands still showed some directional preference, particularly with the orientation of the sides with respect

to the substrate, as some faces were unstable compared to the others due to the relative arrangement of the atoms making up each side.

The hypothesis for Pb/Ge(100) turned out to be more accurate, with height-selected islands nucleating at a critical coverage. However, the critical coverage was unusually high, which we have attempted to explain by the observation that the bare Ge(100) surface was very rough and would have affected the interaction between the wetting layer and the substrate. We also observed the boundary between classical and nonclassical regimes, similar to Pb/Ge(110), with 3D islands observed above 0°C, which competed with the height-selected islands for the deposited Pb and hindered their growth. Like the height-selected islands, the 3D islands did not show a directional preference, either in growth or faceting.

There are still many questions about these two systems, including those that have arisen from the experimental results, and they provide further avenues for future studies. Both low temperatures and high temperatures should allow for some interesting experiments, and this chapter has marked a clear boundary between the two temperature regimes as a starting point. We can see that despite the relatively low level of interest implied by the lack of literature on these two systems, Pb/Ge(110) and Pb/Ge(100) exhibit very strange and intriguing phenomena.

References

[1] P.W. Chen, Y.H. Lu, T.R. Chang, C.B. Wang, L.Y. Liang, C.H. Lin, C.M. Cheng, K.D. Tsuei, H.T. Jeng, S.J. Tang, Consonant diminution of lattice and electronic coupling between a film and a substrate: Pb on Ge(100), Physical Review B, 84, (2011) 205401.
[2] L. Floreano, D. Cvetko, F. Bruno, G. Bavdek, A. Cossaro, R. Gotter, A. Verdini, A. Morgante, Quantum size effects in the low temperature layer-by-layer growth of Pb on Ge(001), Prog. Surf. Sci., 72, (2003) 135-159.
[3] W.S. Yang, X.D. Wang, K. Cho, J. Kishimoto, T. Hashizume, T. Sakurai, Superstructures of the Pb/Ge(001) System, Physical Review B, 51, (1995) 7571-7582.
[4] Y. Zhang, R.G. Zhao, W.S. Yang, Surface Superstructures of the Pb/Ge(001) System, Surf. Sci., 293, (1993) L821-L825.
[5] N. Takeuchi, First-principles calculations of low-coverage phases of Pb on the (100) surface of Ge, Surf. Sci., 412-13, (1998) 358-363.
[6] C.H. Mullet, Growth of Ir on Ge(111) and Ge(110) and Growth of Ag on Ge(111), Ge(110), and Ge(001) Studied by Low Energy Electron Microscopy and Scanning Tunneling Microscopy, PhD dissertation in Physics, University of California Davis, Davis (2012).
[7] B.H. Stenger, A.L. Dorsett, J.H. Miller, E.M. Russell, C.A. Gabris, S. Chiang, Growth and motion of liquid alloy droplets of Au on Ge(110), Ultramicroscopy, 183, (2017) 72-76.
[8] T. Watanabe, Y. Yamada, M. Sasaki, S. Sakai, Y. Yamauchi, Pt- and Au-induced monodirectional nanowires on Ge(110), Surf. Sci., 653, (2016) 71-75.
[9] M. Jalochowski, E. Bauer, Growth of metallic nanowires on anisotropic Si substrates : Pb on vicinal Si(001), Si(755), Si(533), and Si(110), Surf. Sci., 480, (2001) 109-117.
[10] C.C. Hsu, W.H. Lin, Y.S. Ou, W.B. Su, C.S. Chang, C.I. Wu, T.T. Tsong, Effects of electronic confinement and substrate on the low-temperature growth of Pb islands on Si(100)-2 x 1 surfaces, Surf. Sci., 604, (2010) 1-5.
[11] H. Itoh, H. Tanabe, D. Winau, A.K. Schmid, T. Ichinokawa, Growth Mode and Surface Structures on the Pb/Si(001) System Observed by Scanning Tunneling Microscopy, Journal of Vacuum Science & Technology B, 12, (1994) 2086-2089.
[12] L. Li, C. Koziol, K. Wurm, Y. Hong, E. Bauer, I.S.T. Tsong, Surface Morphology of Pb Overlayers Grown on Si(100)-(2x1), Physical Review B, 50, (1994) 10834-10842.
[13] G. Falkenberg, L. Seehofer, R. Rettig, R.L. Johnson, Lead-induced reconstructions of the Ge(001) surface, Surf. Sci., 372, (1997) 155-170.
[14] S.D. Liu, Z.Y. Zhang, G. Comsa, H. Metiu, Kinetic Mechanism for Island Shape Variations Caused by Changes in the Growth Temperature, Physical Review Letters, 71, (1993) 2967-2970.

7 CONCLUSIONS AND FUTURE WORK

In this dissertation, we have worked with all three low-index faces of germanium and have performed Pb deposition experiments on all of them. The LEEM was shown to be a powerful tool for studying the growth of islands and phases in real time, allowing us to study the dynamics of island formation in great detail. Overall, the Pb-Ge system was found to exhibit many novel and exciting phenomena, although there is still much left to be understood.

7.1 Optimizing Cleaning Parameters

In Chapter 3, we experimented with various parameters in the sputter-anneal sample cleaning procedure in order to optimize and control the presence of defects on the substrates used for our experiments. Using information on how sputtering energy affects the formation of contamination-induced pyramids in work done by Marshall van Zijll, we determined that sputtering at multiple energies would target different types of defects, after which the damage from any high-energy sputtering could be repaired with a final sputter sequence using low energy ions. For germanium, this usually meant two different sputtering energies, with the first quarter of the sputter-anneal cycles being performed at a high energy and the rest being performed at a lower energy. We also identified various types of defects that could form on the different faces of germanium, so that the LEEM images in later chapters would be easier to interpret. Optimizing

sample preparation is an ongoing work, and we expect further optimizations to be explored and discovered as more information becomes available.

7.2 Pb/Ge(111) Islands at Low to Room Temperature

In Chapter 4, we deposited Pb on Ge(111) at low to room temperature to nucleate height-selected islands similar to those observed in studies performed by Tringides *et al.* on Si(111). From examining the island nucleation frame by frame, we saw that the islands nucleated explosively, with hundreds of thousands of atoms diffusing across hundreds of nanometers within just a few seconds to form these islands. It was found that the explosive nucleation occurred due to slight compression in the wetting layer, since the critical coverage at which the islands nucleated was found to be about 4/3ML with respect to Ge(111), which is a value that is about 2% above the natural density of Pb(111). This was corroborated by DFT calculations performed by our collaborators at the University of Central Florida (T. Panagiotakopoulos, D. Le, T.S. Rahman), who showed that the chemical potential of the wetting layer remains beneath that of a second layer or islands until 4/3ML.

The diffusion barrier involved with island nucleation was calculated by studying the dependence of island number density with respect to temperature and flux rate. It was found that the island number density strangely conformed well to classical nucleation theory, with a diffusion barrier of 0.82-0.87eV calculated from applying the theory to the data. It was also found that surface defects affect the diffusion barrier, and a comparison between experiments

performed on two separate samples revealed that higher defect density tends to increase the diffusion barrier.

We also tracked the islands' growth over additional deposition, taking advantage of the LEEM's real time recording. Again, our collaborators at the University of Central Florida assisted in processing the thousands of frames of data (V. Stroup, D. Le, and T.S. Rahman), using computer vision to recognize and track the islands in each frame. From this, we were able to see that the islands grew linearly with coverage and therefore time. This is the characteristic trait of collective diffusion, which is significantly faster than the $t^{1/2}$ dependence of classical diffusion. Our collaborators attempted to explain this collective diffusion behavior by DFT calculations of the various binding sites of Pb atoms on the Ge(111) surface (A. Childs, D. Le, T.S. Rahman), and the calculations showed that two of the sites had very similar energy, allowing for Pb atoms to hop from one site to the other very easily.

Finally, we attempted to verify the heights of the Pb islands using the LEEM in Chapter 5, using the Kronig-Penney model method described by Altman *et al*. By modeling each island layer as a series of potential wells, we were able to calculate the reflected intensity of electrons passing through each island as a function of electron energy. By comparing simulated IV curves for each layer thickness with experimentally derived IV curves, we showed that an island grown at -23°C had a height of 7 layers, while an island grown at +3°C was found to be a combination of 10 and 11 layers due to its growing over a step edge. This technique, though somewhat difficult to use, showed that it is possible to determine heights of certain features in LEEM images in situations where the STM may not be viable.

In terms of future work, there are definitely many experiments that could be performed on the STM. Our work was primarily performed using the LEEM due to instrumental problems with our STM, and thus, any STM experiment would be valuable in understanding this system. Since the STM has much greater resolution than the LEEM, STM experiments would likely focus on the details of how each layer on the islands form, including differences between how unstable and stable layers nucleate on existing islands. The STM can also be used to create a histogram of island heights since its direct, topographical imaging is superior to the difficult Kronig-Penney model method used with the LEEM, allowing for the creation of a phase diagram for the Pb/Ge(111) system with respect to coverage and temperature.

On the LEEM side of experiments, one could perform very high coverage experiments beyond the point where the islands begin merging. The experiments in this dissertation stopped before many of the islands began merging, but the real time growth of height-selected thin films may provide further information on the collective diffusion of the Pb/Ge(111) system. Another possible experiment involves the coarsening of the islands at a fixed coverage as temperature is increased, which would give further insight into the diffusion barrier involved in island growth.

On the theoretical side, there is still much to explain about both the explosive nucleation and collective diffusion. Because these systems are highly complex and involve interactions among many atoms, it is difficult to form a theoretical model that is easy to compute while thoroughly explaining the experimental data. In particular, the wetting layer remains quite a mystery, especially in its coordinated movement in delivering Pb atoms to the islands as they grow. Data from STM experiments should be very useful for building a theoretical understanding, since the STM can provide finer details to properly form the models.

7.3 Pb/Ge(110) and Pb/Ge(100)

In Chapter 6, we have performed deposition experiments on Ge(110) and Ge(100) under similar conditions as for the Ge(111) experiments. Pb/Ge(110) turned out to depart considerably from expectations, growing 1-dimensional islands at a critical coverage of 1.06ML with respect to Ge(110) that did not show height selection. These islands grew in the $[1\bar{1}0]$ direction, with their widths remaining constant at about 90-100nm. Their main similarity with the Pb/Ge(111) islands was their linear growth rate, suggesting that collective diffusion is an intrinsic property of the Pb-Ge system, regardless of the substrate's orientation.

Pb/Ge(100), on the other hand, showed explosive nucleation of height-selected islands, thus behaving very similarly to Pb/Ge(111). However, the critical coverage was much higher than was measured for Pb/Ge(111) and even seemed to vary, with 2.03ML with respect to Ge(100) for -2°C and 2.53ML for +1°C. This was attributed to the unusually high defect density on the Ge(100) surface despite extensive sample cleaning efforts, such that the defects affected the wetting layer and thus its ability to compress in a single layer.

In both systems, classical, 3D islands were found to coexist with their nonclassical counterparts in a narrow range of temperatures of 0°C to room temperature, which was found to be the boundary between the nonclassical and classical regimes. The classical islands did not nucleate below 0°C, and they tended to compete with the nonclassical islands for the deposited Pb, which halted the growth of many of the nonclassical islands. While the 3D Pb/Ge(100) islands did not exhibit any interesting features, the ones that formed on the Pb/Ge(110) system showed

preference in their orientation, forming triangles and trapezoids which we hypothesized were hexagons with several short sides due to their instability relative to the other sides.

Since Pb/Ge(111) was the main focus of this dissertation, the experiments on Pb/Ge(110) were more exploratory. This means there is a lot of future work that can be done on these systems, for both low and high temperatures. Pb/Ge(110) in particular seems to be the more interesting of the two with its directional preference, and studying the structures of these islands with the STM would be critical in understanding exactly how the substrate's symmetry affects the islands' growth. These interactions should also be good candidates for theoretical studies, where calculating the different binding energies of various facets of the islands should explain why certain sides grow while the others do not.

As for Pb/Ge(100), since we suspect much of the mechanisms behind its height-selected islands are the same as in the Pb/Ge(111) case, continuing work on Pb/Ge(111) should lead to increased understanding of the Pb/Ge(100) system. The 3D islands are poor candidates for further study, unlike the ones on Pb/Ge(110), since they lack the orientation preference. However, the presence of defects and their role in the critical coverage for explosive nucleation is one possible study that could be performed, since high defect density is something that is unavoidable for Ge(100). In fact, studying the defects themselves may be important, considering how resilient they are compared to the defects on the other germanium faces. We expect this to be very difficult to study on a theoretical level since it involves imperfections on the substrate that are likely very complicated to model.

APPENDIX A: XPS COOLING SYSTEM INTERLOCK

This system was designed to provide additional safety measures in case of a cooling system failure as a response to a previous failure that resulted in damage to multiple components involved with the X-ray source.

A.1 Circuit Diagram for Interlock Controller

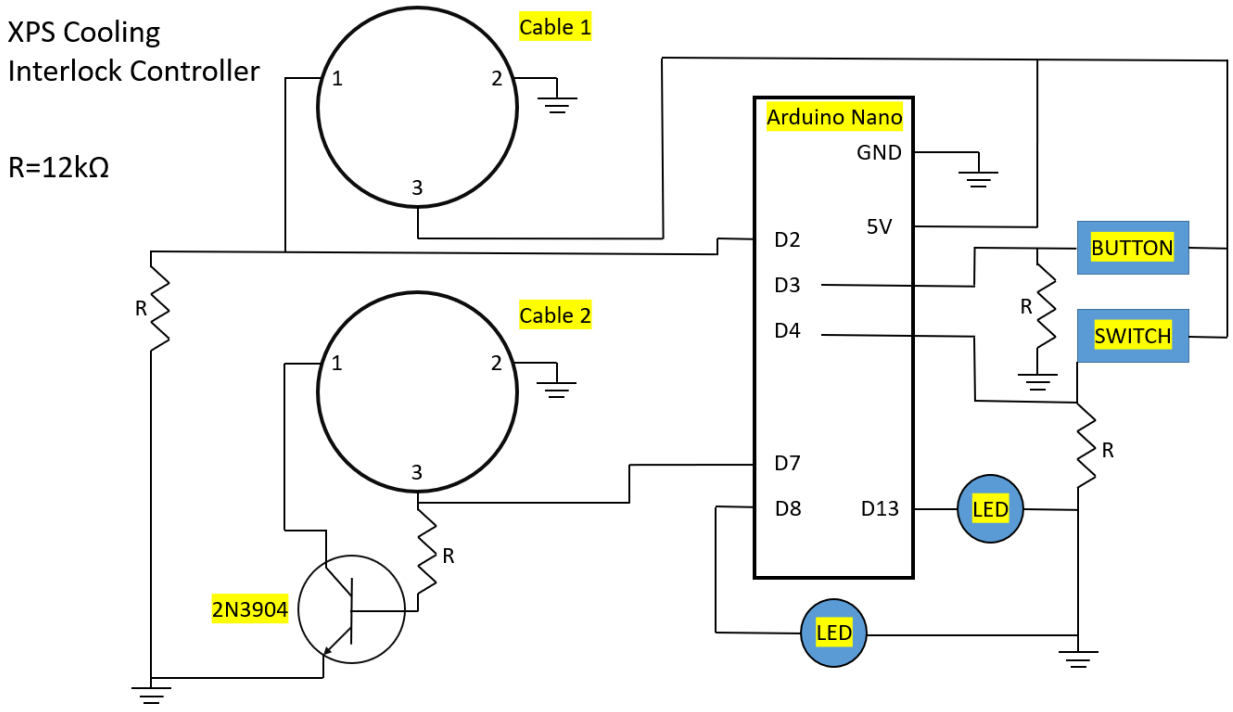

Figure A.1. Circuit diagram of the XPS cooling interlock controller.

Figure A.1 shows the circuit diagram for the interlock controller. Cable 1 connects to the water flowmeter, which consists of a propeller that is driven by the flow of water, which then sends 5V pulses whose period is proportional to the rotation rate. This pulse is fed to pin D2 on the Arduino as the input. Cable 2 connects to the X-ray source power supply's external interlock cable. When enough flow rate is detected in pin D2, pin D7 will activate the transistor and short pin 1 of cable 2, which activates the interlock. D7's signal also goes to the programmable surge protector and turns on the power for the water pump.

In the case that pin D2 fails to detect enough flow rate, pin D7's signal will turn LOW, shutting down the interlock, which will cause the power supply to stop emission. It will also deactivate the power for the water pump. The warning LED (red) will turn on to signal that the interlock has been tripped. Pressing the pushbutton will cause the controller to try detecting the water flow again, after which operations will resume if the problem has been corrected, or the warning light will turn on again if the problem persists.

The other LED (white) is simply a power light to indicate that the Arduino is running. When the interlock is tripped, the light should indicate if it was tripped due to the water flow, or if the Arduino had simply malfunctioned or lost power.

The switch is for turning the system (not Arduino) on and off. If the Arduino is connected to power from an unpowered state while the switch is in the OFF position, the red warning LED will blink (twice rapidly and once slowly) and will not activate the water pump or the interlock until the switch is placed in the ON position. When the switch is toggled from ON to OFF while the cooling system is in operation, the system will wait a certain amount of time defined by the parameter "countdowntime" before turning off the water pump, so that the X-ray source can be

fully cooled down after being shut down. Warning: Make sure the X-ray source power supply is turned OFF first! The warning LED will blink at a constant rate to signal when the controller has entered its shutdown mode. If the switch was toggled in error, it can be toggled back to the ON position during the countdown phase to end it prematurely and resume normal operations.

A.2 Arduino Code for Interlock Controller

```
const int reader=2;
const int signaler1=7;
const int signaler2=13;
const int resetpin=3;
const int pwrswitch=4;
const int lightpin=8;
const float threshold=13; //threshold for breaking interlock
const float countdowntime=10*60000; //countdown time for turning off pump
volatile int counter;
volatile int rstflag;


void setup() {
  pinMode(reader,INPUT); //reads signal from sensor
  pinMode(signaler1,OUTPUT); //interlock signal - HIGH when water flowing,
LOW when not
  pinMode(signaler2,OUTPUT); //For signaling when switch is off
  pinMode(pwrswitch,INPUT); //Switch sensor - HIGH when on, LOW when off
  pinMode(resetpin,INPUT);
  pinMode(lightpin,OUTPUT);


  if (digitalRead(pwrswitch)==LOW) {    //If the switch is turned off, gives
LED signal
    while (digitalRead(pwrswitch)==LOW) {
    digitalWrite(signaler2,HIGH);
    delay(200);
    digitalWrite(signaler2,LOW);
    delay(200);
    digitalWrite(signaler2,HIGH);
    delay(200);
    digitalWrite(signaler2,LOW);
    delay(500);
    digitalWrite(signaler2,HIGH);
    delay(1000);
    digitalWrite(signaler2,LOW);
    delay(1000);
```

```
    }
  }

  if (digitalRead(pwrswitch)==HIGH) {
    digitalWrite(lightpin,HIGH);
  }

  Serial.begin(9600);


  digitalWrite(signaler1,HIGH); //Put interlock in ON mode
  delay(8000); //delay to allow pump to power up


}

void counterscript() {
  counter++;
}

void resettoggle() {
  rstflag=0;
}

void loop() {
  int interval=5000; //counting interval in milliseconds
  counter=0;  //pulse counting variable
  int timecount=0; //time counting variable
  int pwrflag=0; //flag for power switch
  int pulseflag=0; //flag for when pulse is detected
//  unsigned long itime=millis();
//  unsigned long ftime=itime;

  attachInterrupt(digitalPinToInterrupt(reader), counterscript, RISING);
  delay(interval);
  detachInterrupt(digitalPinToInterrupt(reader));


//    if (digitalRead(reader) == HIGH) {
//        counter=counter+1;
//        pulseflag=1;
//
//        while (digitalRead(reader) == HIGH) {
//
//        }
//        while (pulseflag==1) {
//          volatile byte pulsedetect=digitalRead(reader);
//          if (pulsedetect == LOW) {
//            pulseflag=0;
//          }
//          delay(10);
//        }
//        while (pulseflag==1);
//     }


//    ftime=millis();
```

```
//    timecount=ftime-itime;
//    Serial.print(timecount);
//    Serial.print("\n");
//    if (timecount<0) { //case when millis overflows, just redo interval
//      timecount=0;
//      counter=0;
//      itime=millis();
//      ftime=itime;
//      }


  float dtime=interval/1000; //elapsed time in seconds
  float rate=counter/dtime;


  Serial.print("Pulse Rate: ");
  Serial.print(float(rate));
  Serial.print(" Hz");
  Serial.print("\n");

  if (rate<threshold) {

    digitalWrite(signaler1,LOW); //Disable interlock if rate is below
threshold
    digitalWrite(signaler2,HIGH);
    rstflag=1;

    while (rstflag==1) { //use push button to reset
      attachInterrupt(digitalPinToInterrupt(resetpin), resettoggle, RISING);
    }

    detachInterrupt(digitalPinToInterrupt(resetpin));



    digitalWrite(signaler1,HIGH);
    digitalWrite(signaler2,LOW);
    delay(8000);
  }



  if (digitalRead(pwrswitch)==LOW) {   //powering down procedure
    pwrflag=1;
    float countdown=0;
    while ((countdown<countdowntime) && (pwrflag==1)) {

      digitalWrite(lightpin,HIGH);
      delay(500);
      digitalWrite(lightpin,LOW);
      delay(500);
      countdown=countdown+1000;
      Serial.print(countdown);
      Serial.print("\n");
      if (digitalRead(pwrswitch)==HIGH) { //if power switch is flipped back
on during countdown
        pwrflag=0;
```

```
        digitalWrite(lightpin,HIGH);
      }
    }

    if ((pwrflag==1) && (countdown>=countdowntime)) {
      digitalWrite(signaler1,LOW);
    }
  }

  if (pwrflag==1) {
    while (digitalRead(pwrswitch)==LOW) { //stall program while power switch
is off

      digitalWrite(lightpin,HIGH);
      delay(2000);
      digitalWrite(lightpin,LOW);
      delay(2000);
    }

    if (digitalRead(pwrswitch==HIGH)) { //if power switch is turned back on,
resume operations
      pwrflag=0;
      digitalWrite(lightpin,HIGH);
      digitalWrite(signaler1,HIGH);
      delay(8000);
    }
  }

}
```

APPENDIX B: REAL VS THERMOCOUPLE TEMPERATURE RELATIONSHIP

B.1 Discussion of Method and Results

A test was performed on a germanium sample to verify the linear relationship between the thermocouple temperature and the real temperature. During temperature calibration in the XPS chamber for sample cleaning, the temperature was gradually increased towards the target temperature of 800°C. The infrared pyrometer could only read temperatures above 550°C, so readings were only taken between 550 and 800°C. Each time the temperature was raised, we waited 10 minutes for equilibrium to be reached, and the heating filament and high voltage settings were recorded. The sample was then moved into the LEEM, where the recorded settings were used to take the sample to each recorded temperature, and the LEEM's thermocouple reading was recorded after allowing 10 minutes for equilibrium at each step.

The result is plotted in Figure B.1, with a linear fit superimposed. The (20,20) point was a given since the thermocouple would always read room temperature when the sample was allowed to come to equilibrium with the room overnight. The linear fit seems to agree very well with the data, although a quadratic fit was also found to have very low residuals, suggesting that either linear or quadratic relationship would work with very little difference between the two, at least for the temperature ranges involved in these experiments.

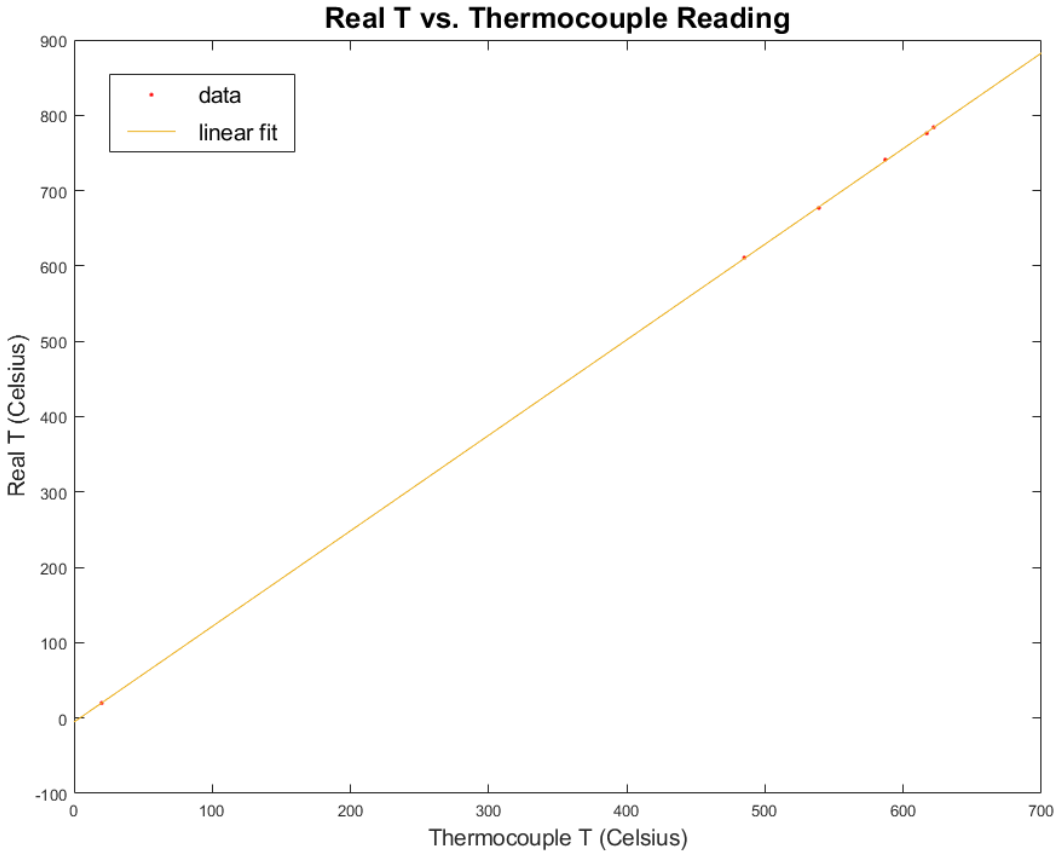

Figure B.1. Plot of the real temperature of a Ge(111) sample as a function of thermocouple reading, with a linear fit superimposed.

With this proof of linear relationship, other experiments do not need to take multiple data points to obtain a linear equation but rather simply need two points to form the first linear extrapolation, namely the room temperature (RT,RT) and the annealing temperature, plotted in Figure B.2 for a hypothetical case in which the thermocouple reads 600°C when the infrared pyrometer reads 800°C (600,800). Given the two points, (RT,RT) and (T_1,T_2), the slope of the extrapolated line is $s = \frac{(T_2 - RT)}{(T_1 - RT)}$, which gives us the linear equation

$$T_{real} = s \times T_{thermo} + y_0, \qquad T_{thermo} \geq RT, \tag{B.1}$$

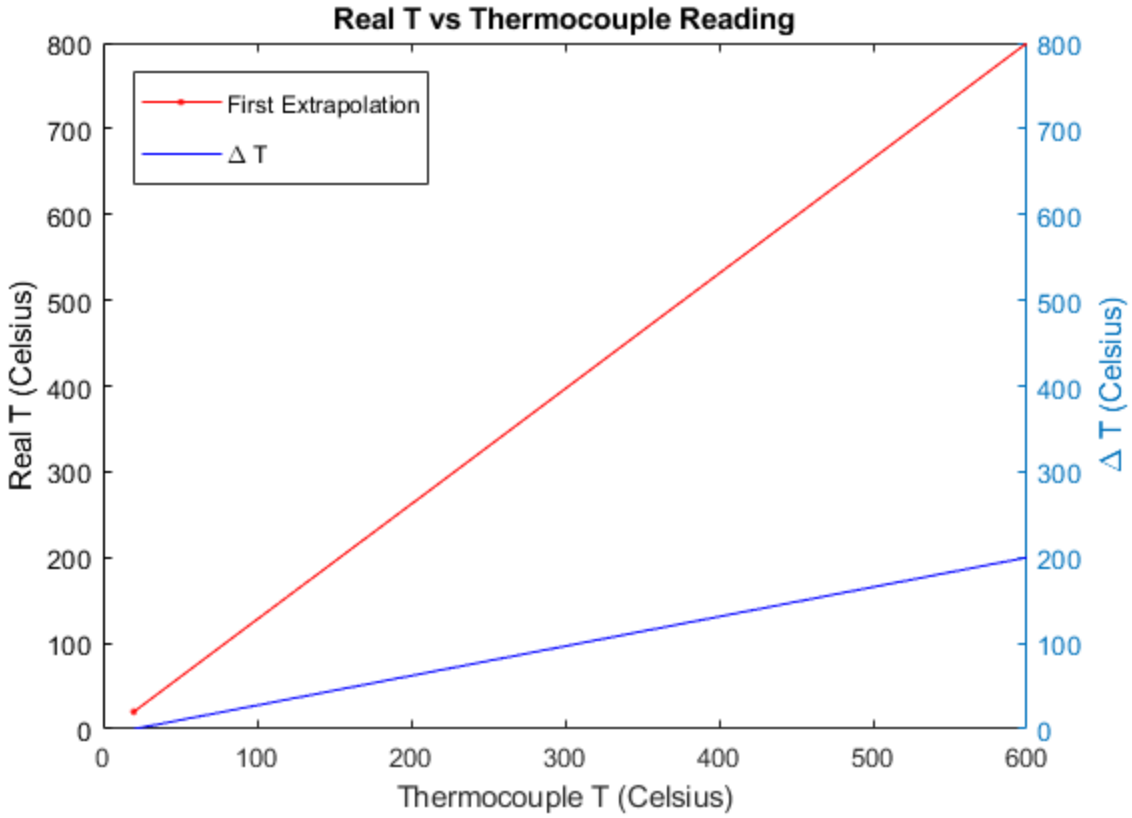

Figure B.2. Plot of real temperature versus thermocouple temperature (red) and the difference between real temperature and thermocouple temperature (blue). The blue line essentially represents the temperature gradient between the sample and the location of the thermocouple.

where $y_0 = RT(1-s)$ is the y-intercept of the equation derived by substituting the point (RT,RT) into Equation B.1. One thing to note is that each sample, as well as each sample holder, behaves differently with a different temperature gradient, so the annealing temperature needs to be calibrated each time a new sample is used to obtain (T_1,T_2), for a new extrapolation specific to that sample and sample holder.

From the first extrapolation, we take the difference between the real temperature and the thermocouple temperature, $\Delta T = T_{real} - T_{thermo}$, and plot it as a function of thermocouple temperature, also shown in Figure B.2. Using Equation B.1, ΔT takes the form

$$\Delta T = (s-1) \times T_{thermo} + y_0, \qquad T_{thermo} \geq RT. \tag{B.2}$$

This represents the gradient between the sample and the location of the thermocouple caused by the heating filament. As mentioned in chapter 4, we expect this gradient effect to be the same at lower temperatures due to the heating filament, which is used to keep the sample temperature constant. The heating filament will cause the sample to always be hotter than the rest of the sample holder, such that the relationship $\Delta T > 0$ still holds as was the case for high temperatures. This means the ΔT line must be reflected horizontally about the (RT,RT) equilibrium point, as shown by the thick, blue line in Figure B.3. For the reflected line, we adjust Equation B.2 to get

$$\Delta T = (1 - s) \times T_{thermo} - y_0, \qquad T_{thermo} < RT. \tag{B.3}$$

To get T_{real} as a function of T_{thermo} for temperatures below RT, we want to put Equation B.3 into the form $\Delta T = T_{real} - T_{thermo}$. This can be done by adding and subtracting T_{thermo} to get

$$\Delta T = (1 - s) \times T_{thermo} + T_{thermo} - T_{thermo} - y_0,$$

$$\Delta T = (2 - s) \times T_{thermo} - y_0 - T_{thermo},$$

$$T_{real} = (2 - s) \times T_{thermo} - y_0, \qquad T_{thermo} < RT. \tag{B.4}$$

Thus, by using the gradient ΔT as a constraint, we can extrapolate the real temperature below room temperature where calibration using the infrared pyrometer is impossible. Equation B.4 is plotted for our example scenario in Figure B.3 as the thick, red line.

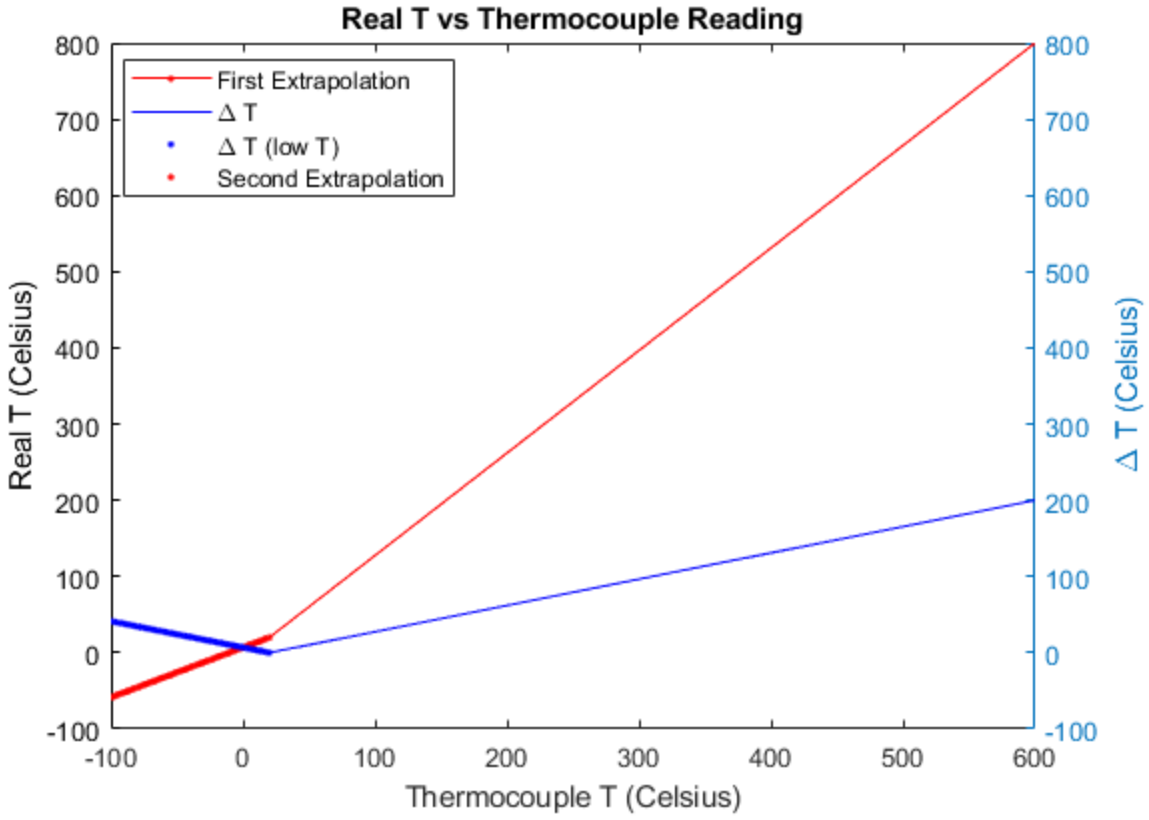

Figure B.3. Plot of real temperature versus thermocouple temperature (red) and the difference between real temperature and thermocouple temperature (blue). The thicker lines are the extrapolations for temperatures below room temperature. Identical to Figure 4.6, reproduced for ease of reference.

B.2 MATLAB Code for Extrapolation

This code was used to automatically extrapolate any temperature given the annealing temperature calibration and the measured, thermocouple reading to be extrapolated to real temperature. It requires three inputs: “thermot,” which is the thermocouple reading at the annealing temperature, “pyrot” which is the infrared pyrometer reading at the annealing temperature, and “measuret” which is the measured thermocouple temperature that is being

extrapolated to the output, which is “realt.” The room temperature can be defined in the code using the variable “rt.” The function will automatically generate the slopes and y-intercepts for the extrapolation lines based on the mathematics discussed in section B.1.

```
function [realt] = tempcalc2(thermot,pyrot,measuret)

rt=20;

slope=(pyrot-rt)/(thermot-rt);

yint=pyrot-slope*thermot;

if measuret==rt
    realt=measuret;

elseif measuret>rt

    realt=slope*measuret+yint;

elseif measuret<rt

    realt=(2-slope)*measuret-yint;

end


end
```

APPENDIX C: MATLAB CODES FOR IV CURVE ANALYSIS

C.1 Image Processing

This code would take images of a chosen island or wetting layer region contained inside a chosen folder and automatically average the intensity and store the values in an array. Since there was no reasonable way to program a method to automatically identify the islands (due to poor intensity at some start voltages), these images had to be prepared beforehand by cropping the desired portions of each data image.

The images were saved with filenames with the format x-y.png, where x is the integer of the start voltage, while y is the tenths digit of the start voltage. For example, an image for the start voltage of 10.4V would be named as 10-4.png. The images were placed in folders named either “island” or “WL” depending on whether they are from an island or from the wetting layer. These two folders would be placed in a single folder named set(n), where (n) is an integer meant to distinguish between each set of images. The actual integer would not include the parentheses; an example folder name would be “set1.” The input parameter “wlflag” was to tell the function to check for the wetting layer folder so that both the island and wetting layer could be processed together (since usually one does not bother to do an IV curve on the wetting layer).

```
function [datais,datawl] = ivprocess(setnum,wlflag)

isfolder=['E:\Main Files\Davis\Chiang Lab\Data\LEEM Data\IV Curve
Analysis\Process\set' num2str(setnum) '\island'];
```

```
wlfolder=['E:\Main Files\Davis\Chiang Lab\Data\LEEM Data\IV Curve
Analysis\Process\set' num2str(setnum) '\WL'];



isinfo=dir(fullfile(isfolder,'*.png'));
wlinfo=dir(fullfile(wlfolder,'*.png'));
for xx=1:1:length(isinfo)
imgname=isinfo(xx).name;

c1=strsplit(imgname,'.');
c2=strsplit(string(c1(1)),'-');
c2a=str2num(c2(1));
c2b=str2num(c2(2));
c3=[num2str(c2a) '.' num2str(c2b)];
datais(xx,1)=str2num(c3);

imguse=imread([isfolder '\' imgname]);
%img1=(imguse(:,:,1)+imguse(:,:,2)+imguse(:,:,3))/3;
datais(xx,2)=mean(imguse,'all');

end


if wlflag==1
for xx=1:1:length(wlinfo)
imgname=wlinfo(xx).name;

c1=strsplit(imgname,'.');
c2=strsplit(string(c1(1)),'-');
c2a=str2num(c2(1));
c2b=str2num(c2(2));
c3=[num2str(c2a) '.' num2str(c2b)];
datawl(xx,1)=str2num(c3);

imguse=imread([wlfolder '\' imgname]);
img1=(imguse(:,:,1)+imguse(:,:,2)+imguse(:,:,3))/3;
datawl(xx,2)=mean(img1,'all');

end
else
    datawl=[];
end


end
```

C.2. Parameter Generation

Since some of the parameters were related to each other through certain constraints as discussed in section 2 of chapter 5, the following code was used to quickly generate the constrained parameters (w_a, v_g) based on a few, chosen parameters.

```
function [params] = kpparam(layers,constraints)

%constraints should have the form
%[layer_thickness,inner potential,w_a,V_a,V_0]

params=zeros(length(layers),6);


wg=constraints(1)-constraints(3);
Vg=(constraints(2)*constraints(1)-constraints(3)*constraints(4))/wg;


for xx=1:1:length(layers)
   params(xx,1)=layers(xx);
   params(xx,2)=constraints(3);
   params(xx,3)=wg;
   params(xx,4)=constraints(4);
   params(xx,5)=Vg;
   params(xx,6)=constraints(5);

end


end
```

C.3 IV Curve Simulation

The following code is the main code that would generate the matrix equation of the Kronig-Penney model as dictated by the input parameters and then solve for the reflected intensity as a function of electron energy. The main curve-fitting script in C.4 was designed to automatically use this code for different layers and plot them with the experimental curves for comparison. Otherwise, this code can be used by itself for generating single IV curves.

```
function [output]=ivKP(param,plotflag,Earray)


hc=197.33;
melectron=511000;
if nargin<3
EEE=0:0.01:30;
else
EEE=Earray;
end
output=zeros(length(EEE),1);
%param should have [n,w_a,w_g,v_a,v_g,v0]
wa=param(2);
wg=param(3);
va=param(4);
vg=param(5);
v0=param(6);


%setting up matrices/arrays
nn=param(1);

matl=zeros(2*(2*nn+1));
matr=zeros(2*(2*nn+1));

solarray=zeros(4*nn+2,1);

xbound=zeros(2*nn+1,1);

karray=zeros(2*nn+2,1);



%filling parameter arrays
```

```
for mm=1:1:length(xbound)

    if mod(mm,2)==1
       xbound(mm)=((mm-1)/2)*(wa+wg);
    end

    if mod(mm,2)==0
       xbound(mm)=(mm/2)*wa+(mm/2-1)*wg;
    end
end

for xx=1:1:length(EEE)
EE=EEE(xx);

karray(1)=sqrt(2*melectron*EE/hc^2); %k0
karray(length(karray))=sqrt(2*melectron*(EE+v0)/hc^2); %kf
for mm=2:1:(length(karray)-1)
    if mod(mm,2)==1 %vg
       karray(mm)=sqrt(2*melectron*(EE+vg)/hc^2);
    end

    if mod(mm,2)==0 %va
       karray(mm)=sqrt(2*melectron*(EE+va)/hc^2);
    end
end


%filling equation matrices
matl(1,1)=1;
matl(2,1)=-1i*karray(1);

matr(2*length(xbound)-
1,2*length(xbound))=exp(1i*karray(length(karray))*xbound(length(xbound)));
matr(2*length(xbound),2*length(xbound))=1i*karray(length(karray))*exp(1i*karr
ay(length(karray))*xbound(length(xbound)));

for mm=1:1:(length(xbound))
    %row, column

    if mm>1

    %first condition
    matl(2*mm-1,2*(mm-1))=exp(1i*karray(mm)*xbound(mm));
    matl(2*mm-1,2*mm-1)=exp(-1i*karray(mm)*xbound(mm));

    %derivative condition
    matl(2*mm,2*(mm-1))=1i*karray(mm)*exp(1i*karray(mm)*xbound(mm));
    matl(2*mm,2*mm-1)=-1i*karray(mm)*exp(-1i*karray(mm)*xbound(mm));

    end

    if mm<length(xbound)

    %first condition
```

```
    matr(2*mm-1,2*mm)=exp(1i*karray(mm+1)*xbound(mm));
    matr(2*mm-1,2*mm+1)=exp(-1i*karray(mm+1)*xbound(mm));

    %derivative condition
    matr(2*mm,2*mm)=1i*karray(mm+1)*exp(1i*karray(mm+1)*xbound(mm));
    matr(2*mm,2*mm+1)=-1i*karray(mm+1)*exp(-1i*karray(mm+1)*xbound(mm));

    end

end

%solution array
solarray(1)=-1;
solarray(2)=-1i*karray(1);

%big matrix
matsol=matl-matr;


sol=linsolve(matsol,solarray);

output(xx)=sol(1)*conj(sol(1));

end
if plotflag==1
plot(EEE,output,'.r');
xlabel('Start Voltage (eV)');
ylabel('Normalized Intensity');
title(['Number of Layers = ',num2str(nn)]);
end
end
```

C.4 Curve Fitting

This code was used to quickly generate simulated IV curves using the previous two codes and plot them over experimental IV curves so that they could be compared for fit quality. With this, many fitting parameters could be tested with reasonable speed. The code also allowed for some artificial shifting of data and simulation to account for instrumental shifts either due to work function differences or due to background. The inputs are as follows:

1. "data" – matrix containing the experimental IV curve points, including start voltage and intensity
2. "fitparams" – parameters for shifting/scaling the simulated IV curves for fitting to experimental curves. The fourth parameter, "background," is for subtracting background from the experimental curve, if such information is available. Leave "background" as 0 if no background subtraction is to be done. The others must be manually chosen for best fit.
3. "layers" – an array containing the different number of layers to be simulated.
4. "constraints" – the set of constraints to be used with the code in C.2 to generate the IV curve simulation parameters.
5. "Earray" – an array of start voltage values for the simulated IV curves.
6. "flag" – set as 0 if doing island, set as 1 if doing wetting layer, which should be the 3rd column of the data matrix.
7. "plotflag" – set as 0 if only the output matrix is wanted, otherwise set as 1 to tell the code to plot the output curves.

```
function [curves] =
ivcurvefit(data,fitparams,layers,constraints,Earray,flag,plotflag)
%constraints should have the form
%[layer_thickness,inner potential,w_a,V_a,V_0

%fitparams should have the form
%[xshift yscale yshift background]


xdata=data(:,1);
if flag==0
    ydata=data(:,2)-fitparams(4)./xdata;
else
    ydata=data(:,3)-fitparams(4)./xdata;
end

[params] = kpparam(layers,constraints);

for xx=1:1:length(layers)
[output]=ivKP(params(xx,:),0,Earray);
curves(xx,:)=output;
figure(xx);
plot(xdata,ydata,'.r');
title([num2str(layers(xx)),' Layers']);
hold on
plot(Earray+fitparams(1),output*fitparams(2)+fitparams(3),'-b');
hold off

end

if plotflag==1
   for yy=1:1:(length(layers)-1)
   curves(yy+length(layers),:)=curves(yy,:)+curves(yy+1,:);
   figure(yy+length(layers));
    plot(xdata,ydata,'.r');
    title([num2str(layers(yy)),'+',num2str(layers(yy+1))]);
    hold on

plot(Earray+fitparams(1),curves(yy+length(layers),:)*fitparams(2)+fitparams(3
),'-b');
    hold off

   end

end

end
```

APPENDIX D: AREAS OF UNIT CELLS AND COVERAGE CONVERSIONS

Since this dissertation often compares coverages with respect to various faces of germanium as well as those of other surfaces, it would be useful to briefly discuss how coverage calculations are performed, and how coverages are converted between different surfaces.

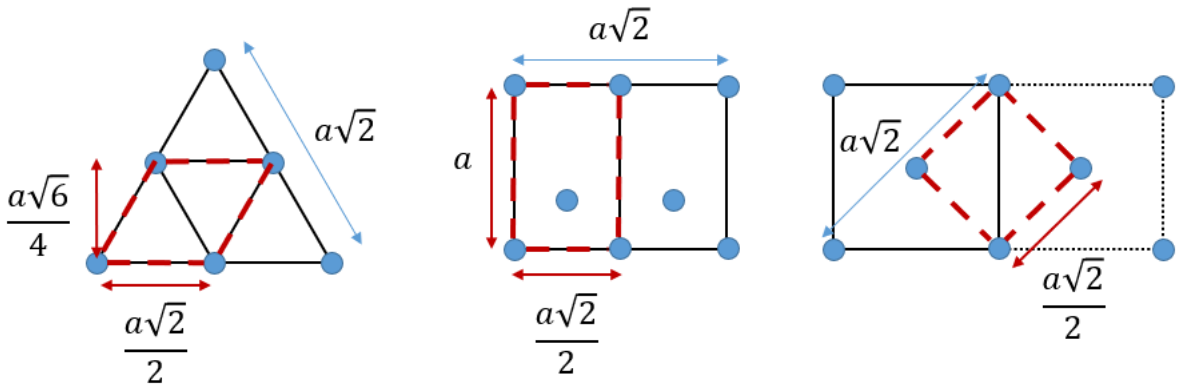

(111) $A = \frac{a^2\sqrt{3}}{4}$ (110) $A = \frac{a^2\sqrt{2}}{2}$ (100) $A = \frac{a^2}{2}$

Figure D.1. Ball-and-stick models of the three faces of germanium from Figure 3.1 reproduced with the areas for the unit cells displayed.

1ML is defined with respect to a surface as 1 atom per primitive unit cell. As such, $1/A_{cell}$ will give the coverage in units of atoms per unit area. In order to convert from a coverage with respect to a surface, θ_1, to coverage with respect to a second surface, θ_2, the conversion equation is simply

$$\theta_2 = \frac{A_2}{A_1}\theta_1,$$

where A_1 and A_2 are the areas of the primitive unit cells of the first and second surfaces, respectively. The lattice constants and primitive unit cell areas for the surfaces considered in this dissertation are listed in Table D.1.

Table D.1. Unit cell values for various surfaces used in this dissertation.

Surface	Lattice Constant (Å)	Primitive Unit Cell Area ($Å^2$)
Ge(111)	5.658	13.86
Ge(110)	5.658	22.64
Ge(100)	5.658	16.01
Pb(111)	4.951	10.61
Si(111)	5.431	12.77

PERMISSIONS TO REPRODUCE FIGURES

Figure 2.1

ELSEVIER LICENSE
TERMS AND CONDITIONS

May 06, 2022

This Agreement between Mr. Andrew Kim ("You") and Elsevier ("Elsevier") consists of your license details and the terms and conditions provided by Elsevier and Copyright Clearance Center.

License Number	5303011217006
License date	May 06, 2022
Licensed Content Publisher	Elsevier
Licensed Content Publication	Materials Science and Engineering: B
Licensed Content Title	A unique facility for surface microscopy
Licensed Content Author	C.L.H Devlin,D.N Futaba,A Loui,J.D Shine,S Chiang
Licensed Content Date	Nov 1, 2002
Licensed Content Volume	96
Licensed Content Issue	2

Licensed Content Pages	6
Start Page	215
End Page	220
Type of Use Portion	reuse in a thesis/dissertation figures/tables/illustrations
Number of figures/tables/illustrations	1
Format	electronic
Are you the author of this Elsevier article?	No
Will you be translating?	No
Title	Nucleation and Growth of Pb Islands on Germanium Via Collective Diffusion
Institution name	University of California Davis
Expected presentation date	Jun 2022
Portions	Figure 1

Figure 2.2

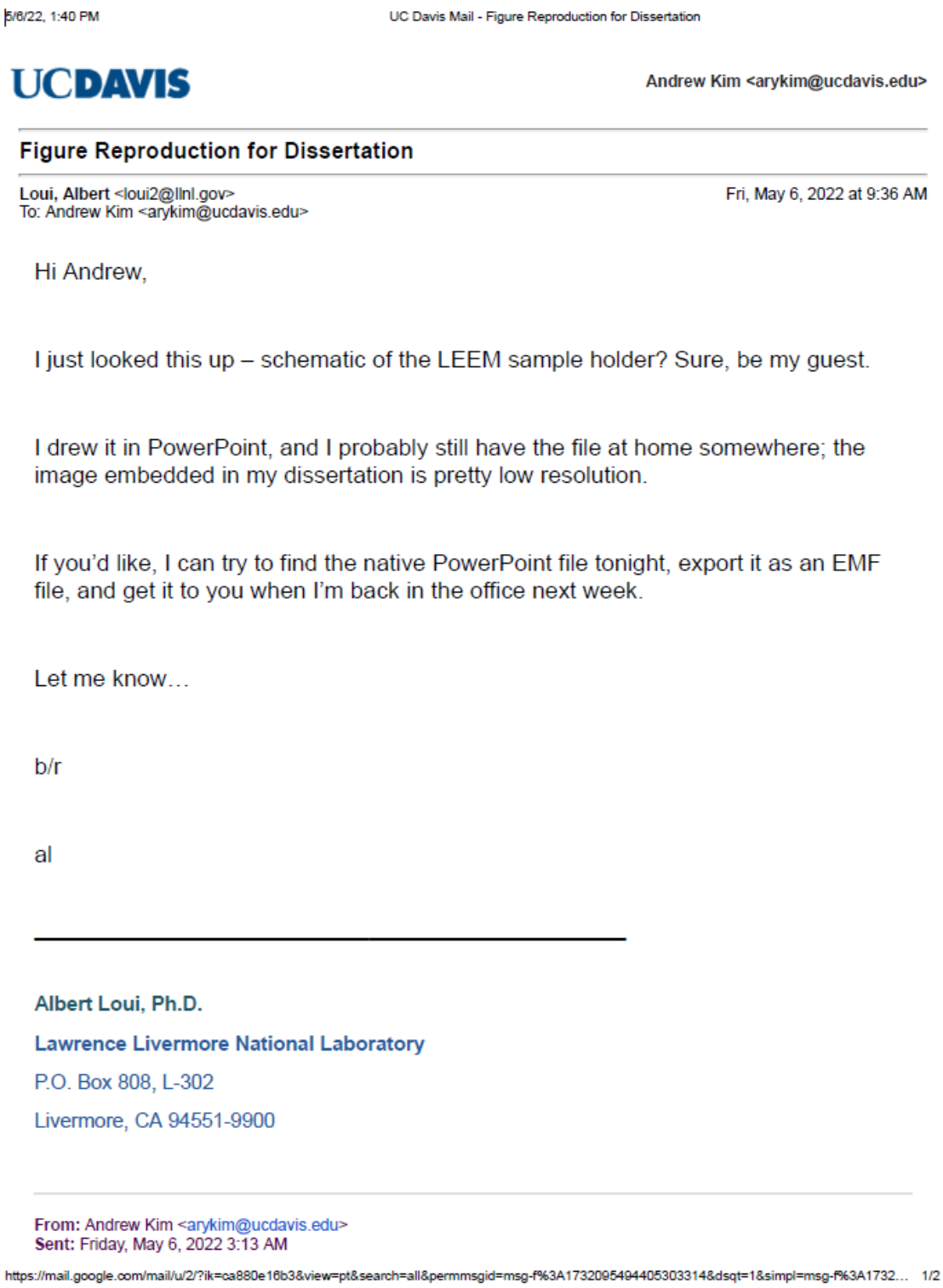

5/6/22, 1:40 PM UC Davis Mail - Figure Reproduction for Dissertation

UCDAVIS

Andrew Kim <arykim@ucdavis.edu>

Figure Reproduction for Dissertation

Loui, Albert <loui2@llnl.gov> Fri, May 6, 2022 at 9:36 AM
To: Andrew Kim <arykim@ucdavis.edu>

Hi Andrew,

I just looked this up – schematic of the LEEM sample holder? Sure, be my guest.

I drew it in PowerPoint, and I probably still have the file at home somewhere; the image embedded in my dissertation is pretty low resolution.

If you'd like, I can try to find the native PowerPoint file tonight, export it as an EMF file, and get it to you when I'm back in the office next week.

Let me know…

b/r

al

Albert Loui, Ph.D.

Lawrence Livermore National Laboratory

P.O. Box 808, L-302

Livermore, CA 94551-9900

From: Andrew Kim <arykim@ucdavis.edu>
Sent: Friday, May 6, 2022 3:13 AM

https://mail.google.com/mail/u/2/?ik=ca880e16b3&view=pt&search=all&permmsgid=msg-f%3A1732095494405303314&dsqt=1&simpl=msg-f%3A1732… 1/2

To: Loui, Albert <loui2@llnl.gov>
Subject: Figure Reproduction for Dissertation

Hello, I hope you are doing well. I'm a graduate student working for Shirley Chiang, and I am in the process of finishing my dissertation. I wish to reproduce Figure 3.2 of your dissertation, so I must ask you for written permission to use it.

If this is no problem for you, then please reply in the affirmative.

-Andrew Kim

Figure 2.4

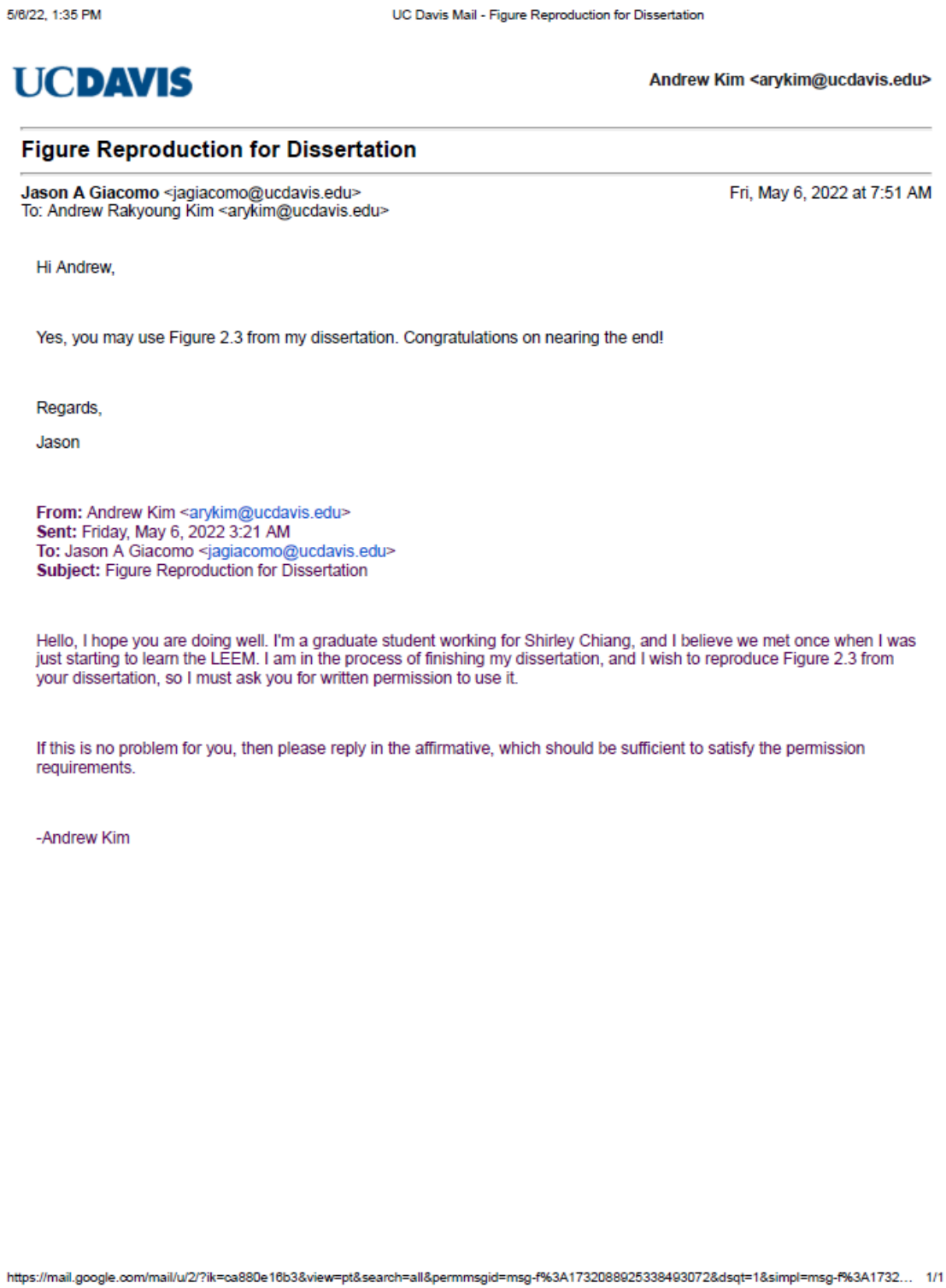

5/6/22, 1:35 PM UC Davis Mail - Figure Reproduction for Dissertation

UCDAVIS

Andrew Kim <arykim@ucdavis.edu>

Figure Reproduction for Dissertation

Jason A Giacomo <jagiacomo@ucdavis.edu> Fri, May 6, 2022 at 7:51 AM
To: Andrew Rakyoung Kim <arykim@ucdavis.edu>

Hi Andrew,

Yes, you may use Figure 2.3 from my dissertation. Congratulations on nearing the end!

Regards,

Jason

From: Andrew Kim <arykim@ucdavis.edu>
Sent: Friday, May 6, 2022 3:21 AM
To: Jason A Giacomo <jagiacomo@ucdavis.edu>
Subject: Figure Reproduction for Dissertation

Hello, I hope you are doing well. I'm a graduate student working for Shirley Chiang, and I believe we met once when I was just starting to learn the LEEM. I am in the process of finishing my dissertation, and I wish to reproduce Figure 2.3 from your dissertation, so I must ask you for written permission to use it.

If this is no problem for you, then please reply in the affirmative, which should be sufficient to satisfy the permission requirements.

-Andrew Kim

https://mail.google.com/mail/u/2/?ik=ca880e16b3&view=pt&search=all&permmsgid=msg-f%3A1732088925338493072&dsqt=1&simpl=msg-f%3A1732... 1/1

Figure 3.7

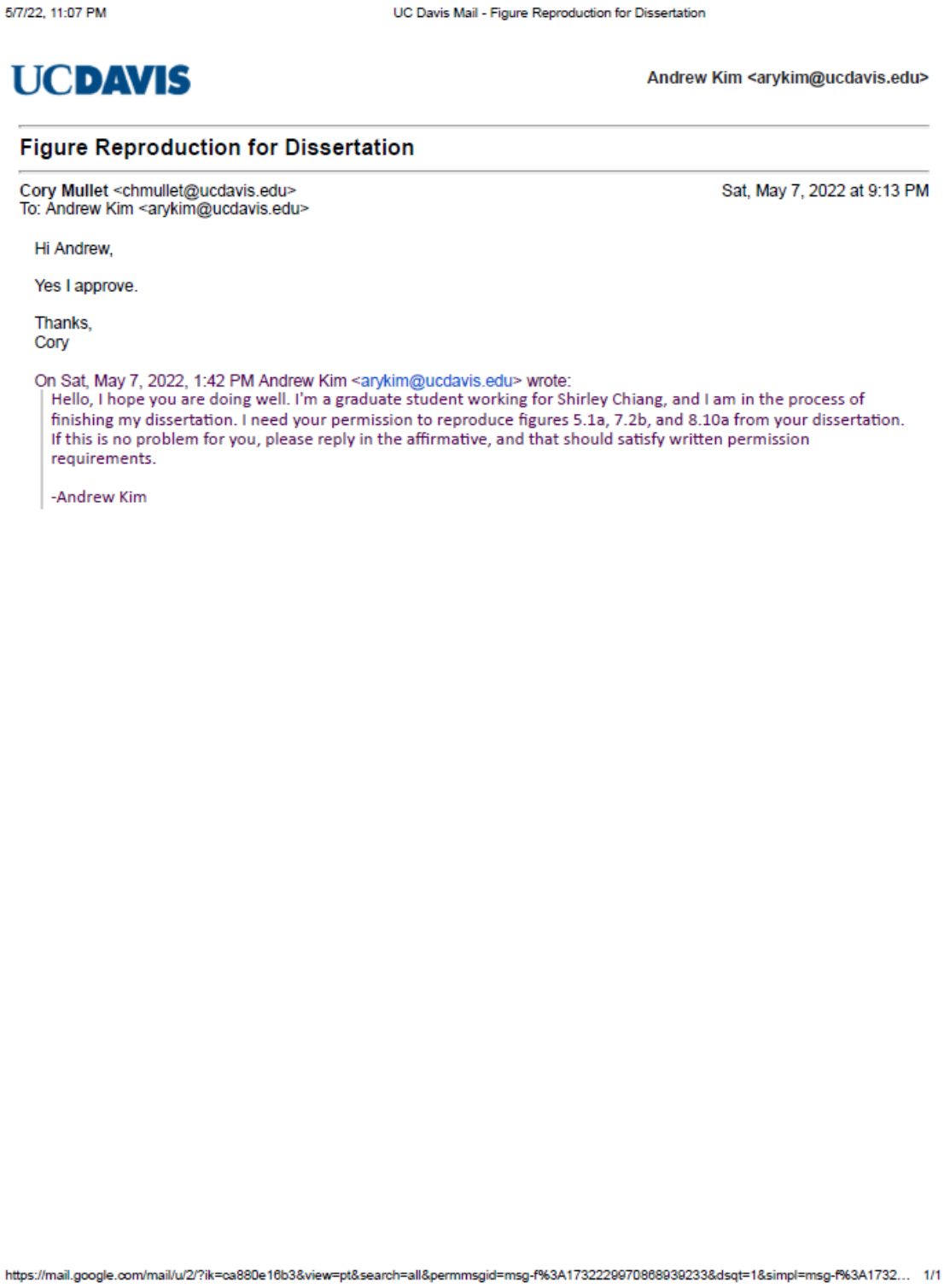

5/7/22, 11:07 PM UC Davis Mail - Figure Reproduction for Dissertation

UCDAVIS

Andrew Kim <arykim@ucdavis.edu>

Figure Reproduction for Dissertation

Cory Mullet <chmullet@ucdavis.edu> Sat, May 7, 2022 at 9:13 PM
To: Andrew Kim <arykim@ucdavis.edu>

Hi Andrew,

Yes I approve.

Thanks,
Cory

On Sat, May 7, 2022, 1:42 PM Andrew Kim <arykim@ucdavis.edu> wrote:

> Hello, I hope you are doing well. I'm a graduate student working for Shirley Chiang, and I am in the process of finishing my dissertation. I need your permission to reproduce figures 5.1a, 7.2b, and 8.10a from your dissertation. If this is no problem for you, please reply in the affirmative, and that should satisfy written permission requirements.
>
> -Andrew Kim

https://mail.google.com/mail/u/2/?ik=ca880e16b3&view=pt&search=all&permmsgid=msg-f%3A1732229970868939233&dsqt=1&simpl=msg-f%3A1732... 1/1

Figure 4.1, Figure 4.2

ELSEVIER LICENSE
TERMS AND CONDITIONS

May 06, 2022

This Agreement between Mr. Andrew Kim ("You") and Elsevier ("Elsevier") consists of your license details and the terms and conditions provided by Elsevier and Copyright Clearance Center.

License Number	5303030455177
License date	May 06, 2022
Licensed Content Publisher	Elsevier
Licensed Content Publication	Surface Science
Licensed Content Title	Uniform island height selection in the low temperature growth of Pb/Si(111)-(7×7)
Licensed Content Author	M. Hupalo,S. Kremmer,V. Yeh,L. Berbil-Bautista,E. Abram,M.C. Tringides
Licensed Content Date	Nov 1, 2001
Licensed Content Volume	493
Licensed Content Issue	1-3
Licensed Content Pages	13

Start Page	526
End Page	538
Type of Use	reuse in a thesis/dissertation
Portion	figures/tables/illustrations
Number of figures/tables/illustrations	2
Format	electronic
Are you the author of this Elsevier article?	No
Will you be translating?	No
Title	Nucleation and Growth of Pb Islands on Germanium Via Collective Diffusion
Institution name	University of California Davis
Expected presentation date	Jun 2022
Portions	Figure 2, Figure 8

Figure 4.3

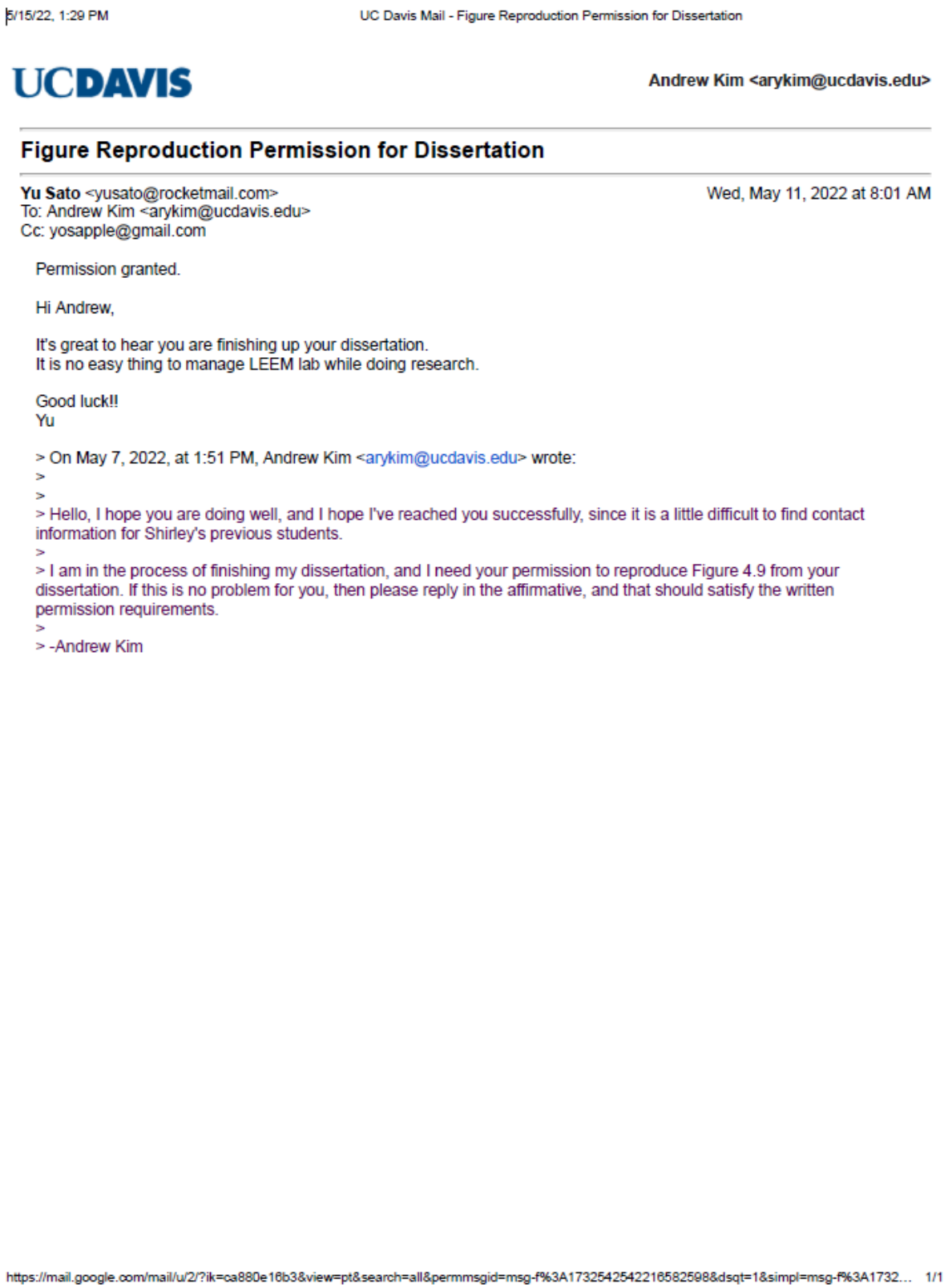

5/15/22, 1:29 PM UC Davis Mail - Figure Reproduction Permission for Dissertation

UCDAVIS

Andrew Kim <arykim@ucdavis.edu>

Figure Reproduction Permission for Dissertation

Yu Sato <yusato@rocketmail.com> Wed, May 11, 2022 at 8:01 AM
To: Andrew Kim <arykim@ucdavis.edu>
Cc: yosapple@gmail.com

Permission granted.

Hi Andrew,

It's great to hear you are finishing up your dissertation.
It is no easy thing to manage LEEM lab while doing research.

Good luck!!
Yu

> On May 7, 2022, at 1:51 PM, Andrew Kim <arykim@ucdavis.edu> wrote:
>
>
> Hello, I hope you are doing well, and I hope I've reached you successfully, since it is a little difficult to find contact information for Shirley's previous students.
>
> I am in the process of finishing my dissertation, and I need your permission to reproduce Figure 4.9 from your dissertation. If this is no problem for you, then please reply in the affirmative, and that should satisfy the written permission requirements.
>
> -Andrew Kim

https://mail.google.com/mail/u/2/?ik=ca880e16b3&view=pt&search=all&permmsgid=msg-f%3A1732542542216582598&dsqt=1&simpl=msg-f%3A1732... 1/1

Figure 5.2

CCC Marketplace™

This is a License Agreement between Andrew Kim ("User") and Copyright Clearance Center, Inc. ("CCC") on behalf of the Rightsholder identified in the order details below. The license consists of the order details, the CCC Terms and Conditions below, and any Rightsholder Terms and Conditions which are included below.

All payments must be made in full to CCC in accordance with the CCC Terms and Conditions below.

Order Date	12-May-2022	Type of Use	Republish in a thesis/dissertation
Order License ID	1220887-1		
ISSN	0218-625X	Publisher	WORLD SCIENTIFIC PUBLISHING CO. PTE. LTD.
		Portion	Chart/graph/table/figure

LICENSED CONTENT

Publication Title	Surface review and letters	Publication Type	Journal
Article Title	LEEM Phase Contrast	Start Page	1129
Date	12/31/1993	End Page	1141
Language	English	Issue	06
Country	Singapore	Volume	05
Rightsholder	World Scientific Publishing Co., Inc.		

REQUEST DETAILS

Portion Type	Chart/graph/table/figure	Distribution	Worldwide
Number of charts / graphs / tables / figures requested	1	Translation	Original language of publication
		Copies for the disabled?	No
Format (select all that apply)	Electronic	Minor editing privileges?	No
Who will republish the content?	Not-for-profit entity	Incidental promotional use?	No
Duration of Use	Life of current edition	Currency	USD
Lifetime Unit Quantity	Up to 499		
Rights Requested	Main product		

NEW WORK DETAILS

Title	Nucleation and Growth of Pb Islands on Germanium Via Collective Diffusion	Institution name	University of California Davis
		Expected presentation date	2022-06-09
Instructor name	Andrew Kim		

ADDITIONAL DETAILS

Order reference number	N/A	The requesting person / organization to appear on the license	Andrew Kim

REUSE CONTENT DETAILS

Title, description or numeric reference of the portion(s)	Figure 9	Title of the article/chapter the portion is from	LEEM Phase Contrast
Editor of portion(s)	Altman, M. S.; Chung, W. F.; Liu, C. H.	Author of portion(s)	Altman, M. S.; Chung, W. F.; Liu, C. H.
Volume of serial or monograph	05	Issue, if republishing an article from a serial	06
Page or page range of portion	1129-1141	Publication date of portion	1998-11-30